Alma Mater Studiorum – Università di Bologna

DOTTORATO DI RICERCA IN

NANOSCIENZE PER LA MEDICINA E PER L'AMBIENTE

Ciclo 35

**Settore Concorsuale:** 02/B1 - FISICA SPERIMENTALE DELLA MATERIA

**Settore Scientifico Disciplinare:** FIS/03 - FISICA DELLA MATERIA

# INVESTIGATION OF ORGANIC SEMICONDUCTOR/WATER INTERFACES FOR OPTOBIOELECTRONIC DEVICES

**Presentata da:** Luca Bondi

**Coordinatore Dottorato**

Dario Braga

**Supervisore**

Tobias Cramer

**Co-supervisore**

Beatrice Fraboni

**Esame finale anno 2023**

# Abstract

The thesis investigates the potential of photoactive organic semiconductors as a new class of materials for developing bioelectronic devices that can convert light into biological signals. The materials can be either small molecules or polymers. When these materials interact with aqueous biological fluids, they give rise to various electrochemical phenomena, including photofaradaic or photocapacitive processes, depending on whether photogenerated charges participate in redox processes or accumulate at an interface.

The thesis starts by studying the behavior of the H2Pc/PTCDI molecular p/n thin-film heterojunction in contact with aqueous electrolyte. An equivalent circuit model is developed, explaining the measurements and predicting behavior in wireless mode.

A systematic study on p-type polymeric thin-films is presented, comparing rr-P3HT with two low bandgap conjugated polymers: PBDB-T and PTB7. The results demonstrate that PTB7 has superior photocurrent performance due to more effective electron-transfer onto acceptor states in solution.

Furthermore, the thesis addresses the issue of photovoltage generation for wireless photoelectrodes. An analytical model based on photoactivated charge-transfer across the organic-semiconductor/water interface is developed, explaining the large photovoltages observed for polymeric p-type semiconductor electrodes in water.

Then, flash-precipitated nanoparticles made of the same three photoactive polymers are investigated, assessing the influence of fabrication parameters on the stability, structure, and energetics of the nanoparticles. Photocathodic current generation and consequent positive charge accumulation is also investigated.

Additionally, newly developed porous P3HT thin-films are tested, showing that porosity increases both the photocurrent and the semiconductor/water interfacial capacity.

Finally, the thesis demonstrates the biocompatibility of the materials in in-vitro experiments and shows safe levels of photoinduced intracellular ROS production with p-type polymeric thin-films and nanoparticles. The findings highlight the potential of photoactive organic semiconductors in the development of optobioelectronic devices, demonstrating their ability to convert light into biological signals and interface with biological fluids.

Table of contents

**Abstract** ..... **1**

**1 Introduction** ..... **9**

1.1 From traditional bioelectronics to organic optoceuticals ..... 9

1.2 State of the art and photophysics of organic optoceuticals ..... 12

1.3 Overview of the thesis results ..... 15

**2 Methods** ..... **18**

2.1 Materials and Sample Fabrication ..... 18

2.1.1 Thin film fabrication ..... 18

2.1.2 Flash Nanoprecipitation ..... 21

2.2 Optical characterizations ..... 22

2.2.1 Spectrometric and Spectrofluorimetric spectroscopy ..... 22

2.2.2 Dynamic Light Scattering (DLS) and z-Potential ..... 24

2.3 Electrochemical characterizations ..... 28

2.3.1 Photoelectrical analysis ..... 28

2.3.2 Electrochemical analysis ..... 29

2.3.3 Photoelectrochemical analysis ..... 34

2.4 Scanning Probe Microscopy ..... 38

2.4.1 Atomic Force Microscopy (AFM) ..... 38

2.4.2 Kelvin Probe Force Microscopy (KPFM) ..... 41

2.5 High energy analyses ..... 43

2.5.1 Grazing-Incidence Wide-Angle X-ray Spectroscopy (GIWAXS) ..... 43

2.5.2 Transmission Electron Microscopy (TEM) ..... 45

2.6 Chemical and biological assays ..... 47

2.6.1 Hydrogen Peroxide determination ..... 47

2.6.2 ROS determination in HUVEC cells ..... 48
2.6.3 AlamarBlue cell viability assay ..... 49
**3 Results ..... 50**
3.1 Understanding Photocapacitive and Photofaradaic Processes in Organic Semiconductor Photoelectrodes for Optobioelectronics ..... 50
3.1.1 Abstract ..... 50
3.1.2 Introduction ..... 50
3.1.3 Results ..... 53
3.1.4 Conclusions ..... 65
3.1.5 Methods ..... 66
3.2 Supporting Information ..... 68
3.3 P-type Semiconducting Polymers as Photoreducing Electrodes: a Comparative Study for Optobioelectronics ..... 75
3.3.1 Abstract ..... 75
3.3.2 Introduction ..... 76
3.3.3 Results ..... 79
3.3.4 Conclusion ..... 91
3.3.5 Methods ..... 92
3.4 Photovoltage Generation at p-Type Semiconducting Polymer/Electrolyte Interfaces ..... 96
3.4.1 Abstract ..... 96
3.4.2 Introduction ..... 96
3.4.3 Results and discussion ..... 99
3.4.4 Conclusion ..... 110
3.4.5 Methods ..... 111
3.5 Supporting information ..... 113
3.6 Photoactive Polymeric Nanoparticles for in-loco Hydrogen Peroxide Photoproduction ..... 117
3.6.1 Introduction ..... 117
3.6.2 Results ..... 119

3.6.3 Conclusions ..... 133
3.6.4 Methods ..... 134
3.7 Porous rra-P3HT Thin-film Photoelectrochemical Response Characterization ..... 138
3.7.1 Introduction ..... 138
3.7.2 Results ..... 140
3.7.3 Conclusions ..... 146
3.7.4 Methods ..... 147
**4 Conclusions ..... 151**
**5 Bibliography ..... 157**

# List of Acronyms

| | |
|---|---|
| Abs | Absorbance |
| AFM | Atomic Force Microscopy |
| BV | Butler-Volmer |
| CE | Counter Electrode |
| CV | Cyclic Voltammetry |
| DFT | Density Functional Theory |
| DLS | Dynamic Light Scattering |
| DOS | Density Of States |
| DW | De-Ionized Water |
| EIS | Electrochemical Impedance Spectroscopy |
| EQE | External Quantum Efficiency |
| FBR | Foreign Body Reaction |
| Flash-DSC | Flash Differential Scanning Calorimetry |
| GIWAXS | Grazing-Incidence Wide-Angle X-ray Spectroscopy |
| $H_2$-DCF-DA | 2',7'-Dichlorodihydrofluorescein Diacetate |
| HEPES | N-(2-Hydroxyethyl)piperazine-N′-(2-ethanesulfonic acid) |
| HER | Hydrogen Evolution Reactions |
| HOMO | Highest Occupied Molecular Orbital |
| HRP | Horseradish Peroxidase |
| HUVECs | Human Umbilical Vein Endothelial Cells |
| IQE | Internal Quantum Efficiency |
| ITO | Indium Tin Oxide |

| | |
|---|---|
| KPFM | Kelvin Probe Force Microscopy |
| KRH | Krebs Ringer HEPES |
| LUMO | Lowest Unoccupied Molecular Orbital |
| NP | Nanoparticle |
| OCP | Open-Circuit Potential |
| OPV | Organic Photo Voltaics |
| ORR | Oxygen Reduction Reactions |
| OSC | Organic Semiconductor |
| PBS | Phosphate Buffered Saline |
| PC | Photocurrent |
| PDMS | Polydimethylsiloxane |
| PEC | Photoelectrochemical |
| PL | Photoluminescence |
| PV | Photovoltage |
| RE | Reference Electrode |
| ROS | Reactive Oxygen Species |
| rpm | Revolutions Per Minute |
| rr-P3HT | Regio-Regular P3HT |
| rra-P3HT | Regio-Random P3HT |
| SC | Semiconductor |
| SSE | Standard Silver Electrode |
| $T_g$ | Glass Transition Temperature |
| THF | Tetrahydrofuran |
| TMB | 3,3′,5,5′-Tetramethylbenzidine |

| | |
|---|---|
| $V_L$ | Vacuum Level |
| VOC | Voltage Open-Circuit |
| WE | Working Electrode |
| WF | Work Function |
| $X_{OC}$ | “X” Open Circuit |
| $X_{SC}$ | “X” Short Circuit |

# 1 Introduction

## 1.1 From traditional bioelectronics to organic optoceuticals

Advances in micro-electronics and material sciences provide new opportunities for biomedical devices. The interface between the human body and electronic technology is a burgeoning field of study to realize novel diagnostic and therapeutic tools. Inorganic metals, as well as inorganic semiconductors and organic electronic materials have been developed for the different purposes that emerge when biological cells and tissue get in contact with external devices. Metals have been the first material class to be employed already in the 18$^{th}$ century. Noteworthy are the historic experiments performed by Galvani in the end of the '700.[12] Still today, noble metals are the most relevant interface material due to their high conductivity, chemical stability and the good biocompatibility.[13]

Inorganic semiconductors can offer advanced electronic properties bringing optoelectronic functionalities, diode and transistor capabilities and modern microfabrication techniques for integrated circuits to the abiotic/biotic interface. Such multifunctional properties have significantly increased the complexity of bioelectronic devices in the last two decades. However, for low-invasive implantable devices, these traditional materials have an important drawback as they do not match the organism's paradigm of soft mechanical compliance. Living tissue is soft (0-50kPa organs, 1-20MPa bones and cartilage) whereas inorganic noble metals and semiconductors have a much higher Young's modulus (10-1000GPa). In addition, the traditional materials cannot interface directly with the cellular communication processes. Electrodynamic signals in the materials are transported by electronic carriers. In biological signals carriers are instead either ionic currents or molecular messengers. This incompatibility creates a high impedance for transduction processes across the abiotic/biotic interface and renders them non-specific. Given these two major short-comings of traditional materials, there is a quest for materials science to discover novel materials that are compliant to the stringent conditions of implantable devices and offer soft mechanical properties combined with designed transduction pathways to achieve both, specific recording, and stimulation of selective biological signals.

Within this framework, organic materials have become very appealing for their vast chemical diversity as offered by synthetic organic chemistry. Organic materials span over a wide range of

elastic moduli, from the very soft gels (10s of KPa) to the much more rigid molecular crystals (10s to 100s of GPa). Moreover, conjugated pi-orbital systems offer semiconducting properties to organic materials and with suitable dopants or with field effect, metallic conductivity can be realized in organic materials. In addition, the semiconducting properties are relevant for interesting photoelectric or photoelectrochemical properties. Furthermore, composite organic polymer structures can be realized that offer mixed electric and ionic conductivity. This last attribute allows for a low impedance interface with the cellular environment which is not easily achieved with metals, and which is being developed in the last decade. Accordingly, such materials offer novel perspective for low-invasive and highly specific interfaces between the biotic and the abiotic world. In addition, in organic materials thanks to the broad synthetic possibilities offered by organic chemistry it is possible to add functionalization both inside the material to change the electro-optic properties, and on its surface to tune the interactions with the surroundings thus opening a large space for tuning multifunctional properties.

When an external body comes into contact with living cells, a complex network of interactions is established. These can span from mechanical stresses and adaptations, to chemical interactions, as well as concentration gradients, and so on. When, more specifically, such an external body is put into a living animal, it might undergo a reaction called Foreign Body Reaction (FBR).[14] It is the typical tissue response to a mismatch in mechanical properties or chemical recognition. It usually includes the formation of a foreign body granuloma, which consists of protein adsorption, macrophages immune reaction, multinucleated foreign body giant cells formation due to macrophage fusion, the appearance of fibroblasts and finally angiogenesis. In the long term, the FBR results in encapsulation within fibrotic tissue and eventually in a calcified shell. This response can be most detrimental if the aim of the implanted device is the collection of information as well as the bidirectional communication with a living target. The low elastic moduli that can be achieved with polymeric organic materials in addition to a suitable biochemical surface functionalization offers novel means to tackle the FBR problem in future interfaces. Mechanical compliance to the body mechanics allows further implantation of devices into soft and muscular tissue that is subjected to continuous motion in the human body. An example for such an interface regards peripheral nerves and soft inner organs such as the beating heart.

An important issue for implantable biomedical devices is the energy supply necessary for operation. Packaged batteries can only power implants for a limited lifetime,[15] and surgical intervention is

required to replace them. With an increase in longevity of patients, the need for long-term sustainable wireless powering and overcoming the finite battery capacity has become imperative.[16] The natural progression must then be the development of external powering allowing the complete removal of wires. Literature reports multiple approaches to the wireless, battery-less bioelectronics.[17–20] Extensive research is being conducted to achieve such devices with properties combining soft mechanical behavior, biocompatibility and small form factors.[1,3,21–32] Wireless power transfer (WPT) is primarily realized through the electromagnetic field and by ultra-sound waves. In general, electromagnetic power transmission can be categorized into three types according to the transmission distance and the employed frequency: near-field, far-field, and light.

An emerging approach uses acoustic waves to deliver power and could take advantage of the high power density and penetration depths up to 85mm[33] of the ultra-sound wave inside tissues. The received ultrasonic wave can be converted to electrical power through implanted mechanical energy harvesting, e.g., a piezoelectric or triboelectric nanogenerator.[34]

Based on electromagnetic inductive coupling between a pair of coils, the near-field WPT, e.g., the near-field communication (NFC), has been the most widely adopted method for powering implantable devices. Its prominent advantage is a high transmission efficiency greater than 80%,[35] which could therefore deliver a power output of milliwatts to implanted devices. However, the small coverable transmission distance (a few millimeters) and the strict requirement of two-coil alignment, limits the use of near-field WPT to subdermal devices.[20] Different from near-field WPT, far-field WPT operating at a higher frequency range (megahertz to gigahertz) has larger transmission distances (up to several meters).[36] However the power transmission efficiency is less than 1%.

Light provides an alternative possibility to power implanted bioelectronic devices wirelessly. Light has the advantage of: superior spatio-temporal resolutions due to the small electromagnetic wavelength, lower invasiveness, and higher selectivity with respect to traditional electrical methods. The efficiency is given by the implanted photovoltaic system and modern cells can exceed 18% of conversion efficiency. However, one limitation comes from the opacity of the body tissues to NIR, visible and UV light. The highest penetration depth is within the so called Therapeutic Window, which is located between 626nm and 1316nm.[37]

Organic semiconductors offer several advantages for such light-operated bioelectronic devices.[38] They combine biocompatibility, with flexible and even soft mechanical properties, high optical

absorption coefficients and photoconversion properties as exploited in organic photovoltaic devices with efficiencies reaching up to 18%[39]. Many organic polymers are in addition stable in the aqueous environment of biological cells and do to not need a dielectric encapsulation to maintain their properties. This opens the possibility to engineer direct transduction pathways of light being absorbed in the organic semiconductor and transduced into a physico-chemical stimulus able to impact on biological pathways relevant for therapeutic purposes. Even though a complex transduction chain is targeted, a potential device could be very simple relying only on the multifunctional properties of a single organic semiconducting material. Such a kind of optoceutical device would be minimally invasive due to its wireless activation, small formfactor and mechanical properties. It would be highly specific as it is activated only by illumination. Therefore, it would provide an alternative to unspecific drug-based therapies, or specific light-based genetic engineering approaches.

The hypothesis of organic implantable phototransducers was successfully tested by different research groups. An important first example was the demonstration of organic bulk-heterojunctions that could activate or deactivate neurons in close proximity when illuminated by strong laser light. Other demonstrations regard organic semiconducting thin films that activate retinal neurons upon illumination and that are possible candidates to treat certain blindness conditions. Recently polymer thin films activated by light were also found to impact on differentiation processes of epithelial cells and could provide a novel tool for regenerative medicine. Along these lines the project “Light and Organic Nanotechnology for Cardiovascular Disease” (LIONHEARTED) is active and provided the frame for this PhD thesis. The objective of the project is to develop an organic semiconductor based optoceutical that supports the regeneration of cardiac tissue after damage due to heart disease. The multidisciplinary project covers all the research necessary to pursue such an objective and ranges from materials development by chemists to medical doctors testing the developed devices in large animal experiments. My part as a physicist was to study the possible physico-chemical transduction pathways and to provide a microscopic interpretation of the relevant processes occurring at the semiconductor/water interface.

## 1.2 State of the art and photophysics of organic optoceuticals

Illumination with photon energies higher than the optical bandgap generates excitons in organic semiconductors. The excitons diffuse through the bulk and can split into separated charge carriers. The low dielectric constant makes exciton splitting unlikely in organic semiconductors and it occurs

spontaneously only at very low quantum yields. Improved conditions for exciton splitting can be present at interfaces due to the difference in energy of the neighboring states located in the two phases. By using the photoelectronic approach, the maximum achievable photovoltage is dictated by the energy carried by the absorbed photon. Practically this value must be scaled down for multiple reasons. First, for most of the organic materials the exciton binding energy is much higher (up to 1.4eV of $Alq_3$)[40] than, as a comparison, in Silicon (13meV).[41] In addition, energy is lost to overcome the electrical resistance, to overcome energy barriers between materials, and through thermalization in non-perfectly aligned energy levels, to cite some. Despite all these limitations, it has been proven in literature that it still is enough to produce sufficient effects in the surrounding biotic environment.[42]

The ways by which this energy can be exploited to influence the nearby cells are mainly three: Photothermal, Photocapacitive and Photofaradaic.[43] The photothermal process results when light absorption causes an increase in the polymer's temperature, followed by thermal diffusion and propagation to the surrounding, generating a temperature gradient through the electrolyte and in the cell. This effect will not be covered in this dissertation because we are mainly interested in the photoelectronic and photoelectrochemical mechanisms, which are more selective, localized, and efficient. In order to achieve significant changes in temperature light intensities above 500mW are needed.

The photocapacitive mechanism denotes a situation where the light driven generation of carriers leads to the formation of a dipole with consequent local transient electric fields occurring at any device interface. Transient electric fields are rapidly screened by the redistribution of electronic carriers in the organic semiconductor and ions in the electrolyte. Examples for interfaces where dipoles can generate are (i) internal ones between crystallites and amorphous polymer[44], (ii) heterojunctions between different semiconducting layer (i.e. p/n junction) or between semiconductor and metal,[45–47] and (iii) the semiconductor/electrolyte interface.[47,48] To achieve the stimulation of neuronal cells with photogenerated transient electric fields, it is important that the field extends outside the device and passes through the target cell. This requires a strong adhesion of the cell to the semiconducting interface to increase the so-called seal resistance. Else the electric field would be screened by ionic displacement currents before effecting the cell membrane.

The third phototransduction mechanism is called photofaradaic stimulation. This denotes a situation where light absorption causes the semiconductor to electrochemically reduce or oxidize molecules that are present in the electrolyte. These photoelectrochemical reactions can have different degrees of

reversibility but by using organic semiconductors they are often irreversible. Frequently, the reaction products are reactive intermediates that can react with the semiconductor inducing degradation.[49] But they can also impact on cellular proteins or other biological structures, initiating in this way a transduction chain that impact on cellular messaging or phenotype. Photogenerated redox product can diffuse into the cell from outside, when generated with a macroscopic thin film devices[7,8,10,50] or using sufficiently small devices or semiconducting nanoparticles, they can be directly generated inside the cytosol.[9,23,51]

Looking at the structure of the device, we can trace a division between the use of p/n junctions [3,30,47] and the use of a single polymer layer. [7,52–54] Both can be employed in the form of thin films, mostly prepared with spin-coating techniques and possibly with microstructures able to enhance both cell adhesion and device performances,[8,55,56] or in the form of nanoparticles. In the last decade, a lot of attention has grown on the possibility to employ such phenomena as photoactivated biochemical signals.[5,30,43,57–61] In literature we can find examples of heterojunctions employed as photocapacitors for peripheral nerves stimulation[62] and retina stimulation[3,5], as well as for photofaradaic $H_2O_2$ in-loco generators.[57] In single polymer device on the other hand, a lot of attention was devoted to P3HT, which is a well-known and widely studied polymeric semiconductor that together a wide range of polythiophene ring based materials was proven to be biocompatible with both in-vitro and in-vivo experiments.[24,63] The energetic landscape at the interface between this polymer and the electrolyte is the key factor in its photostimulated response[48,52], leading mainly to the Oxygen Reduction Reaction (ORR) forming Hydrogen Peroxide ($H_2O_2$) as an end product. This in turn is the responsible for cell stimulation through cascade processes which cause eventually a modulation of calcium channel activity.[64] We will see in the following that depending on the alignment between the valence or conduction band of the OSC and the Density of States (DOS) of the species dissolved in the liquid phase, the energetic conditions can be favorable for an electron or hole transfer between the two materials [65]. Another interface that has been shown to be important for charge separation, for example in rr-P3HT [44], is the one that forms between the crystalline and the amorphous fractions. In this case, after the separation the charge itself would diffuse in the material and if it reaches the interface before the recombination can cause a redox process.[52]

Since the energetics at the interface between OS and the electrolyte dictate the redox behavior of the device, the presence of an additional semiconducting layer to realize a p/n heterojunction could cause charge more effective generation and accumulation, thus leading to a photocapacitive behavior.[47]

Examples in literature for such a kind of device that have already been successfully employed for neural photostimulation through cell depolarization are the $H_2$Pc-PTCDI heterojunctions studied by Glowacki and coworkers.[3–5,66,67] They were also able to detect and possibly tailor these structures for photofaradaic production of $H_2O_2$.[57,68,69]

When such phototransducer devices are operated wireless, they are electrically floating. Since there are no low impedance routes to close the circuit, the only possible pathways for the photogenerated charges are thus accumulation and recombination or accumulation followed by redox processes or both. In this case the knowledge of the thermodynamics and the kinetics of such materials makes it possible to develop predictive models for their behavior when no external electronic is connected. Such a model becomes fundamental when dealing with nanoparticles (NPs) since here it is also not possible to probe photoelectronic and photoelectrochemical properties without perturbing the system under examination.

## 1.3 Overview of the thesis results

In the first chapter of this thesis, I will explain the fabrication and the investigation techniques I used in this thesis. I start with introducing the thin-film protocol used for macroscopic sample production, followed by the flash nanoprecipitation technique used to make nanoparticles. Next, spectroscopic techniques used to probe the energy levels and their optical activity are described. In the case of NPs, I employed Dynamic Light Scattering (DLS) for the hydrodynamic radii evaluation and z-Potential for stability assessment. We developed a Photoelectrochemical (PEC) cell to study thin films, which is here introduced, through both electrochemical and photoelectrochemical means such as voltammetry, impedentiometry, photocurrent spectroscopy and transient photocurrent and photovoltage investigations. Scanning Probe Microscopy (SCM) techniques are then introduced. Kelvin Probe Force Microscopy (KPFM) is used to evaluate the surface potential and non-contact Atomic Force Microscopy (AFM) is used to probe the surface morphology of the films and to determine the size and shape distributions of the nanoparticles. Transmission Electron Microscopy (TEM) is used to supplement the latter information. Finally, I introduce HRP-TMB assay for $H_2O_2$ concentration measurements, and I explain in-vitro techniques such as and $H_2$DCF-DA assay for intracellular ROS evaluation and AlamarBlue assay for cell viability.

Following the methods, I will present the main results obtained during my PhD studies divided by topic. I begin with the study of the ITO-$H_2$Pc-PTCDI p/n heterojunction where we a detailed characterization of photoelectrochemical current transients is combined with spectroscopic measurements, impedance spectroscopy, and local photovoltage measurements to establish a model that predicts quantitatively faradaic or capacitive current transients. The decisive elements of the model are the alignment between the energy levels at the interface, influenced by the voltage building up, and the acceptor molecules in the electrolyte. The result is a comprehensive model of photocapacitive and photofaradaic effects that can be applied to developing wireless bioelectronic photostimulation devices.

Then I compare the well-known P3HT with two other thiophene-ring based polymers as p-type thin-film photocathodes, namely PBDB-T and PTB7. I quantify their photogeneration capabilities at physiologic conditions through photocurrent transient analysis and HRP-TMB assay. I find a superior photocurrent generation capability in PTB7 as compared to the other two polymers, which is reflected in a better $H_2O_2$ photogeneration yield. Additional spectroscopic and structural investigations are used to compare the energy levels of the materials at the electrochemical interface and their thin film morphologies to rationalize the differences in materials performances. Finally, I test the biocompatibility of the new materials both in dark and illuminated conditions and demonstrate effective intracellular ROS production in in-vitro experiments. The findings point to the relevant physico-chemical material properties that will be crucial for novel, less invasive, optically operated bioelectronic interfaces.

Following this, I report systematic spectroscopic and transient photovoltage measurements on P3HT and PBDB-T thin films in contact with PBS electrolyte to identify the role of the electrolyte and the impact of electrochemical reactions for photovoltage generation. I compare the measurements to intrinsic photovoltage generation as observed in capacitively coupled photoelectrodes in the absence of electrolyte. By combining these measurements with electrochemical impedance spectroscopy, I develop a simple circuital model to explain the large observed photovoltage and its build-up dynamics. Based on Butler-Volmer kinetics describing the photoreduction process, I obtain a quantitative description of the photovoltage transients and charging behavior of p-type photoelectrodes. By analyzing the initial photovoltage charging and discharging slopes I identify the forward and back electron transfer contributions. The findings are of particular relevance to

understand wireless, optically triggered bioelectronic transduction as achieved with p-type OSC in the form of transducer patches or micro- and nanoparticles in contact with biological cells.

Following the work on p-type polymeric thin-films, I report on P3HT, PBDB-T and PTB7 in the form of NPs exploring diverse preparation conditions and how they impact on the optical, physical and photoelectrochemical performances. This with the aim to open the possibility to employ variable routes of low invasive administration, as well as to selective cell targeting down to the subcellular length scale. Additionally, we demonstrate that there are no adverse responses to administration and internalization in Human umbilical vein endothelial cells (HUVECs), employed here as a valuable model for the study of the endothelium function.

Finally, I describe the work done on porous regiorandom P3HT (rra-P3HT) developed by our collaborators in POLYMAT (San Sebasti*án*, Spain) as a next generation thin-films for biological applications to enhance the surface area exposed to the electrolyte. The porosity is intended to favor the photo-stimulation for the next in vitro and in vivo studies. Based on in depth characterization of the optical, microscopy, electrical and electrochemical properties of the material in form of thin films exposed to an electrolyte, I investigated the phototransduction performances in light-activated redox processes occurring at the polymer surface. Taking into account that the photo-electrochemical processes highly influence the angiogenesis activity in endothelial cells and modulate the intracellular $Ca^{2+}$ concentration in cardiac and endothelial cell models[6,7,9,10,51], the ability of the porous P3HT-based films to generate Reactive Oxygen Species (ROS) upon illumination in extracellular-like conditions is evaluated as a function of the pore size.

All the reported studies have been done within the framework of the LIONHEARTED European project (Horizon 2020). Being active part in this project I had the opportunity to spend my period abroad at the Chemistry laboratories at EHU/UPV and POLYMAT in San Sebasti*á*n (Spain), in the Mecerreyes' group, where together with experts in the field I fabricated and characterized the nanoparticles shown in the results and other novel nanoparticles. I also went multiple times at IIT-CNST@PoliMi in Milano (Italy) to collaborate, at Antognazza's group laboratories, to the in-vitro experiments on Human Umbilical Vein Endothelial Cells (HUVECs).

# 2 Methods

## 2.1 Materials and Sample Fabrication

### 2.1.1 Thin film fabrication

#### The substrate

As a back-electrode for our samples we chose indium tin oxide (ITO) deposited over 1mm thick glass substrate from Ossila. Indium tin oxide (ITO) is a ternary composition of indium, tin, and oxygen in varying proportions. Depending on the oxygen content, it can be described as either a ceramic or an alloy. Indium tin oxide is typically encountered as an oxygen-saturated composition with a formulation of 74% In, 18% Sn, and 8% O by weight. Oxygen-saturated compositions are so typical that unsaturated compositions are termed oxygen-deficient ITO. It is transparent and colorless in thin layers, while in bulk form it is yellowish to gray. In the infrared region of the spectrum it acts as a metal-like mirror.

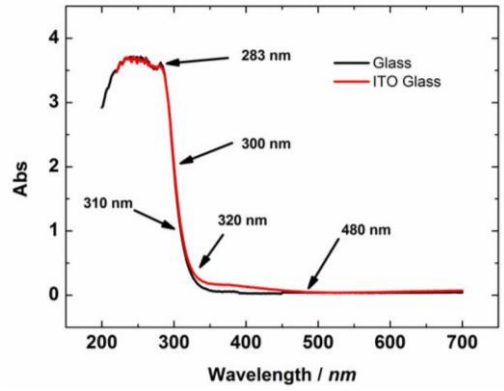


***Figure 1.*** *Typical absorption spectra of glass and ITO glass samples (1.1mm glass, 100nm ITO).*

Indium tin oxide is one of the most widely used transparent conducting oxides because of its electrical conductivity, sufficient local flatness (1.8nm RMS roughness) and optical transparency (**Figure 1**), the ease with which it can be deposited as a thin film, and its chemical resistance to moisture. Thin films of indium tin oxide are most commonly deposited on surfaces by physical vapor deposition. Often used is electron beam evaporation, or a range of sputter deposition techniques. The work

function of the ITO we used was measured via KPFM to be 4.9eV. The polymeric thin-film was deposited over the ITO back-electrode through spin-coating technique.

## Spin-coating

Spin-coating is a procedure used to deposit uniform thin films onto flat substrates. Usually, a small amount of coating material dissolved in a proper solvent is applied on the center of the substrate, which is either spinning at low speed or not spinning at all. The substrate is then rotated at speed up to 10,000 rpm to spread the coating material by centrifugal force (as illustrated in **Figure 2**). A machine used for spin coating is called a spin coater, or simply spinner.[70]

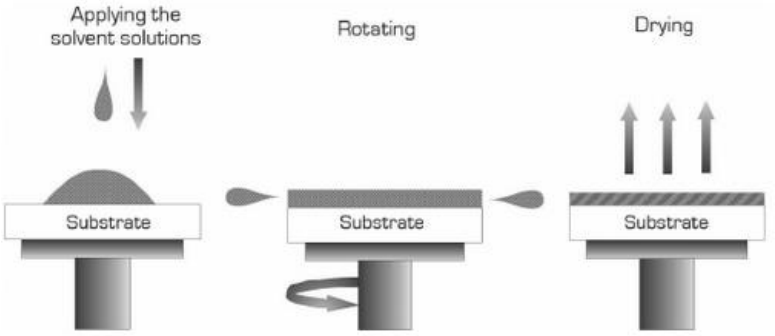


***Figure 2.*** *The stages of thin-film deposition by spin coating method* [71]

Rotation is continued until flat surface and eventually complete evaporation is achieved. The higher the angular speed of spinning, the thinner the film. The applied solvent is usually volatile, so that it easily evaporates during rotation. The thickness of the film also depends on the viscosity and concentration of the solution.[72] Pioneering theoretical analysis of spin coating was undertaken by Emslie et al.,[73] and has been extended by many successive authors.[74,75] The main advantage of spin-coating is the uniformity of the film thickness. If the substrate is sufficiently small compared to the viscosity of the solution to spin, owing to self-leveling, thicknesses vary less than 1% throughout the film. In the case of the polymers we used, the thickness could be tuned between 10nm and 250nm, while the average roughness was in the order of the nanometer. However, spin coating thicker films of polymers can result in relatively large edge beads whose planarization has physical limits. In this occurrence, blade coating is preferred.

## Physical Vapor Deposition (PVD)

When dealing with small molecules such as the H2Pc-PTCDI heterojunction we will introduce in this dissertation, a technique widely used in the fabrication of organic solar cells (OSC) is the physical vapor deposition (PVD) [76,77]. This term describes a variety of vacuum deposition methods which can be used to produce thin films and coatings. As illustrated in **Figure 3**, PVD is characterized by a process in which the material transitions from a condensed phase to a vapor phase and then back to a condensed phase. In our case, the Evaporation method was used. It involves two basic processes: a hot source material evaporates and then condenses on the substrate. Evaporation takes place in a vacuum, i.e. vapors other than the source material are almost entirely removed before the process begins in order to avoid side reactions. In high vacuum (with a long mean free path), evaporated particles can travel directly to the deposition target without colliding with the background gas. At a typical pressure of $10^{-4}$ Pa, a 0.4nm particle has a mean free path of 60m.

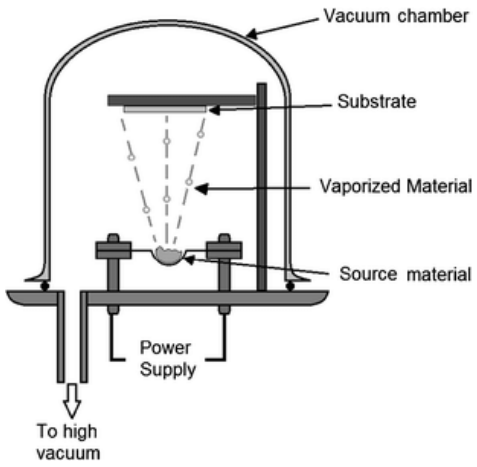


***Figure 3.*** *Schematic sketch of thermal evaporation deposition* [78]

Because the evaporated material attacks the substrate mostly from a single direction, protruding features block the evaporated material from some areas in a phenomenon called "shadowing" or "step coverage". Evaporated materials deposit nonuniformly if the substrate has a rough surface as integrated circuits often do. ITO used for our depositions had on the other hand an average roughness of 1.8nm RMS.

### 2.1.2 Flash Nanoprecipitation

When a material is brought in an oversaturated condition, precipitation takes place. In this scenario, mixing conditions control the final particle size distribution. Mixing characteristics can be categorized as macromixing (decimeter scale, e.g. on the order of the vessel), mesomixing (millimeters, on the order of the turbulent eddies that form when viscous forces dominate over inertial ones), or micromixing (micrometer scale, on the order of molecular diffusion in fluid lamellae).[79,80] Micromixing conditions are required to afford characteristic times on the order of nucleation and growth times needed for the formation of NP with controlled size distributions. Starting from a single phase of molecularly dissolved molecular species in solution, rapid precipitation is achieved through imposing a condition of high supersaturation. This leads to nucleation and growth of particles at a nucleation rate J given by: [81]

$$J = Ae^{\left(-\frac{16\pi\gamma^3\nu^2}{3k^3T^3(\ln S)^2}\right)} \qquad [1]$$

Where A is a constant, γ is the surface tension, ν is the molar volume, k is Boltzmann's constant, T the absolute temperature, and S the supersaturation. This relation show the strong dependence of nucleation on both supersaturation condition and temperature. Starting from the supersaturated state, nuclei start to form once the critical nucleation concentration is reached. As a result, the bulk solute concentration decreases. The concentration drop freezes any additional nuclei formation and leads to the growth of the already formed nuclei by aggregation and association with solute molecules in the bulk. In order to afford NP smaller than a few hundred nanometers, nucleation should be favored overgrowth.

Flash nanoprecipitation (FNP) process consist in the dissolution of a hydrophobic material and an amphiphilic block copolymer (as Pluronic F127, which was used throughout the thesis) in a water-miscible organic solvent (in our case THF), which is then impinged at high velocity against an antisolvent (water or aqueous electrolyte) to create turbulent mixing and high supersaturation.

The FNP process provides the local supersaturation needed for particle nucleation by fast mixing of a stream containing a molecularly dissolved solute and stabilizing molecule with an opposing stream containing a miscible solvent, which acts as a non-solvent for the solute and stabilizer. Mixing occurs in the turbulent regime in a confined volume, affording high-energy dissipation rates, and providing the supersaturation conditions required for simultaneous precipitation of the solute and stabilizer. The

block copolymer inhibits further growth of the solute particles, and provides steric stabilization through the hydrophilic block on the surface of the particle. Molecularly dissolved amphiphilic block copolymers, also known as surfactant, self-assemble when the solvent quality for one block is decreased. This feature makes them useful as surface stabilizers and help control the particle size distribution by adsorbing on the particle surface and preventing particle aggregation. In the context of FNP, the solvent quality jump imposed by rapid mixing leads to precipitation of the organic solute and adsorption of the hydrophobic block of the copolymer on the particle surface through hydrophobic interactions. Further growth of the solute particles is inhibited through the steric stabilization provided by the polymer's hydrophilic block.

The final state of block copolymer NPs formed via FNP is non-equilibrium, kinetically frozen. A study by Dormidontova provides insight into the kinetics of formation of block copolymer NP from a unimer solution.[82] The results show micelle fusion/fission dominates at early stages of micelle formation, while unimer exchange becomes active at longer times to bring the micelle to the equilibrium size. Supersaturation conditions can be tuned through solute concentration or solute solubility in the mixed solvent. After FNP is performed, high boiling point solvents such as dimethyl sulfoxide (DMSO) are best removed by dialysis, while low boiling point solvents such as tetrahydrofuran (THF) can be removed by vacuum evaporation.

## 2.2 Optical characterizations

### 2.2.1 Spectrometric and Spectrofluorimetric spectroscopy

#### Absorption

When radiation interacts with matter, a number of processes can occur, including reflection, scattering, absorption, fluorescence/phosphorescence (absorption and reemission), photoelectrochemical reaction (absorption and electron transfer) and photochemical reaction (absorption, bond rearrangement). In general, when measuring UV-visible absorption spectra, we want only absorbance to occur. Absorption of light causes the energy content of the molecules (or atoms) to increase. The total potential energy of a molecule generally is represented as the sum of its electronic, vibrational, and rotational energies:

$$E_{total} = E_{electronic} + E_{vibrational} + E_{rotational} \qquad (2)$$

The amount of energy a molecule possesses in each form is not a continuum but a series of discrete levels or states. The differences in energy among the different states are in the order: $E_{electronic} > E_{vibrational} > E_{rotational}$

In some molecules and atoms, photons of UV and visible light have enough energy to cause transitions between the different electronic energy levels. However, for molecules and solids (crystalline, amorphous, or the phases in between), vibrational and rotational energy levels are superimposed on the electronic energy levels. Because many transitions with different energies can occur, the bands are broadened. The broadening is even greater in solutions owing to solvent-solute interactions.

When light passes through a sample, the amount of light absorbed is the difference between the incident radiation ($I_{incident}$) and the transmitted radiation ($I_{measured}$). The amount of light absorbed is expressed as either transmittance or absorbance:

$$T = \frac{I_{measured}}{I_{incident}} \qquad A = -\log T \qquad (3)$$

For most applications, absorbance values are used since the relationship between absorbance and both concentration and path length normally is linear.

The position of the absorbance peaks is not a fixed value, but depends partially on the molecular environment of the chromophore (namely a part of the molecule responsible for light absorption). Other parameters, such as pH and temperature, also may cause changes in both the intensity and the wavelength of the absorbance maxima. Conjugating the double bonds increases both the intensity and the wavelength of the absorption band. For some molecular systems, such as conjugated hydrocarbons or carotenoids, the relationship between intensity and wavelength has been systematically investigated.

This equation can be transformed into a linear expression by taking the logarithm and is usually expressed in the decadic form:

$$A = -\log T = \varepsilon t = \varepsilon \mathrm{cd} \qquad (4)$$

where ε is the molar absorption or extinction coefficient, and in the case of liquids *c* is the concentration and *d* the absorption path, while in solids *t* is the material thickness. This expression is commonly known as Beer's law.

The extinction coefficient (ε) is characteristic of a given substance under a precisely defined set of conditions, such as wavelength, solvent, and temperature. For electronic transitions, the difference in energy between ground and excited states is relatively large. Therefore, at room temperature, it is highly likely that all molecules are in the electronic ground state. Absorption and return to ground state are fast processes, and equilibrium is reached very quickly. Thus, absorption of UV-visible light is quantitatively highly accurate and in our case it is important to gain information about how many photons are involved in the process under investigation.

### Fluorescence/Phosphorescence

In fluorescence, the species is first excited, by absorbing a photon, from its ground electronic state to one of the various vibrational states in the excited electronic state. Energy is then lost by thermalization to the lowest vibrational state of the excited electronic state. Depending on the energetic landscape, the excited state can either thermalize to the ground state or lose its energy by photon emission. If in this last case the electron state multiplicity is conserved we talk about fluorescence, otherwise we talk about phosphorescence. In Spectrofluorimetry we can be either interested in acquiring emission spectra by exciting at particular energy, or acquiring excitation spectra while measuring the emission intensity at a particular wavelength. In modern spectrofluorometers it is even possible to trace a bidimensional plot with both the information for every wavelength of interest. By using Spectrofluorimetry it is possible on one hand to explore photoactive states, and on the other to grasp information on the energetic pathways taken by the excited states to recombine.

## 2.2.2 Dynamic Light Scattering (DLS) and z-Potential

### Dynamic Light Scattering (DLS)

DLS is most commonly used to analyze nanoparticles in the size regime ranging from microns to nanometers for the purposes of size measurement. When in solution or in dispersion, particles are buffered by the solvent molecules. This leads to a random thermal motion known as Brownian motion. Each particle is constantly moving, and its motion is in most of the cases uncorrelated with that of other particles. This random motion is easily modeled by the Stokes-Einstein equation:

$$d_h = \frac{k_b T}{3\pi\eta D_t} \qquad (5)$$

where $d_h$ is the hydrodynamic diameter, which is the parameter of interest, $D_t$ is the translational diffusion coefficient, found by the measurement, $k_b$ is the Boltzmann's constant, T the thermodynamic temperature and η the dynamic viscosity of the solvent. In order to interpret the measurement results and extract the hydrodynamic diameter, liquid refractive index and viscosity needs to be known.

If we illuminate such random-moving objects, the motion shifts in a different way the phase of each photon. When the scattered light emerging from two or more particles is added, there is a time dependent fluctuation in the intensity of the scattered light due to constantly changing destructive or constructive interference. The most common angle to collect the scattering information is at 173° : this is known as backscatter detection. Contaminants such as dust particles within the dispersant are typically large compared to the sample size. Large particles mainly scatter in the forward direction. Therefore, by using backscatter detection, the effects of dust are significantly reduced . The intensity fluctuations in the signal due to the change in position of the particles are shown schematically in the graph below:

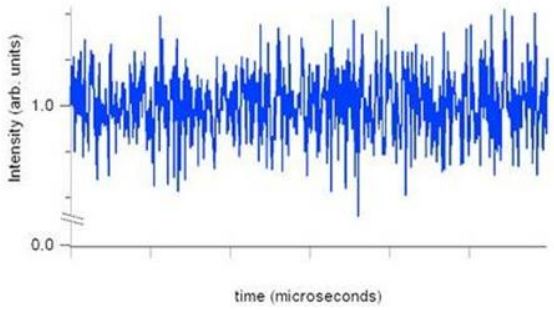


***Figure 4*** *optical signal oscillating during time*

Although it could appear be only noise, if we interpret it in terms of autocorrelation functions we can extract useful data. By processing in real time, the incoming data with an autocorrelator device it is possible to extract the delay time, τ. In the approximation where all the particles have the same size, the baseline-subtracted autocorrelation function, *C*, is simply an exponential decay of the following form:

$$C = e^{-2\Gamma\tau} \qquad (6)$$

where Γ is derivable from experimental data by a curve fit of the calculated autocorrelation function.

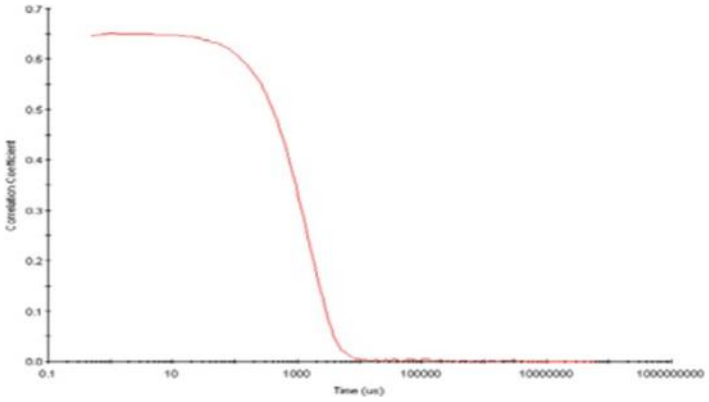


***Figure 5.*** *plot of Correlation function vs Time*

The diffusion coefficient is obtained from the relation $\Gamma = D_t q^2$ where $q$ is the scattering vector, given by $q = \frac{4\pi n}{\lambda} \sin\frac{\theta}{2}$ , $n$ is the refractive index of the liquid, $\lambda$ the wavelength of the laser light and $\theta$ the scattering angle. Inserting $D_t$ into the Stokes-Einstein equation above and it is possible to obtain the size of the particle. Such size is expressed in terms of Stokes diameter or Stokes–Einstein diameter. Stokes diameter (or more commonly, radius) of a particle is the radius of a hard sphere that diffuses at the same rate as that particle. Named after George Gabriel Stokes, it is closely related to the mobility, factoring-in not only the size but also solvent effects. A smaller ion with stronger hydration, for example, may have a greater Stokes radius than a larger ion with weaker hydration. This is because the smaller ion drags a greater number of water molecules with it as it moves through the solution.

Stokes radius is sometimes used synonymously with effective hydrated radius in solution. Hydrodynamic radius, $R_H$, can refer to the Stokes radius of a polymer or other macromolecule.

## Z-potential

Zeta potential is defined as the charge on a particle at its shear plane. This value of surface charge is useful for understanding and predicting interactions between particles in suspension. Manipulating zeta potential can be a powerful method of enhancing suspension stability, or control particle flocculation.

The liquid layer surrounding the particle exists as two parts: an inner region (Stern layer) where the ions are strongly bound and an outer diffuse region where they are less firmly associated. In the latter

we can recognize a notional boundary inside which the ions and particles moves together as one: the potential at this "slipping plane" is the Zeta (ζ) potential. The magnitude of the zeta potential gives an indication of the stability of the colloidal system. If all the particles in suspension have a large negative or positive zeta potential, then they will tend to repel each other and there will be no tendency for the particles to aggregate. However, if the particles have low zeta potential values, then there will be no electrostatic repulsion to prevent the particles clump together. The general dividing line between stable and unstable suspensions is generally taken at either +30 or -30 mV. This lose part of its significance in the presence of other non-electrostatic stabilizers such as capping agents or surfactants.

The thickness of the double layer ($\kappa^{-1}$) depends also on the concentration of ions in solution and can be calculated from the ionic strength of the medium. The higher the ionic strength, the more compressed the double layer becomes, thus shielding more effectively the central charge and providing a lower z-potential measure for the same suspended material.

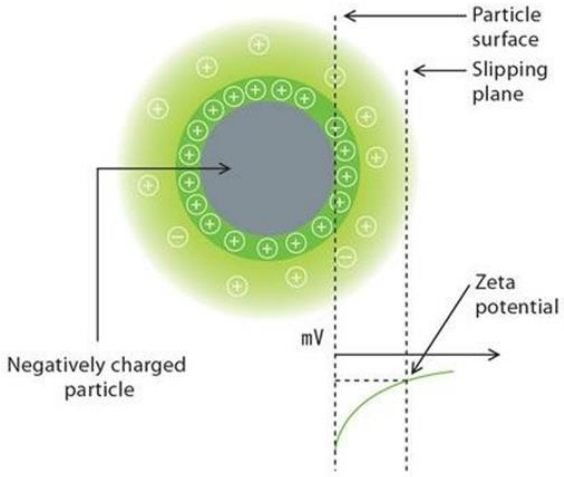


***Figure 6.*** *representation of the ionic envelope of particles*

In order to measure the Z-potential a laser doppler velocimetry coupled with a scattering phase analyzer and an electrophoretic capillary are used. The particle motion due to the applied electric field is measured by light scattering. The frequency of the scattered light is a function of particle velocity by Doppler shift. The scattered light is collected at an angle of 13°. A second beam of light, the reference beam, is mixed with the scattered beam in order to extract the frequency shift. The measured magnitude of the frequency shift is then used to determine the particle velocity.

## 2.3 Electrochemical characterizations

### 2.3.1 Photoelectrical analysis

KPFM is the perfect experimental method when high spatial resolution is needed, at the same time it is limited in time resolution even in Heterodyne configuration.[83] When the spatial resolution is not the priority and higher time resolutions are needed, a simpler macroscopic detection method via a capacitively coupled electrode can be used. This method has been used several times[84–86] to measure surface potential, especially for photovoltage transients in p-n junctions.

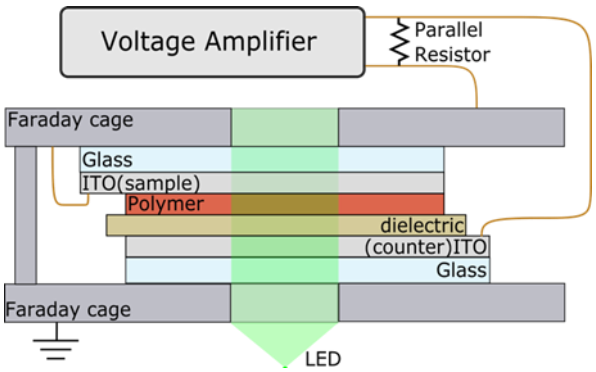


***Figure 7.*** *Setup of a capacitively-coupled macroscopic transient experiment. The sample is enclosed in a Faraday cage to minimize the noises. The counter electrode's signal against the grounded sample is collected and amplified. A resistor is placed in parallel to the capacitively coupled device in order to have zero potential difference between the sample and the ITO counter electrode in dark conditions.*

A sketch of a basic setup for this kind of experiment is shown in **Figure** 7. In this circuit, the sample being measured is the polymeric thin film deposited over a transparent ITO back-electrode (sample ITO) and it represent one plate of the capacitor. The other plate is a second ITO electrode (here referred to as counter), isolated from the junction through a 30$\mu m$ thick dielectric layer. The whole sandwich is placed in a Faraday cage in order to avoid external noises. The light, which comes from a monochromatic source such as a LED, passes through a hole in the Faraday cage, hits the sample and passes through a second hole on the opposite to avoid reflections. The measured electric field is

the sum of that generated at the interface between the polymer and the back-electrode, the one that forms within the semiconductor and that which forms at the free surface. As one plate of the capacitor charges up due to photovoltage generation, charge accumulation also occurs on the other conductive electrode. The voltage difference between the two plates can now be measured as a quantity proportional to the actual photovoltage. A resistor with a high resistance modulus ($1M\Omega$ to $10G\Omega$) is placed in parallel with the so formed capacitor in order to keep the potential difference between the plates equal to zero when no light is shined. The chosen resistance value is the result of a compromise between a low Johnson-Nyquist noise and low current flux between the condenser armors.

### 2.3.2 Electrochemical analysis

#### Potentiostat

When measuring the electrochemical properties of a material in contact with an electrolyte, the circuit that we build must be composed of the material under investigation, the electrolyte, and an electrode which is capable to close the circuit through a redox reaction with any of the species present in the electrolyte. We call the first one Working electrode (WE) and the second one Counter electrode (CE). If we are already using an electrolyte as the liquid phase, we ensure that a low resistance path exist between the WE and the CE. In this way, though we can measure the potential difference between the two contacts connected to the measuring electronics, we do not have information about what happens at the interface between the material under investigation and the conductive back-electrode, and about the interfaces between the WE and CE and the electrolyte. In order to have a fixed potential, we need to introduce what is known as Reference electrode (RE), which is an electrode characterized by a stable and well-known potential reached by employing a redox system with constant (buffered or saturated) concentrations of each participant of the redox reaction.[87] The RE can be used as a CE in a two-electrode configuration or in addition to a best suited CE in a three-electrode configuration. In our case the RE employed was an Ag(s)|AgCl(s)|KCl(3M) known as Silver Chloride electrode, with a reduction potential of +210mV vs Normal Hydrogen Electrode (NHE). The electrode functions as a reversible redox electrode and the equilibrium is between the solid (s) silver metal (Ag(s)) and its solid salt—silver chloride (AgCl(s), also called silver(I) chloride) in a chloride solution of a given concentration.

Since during measurement a current flow through the cell, an ohmic drop will perturb the measured potential also if we use a RE. Moreover, when using a RE as a CE the solid components are consumed. To address these problems, a three-electrode setup is employed, where a device called potentiostat is connected in a low impedance mode to the CE and in a high impedance mode to the RE. The potentiostat has at its core an operational amplifier connected to the three electrodes as shown in Figure 7. The operational amplifier has a high input impedance and thus any branch connected to its inputs will be traversed by a low current (ideally zero). In this way the measured potential is independent from the current passing through the low impedance branch of the circuit, and the RE does not wear out during the operation. It also tries to keep the potential at its two inputs equal and it sources all the current necessary to do so to the CE from its output. The CE on the other hand, must be made of a material with facile reduction and oxidation kinetics towards the solution so that a low resistance path is established independently from the potential in which we are working. Such an electrode in our case is made of a Platinum wire which is a good catalyzer both for the water reduction reaction $2H^+ + 2e^- \rightleftarrows H_2$ and can for the water oxidation reaction $2H_2O \rightleftarrows O_2 + 4H^+ + 4e^-$.

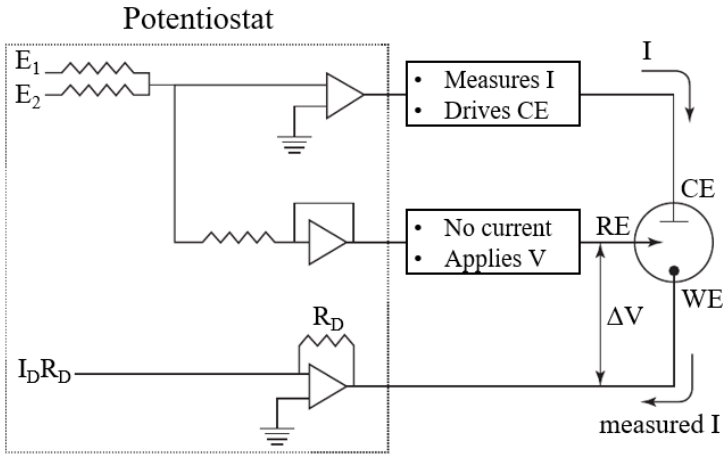


***Figure 8.*** *A schematic of the three-electrode cell and the connections to the potentiostat operational amplifier.*

## Cyclic Voltammetry

Cyclic voltammetry consists of measuring current at the WE while scanning the potential in contact with a solution of electroactive species or the system of interest. Cyclic voltammetry is known as a transient technique, for which the working electrode is stationary, and the experiment is performed in an unstirred solution. The potential is linearly (or staircase) scanned forward from the starting potential to the switching potential and then backward, giving a triangular potential cycle. In cyclic voltammetry, the starting and the final voltage have often the same values although this is not a necessary condition. A regular cyclic voltammetry consists of two potential ramps known as half-cycles. Depending on information that is about to be measured, such as stability of electrochemically generated species or formation of new electroactive compounds, multiple half-cycles or just a half-cycle can be performed, and the techniques are known as multicyclic voltammetry or linear sweep voltammetry (LSV), respectively. The rate of potential change, or potential scan rate ($v = \delta E/\delta t$), range form few millivolts per second to several volts per second. Depending on the scan rate a different contribution from the displacement currents impact on the total measured current: the lower the scan rate, the lower the capacitive contribution. At the same time, a slower scan rate would result in a more pronounced perturbation of the equilibrium concentration of chemical species at the interface between the WE and the electrolyte. Depending on the structural and chemical context, and on the information of interest, the scan rate must be adjusted.

Operatively, starting from the resting potential of the system, in which the forward and recombination currents are equal, as we approach higher positive potentials we will see a faradaic current appearing and adding to the capacitive one. This current grows with the potential applied, but at the same time the volume of solution around the electrode where the reduced form of the analyte is depleted grows. However, in our case the current density flowing through the WE does not grow enough to become dictated by mass transport instead of electron transfer kinetics.

In this work, cyclic voltammetry is primarily used to verify the stability window of the semiconductor-water system. Such stability window depends on the alignment between the semiconductor energy levels capable of being oxidized (valence band) and reduced (both conduction and valence band) at the interface with the electrolyte, and the donor and acceptor levels in water, as well as their kinetic facility towards such processes.

## *Electrochemical impedance spectroscopy*

From a mechanistic point of view, an electrochemical reaction at an electrode–electrolyte interface can be decomposed into a series of multistep processes (mass transport, charge transfer processes, adsorption, capacity charging), each occurring at distinct rates. The individual steps are time dependent and may occur at different timescales. Therefore, the use of transient techniques such as electrochemical impedance spectroscopy (EIS), which enables the analysis of time dependent (or in an equivalent manner, frequency dependent) mechanisms based on the response of the electrochemical system collected at selected frequencies, is required to facilitate evaluation of electrochemical systems.

The EIS technique is broadly applicable because it can provide an understanding of the electrochemical mechanisms occurring at an interface in a single measurement. Textbooks, monographs[88–90] and review articles have been dedicated to EIS that are specific to the applications.[91–95] In the case of an electrochemical system, the main difficulty is that the system must remain in a stationary state throughout the measurement.

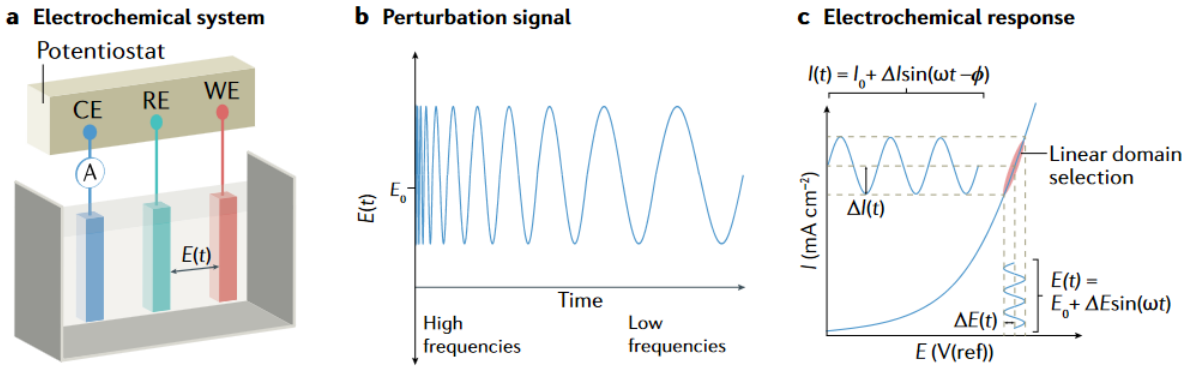


***Figure 9.*** [96] *An electrochemical system with a working electrode (WE), a counter electrode (CE) and a reference electrode (RE). The potential E(t) is applied between the working and reference electrode, and the resulting current is measured at location (a). In this example, a periodic perturbation signal with amplitude (ΔE) is applied between the WE and RE from high to low frequencies (b), and the electrochemical response to this perturbation is measured in the linear domain (c).*

EIS uses a small amplitude potential or current periodic perturbation to excite the electrochemical system at different frequencies, as illustrated in **Figure 9**. By measuring the response of the system to this perturbation, a transfer function is calculated. This function is the electrochemical impedance of the system. The impedance, Z, can be expressed as:

$$Z(\omega) = \frac{V(\omega)}{I(\omega)} = \left|\frac{V(\omega)}{I(\omega)}\right| \left(\cos\left(\phi(\omega)\right) + i \sin\left(\phi(\omega)\right)\right) = Z_R + i\, Z_I \qquad (7)$$

where $\omega$ is the angular frequency, $\varphi$ is the phase angle between the input and output signals, and $i$ is the imaginary unit. The electrochemical impedance, as defined by Eq. (7), is a frequency dependent complex number, whose real part, $Z_R$, is a frequency dependent Resistance and imaginary part $Z_I$ is a frequency dependent Reactance. EIS measurements should be designed to conform to the Kramers–Kronig relations, which are derived under the assumptions that the system under investigation is linear, stable, and causal. The perturbation amplitude required to achieve a linear response with an appropriate signal to noise ratio is generally determined experimentally for each system through Cyclic Voltammetry. A typical amplitude for potentiostatic modulation is in the order of 10 mV.

The power of EIS lies in its ability to probe processes in systems across a wide frequency range. Ideally, the frequency range should be set to match the dynamic range of the system under study. The typical frequency range for electrochemical measurements is 100 kHz–100mHz. Usually, seven to ten points per frequency decade equally spaced logarithmically, are required for measuring an impedance spectrum with sufficient accuracy for a detailed data analysis. It is preferable to start the measurement from the high frequency limit sweeping towards the low frequency limit. This because at high frequency capacitive currents and charge transfer inside the WE are predominant, while at low frequency the faradaic behavior against the liquid phase becomes significative and the generation of new chemical species at the interface might interfere with subsequent measurements.

The first step towards data analysis is the use of graphical methods to visualize and interpret the impedance data. To emphasize a specific feature or behavior, impedance data need to be presented in different formats that include the Nyquist representation (**Figure 10a**) for mass transfer and kinetic behavior and the Bode representation (**Figure 10b**) for frequency dependent behavior.

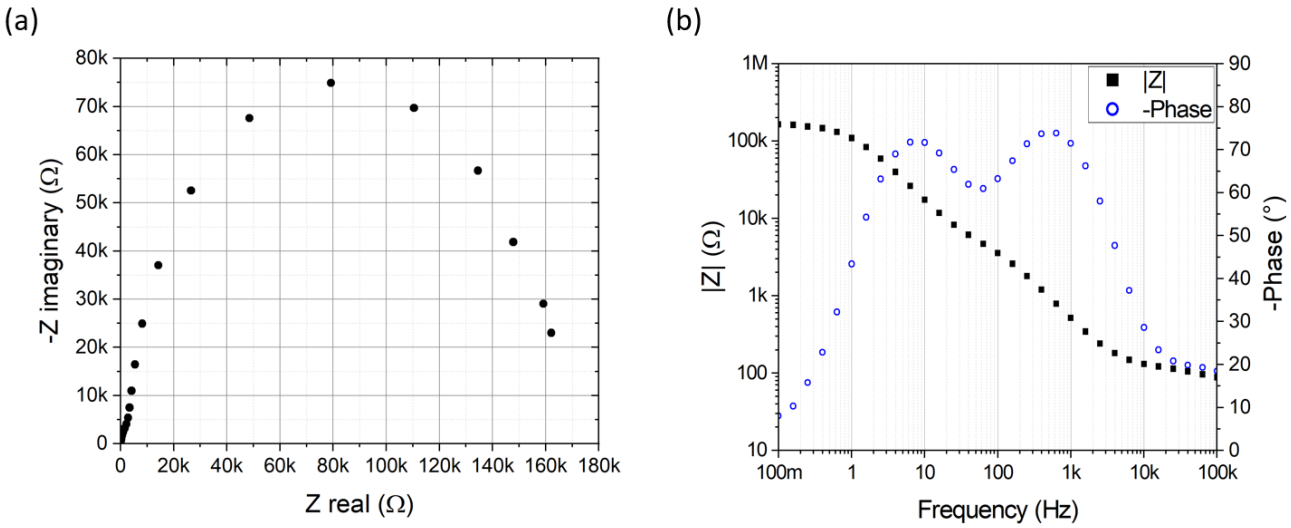


***Figure 10.*** *Example of a Nyquist Plot (a) and the relative Bode Plot (b) of an ITO-OSC thin-film*

By fitting these data with equivalent circuits, it is possible to correlate the frequency response of the system with specific interfaces and processes, such as interfacial capacitances and charge transfers.

### 2.3.3 Photoelectrochemical analysis

#### Photocurrent

Photocurrent measurements can be performed both as transient measurement in time by illuminating with a high irradiance LED source (up to 500mWcm$^{-2}$) or as spectroscopic measurements spanning from the upper limit of 350nm imposed by ITO absorption, down to 800nm where the Xenon lamp has still a good spectroscopic response. These measurements can be performed applying a potential to the WE in order to, as an example, grasp information on the photoelectrochemical conversion yield at open circuit potential and moving towards maximum photovoltage. Caution must be taken about the sizing of the CE if the currents are elevated. At the microampere scale, in which our experiments fall, a Pt wire is enough to ensure a low impedance path for the current to flow in. It is important to acquire EIS spectra before performing photocurrent measurements in order to be able to choose the best timescale to observe the desired phenomenon. A synthetic sketch of the Photocurrent setup in the case of LED illumination is presented in **Figure 11**.

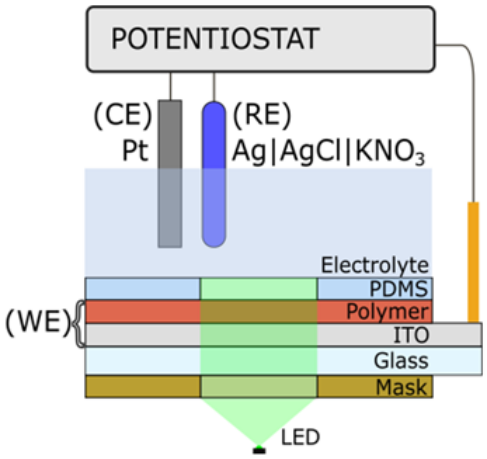


***Figure 11.*** *Scheme of the photoelectrochemical cell. A three-electrode setup is used for the Photocurrent measure. The LED can be placed on both sides of the film and can be substituted with a monochromated Xenon light in order to acquire spectra.*

By mounting the photoelectrode in a dedicated cell only a $1cm^2$ area of the semiconducting layer is exposed to the electrolyte, while the ITO surface and the electrical contacts remain separated through a PDMS O-ring. The cell allows the exposition to the illumination from either the ITO side or the solution side, the latter through a quartz window, only in the $1cm^2$ area exposed to the electrolyte. The photoelectrode was operated as the working electrode in a three-electrode configuration where an Ag|AgCl (3M KCl) was used as the reference electrode in combination with a Pt counter electrode. In spectroscopic measurements the monochromatic illumination of the photoelectrode at a defined wavelength was achieved with a Xenon lamp combined with a monochromator (Cornerstone 260). The amplified current signal was filtered and digitized with a lock-in amplifier (Zurich Instruments) connected to the monitoring output of the potentiostat (Metrohm PGSTAT204). For transient measurements the monochromated Xenon lamp light was replaced with monochromatic LEDs (Thorlabs M530L4) driven by a source-measure unit (Thorlabs DC2200).

## Photovoltage

Photovoltage measurements employ the same illumination conditions as the aforementioned Photocurrent measurements but are performed using a two-electrode setup. Photovoltage experiments are performed to probe the potential difference between the ITO back-electrode and the RE while approximately no current flow in the circuit, thus mimicking open circuit conditions.

These information, combined with those from other experiment such as EIS and Photocurrent transients, can be then employed both to extract important data such as the recombination currents or the photocharging dynamics, and to develop equations to fit, describe or predict the wireless behavior.

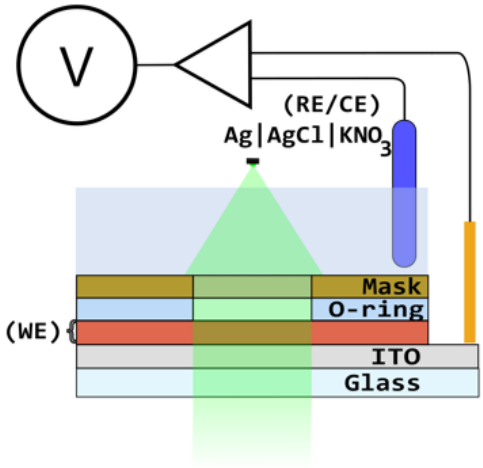


***Figure 12.*** *Experimental measurement of photovoltage: scheme showing photovoltage experiment. A two-electrode setup is used for the Photovoltage measure connected to a high impedance voltage amplifier. The LED can be placed both sides of the film and can be substituted with a monochromated Xenon light in order to acquire spectra.*

The cell is the same as for Photocurrent experiments but used in a two-electrode configuration composed by the WE and the Ag|AgCl functioning as RE and CE. Here the signal can be acquired both with a high-impedance FEMTO DLPVA-100-F-D voltage amplifier in which the impedance can be reduced through a 1MΩ to 1GΩ resistor placed in parallel to it, or with a Potentiostat in Galvanostatic mode.

In spectroscopic measurements the monochromatic illumination of the photoelectrode at a defined wavelength was achieved with the same illumination setups as in Photocurrent: Xenon lamp combined with a monochromator (Cornerstone 260). The amplified photovoltage signal was filtered and digitized with a lock-in amplifier (Zurich Instruments) connected either to the voltage amplifier or to the monitoring output of the potentiostat (Metrohm PGSTAT204). For transient measurements the monochromated Xenon lamp light was replaced with the aforementioned monochromatic LEDs (Thorlabs M530L4) driven by a source-measure unit (Thorlabs DC2200).

## Nanoparticles Photocharging Spectroscopy

When put in biological systems, nanoparticles are surrounded by aqueous electrolytes and find themselves in an electrically floating condition. In order to probe them in such a state, they cannot be directly addressed with a stable electric contact. This because thanks to their nanoscopic to microscopic dimensions, they would be a perturbation to the far bigger system composed by the electrically contacting material. This could significantly change or mask the electrical and photoelectrochemical response of such nanoparticles. In order to circumvent the problem, a possibility is to probe the accumulated charge through a short time-scale electric contact.

We achieved this by developing a system in which the NPs floating in the dispersing agent with a Brownian motion eventually hit a conducting surface made of ITO and discharge during its proximity moment. Depending on the expected Fermi energy of the investigated semiconductor and on the expected photovoltages, a potential can be applied to the ITO electrode to raise its Fermi level and promote NP discharge. Since no charge is accumulated in dark conditions, the signal is flat when no light impinge on the suspension. When light is switched on, by using a macroscopic electrode and a concentrated dispersion, the hit frequency is high enough to generate an easily observable signal. In order for the current to close the circuit, a Silver Chloride semi-reference electrode is employed. To ensure that the signal is not coming from polymer agglomerated, stuck or deposited over the ITO electrode, microscopy and AFM measurement should be performed. In our case, these confirmed that the signal was coming from nanoparticles. It was also double checked by using only electrolyte in the cell that the signal was not due to interaction induced by light absorption on the ITO electrode. When these measurements are performed in a spectroscopic manner, informations can be extracted on the spectral response of the nanoparticles to light. By comparing it to Absorption spectra it can be possible to trace which energies are involved in the photocurrent production and which ones are inactive, and to relate the wavelength to the photovoltage build-up process.

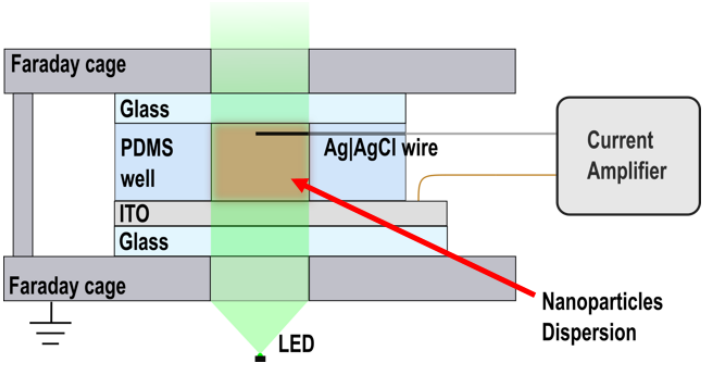


***Figure 13.*** *Scheme of the setup used to detect nanoparticles discharge on ITO electrode with illumination. The silver wire is placed opposite to the ITO and its area is negligible. A PDMS well contains the NPs dispersion that can be illuminated both sides with a LED or with a monochromated Xenon Light for spectroscopy purposes.*

The cell is similar to the one used for Photovoltage experiments in absence of an electrolyte, being composed by a Faraday cage with a $1cm^2$ hole to let the light in and out, and by a sandwich structure in the center. Such structure is composed by the ITO electrode and a glass slide enclosing a PDMS well, within which the NPs dispersion is situated. Here the signal is collected with a FEMTO DLPCA-200 current amplifier and digitized with an ADC, in order to be then filtered with a PC.

In spectroscopic measurements the monochromatic illumination is achieved with the same illumination setups as in Photocurrent and Photovoltage: Xenon lamp combined with a monochromator (Cornerstone 260). For transient measurements a monochromatic LED is employed (Thorlabs M530L4), driven by a source-measure unit (Thorlabs DC2200).

## 2.4 Scanning Probe Microscopy

### 2.4.1 Atomic Force Microscopy (AFM)

One of the most suitable methods to investigate morphology, electric, magnetic, or other surface characteristics at the micro- and nano-scale is the Scanning Probe Microscopy (SPM). The instrument uses specially prepared tips in the form of needles as probes, with the working part (apex) usually of the size of ten nanometer or lower, mounted on a flexible supporting cantilever. One side of the cantilever is fixed to a support, while the other edge, where the tip is located, is free to move and is

approached to the sample at tip-surface distances down to 0.1-20 nm, according to the technique used for the measurement. When the tip approaches the sample, several interactions between the tip and the substrate can be studied in order to get information on the sample surface features. Let the interaction be van der Waals forces between the two elements, as in the case of our morphology analysis, and the technique is thus referred as non-contact Atomic Force Microscopy (nc-AFM); then, the tip will induce a deflection of the cantilever. A schematic of the experimental technique, its working principle and data trace obtained are represented in **Figure 14**. Since the dimension of the edge of the tip is one to two orders of magnitude higher than the atomic size, the van der Waals energy of two atoms can be used to approximate the potential energy of the tip, as plotted in **Figure 14b** and approximated by the following:

$$U_{LD}(r) = U_0\left\{-2\left(\frac{r_0}{r}\right)^6 + \left(\frac{r_0}{r}\right)^{12}\right\} \qquad (8)$$

where *r0* is the equilibrium distance between the atoms.

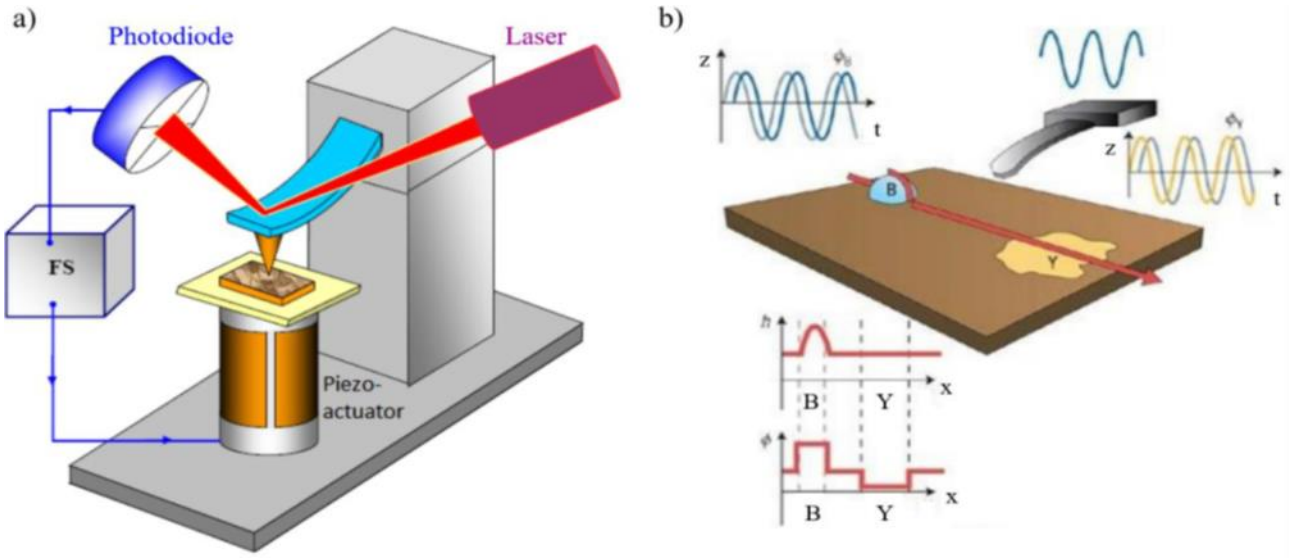


***Figure 14.*** *a) Schematic of an AFM. A laser shine on the cantilever head and the reflected beam is collected by a photodiode, thus obtaining the bending of the cantilever due to atomic forces. The feedback mechanism (FS) is used to control the tip-surface distance, through the piezoelectric actuator under the sample holder, according to the deflection of the cantilever.*[97] *b) Scheme of the AFM operation, with the cantilever oscillation depending on the topography and its surface*

*composition. The height and the phase images are registered, with phase-shift signal changing with dissipated energy variations on the sample surface.*[98]

To detect the cantilever deflections, a laser beam is reflected from its surface and collected by a photodiode divided in four quadrants: from the measurement of the laser intensity variations on the different sections it is possible to extract the amount of vertical and lateral deflection of the cantilever.

Imaging of morphological surfaces were carried out with Park NX10 AFM system, operating in non-contact mode with the tip oscillating close to its resonance frequency, *ω0*. The height of the samples surface is then described by the equation:[97]

$$z(t) = z_0 + A_0 \cos(\omega t - \phi) \qquad (9)$$

where $z_0$ is the mean height of the cantilever, $A_0$ is the amplitude of the free oscillation, $\omega$ is the oscillation frequency and $\varphi$ is the phase constant. The non-contact mode is obtained when the tip is far enough from the surface of the sample to remain in the attractive regime of the Lennard-Jones potential, where $F = \frac{dU}{dz} > 0$). When the tip is approached to the sample, the oscillation amplitude decreases to *A(z)*, with $A(z) < A_0$. A value in this range must be fixed as a set-point in order to control the height of the tip through a feedback system. From the amplitude variations it is then possible to extract the sample topography and morphology.

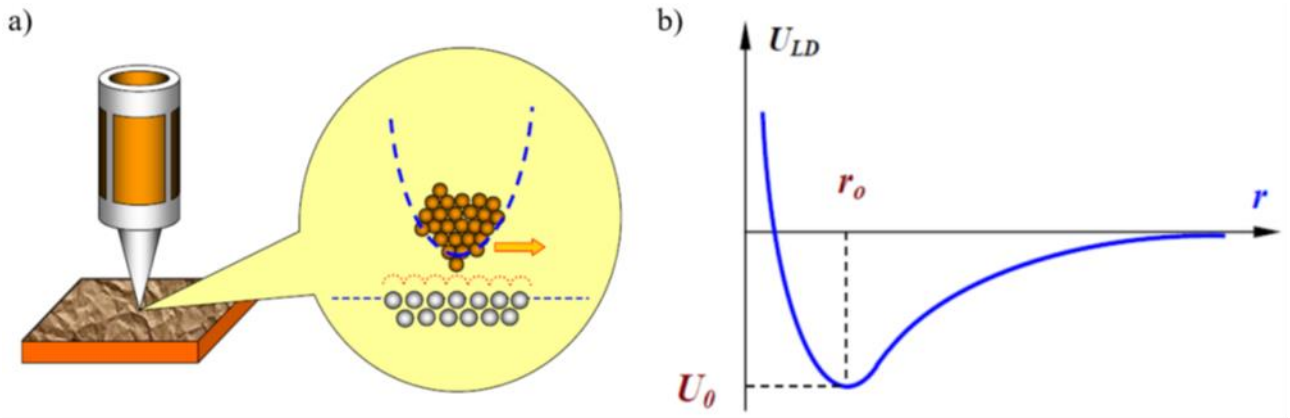


***Figure 15.:*** *a) Atomic resolution with the AFM: the tip edge dimensions allow for an atom-atom interaction with the sample surface.*[97] *b) Qualitative form of the Lennard-Jones potential*[97]

## 2.4.2 Kelvin Probe Force Microscopy (KPFM)

In Kelvin Probe Force Microscopy (KPFM) the probe and sample are electrically connected through a voltage supplier to form a tip-to-plate capacitor, which can be in suitable conditions approximated as a parallel plate capacitor. The probe is usually composed of a different material from the sample one, therefore each component has initially a distinct Fermi level. When electrical connection is made between the probe and the sample, electrons can flow between them from the less to more negative Fermi level. This electron flow causes the equilibration of such Fermi levels. Also, a surface charge develops on the probe and an opposite one on the sample, with an associated potential difference that builds up between them known as the contact potential ($V_c$). In Scanning Kelvin Probe (SKP) the probe is vibrated along an axis perpendicular to the plane of the sample.[99] This vibration causes a periodic change in probe to sample distance, which results in an alternated flow of current. The resulting sine wave is demodulated to a DC signal through the use of a lock-in amplifier.[100] Once the DC potential is determined, an external potential, known as the backing potential ($V_c$) can be applied to null the charge between the probe and the sample (**Figure 16**). When the charge is nulled the Fermi level of the sample returns to its original position. This is achieved when the electrostatic force between the tip and the sample is cancelled. [101]

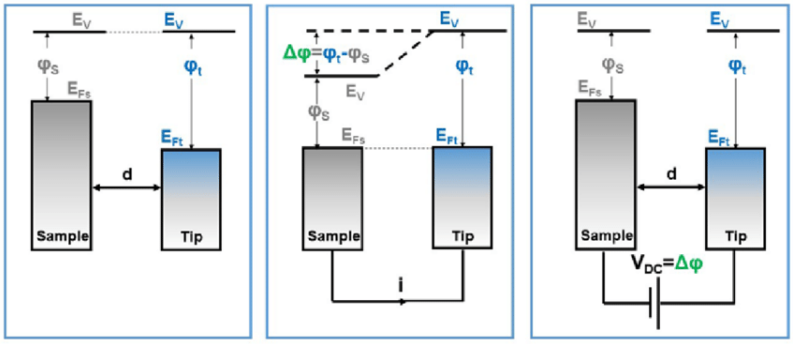


***Figure 16.*** *KPFM steps: initially the tip and the sample are separated, each one with its Fermi level. When electrically connected, they will reach equilibrium by flow of charge equilibrating on the same Fermi level. In this way an electric field, and so a net force, is set between the two. A DC potential is applied to the tip to nullify this force. Such a potential is the KPFM potential.*

Tuning the AC-frequency to the resonant frequency of the AFM cantilever results in an improved sensitivity. The electrostatic force in a capacitor may be found by differentiating the energy function with respect to the separation of the elements and can be written as

$$F = \frac{1}{2}\frac{dC}{dz}V^2 \qquad (10)$$

where *C* is the capacitance, *z* is the separation, and *V* is the voltage, each between tip and surface. Substituting the previous formula for voltage (*V*) shows that the electrostatic force can be split up into three contributions, as the total electrostatic force F acting on the tip then has spectral components at the frequencies ω and 2ω.

$$F = F_{DC} + F_{\omega} + F_{2\omega} \qquad (11)$$

The DC component, FDC, contributes to the topographical signal, the term $F_{\omega}$ at the characteristic frequency $\omega$ is used to measure the KPFM signal and the contribution $F_{2\omega}$ can be used for capacitance microscopy.

$$F_{DC} = \frac{dC}{dz}\left[\frac{1}{2}(V_{DC} - V_{CPD})^2 + \frac{1}{4}V_{AC}^2\right] \qquad (12)$$

$$F_{\omega} = \frac{dC}{dz}[V_{DC} - V_{CPD}]\, V_{AC} \sin(\omega t) \qquad (13)$$

$$F_{2\omega} = -\frac{1}{4}\frac{dC}{dz}V_{AC}^2 \cos(2\omega t) \qquad (14)$$

The quality of the measurement is affected by a number of factors. This includes the diameter of the probe, the probe to sample distance, and the material of the probe. The probe diameter is important in these measurement because it affects the overall resolution, with smaller probes leading to improved resolution.[102,103] On the other hand, reducing the size of the probe causes an increase in fringing effects which reduces the sensitivity of the measurement by increasing the measurement of stray capacitances.[103] The probe to sample distance affects the final measurement so that with smaller probe to sample distances the lateral resolution is improved[104] together with the signal-to-noise ratio of the measurement. Furthermore, by reducing the probe-to-sample distance increases the intensity of the measurement, which is proportional to $1/d^2$.[105]

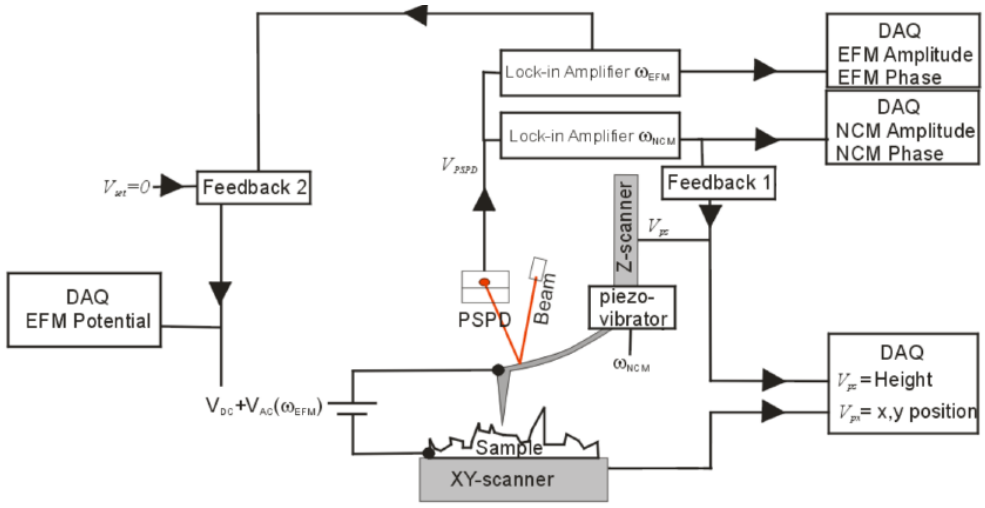


***Figure 17.*** *Schematic of KPFM setup.*

## 2.5 High energy analyses

### 2.5.1 Grazing-Incidence Wide-Angle X-ray Spectroscopy (GIWAXS)

Thin-film morphologies are different from bulk structure. Because of the small thickness, small-angle X-ray scattering (SAXS) and wide-angle X-ray scattering (WAXS) are less suitable to use. To solve this problem, reflection is use instead of transmission. A very shallow incident angle is applied as compared with the incident angle of 90° used in transmission. Resultantly, the beam travels a significantly longer path inside the thin film. This new technique is named grazing-incidence X-ray scattering (GIXS) and a simple sketch of its working is shown in **Figure 18**.

The monochromatic X-ray beam of wavevector $k_i$, with a wave number $k_0=(2\pi)/(\lambda)$, impinges onto the sample surface under an incident angle $\alpha_i$ and is scattered by an exit angle $\alpha_f$ and an out of plane (OOP) angle $\psi$. The z-axis represents the axis normal to the surface and as a consequence, the scattering plane is the (x,z)-plane.[106] Thus, all these angles are typically smaller than 1° (in a range of a few tenth of degrees).[107]

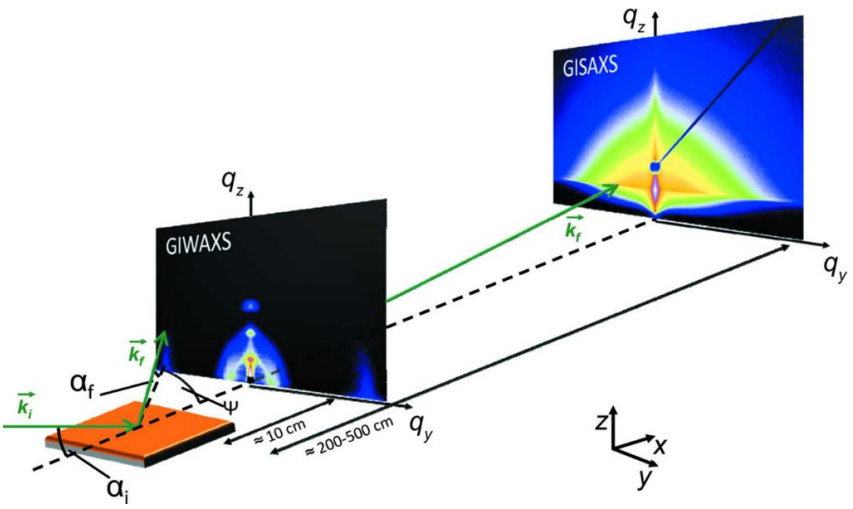


***Figure 18.*** *A sketch of the scattering geometry used in GISAXS and GIWAXS. The sample surface is inclined by an incident angle $\alpha_i$ with respect to the horizon. The exit angle is denoted $\alpha_f$ and the out-of-plane angle ψ. The color coding visualizes differences in the scattered intensity on a logarithmic scale. Typical sample-to-detector distances for GIWAXS and GISAXS are given.* [108]

Because of energy conservation, the X-ray beam is scattered along $k_f$ and the scattering wave vector q is based on three components $(q_x, q_y, q_z)$ that are defined by following equations:

$$q_x = \frac{2\pi}{\lambda}\left[\cos(\psi)\cos(\alpha_f) - \cos(\alpha_i)\right] \quad ; \quad q_y = \frac{2\pi}{\lambda}\left[\sin(\psi)\cos(\alpha_f)\right] \tag{15}$$

$$q_r = \sqrt{q_x^2 + q_y^2} \tag{16}$$

$$q_z = \frac{2\pi}{\lambda}\left[\sin(\alpha_i) + \sin(\alpha_f)\right] \tag{17}$$

The incident angle is usually chosen to be slightly larger than the critical angle of the material under investigation in order to ensure full penetration.[109] This geometry is particularly important for weakly scattered organic thin films to achieve a good signal-to-noise ratio. To increase the scattering intensity, a high-brightness synchrotron radiation is often used for such measurements. In our case, the ALBA synchrotron facility in Barcelona.

Typically, grazing-incidence angle is shifted between 0.05° and 0.50° using a sample-tilt stage. X-ray beam efficiently reflects from sample due to shallow incident angle. Scattering signal coming from sample is then recorded on 2D X-ray detector. Different scattering features (rings, peaks, and diffuse scattering) are obtained. These contain the nanoscale profile of sample under examination.

The length scale of the microstructure probed can be easily tuned by adjusting the sample to detector distance while fixing the beam energy (≈10 keV).

The Scherrer equation is simple and well-known expression to get crystallite size from diffraction peaks[110] :

$$d = \frac{K\lambda}{FWHM \cdot \cos\theta} \qquad (18)$$

*d* is average size of crystalline domains that can be smaller or equal to the grain size, $\lambda$ is X-ray wavelength, *K* is a dimensionless shape factor, normally with a value of 0.9. *FWHM* is the full-width at half-maximum of the measured peak and $\theta$ is Bragg's angle. The position of a specific peak indicates specific crystalline lattice spacings. The orientation of crystallite will be preferentially "face-on," if the π–π stacking scattering is appear in the $q_z$ direction and the lamellar scattering is in the $q_r$ direction. The orientation of crystallite will be preferentially "edge-on" if the π–π stacking scattering is in the $q_r$ direction and the lamellar peak is appearing in the $q_z$ direction.[109] Peak width is use to find the Crystallite Correlation Length (CCL). A narrow peak indicates large CCL, which in turn is indicative of a sharp crystal length distribution, and vice versa.[111] Scattering pattern indicates arrangement and orientation of molecules, i.e., film with no preferred crystallographic orientation produces sharp rings. Film with partially ordered crystallographic orientation results an arc-like peaks. Finally, highly ordered crystallographic orientation form ellipse.[112]

## 2.5.2 Transmission Electron Microscopy (TEM)

Transmission electron microscopy (TEM) is a microscopy technique in which a beam of electrons is transmitted through a specimen to form an image. The wavelength of electrons is related to their kinetic energy via the de Broglie equation, which states that the wavelength is inversely proportional to the momentum. Taking into account relativistic effects (as in a TEM an electron's velocity is a substantial fraction of the speed of light, *c*)[113] the electrons' wavelength is calculated as:

$$\lambda_e = \frac{h}{\sqrt{2m_0E\left(1+\frac{E}{2m_0c^2}\right)}} \qquad (19)$$

where, *h* is Planck's constant, $m_0$ is the rest mass of an electron and *E* is the kinetic energy of the accelerated electron. Electrons are usually generated in an electron microscope by a process known

as thermionic emission from a tungsten filament, usually made of tungsten. The electrons are then accelerated by an electric potential and focused by electrostatic and electromagnetic lenses onto the sample. The transmitted beam contains information about electron density, phase, and periodicity of the targeted material in the hit area; this beam is used to form an image.

Imaging methods in TEM use the information contained in the electron waves exiting from the sample to form an image. Different imaging methods therefore attempt extract from the electron waves exiting the sample different information about the sample. To improve the contrast in the image, the TEM may be operated at a slightly defocused setting, owing to convolution by the contrast transfer function,[114] which would normally decrease contrast if the sample is not a weak phase object. In Imaging mode, which is the one employed in this dissertation, the objective aperture is inserted in a back focal plane (BFP) of the objective lens. By using the objective aperture to select only the central beam, the transmitted electrons pass through the aperture while all others are blocked, and a bright field image (BF image) is obtained. Otherwise, if the signal is selected from a diffracted beam, a dark field image (DF image) is received. The selected signal is then magnified and projected on a camera with the help of Intermediate and Projector lenses. An image of the sample is thus obtained.

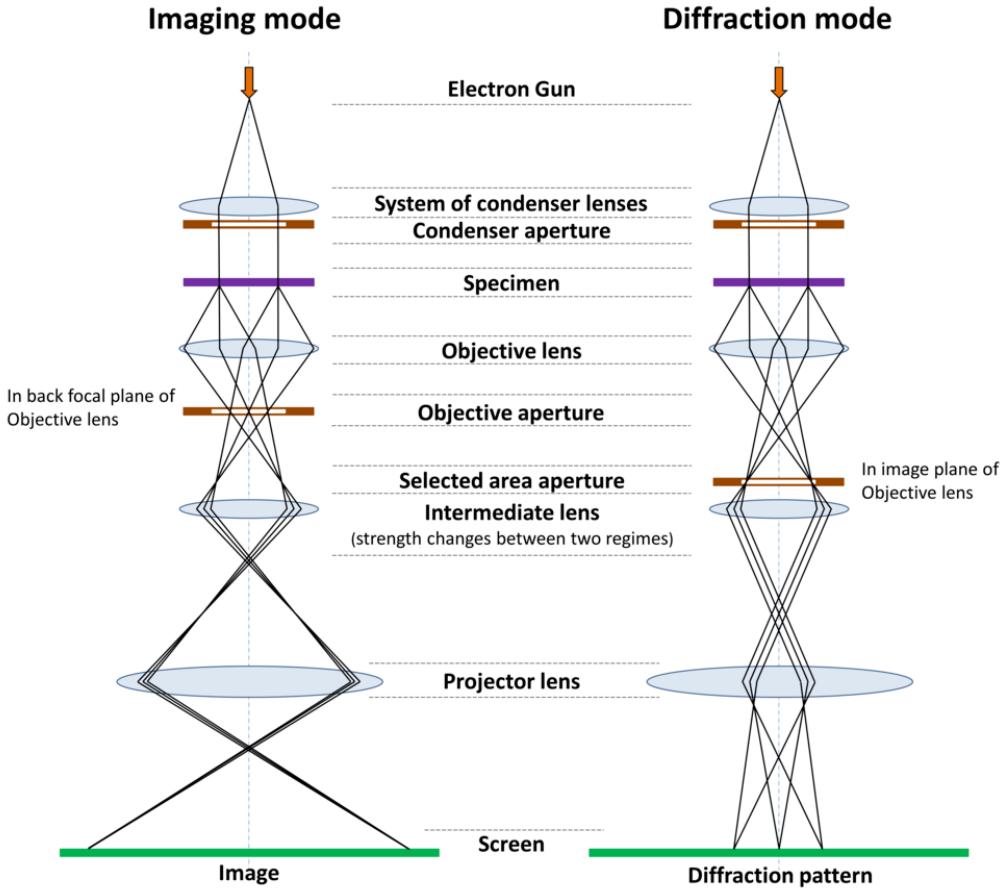


***Figure 19.*** *Schematic view of imaging and diffraction modes in TEM* [115]

# 2.6 Chemical and biological assays

## 2.6.1 Hydrogen Peroxide determination

In physical and analytical chemistry, colorimetry is a technique used to determine the concentration of colored compounds in solution.[116] Colorimetric assays use reagents that undergo a measurable color change in the presence of the analyte.

Peroxidases catalyze the oxidation of a wide variety of substrates, including benzidine and other aromatic amines. A positive "benzidine test" is indicated by the formation of a blue oxidation product of benzidine.[117] The oxidation of aromatic amines by peroxidases has been studied for many years. Horseradish peroxidase, an enzyme frequently used in these studies, is believed to be capable of both one- electron and two-electron oxidations, depending on the substrate employed.[118]

In the case of the HRP-TMB, procedure consist in the addition of the sample to be tested to a vessel where 3,5,3',5'-Tetramethylbenzidine (TMB) and Horseradish peroxidase (HRP) are already dissolved in water. The first one needs to be present in a concentration that is moderately higher than the maximum Hydrogen peroxide ($H_2O_2$) concentration expected in order not to surpass one equivalent of reaction. HRP is dissolved in water with the help of a droplet of DMSO. This reactant serves to the sole purpose of mediating and catalyzing the oxidation of the substrate. The reaction speed is proportional to the HRP concentration, therefore a high concentration (>1mg/l) of this reagent ensure an almost instantaneous oxidation reaction.[118] The absorbance of the sample is then measured between 600nm and 700nm (the absorption peak is centered at 652nm). In order to extrapolate the $H_2O_2$ concentration, a calibration curve must be performed before the experiment.

### 2.6.2 ROS determination in HUVEC cells

Reactive Oxygen Species (ROS) can be detected through their selective reactivity, in the chosen environment, with specific molecules. In the specific case of living cells, the reactant must be biocompatible, non-bioactive and must be able to enter the cells. One of the fastest, easiest, most user-friendly, and accessible methods for monitoring ROS production is based on the detection of ROS-sensitive fluorescent probes using a fluorescence microplate reader.[119] These probes are all oxidized to form intermediate probe-derived radicals that are successively oxidized to generate the corresponding fluorescent products.[120] Dichlorofluorescein diacetate ($H_2$DCF-DA) is one of the most used molecule in this sense.

$H_2$DCF-DA freely permeates the plasma membrane and is hydrolyzed in the cytosol to form the DCFH carboxylate anion.[120] Oxidation results in the formation of fluorescent DCF, which is maximally excited at 495 nm and emits at 520 nm. The oxidation of H2DCF to DCF is a two-step process: first, the DCF radical is formed, and then it is further oxidized to DCF in a reaction with molecular oxygen.[121] $H_2O_2$ does not react with $H_2$DCF directly but requires the presence of peroxidases or other enzymes containing transition metals which are present in the cytoplasm of our cells of interest, namely Human Umbilical Vein Endothelial Cells (HUVECs).

First, HUVECs are seeded on polymer and control substrates and incubated. Illumination protocol is performed, and immediately after the cell medium is removed to avoid chronic $H_2O_2$ effects on cells

and artifacts in the assay. Then the cell cultures are washed and incubated with $H_2$DCF-DA 10uM in KRH for 30 min. After incubation, the fluorescence of the probe is recorded (excitation 490nm, 520 nm) with an inverted microscope. Variation of fluorescence intensity are evaluated over regions of interest covering single-cell areas, and reported values represent the average over multiple cells.

### 2.6.3 AlamarBlue cell viability assay

The resazurin/resorufin assay (AlamarBlue cell viability assay) is commonly used to quantify the number of live cells in a sample, and to monitor cell viability / cytotoxicity. It is a fast, simple, accurate and homogeneous / no-wash high throughput assay that can be used to monitor cells for up to 24-48 hours. The resazurin assay protocol is based on the reduction of oxidized non-fluorescent blue resazurin to a red fluorescent dye (resorufin) by the mitochondrial respiratory chain in live cells. The amount of resorufin produced is directly proportional to the number of living cells. Resorufin has an excitation peak at 572nm and a fluorescence observable between 586 nm. The typical excitation wavelength chosen for this assay lays between 530nm and 560nm and the fluorescence is monitored at 600nm where the contribution of excitation is minimal. The resazurin dye can be measured either in fluorescence or absorbance mode. However, fluorescence mode measurement offers greater assay linearity, reproducibility, robustness, and sensitivity. AlamarBlue has the advantage to be a non-destructive viability assay as opposed to other techniques for the evaluation of cell proliferation.

The number of cells that must be plated per sample is in the order of 50’000, and for the reliability of the method, at least three replicates must be performed.[122] After the addition of $0.1\frac{V}{V}$ AlamarBlue reagent to the cell medium, the samples are incubated for 3h in physiological conditions. Fluorescence is recorded through a confocal microscope and the cell medium is replaced with a new cell medium without AlamarBlue. The assay is repeated after a certain amount of time that depends on the particular experiment.

# 3 Results

## 3.1 Understanding Photocapacitive and Photofaradaic Processes in Organic Semiconductor Photoelectrodes for Optobioelectronics

*Tommaso Paltrinieri, Luca Bondi, Vedran Đerek, Beatrice Fraboni, Eric Daniel Głowacki, and Tobias Cramer*

### 3.1.1 Abstract

Photoactive organic semiconductor substrates are envisioned as a novel class of bioelectronic devices that transduce light into stimulating biological signals with relevance for retinal implants or guided cellular differentiation. The direct interface between the semiconductor and the electrolyte gives rise to different competing optoelectronic transduction mechanisms. A detailed understanding of such faradaic or capacitive processes and the underlying material science is necessary to develop and optimize future devices. Here we address the problem in organic photoelectrodes based on a planar p/n junction containing phthalocyanine ($H_2Pc$) and *N*,*N*′-dimethyl perylenetetracarboxylic diimide (PTCDI). We combine the detailed characterization of photoelectrochemical current transients with spectroscopic measurements, impedance spectroscopy, and local photovoltage measurements to establish a model that predicts quantitatively faradaic or capacitive current transients. The decisive elements of the model are the energy levels present at the interface and the voltage building up in the photoelectrode. The result of our efforts is a comprehensive model of photocapacitive and photofaradaic effects that can be applied to developing wireless bioelectronic photostimulation devices.

### 3.1.2 Introduction

Organic semiconductors are attracting increasing interest as photoactive substrates for the stimulation of biological cells and tissue.[43,123] Exposure to light efficiently generates excitons in organic

semiconductors and localizes the electromagnetic energy of the radiation in close vicinity to the biological interface. Depending on the type of semiconductor and the interfaces present, the excitons can release the excess energy either by recombination into local heat or else by separating into a charge-separated state that initiates further electrical or electrochemical processes.[123] The thermal as well as the optoelectronic pathway both lead to a variation in local physicochemical properties of the illuminated photoactive substrate with possible impact on the biochemistry or bioelectronics of nearby cells. Thus, photoelectrodes offer a means to trigger optically a biological response with high temporal and spatial resolution and without the need for invasive wires to connect external power sources. First proof-of-principles applications that exploit this optoelectronic transduction pathway with organic semiconductors have been realized and regard optical stimulation of neurons for retinal implants,[3,31,42] optical activation of differentiation pathways for regenerative medicine[7,51] and modulation of neuronal signaling in in-vitro cultures.[124]

In addition to enabling an optical transduction pathway, a range of properties make organic semiconductors interesting candidates for photoactive substrates in biomedical applications.[43,125] As organic semiconductors are molecular or polymeric materials, they can be designed to offer soft mechanical properties allowing integration into flexible or stretchable devices.[26,126,127] The consequence is a better adaptation to curved biological formfactors and a larger compliance to the mechanics of biological tissue, both improving the interface quality and reducing invasiveness.[128] Also, for many organic semiconductors biocompatibility with different cell types has been demonstrated.[129–131] Finally, organic semiconductors offer stable electrochemical properties when in direct contact with aqueous electrolyte and a dielectric encapsulation layer can be avoided.[132,133] Hence extremely low-impedance interfaces between the electronic processes in the semiconductor and the ionic ones in the cellular environment have been realized.[134] The low-impedance properties are at the core of many emerging organic semiconductor based bioelectronic devices such as organic electrochemical transistors[135] or low-invasive recording and stimulation arrays[128,136].

In photoelectrodes the direct interface between the semiconductor and the electrolyte opens several physicochemical pathways for light activated stimulation.[123] Photoexcited states can directly participate in electrochemical reactions in the nearby cell medium and organic semiconductors have been reported to show photocathodic[137–139] or photoanodic[140,141] reactions in aqueous electrolytes. A well-documented effect regards the reduction of dissolved oxygen to hydrogen peroxide by photoactivated electrons.[49,68] At variance to such faradaic reactions is photocapacitive behavior.[3] In

this case, no electrons are transferred across the semiconductor/electrolyte interface. Instead, excitons dissociate into a charge separated state at an internal interface such as the semiconductor/metal electrode or a p/n heterojunction. This causes an ionic displacement current until the electric field of the charge separated dipole is screened. Photofaradaic and photocapacitive effects impact very differently on biological cells. Reactive oxygen species formed during faradaic reactions have been demonstrated to impact on the cell's biochemistry causing alterations in intracellular calcium level and inflammation reactions at higher concentrations.[7,51] Instead photocapacitive currents vary locally the cell's membrane potential[5] and can trigger action potentials in neurons.[3] Clearly, effective photoelectrodes must enable a single stimulation mechanism, based on either photofaradaic or photocapacitive transduction. However, to date it is not clear whether such a strict separation can be achieved in photoelectrodes based on organic semiconductor in direct contact with the electrolyte. Progress will require a detailed understanding about how the photoelectrode architecture and the semiconductors electronic material properties impact on photocapacitive versus photofaradaic processes.

To address this problem, we report here detailed photoelectrochemical characterizations and theoretical analysis on photoelectrodes with a phthalocyanine ($H_2Pc$) and perylenetetracarboxylic diimide (PTCDI) heterojunction. Such photoelectrodes have been demonstrated to work as effective photocapacitors that enable the stimulation of retinal neurons or single cell oocytes in in-vitro experiments.[3,5] At the same time PTCDI based photoelectrodes have also been reported to act as photocathodes with strong faradaic reactions yielding effective hydrogen peroxide generation.[49,68] In $H_2Pc$/PTCDI heterojunctions, this faradaic process is enhanced when electron donors such as glucose are present to close the electrochemical cycle with anodic oxidation at the back-electrode.[57] Based on these to-date findings, the $H_2Pc$/PTCDI heterojunction photoelectrode represents a model system with both photocapacitive as well as photofaradaic behavior. The factors affecting the prevalence of either regime remain ambiguous and quantitative understanding of transient photocurrent signals is currently missing. We address this issue by combining transient and spectroscopic photocurrent measurements with electrochemical impedance spectroscopy and microscopic characterizations on $H_2Pc$/PTCDI photoelectrodes. Our findings lead to an equivalent circuit model that reproduces quantitatively photocurrent transients and explains the transition between capacitive and faradaic behavior. The model shows how intrinsic material properties such as semiconductor energy-levels and reorganization energy determine photocurrent signals and how the photoelectrode geometry can

be tuned to control and optimize photocurrent generation. The model can easily be extended to more complex photoelectrode operation modes. As examples we explain the large electrochemical photovoltage generation observed in the photoelectrodes and rationalize the impact of the back-electrode in floating photocapacitor pixels for wireless operation, such as in retinal stimulation applications.

### 3.1.3 Results

#### Faradaic and capacitive photoelectrode processes

**Figure 1a** depicts a scheme of the basic experiment used to characterize photoelectrodes made of an indium tin oxide (ITO) substrate onto which an organic planar heterojunction of p-type $H_2Pc$ (30 nm) and n-type PTCDI (30 nm) were thermally evaporated. The border of the photoelectrode is sealed by a silicone O-ring to expose an area of 0.785 $cm^2$ diameter to the aqueous electrolyte (0.1 M phosphate buffered saline - PBS). A potentiostat connected to the ITO substrate (WE) and to the Ag/AgCl reference electrode (RE) and Pt-wire counter electrode (CE) controls the voltage $V_r$ applied to the photoelectrode with respect to reference in the electrolyte and measures transient photocurrents. The Figure also shows schematically the basic mechanisms that can contribute to photocurrent signals. Upon illumination, excitons are generated in the organic semiconducting layer and separate into holes and electrons at the planar p-n junction. The separated charge carriers can follow two principally different reaction pathways to contribute to the photocurrent transient. First, charge separation into positive and negative carriers in the p-type and n-type layer, respectively, gives rise to an electric field that attracts cations to the surface and repels anions. In this way a transient ionic displacement current $I_C$ is generated in the electrolyte that persists until the ionic double layer at the semiconductor/electrolyte interface is charged. This capacitive mechanism is indicated by a blue arrow in Figure 1c. Second, free electrons in the n-type layer can tunnel onto acceptor molecules in the liquid and give rise to reductive faradaic processes. A typical acceptor state in ambient conditions regards dissolved oxygen.[49,142] This faradaic current $I_F$ does not cause the accumulation of charges at the interface, as both, the remaining hole charge as well as the negatively charged acceptor, are free to diffuse away from the interface. Consequently, a constant steady current is generated from the

faradaic process, as long as mass transport of acceptor molecules does not become limiting. This mechanism is indicated by the red arrow in the Figure 1a.

Figure 1b shows two photocurrent transients measured at different photoelectrode voltages. The two transients are presented here as the first evidence that both, capacitive as well as faradaic mechanism coexist and can be controlled by external parameters. When applying a positive voltage ($V_r$ = 0.25 V), a negative current spike is observed at the onset of illumination (590 nm, 12.4 mW/cm$^2$), corresponding to the formation of a positively charged ionic layer at the photoelectrode surface. Upon switching off the light, the double layer discharges and a similar current spike of positive sign is present. In contrast, at negative photoelectrode voltage ($V_r$ =-0.15 V) an almost constant negative current is observed during illumination and no current spikes are generated. Consequently, the current is caused purely by the faradaic process and no variation in double layer charge occurs.

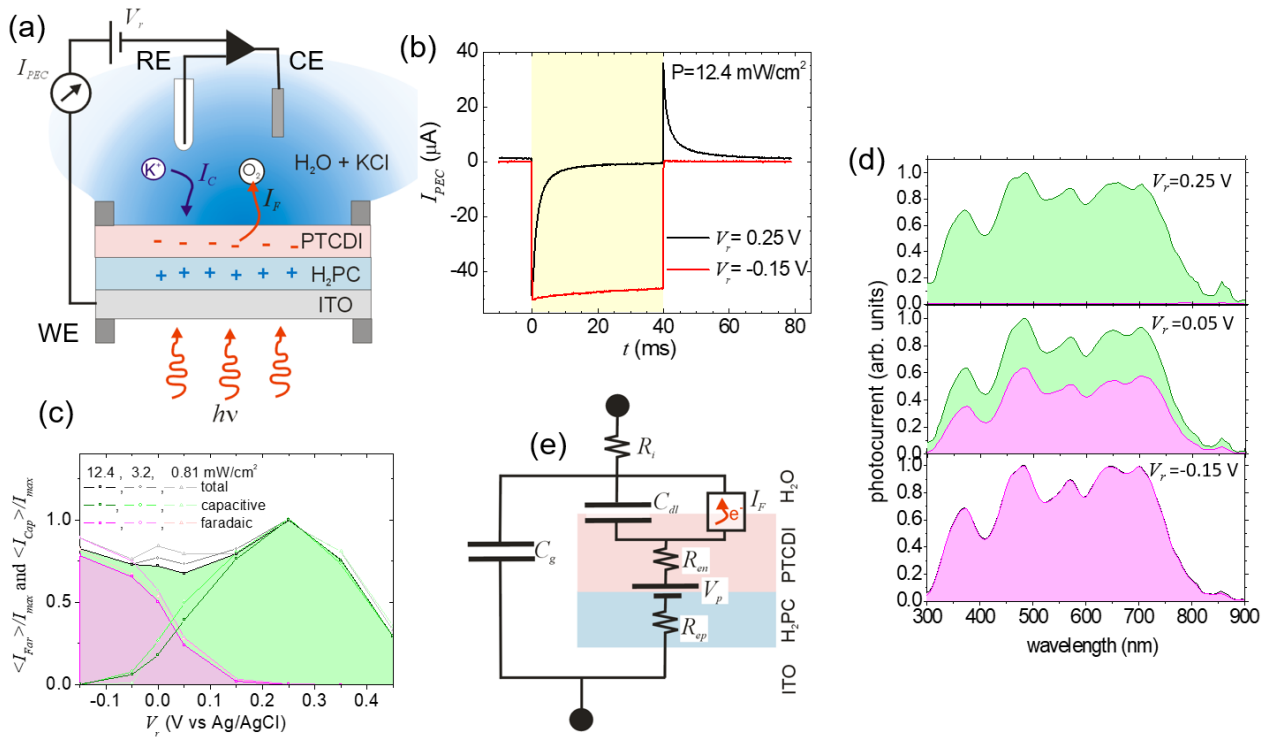


***Figure 1.*** *Capacitive and faradaic currents in organic photoelectrode. (a) Scheme of the experiment. Optically evoked capacitive currents $I_C$ involve ionic displacement currents as indicated by the blue arrow. Faradaic currents $I_F$ instead involve an electron transfer from the electrode onto oxygen, that acts as an electron acceptor in solution. (b) Current transients acquired during an illumination cycle*

*(595 nm, 12.4 mW/cm$^2$) for two different voltages $V_r$ applied to the working electrode. At positive voltages, the transient shows characteristic features of a capacitive mechanism. At more negative voltages, a faradaic behavior is observed. (c) Ratio of capacitive and faradaic current contributions as a function of the voltage and in (d) as a function of excitation wavelength. (e) equivalent circuit proposed to model the photoelectrode. Crucial elements are the double layer capacitance of the photoelectrode $C_{dl}$, a voltage source simulating the photovoltage $V_p$ generated at the p/n junction, an element describing faradaic charge transfer $I_F$ and the resistance of the semiconducting layers $R_e$.*

To distinguish faradaic from capacitive currents quantitatively we compute the net total charge transferred across the photoelectrode interface per illumination cycle by integrating over the current transient:

$$Q_F = \int_{t=0}^{T} I(t)dt \qquad (1)$$

The resulting number is the total amount of faradaic charge $Q_F$ assuming an irreversible electron transfer process. Instead, capacitive displacement currents cancel each other out in this integral as they appear with both, positive and negative polarity. To count capacitive charges $Q_C$ we have to consider the absolute value of the current transient and subtract the amount of faradaic charge:

$$Q_C = \frac{1}{2}\left(\int_{t=0}^{T} |I(t)|dt - |Q_F|\right) \qquad (2)$$

From the charges $Q_F$ and $Q_C$ we define average photocurrent values as $\langle I_F \rangle = Q_F / T$ and $\langle I_C \rangle = Q_C / \tau$, where $T$ is the period of the illumination cycle and $\tau$ is the characteristic time constant describing the capacitive transient decay time (see Suppl. Inf. S1). Figure 1c plots the average faradaic and capacitive photocurrents as well as the total averaged photocurrent $\langle I_F \rangle + \langle I_C \rangle$ as a function of photoelectrode voltage $V_r$. The plot demonstrates the fundamental role of the electrochemical voltage $V_r$ for controlling the transients at the semiconducting photoelectrodes. At positive voltages we observe purely capacitive behavior. The transition to a faradaic regime sets in at 0.1 V and until -0.1V both mechanisms coexist. Below this voltage a purely faradaic regime is observed. In a similar experiment we investigated the impact of the excitation wavelength on the ratio between faradaic and capacitive processes. Figure 1d shows photocurrent spectra obtained at three different voltages. In the positive range, the spectrum constitutes only capacitive current contributions, while at negative voltages the processes are almost entirely faradaic. Despite the change in mechanism, the overall

shape of the spectra remains unaltered and the ratio of capacitive to faradaic processes is not influenced by the wavelength. The finding clearly demonstrates that the electrochemical reactions happen on a slower time scale and only depend on the number of charges separated at the p-n junction. The energetics and dynamics of exciton formation and separation as well as charge transfer state relaxation dynamics are much faster and do not have a direct impact on the following electrochemical process.

Based on these findings and on the qualitative understanding of the p-n junction photoelectrode we propose the equivalent circuit depicted in Figure 1c to arrive at a quantitative model. The circuit is composed of a voltage source that represents the dipole and associated photovoltage $V_p$ present at the p-n junction during illumination. Transport of electronic carriers across the semiconductor is described by the resistances $R_{ep}$ and $R_{en}$. In the electrolyte the transport of ions is modelled by the resistance $R_i$. The semiconductor/electrolyte interface is modelled by two elements: first, a capacitance $C_{dl}$ that represents the double layer containing electronic charges in the semiconductor and ionic charges in the electrolyte. Second, a non-linear element that causes the faradaic charge transfer processes $I_F$. Finally, a smaller capacitance $C_g$ is put in parallel to the circuit to account for the geometric capacitance of the organic semiconductor layer. Clearly, this circuit is simplified but it allows to grasp the most relevant processes at the p-n or ITO-p interfaces. In the following, we provide a characterization for each individual circuit element based on electrochemical impedance spectroscopy and photovoltage measurements. Only then we turn back to transient behavior and apply the parametrized circuit to achieve a quantitative description of the current transients.

## Surface photovoltage measurements

Electrical stimulation with the photoelectrode is driven by photovoltage generation. In the equivalent circuit model this process is attributed to the p-n junction and in first approximation independent on the presence of electrolyte. To confirm this hypothesis and to arrive at quantitative photovoltage values that characterize the voltage source in the equivalent circuit we perform Kelvin-Probe Force Microscopy (KPFM) on photoelectrode/air interfaces in darkness and during illumination. **Figure 2a, b and c** show, respectively, images of the surface height, work function, and surface photovoltage $V_p$ obtained from such measurements. The surface topography is dominated by the nanocrystalline structure of the evaporated organic semiconductor with crystallite sizes on the order of 10 – 20 nm. The work function is close to the level of the underlying substrate (ITO) and reveals that in darkness

interfacial dipoles due to thermally activated charge transfer states are not present.[143] Upon illumination, we observe the formation of a negative photovoltage. The precise values of both, work function as well as photovoltage, depend strongly on the local topography. The profiles of height, work function, and surface photovoltage in Figure 1d obtained from the images show the effect more clearly. Overall, the length scale of the local fluctuations match to variations in surface height. Therefore, we suggest that changes in nanocrystallite orientation are responsible for the variations in work function and surface photovoltage. We note that the length scale of the surface photovoltage fluctuations is however orders of magnitude below the typical size of cells. Therefore, we consider the average photovoltage to be relevant for photoelectrode biological activity (and not the local fluctuations). Figure 1e then shows how the average photovoltage increases with light intensity *P*. At relatively low light intensities of $P$=3 mW/cm$^2$ we observe photovoltages exceeding 30 mV. For strong cell-photoelectrode contacts with high sealing resistance, such a value can already be sufficient for cell membrane depolarization. Higher light intensities lead to even stronger photovoltage response as required for efficient cell depolarization.[5] The inset of the Figure shows the photovoltage transient and confirms the fast rise and decay times of the photovoltage (<< 1ms). The functional dependence of photovoltage on light intensity is described by a logarithmic function similar to photovoltages observed in inorganic heterojunctions.[144] KPFM photovoltage measurements were done on pristine samples and after photocurrent measurements in electrolyte. No significant difference in response due to degradation was found (see Supp. Inf. S8)

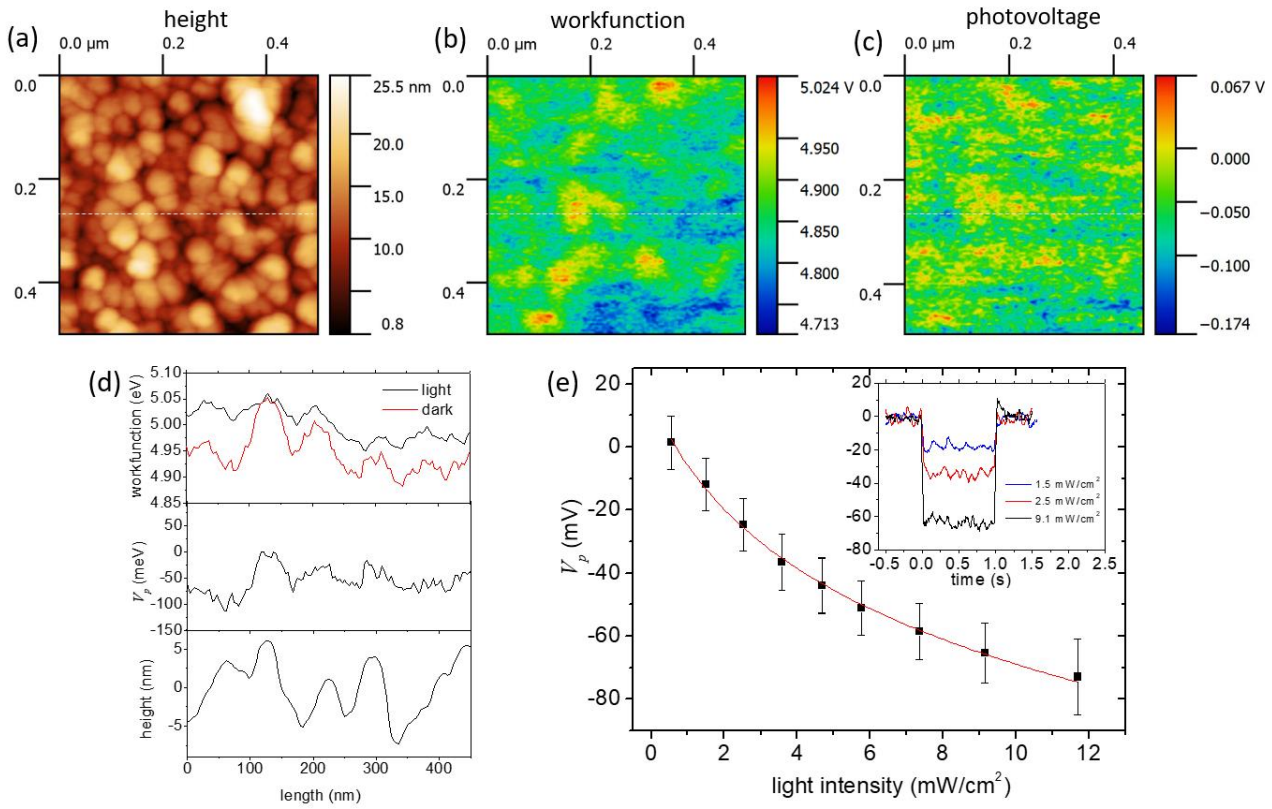


***Figure 2.*** *Kelvin Probe Force microscopy (KPFM) on the photoelectrode surface. (a) Topography of sample (b) local work function calculated from KPFM potential in darkness. (c) local photovoltage $V_p$ calculated from KPFM potential measured during illumination and darkness. (d) Line profiles of the images. (e) Averaged KPFM photovoltage as a function of light intensity. The inset shows typical measurement transients.*

## Electrochemical impedance spectroscopy

EIS performed in darkness and during illumination provides quantitative data describing passive elements in the photoelectrode equivalent circuit. Bode plots of impedance and phase measured at different photoelectrode voltage $V_r$ are shown in **Figure 3a** and b. As EIS measures the passive circuit properties, we do not consider the voltage source in the model to fit the measurement data. Due to the small modulation amplitude the faradaic element is treated as a charge transfer resistance $R_{CT}$. All other elements in the fitting model are kept as depicted in Figure 1d. The resulting fit describes well the experimental data, and we obtain quantitative values for $C_{dl}$, $C_g$, $R_{Ct}$, $R_i$ and $R=R_{ne}+R_{np}$. In darkness, the heterojunction behaves as a dielectric and the impedance response is dominated by the geometric capacitance $C_g$ and the ionic resistance $R_i$. This is a direct consequence of the fact that the

organic materials are intrinsic, undoped semiconductors with very low conductivity in the dark. During illumination, the impedance drops by orders of magnitude and typical features appear in the amplitude and phase spectra that are well reproduced by the simple model circuit. Deviations between model and measured data are only notable in the EIS phase spectra at positive photoelectrode voltages ($V_r$ >0.15). At these voltages, the peak associated to the double layer capacitance broadens. This disagreement between model and data is associated to positive charge carriers that migrate from the ITO electrode into the p-type layer and are subjected to disorder and surface roughness at the ITO/$H_2$Pc interface which is not considered in our idealized model.

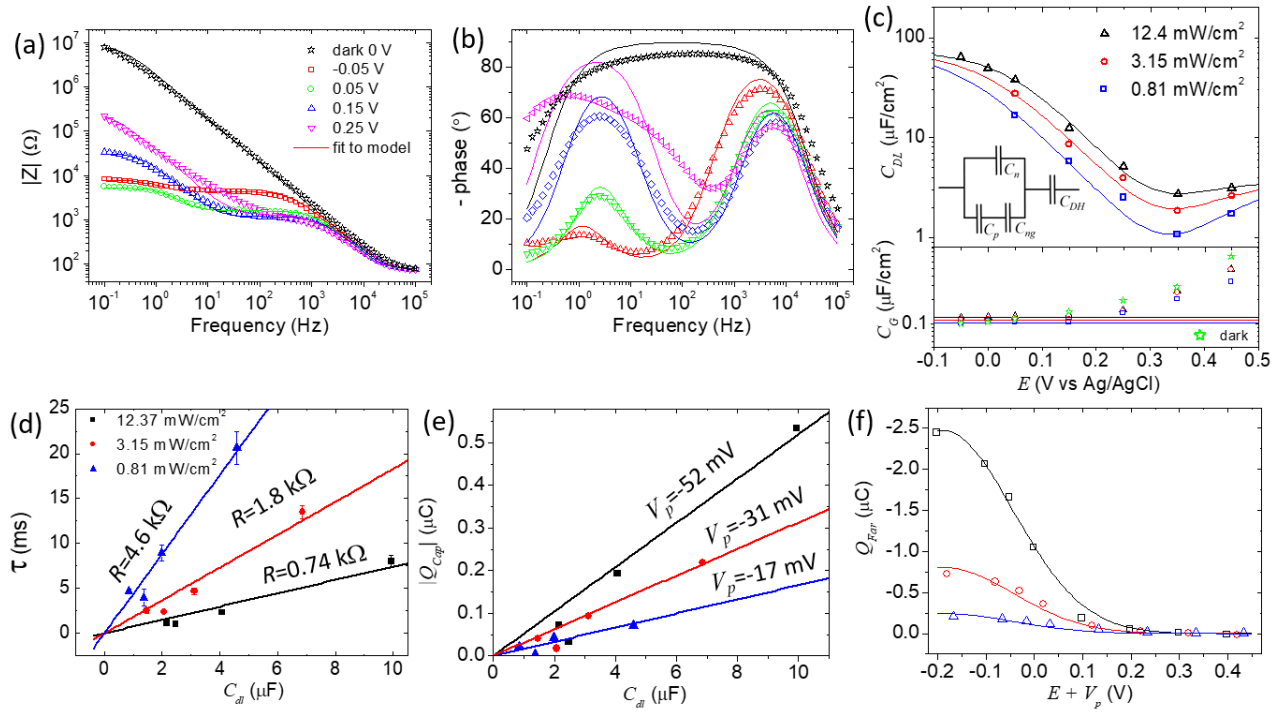


***Figure 3.*** *Determination of parameters for photoelectrode equivalent circuit. (a,b) Electrochemical impedance spectroscopy data and fit to model. Data measured in darkness and during illumination at 595 nm with 12.4 mW/cm$^2$ at different voltages $V_r$. (c) Extracted double layer capacitance and geometric capacitance as a function of $V_r$. Solid lines show fits to capacitance models as detailed in the text. (d) Plot of capacitive photocurrent time constant τ as a function of double layer capacitance $C_{dl}$ to determine the characteristic resistance R of the junction. (e) plot of capacitive charge $Q_C$ as a function of $C_{dl}$ to determine the photovoltage $V_p$. (f) Plot of faradaic charge $Q_F$ as a function of effective voltage $V_r$ + $V_p$ and fit to Marcus-Gerischer model describing faradaic charge transfer.*

Most importantly, the EIS model provides access to $C_{dl}$ and $C_g$ of the photoelectrode. Figure 3c shows these capacitances normalized per photoelectrode area as a function of photoelectrode voltage. The geometric capacitance $C_g$ is independent on light intensity and shows almost no dependence on $V_r$. Only at larger positive photoelectrode voltage a slight increase in $C_{dl}$ is observed which is attributed to hole carriers that start to enter into the p-type $H_2Pc$ layer. Instead a strong dependence of the double layer capacitance $C_{dl}$ on photoelectrode voltage and illumination power is present and variations exceeding an order of magnitude are observed. Maximized capacitance with values typical for the Debye-Helmholtz layer are only reached at negative voltages. Towards more positive voltages the value of $C_{dl}$ drops by more than an order of magnitude. This effect can only be explained by an additional, strongly voltage dependent capacitance in series to the Debye Helmholtz capacitance $C_{DH}$. The semiconductor in direct contact with the electrolyte is the n-type PTCDI. Consequently, a more positive voltage applied to the photoelectrode causes a drop in the Fermi-level and reduces the number of negative carriers in the conduction band. The resulting decrease in capacitance for an undoped semiconductor is described by[145]:

$$C_n = A\frac{\varepsilon\varepsilon_0}{L_n}\exp\left(-\frac{qV_r}{ikT}\right) \qquad (3)$$

with the intrinsic screening length $L_n$, dielectric constant ε and a non-ideality factor $i$. Only at very positive voltages the total measured capacitance starts to rise again. Now, positive charges in the close-by p-type $H_2Pc$ layer start to accumulate and interact with the counterions in solution resulting in a capacitance that is a series combination of the undoped p-type semiconductor $C_p$, described by an equation similar to eqn. [3], and a geometric capacitance $C_{ng}$ describing the depleted n-type PTCDI layer. The inset in Figure 3c shows how the different capacitances are combined in series and in parallel to achieve a quantitative fit to the capacitance data (see Suppl. Inf. S2 for more detailed description).

In the next step, we use the quantitative description of the capacitance $C_{dl}$ to achieve a first estimation of the effective resistance $R$ and photovoltage $V_P$ of the heterojunction based on the PEC transient data. For transients in the capacitive regime ($V_r$ >0.05 V) we plot in Figure 3d and 3e the characteristic time constant $\tau$ and the total charge stored on the double layer capacitor $Q_C$ as a function of $C_{dl}$. In both cases the linear fit to the data confirms the simple capacitor relations $Q_C = V_p \cdot C_{dl}$ and $\tau = R \cdot C_{dl}$ allowing to extract $R$ and $V_p$ values for different light intensities. Notably, the photovoltage values $V_p$

are in good agreement with the KPFM based measurements and confirm our initial hypothesis that the photoelectrode is driven also in electrochemical environment by exciton separation at the p-n junction.

The last missing element regards the faradaic processes. In Figure 3f we plot the faradaic charge extracted from the PEC transient as a function of photoelectrode voltage. For the three different light intensities a similar functional dependence is obtained that shows the onset of faradaic processes at 0.1 V and exhibits a strong increase towards negative voltages until a saturation is reached. The stable current plateau in the PEC transient and the CV-data (see Suppl. Inf. S3) indicates that the process is not limited by mass transport. Instead, the heterojunction resistance in series with the charge transport process on the acceptor state dominate the current. We thus model the rate limiting process of the oxygen reduction reaction by applying a Marcus-Gerischer rate equation leading to the expression:

$$Q_F = \Delta t \cdot I_F = \Delta t \cdot I_{F,0} exp\left[-\frac{\left(\Delta G^0 + qV_r - I_F R + V_p + \lambda\right)^2}{4\lambda kT}\right] \qquad (4)$$

In which $I_F$ is the faradaic current, $\Delta t$ is the duration of the light excitation, λ is the reorganization energy, and $\Delta G^0$ the free energy of the charge transfer process. Eq. 4 depends recursively on the current $I_F$ that passes through the heterojunction of resistance $R=R_{ne}+R_{np}$ as it creates an additional potential drop across the photoelectrode. A solution for eq. 4 was obtained numerically. For the different light intensities, we varied only the prefactor $I_{F,0}$ and obtain excellent fits to the data (lines in Figure 3c) with an overall reorganization energy of λ = 0.43 ± 0.07 eV. Such a value is in the typical range for single electron CT processes at aqueous interfaces.[145] The free energy of the charge transfer process amounts to $\Delta G^0$ = -0.24 ± 0.04 eV and represents the difference between the edge of the PTCDI conduction band and the standard potential of the oxygen acceptor state.

## The full photoelectrode model

At this point we have numerical representations for all elements in the equivalent circuit of the photoelectrode. The combined set of differential equations describing the current flow is solved numerically using Runge-Kutta algorithm (see Suppl. Inf. S4). Measured and simulated transients are compared in **Figure 4** for different light intensities and photoelectrode voltages. The simulations that are based on the parameters obtained as described above (red curve in Figure 4) achieve a reasonable description of the relevant features in the transients such has the capacitive current spike at positive voltages and the transition towards pronounced faradaic currents during illumination at negative

voltages. However, stronger differences between simulated and measured transients exist in the capacitive contribution at positive photoelectrode voltages. To improve the agreement, we introduce the photovoltage as a fitting parameter, that depends on the light intensity and also on the voltage $V_r$. This is justified by the strong impact of electric fields on recombination processes at the p-n heterojunction. For example, stronger photovoltages should be present at negative photoelectrode voltages where the electric field facilitates exciton splitting and charge separation. After the numerical fitting procedure, we obtain an almost quantitative agreement with the measured transients. The Suppl. Inf. S5 contains all the numerical values of the parameters/functionals used in the fit.

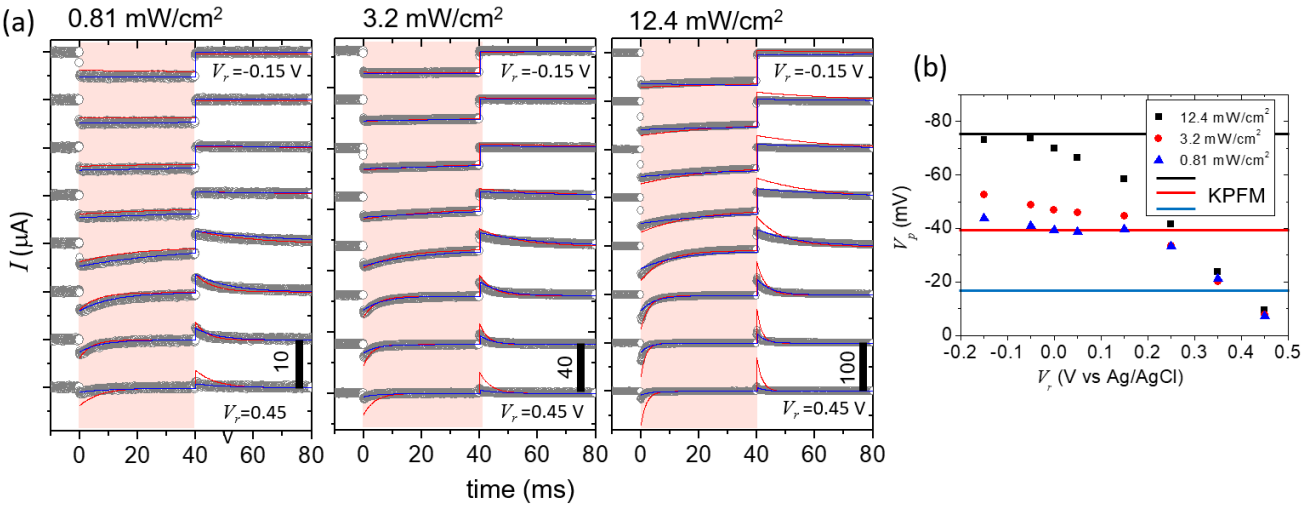


***Figure 4.*** *Measured (grey points) and simulated photocurrent transients (red and blue lines) obtained at different light intensities and photoelectrode voltages. For clarity transients with different photoelectrode voltage are shifted by an offset. The red lines correspond to the model with parameters determined a priori from EIS and photovoltage measurements. The blue line corresponds to the model optimized directly with the transient data using photovoltage and heterojunction resistance as fitting parameters.*

With the full model in hand, we can arrive at important conclusions regarding the p-n heterojunction based photoelectrode. **Figure 5a** shows the energy diagram of the heterojunction in contact with the electrolyte in darkness. During illumination excitons are generated in the p-type and n-type layer. After diffusion to the junction the excitons separate into a hole charge in the valence band of the $H_2Pc$ layer close to the ITO back electrode and an electronic charge in the conduction band of the PTCDI layer in contact with the electrolyte. The charge separation leads to the formation of the dipole layer

at the p-n junction and generation of photovoltage. After charge separation, two reactions are possible and indicated in the energy diagram: In the first case, the electron interacts with counterions in the electrolyte and gives rise to the capacitive current pulse (blue arrow). Once the Debye-Helmholtz layer is established, no further current is generated and charge separation and recombination at the heterojunction occur at equal rate. In the second case, the free electron in the PTCDI conduction band can tunnel onto the $O_2$-acceptor state in the electrolyte (red arrow). As new charges are continuously generated in the heterojunction, this process gives rise to the steady faradaic current.

The efficiency of the tunneling process involved in the faradaic process depends strongly on the energetics of the involved states. From our measurements we obtain a free energy of $\Delta G^0$=-0.24 eV. Combining this value with the electron affinity of PTCDI, $E_{A,PTCDI}$ = 4.1[146] and the PTCDI/PBS surface dipole in darkness estimated to be $q \cdot V_d$ = 0.23 eV from KPFM measurements (see Suppl. Mat. S6), we obtain the energy level of the acceptor state, $E^0_{OxRed} = E_{A,PTCDI} + \Delta G^0 - q \cdot V_d$ = 4.11 eV. This value compares well to the standard potential of the rate limiting, one-electron oxygen reduction process leading to the superoxide radical anion $E^0_{O2/O2-}$ = 4.1 eV[147] and is significantly above the level for the two-electron process reported for the final reaction product hydrogen peroxide $E^0_{O2/H2O2}$ = 4.8 eV.[142]

The energy diagram explains the relevant factors that decide on capacitive or faradaic photoelectrode behavior. A negative photoelectrode voltage $V_r$ shifts the semiconductor levels upwards with respect to the oxygen acceptor level, thus making electron transfer more probable and causing a larger faradaic current. Instead, a positive voltage $V_r$ suppresses faradaic transfer as the acceptor state rises above the PTCDI conduction band level. From these findings we predict that the capacitive mechanism becomes favored in semiconductors with lower conduction band levels (high electron affinity) and strong reorganization energy, whereas larger bandgaps and high lying conduction bands support the faradaic process.

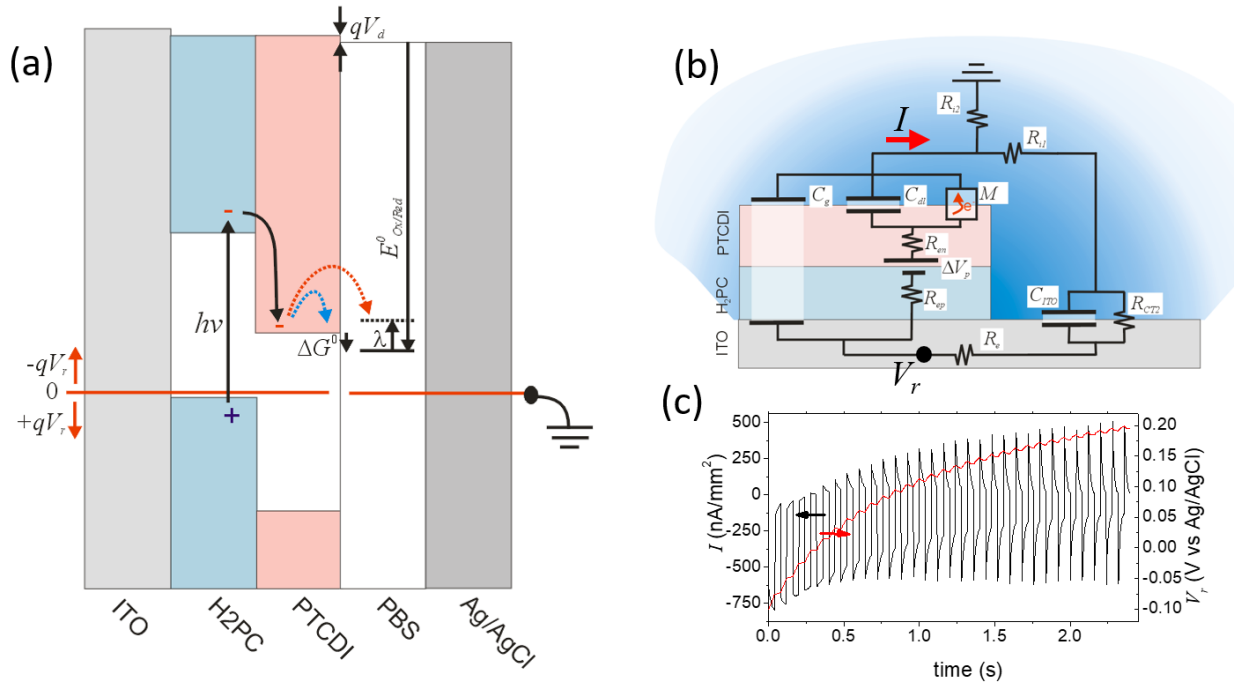


***Figure 5.*** *Implications of photocapacitor equivalent circuit model. (a) Energy diagram of photocapacitor junction in darkness and interpretation of capacitive and faradaic currents. The model provides estimates for the reorganization energy λ = 0.43 +/- 0.07 eV and for the free energy* $\Delta G^0$ *= -0.24 +/- 0.04 eV. (b) Equivalent circuit of floating photocapacitor pixel. (c) Simulated floating photocapacitor response showing transition from faradaic to capacitive operation regime without external control.*

To highlight the relevance of the photoelectrode circuit model we employ it to simulate floating photocapacitor pixels. A floating configuration is important in bioelectronic applications as the pixel should activate by light without any wire attached. To provide a circular pathway for the generated current in a floating electrode pixel, the ITO back electrode must be put into direct contact with the electrolyte as shown in Figure 5b. The ITO/electrolyte interface is modelled by the resistance $R_{ITO}$ and the capacitance $C_{ITO}$. The two elements are crucial as they close the circuit for photocurrent generation in the floating electrode necessary to maintain charge balance. Values for both are obtained from EIS measurements on ITO. Experimentally, there is no way to measure or control the photoelectrode voltage Vr in the floating configuration. Thus, at first sight it might be unclear how to control capacitive or faradaic contributions in such a floating pixel. To understand the situation, we

run simulations for the worst-case scenario for wireless stimulation: the photoelectrode is for some reason at a negative potential. As shown above, the negative potential should lead to a faradaic process, although a capacitive one would be desired to avoid reactive oxygen species to be generated. The simulation of such an initial condition with Vr=-0.1 V is shown in Figure 5d. As expected, the simulated current transient shows in initially a faradaic shape. However, already after a few illumination pulses the shape changes and becomes charge balanced and capacitive. Accordingly, the Vr drifted from the negative initial condition to a stable positive value. Therefore, even in the worst case, a faradic mechanism cannot prevail on the floating photocapacitor pixel when ITO is employed as a back-electrode. The effect explains our earlier work in which $H_2$Pc-PTCDI based floating photoelectrodes behave as photocapacitors with charge balanced stimulation profiles that do not show faradaic current contributions. We note that the effect can be further influenced directly by the electro-chemical properties of the back electrode such as the Nernst-potential.[57]

### 3.1.4 Conclusions

In this work we analyze in detail the photoelectrochemical processes that lead to photocurrent generation in organic heterojunction based photoelectrodes operated in contact with aqueous electrolyte. Electrochemical impedance spectroscopy, Kelvin probe force microscopy and spectroscopic photocurrent measurements are used to determine basic properties of the heterojunction/electrolyte interface such as photovoltage, capacitive coupling and charge transfer resistance. The findings are combined into an equivalent circuit model that is in quantitative agreement with measured photocurrent transients and provides a clear explanation for photocapacitive as well as photofaradaic processes. Photofaradaic processes, that are undesired in bioelectronic stimulations, can be avoided by applying positive voltage to the photoelectrode. In this way electrons emerging out of charge separated states do not tunnel onto electrochemical acceptor states but remain in the conduction band and interact only electrostatically with the electrolyte generating an ionic displacement current. The equivalent circuit model relates the magnitude and the time constant of the displacement current to the double layer capacitance, the photovoltage generated at the organic p-n junction and the total resistance of the heterojunction. We further employ the model to provide important insight into the response of floating photoelectrodes as employed for retinal

neuron stimulation. The simulation shows that in the floating configuration the photoelectrode automatically charges positively and operates in the purely capacitive mode.

We are convinced that our findings provide guidance for the design and optimization of future organic optobioelectronic interfaces. Our results demonstrate how semiconductor energy levels impact on capacitive or faradaic processes. To maximize the capacitive pathway exploited in artificial retina interfaces, transport properties of the heterojunction as well as electronic photovoltage generation have to be optimized. The equivalent circuit model presented here shows how these properties are interrelated and dependent on semiconductor material properties as well as device architecture.

## 3.1.5 Methods

### Photoelectrode fabrication

15×15mm square ITO slides (Kintec, 15-20 Ohm/sq) were cleaned by consecutive ultrasonication for 5 minutes in acetone, 2-propanol and 2% Hellmanex III cleaning solution. The substrates were then rinsed with DI water and dried under a stream of $N_2$. Next, $O_2$ plasma treatment was applied (100W, 5 minutes) and the ITO surface was modified by a vapor-phase deposition of *n*-octyltriethoxysilane (OTS) by placing the samples in an OTS-vapor saturated chamber heated to 80 °C for 1 h. This improves the adhesion of organic PN layers to the ITO substrate. Excess physisorbed OTS was removed by sonicating the samples in acetone for 5 min followed by rinsing with DI water and drying under $N_2$ stream. Phthalocyanine $H_2Pc$ (Alfa Aesar) and *N,N′*-dimethyl-3,4,9,10-perylenetetracarboxylic diimide, PTCDI (BASF) were purified thrice by temperature-gradient sublimation. The $H_2Pc$/PTCDI layers were formed by evaporative deposition at a base pressure of < $2 \times 10^{-6}$ Torr using a rate of 0.1-0.5 nm/s. 30 nm of P-type $H_2Pc$ and 30 nm of N-type PTCDI were successively deposited. Kapton tape was used to mask the edges of the ITO substrate to leave areas convenient for electrically contacting for later measurements. All samples were then stored in 0.1 M KCl for 24 h before further use.

### Photoelectrode electrical characterizations

The photoelectrode was mounted in a homemade PEC-cell (design inspired from literature[148]). A silicone O-ring confined the photoelectrode area to a diameter of 10 mm in contact with aqueous

electrolyte (PBS 0.1 M) and prevented electrochemical contact with the back ITO electrode. A Pt-wire and Ag/AgCl (3M KCl) reference electrode were used to control the potential of the electrolyte with respect to the photoelectrode. The ITO back electrode was connected as the working electrode. A potentiostat (Metrohm PGSTAT 204) was used for transient current measurements and electrochemical impedance spectroscopy. For spectroscopic measurements a Xenon lamp (Hamamatsu 150W) combined with a Czerny-Turner monochromator (Cornerstone 260) was used as light source. For other measurements a surface mounted LED (595 nm CREE XPE AMB-L1) was used. Data analysis was done with MATLAB (code available upon request). Light intensity was calibrated using a Hamamatsu photodiode (S2281). Electrochemical impedance spectroscopy was conducted on the same photoelectrodes exposing an area of 0.78 $cm^2$.

## Surface photovoltage measurements

Measurements were done with a Park NX10 AFM in KPFM mode. A PPP-NCST-Au probe (Nanosensors, k=7.4 N/m) was operated in non-contact mode at resonance frequency to trace the topography. In parallel a 3V amplitude AC-voltage was applied to the tip to modulate electrostatic forces at 17 kHz. The resulting tip oscillation was nullified by the KPFM feedback circuit applying a DC voltage to the tip. The DC voltage is reported here as the surface voltage. Surface voltages were measured in darkness and during light exposure from below the sample. The difference is the surface photovoltage.

## 3.2 Supporting Information

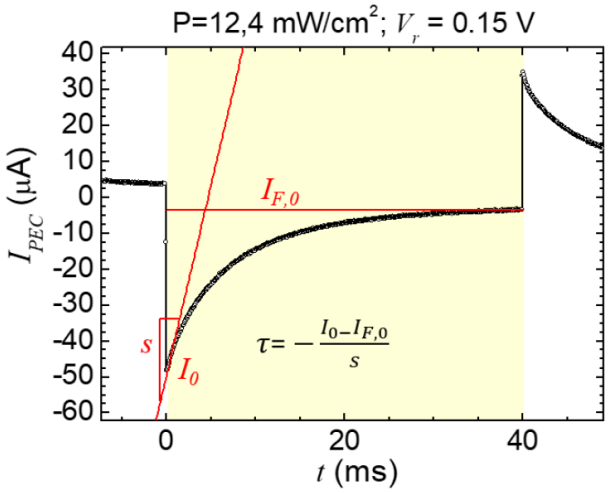


***Figure S1.*** *Determination of characteristic time constant τ from photocurrent transients. The initial slope s of the transient is determined as well as maximum initial current $I_0$ and final current plateau $I_{F,0}$. The values then lead to an estimate of τ .*

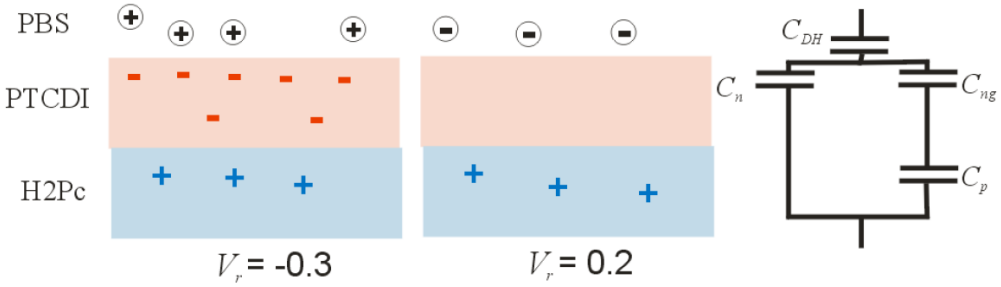


***Figure S2.*** *Capacitance model of the semiconductor p/n junction / electrolyte interface. At negative photoelectrode potential ($V_r$ = -0.3) the PTCDI layer is populated by photogenerated negative carriers, and the total capacitance is only limited by the Debye-Helmholtz capacitance of the ionic layer. Increasing $V_r$ depletes the n-type layer from carriers, increasing the screening length and hence reducing $C_n$. The reduction in total capacitance $C_{dl}$ stops at positive potentials ($V_r$ = 0.2), when carriers in the p-type layer start to screen the field with a capacitance $C_P$. The overall capacitance is then obtained as:*

$$C_{dl} = \frac{\left(C_n + \frac{C_{ng}C_p}{C_{ng}+C_p}\right)C_{DH}}{C_n + \frac{C_{ng}C_p}{C_{ng}+C_p} + C_{DH}}$$

*With* $C_n = A\frac{\varepsilon\varepsilon_0}{L_n}e^{\left(-\frac{qV_r}{ik_bT}\right)}$ *and* $C_p = A\frac{\varepsilon\varepsilon_0}{L_p}e^{\left(\frac{qV_r}{ik_bT}\right)}$

We set ε=3, a typical value for the permittivity in organic semiconductors. Fitting the equation to the $C_{dl}(V_r)$ data we arrive at the following parameters:

| light intensity ($mW/cm^2$) | $L_n$(nm) | $L_p$(nm) | $C_{ng}$($\mu F/cm^2$) | $C_{DH}$($\mu F/cm^2$) | i |
|---|---|---|---|---|---|
| 12.4 | 0.019 | 105 | 3.1 | 60 | 2.9 |
| 3.15 | 0.031 | 170 | | | |
| 0.81 | 0.057 | 380 | | | |

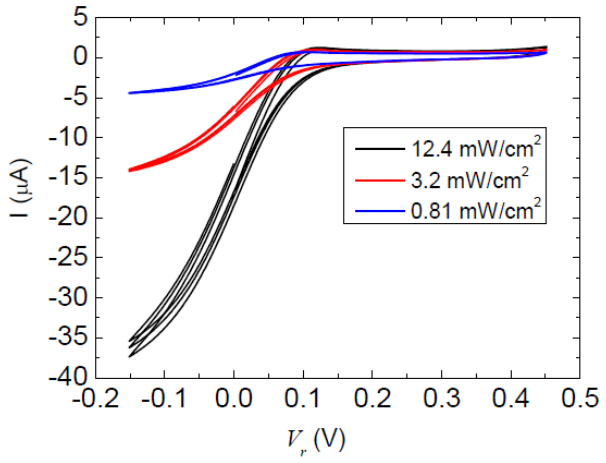


***Figure S3.*** *Cyclovoltammetry of $H_2$Pc/PTCDI photoelectrodes at 0.1V/s scan rate at different light intensities.*

**S4. Methods to solve the differential equation**

We consider the following equivalent circuit to calculate transients:

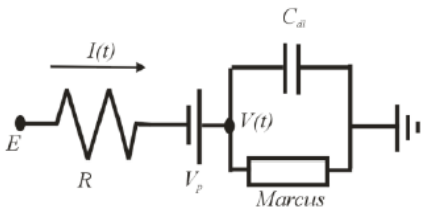


Marcus is an element that is described by the following equation:

$$I_M = -a \exp\left[-\frac{\left(\Delta G^0 + qV(t) + \lambda\right)^2}{4\lambda k_b T}\right] \qquad \text{[SE2]}$$

Using Kirchoff's law on current conservation we obtain the following differential equation:

$$I_M + C\frac{dV(t)}{dt} = \frac{V_r - \left(V(t) - V_p\right)}{R} \qquad \text{[SE3]}$$

The time derivative of the voltage is separated:

$$\frac{dV(t)}{dt} = \frac{1}{C}\left[\frac{V_r - \left(V(t) - V_p\right)}{R} - I_M\right] \qquad \text{[SE4]}$$

In this form we can apply the Runge-Kutta algorithm for iterative integration over a given time interval. The initial condition is determined as $V(t=0) = V_r$.

In darkness the expression SE4 simplifies as $V_p$=0 and $I_M$=0.

The Runge-Kutta algorithm is implemented in MATLAB with the *ode45* command and yields the function V(t). The current is then obtained by:

$$I(t) = \frac{V_r - \left(V(t) - V_p\right)}{R} \qquad \text{[SE5]}$$

**S5: Data tables containing parameters used to calculate transients in Fig. 4**

| **Light intensity (mW/cm$^2$)** | ***a* (μA)** | **λ(eV)** | **$\Delta G^0$ (eV)** |
|---|---|---|---|
| **0.81** | 5.1 ± 0.3 | 0.43 ± 0.07 | -0.24 ± 0.04 |
| **3.15** | 21.2 ± 2 | | |
| **12.37** | 73.4 ± 2 | | |

***S5a.*** *Parameters used in the Marcus equation SE2.*

| **Light intensity ($mW/cm^2$)** | ***R*(kΩ)** | **$V_p$ (mV)** |
|---|---|---|
| **0.81** | 4.6 ± 0.1 | -17 ± 2 |
| **3.15** | 1.8 ± 0.1 | -31 ± 2 |
| **12.37** | 0.74 ± 0.03 | -52 ± 2 |

***S5b.*** *Parameters used for the series resistance and the photo voltage source. The double layer capacitance is described by eq. SE1*

| **Light intensity ($mW/cm^2$)** | ***R*(kΩ)** | **$V_p$(mV)** | | | | | | | |
|---|---|---|---|---|---|---|---|---|---|
| | | **$V_r$=0.45 V** | **$V_r$ =0.35 V** | **$V_r$ =0.25 V** | **$V_r$ =0.15 V** | **$V_r$ =0.05 V** | **$V_r$ =0.0 V** | **$V_r$ =-0.05 V** | **$V_r$ =-0.15 V** |
| **0.81** | 8.6 ± 0.2 | -9.5 | -23.9 | -41.6 | -58.3 | -66.5 | -69.8 | -73.8 | -73.1 |
| **3.15** | 2.9 ± 0.1 | -7.7 | -20.1 | -33.4 | -44.6 | -45.9 | -46.7 | -48.7 | -52.4 |
| **12.37** | 1.3 ± 0.05 | -7.4 | -21.2 | -33.5 | -39.6 | -38.6 | -39.3 | -41.0 | -43.7 |

***S5c.*** *Values for photo voltages obtained by least square fit to transients at different photoelectrode potentials $V_r$.*

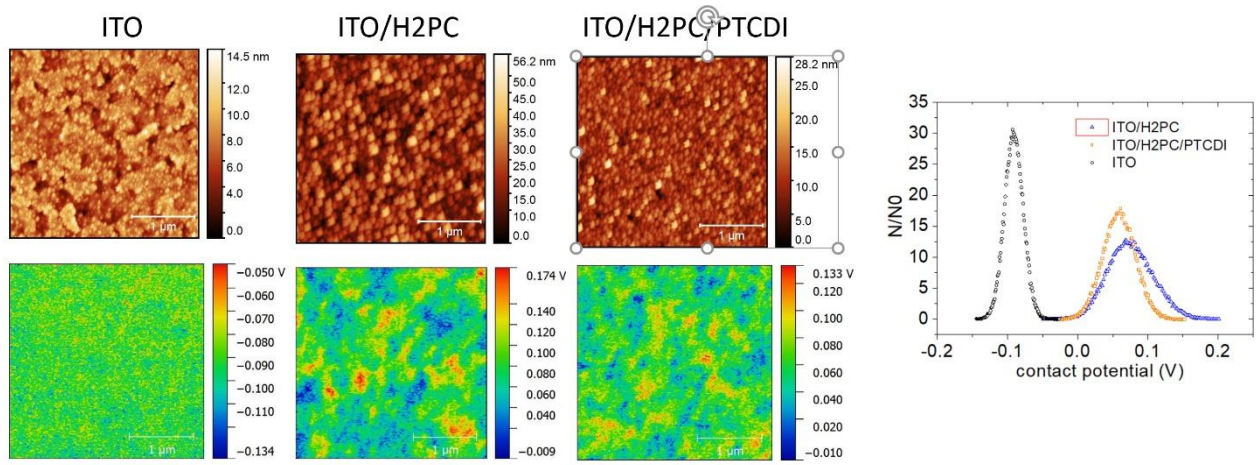


***Figure S6***. *Kelvin Probe Force Microscopy to determine vacuum-level offsets at interfaces. a) KPFM of ITO b) ITO/H2PC and c) ITO/H2PC/PTCDI obtained in darkness. The results show that the offset at the ITO/KPFM interface is 0.18 V whereas only a small offset is present at the H2PC/PTCDI interface (-0.01 V). Combining these values with the work function of ITO (5.1 eV) and Ag/AgCl (4.7 eV) an offset of $V_d$=0.23 V is estimated for the PTCDI/electrolyte interface.*

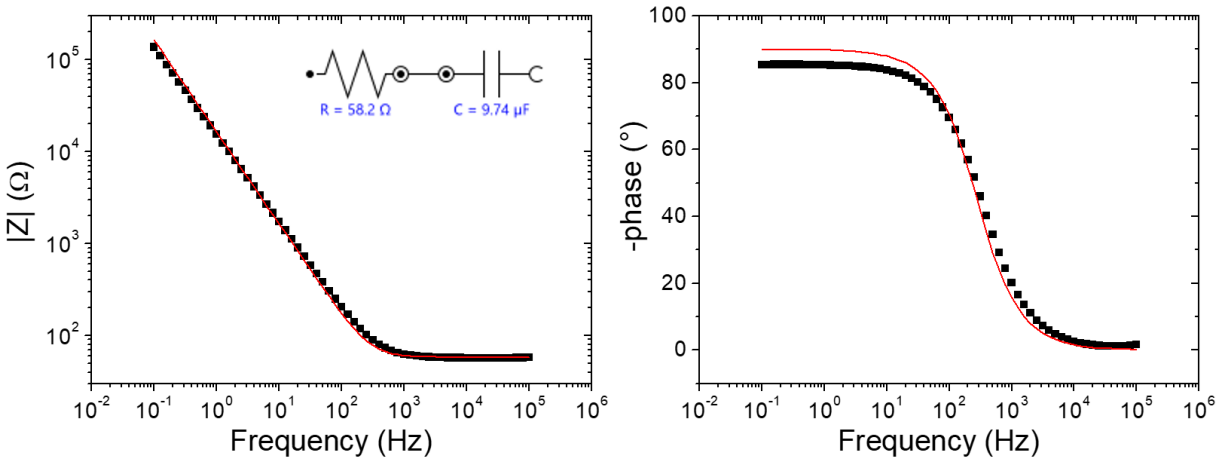


***Figure S7.*** *Electrochemical impedance spectroscopy on pure ITO substrate (area 0.78 $cm^2$). The data is fitted to the RC circuit shown in the inset. The resistance value corresponds to the resistance of the electrolyte solution and matches the findings for the more complex photoelectrode.*

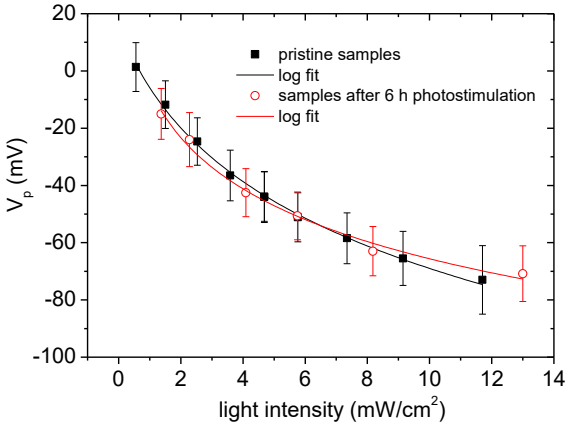


***Figure S8.*** *KPFM surface photovoltage $V_p$ measured in pristine samples and after 6 h of photostimulation in PBS solution.*

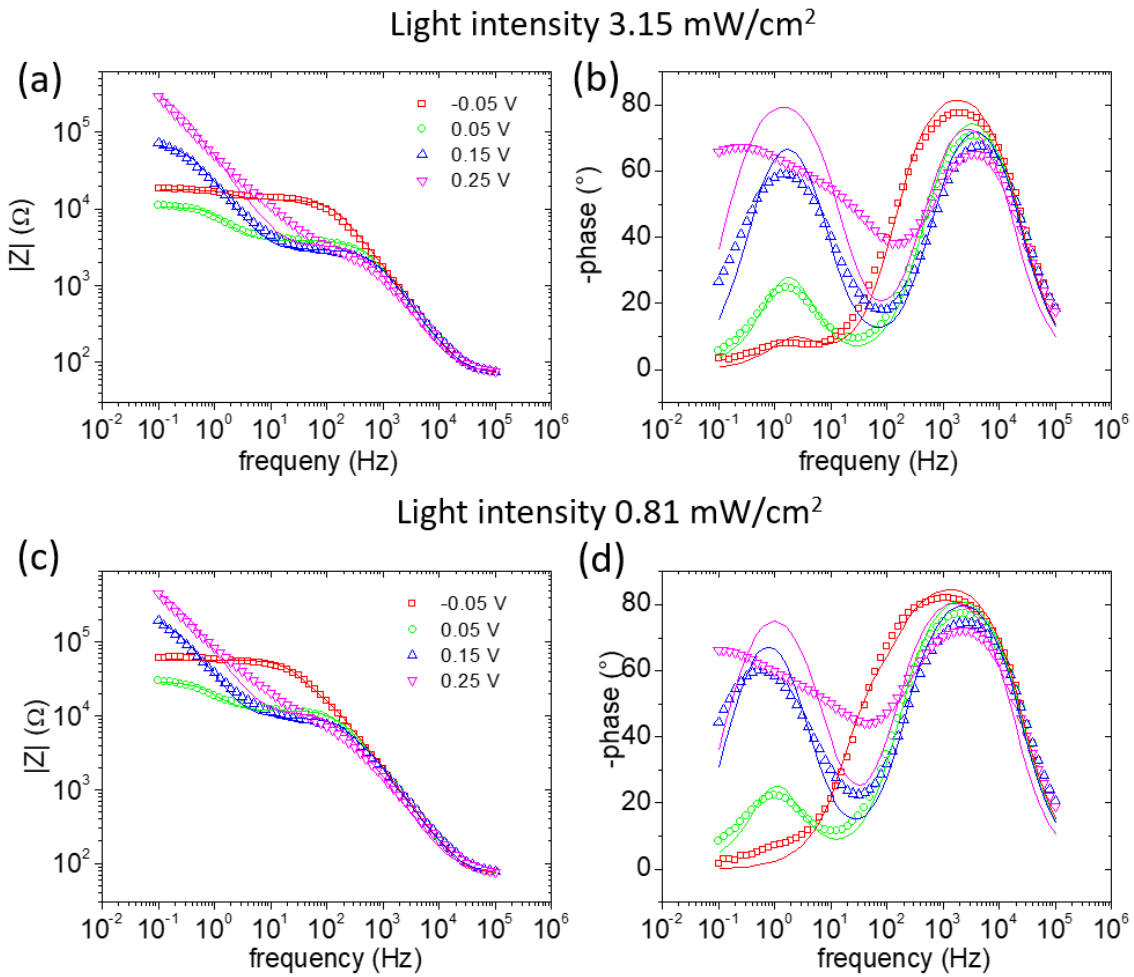


***Figure S9.*** *Electrochemical impedance spectroscopy of H2PC/PTCDI photoelectrode during illumination and fit to equivalent circuit described in figure 1. (a,b) Modulus and phase of impedance with illumination of 3.15 mW/cm2. (c,d) Modulus and phase of impedance with illumination of 0.81 mW/cm2.*

## 3.3 P-type Semiconducting Polymers as Photoreducing Electrodes: a Comparative Study for Optobioelectronics

*Luca Bondi, Edgar Gutiérrez-Fernández, Gabriele Tullii, Maria Rosa Antognazza, Camilla Marzuoli, Jaime Martín Pérez, David Mecerreyes, Beatrice Fraboni, Tobias Cramer*

### 3.3.1 Abstract

Recent studies show that p-type polymeric semiconductors are enabling a novel type of wireless, optically triggered interface with biological cells. Such organic optobioelectronic interfaces have been realized with the polymer P3HT, that exhibits a photofaradaic behavior to generate reactive oxygen species and hydrogen peroxide. These molecules act as messengers in biological systems impacting on cell-signaling and proliferation. However, the use of P3HT to trigger photoelectrochemical reactions in biomedical applications is limited as its optical absorption maxima is not aligned with the transparency window of tissue and characterization of novel materials with improved properties at optobioelectronic interfaces is desired. Here we compare the performance of P3HT with two low band-gap conjugated polymers commonly employed in high performance organic solar cells, namely PBDB-T and PTB7. We quantify their photogeneration capabilities at physiologic conditions through photocurrent transient analysis and HRP-TMB assay. We find a superior photocurrent generation capability in PTB7 as compared to the other two polymers, which is reflected in a better $H_2O_2$ photogeneration yield. Additional spectroscopic and structural investigations are used to compare the energy levels of the materials at the electrochemical interface and their thin film morphologies to rationalize the differences in materials performances. Finally, we test the biocompatibility of the new materials both in dark and illuminated conditions and we demonstrate effective intracellular ROS production in in-vitro experiments. The findings point to the relevant physico-chemical material properties that will be crucial for novel, less invasive, optically operated bioelectronic interfaces.

## 3.3.2 Introduction

Organic semiconductors are soliciting strong interest as active materials in novel bioelectronic interfaces. As organic materials they have an enormous chemical versatility and can be designed to meet the multifunctional properties requested for interfaces with living biological cells. Recent literature examples demonstrate how semiconducting charge transfer properties are combined with soft mechanical behavior as well as chemical stability and biocompatibility to improve traditional microelectrode based interfaces for bioelectronic recordings and stimulations.[136,149–151] On top of that, recent findings show that the outstanding optoelectronic properties of organic semiconductors enable conceptually novel types of optobioelectronic interfaces.[43,123] The aim is to substitute invasive wires and implantable electronics by a single unconnected organic transducer device that is operated by light pulses transmitted through the surrounding tissue. First examples for this concept are organic semiconductor based retinal implants[1,3,24,152,153] or nerve stimulators[154,155] as well as optically controlled smart surfaces to guide tissue growth and cell regeneration.[6,9,156,157] All these applications rely on the transduction of light pulses to physico-chemical stimuli at the semiconductor/electrolyte interface further effecting on biological processes. Accordingly, materials science is required to investigate the different light enabled transduction mechanisms and performances that can be achieved in this context with organic semiconductors.

Different architectures of organic optoelectronic interfaces have been presented in the literature such as planar p-n heterojunctions[3,5,46,47], polymeric thin films[58,153], structured polymeric films[8,158], and polymeric nanoparticles[23,51,53]. In these architectures, semiconducting polymers offer several advantages compared to other materials such as high optical absorption and multiple photostimulation mechanisms[47], high biocompatibility, mechanical compliance and synthetic flexibility. As the application requires a direct contact with the aqueous electrolyte containing the biological target, a suitable energetic alignment with the redox species present in water[50,52] is required. P-type organic semiconductors can fulfill this requirement and a high stability towards electrochemical degradation processes has been demonstrated combined with the selective activation of photoelectrochemical processes.

Depending on the architecture and the materials, different optically excited transduction mechanisms impacting on adjacent cell have been established. Thermal activation aims at a significant increase in temperature close to the illumination site. Due to the high thermal transport properties of water,

localized increases of temperature are only achieved with high light intensities (>>100mW/cm$^2$).[159] At lower light intensities two different electrochemical transduction mechanisms can remain active: Photocapacitive stimulation occurs when the semiconducting layer builds-up a photovoltage upon illumination.[46] The photovoltage drives an ionic displacement current that charges the Debye-Helmholtz capacitance at the semiconductor's interface. The transient displacement current affects cells adhering to the surface similar to current injecting stimulation electrodes.[5] Consequently light pulses can be transduced into cell membrane depolarization triggering action potentials in neuronal tissue. Heterojunctions of p- and n-type organic semiconductors or metal/semiconductor interfaces have been exploited to maximize photovoltage generation. The first example demonstrating this concept is the bulk heterojunction developed by the Lanzani group[30] which consist of a binary polymeric blend made of the polymerP3HT and PCBM. A highly stable junction for photocapacitive stimulations is made by the organic pigments H2PC-PTCDI thin-film molecular planar heterojunction developed by Glowacki and coworkers[3,47]. Recently it has been demonstrated that also a single layer of p-type polymer such as P3HT can build-up photovoltage due to photoelectrochemical reactions.[48,160] This simplification has important implications, as it can be applied to p-type semiconducting nanoparticles interacting directly with the cell membrane to stimulate cells, even though the operating mechanism is still under debate.[161,162]

A second relevant pathway to stimulate cells relies on semiconductor photo-electrochemistry. Here excited charge carriers transfer through the semiconductor/water interface and cause oxidation or reduction reactions in the biological system. Such photofaradaic processes have to be tuned to generate electrochemical messenger molecules that impact on cellular processes.[43] We note that an organic semiconductor device in direct contact with the aqueous electrolyte can follow both stimulation mechanisms, photocapacitive as well as photofaradic.[47] Which one of the two prevails depends on the semiconductor energy levels and their alignment with redox species as well as kinetic barriers for electron transfer. Both processes start under illumination by the generation of localized excitons and their subsequent dissociation into free carriers occurring at interfacial electric fields or spontaneously.[48] In the capacitive case, the free carriers accumulate and modulate the space charge in the device also affecting the Debye Helmholtz layer and generating ionic displacement currents. In photofaradaic reactions, free electrons in the conduction band are transferred to acceptor states in solution or alternatively hole carriers in the valence band oxidize donors in solution. Photofaradaic or photocapacitive processes can be easily distinguished through chronoamperometric measurements

in dark-light-dark conditions: the integral of a cycle amounts to the overall photofaradaic current; the photocapacitive contribution is then the total current minus the photofaradaic one.[47]

In the case of p-type polymers such as P3HT or PEDOT the typical acceptor molecule taking free electrons is oxygen as it is always present in biological conditions.[49,142,160,163] The oxygen reduction reaction (ORR) generates $H_2O_2$ on organic semiconductor surfaces and other intermediate Reactive oxygen species (ROS).[49,164] Importantly, the ORR products are known to act as messenger substances with impact on cell homeostasis, cell metabolism and regenerative processes. The photofaradaic generation of ROS species has been employed through the use of organic semiconductor thin films as well as injectable nanoparticles and was demonstrated to be effective in stimulating cardiac cell regeneration.[30,57–60,165] The detailed mechanism of the photofaradaic transduction chain depends on the physico-chemical interactions occurring at the interface with the cellular medium[43,47] and between the ROS and the particular cell line[166]. Steady state physiological flux of $H_2O_2$ to specific protein targets leads to reversible oxidation, altering protein activity, localization and interactions.[167] This contributes to adaptation of various processes in cells and organs, including cell proliferation, differentiation, migration and angiogenesis[168–170]. Overall, physiological targets of ROS serve as redox switches in signal transduction acting in response to stressors or external perturbations[167].

Most of the studies were conducted on single-polymer photoelectrodes and relied on the use of regioregular poly-3-Hexylthiophene (rr-P3HT), a semicrystalline polymer with a low glass transition temperature ($T_g \approx T_{amb}$) and a noticeable chain mobility[171]. This material has recently been under the spotlight as an effective photocathode for triggering cell differentiation pathways through the production of Reactive Oxygen Species (ROS)[50,51], nevertheless it have some weak spots in perspective of human implementation. For instance, its absorption spectrum (c.a. 300-650nm) is not well superimposable with the therapeutical window (650-1350nm). In this context, the introduction of novel materials and the study of how they interface with the biological medium is important to overcome current limitations and to improve the desired photoelectrochemical behavior. From OPV research similar p-type semiconducting polymer materials are known which feature high performances and lower bandgaps, such as PTB7, PBDB-T, PTB7-Th, and PCPDTBT. The HOMO levels of these materials are between -4.6eV and -5.3eV [172–175] and the optical bandgap between 1.5eV and 2eV.[176–178] The position of the energy bands relative to donor and acceptor levels at the semiconductor-water interface is of fundamental importance also in determining the stability of the photoelectrode[160,179–181], as well as the possible back electron transfer pathways. Among the latter,

are worth of mention the polymer reduction by means of ROS species and the oxidation of water by means of positively charged states in the polymer. In addition to energetic aspects, the polymers differ in the processability, the solubility in common solvents, the chemical stability and in structural factors. For example, the structural order can space from totally amorphous to paracrystalline in regiorandom polymers or polymers with a small number of repetitive units, up to semicrystalline order in regioregular and high molecular weight polymers like rr-P3HT[182]. Moreover, the $T_g$ of all the mentioned OPV materials is much higher than the sub-room temperature $T_g$ of rr-P3HT[183], implying a lower chain mobility.

The aim of the work is to compare different p-type organic semiconductors for photofaradaic ROS generation at optobioelectronic interfaces, in aqueous environment. Among the possible p-type low-bandgap biocompatible polymeric materials, we chose for our studies 2 materials to compare to the extensively used P3HT, namely PBDB-T and PTB7, based on their chemical-physical properties. These are low bandgap, highly absorbing polymers[184] with high photoconversion yield reviewed in OPV applications[185,186], and are characterized by a chemical structure and a LUMO energy compatible with oxygen photoreduction while having a HOMO energy not suitable for efficient water oxidation processes. We perform photoelectrochemical experiments under physiologic conditions to determine photocurrent generation efficiency and efficiency in H2O2 generation. Absorption spectra and photocurrent spectra are acquired and combined with Kelvin-Probe force microscopy measurements to determine the energy level diagrams for the ITO/polymer junction. We conclude our physicochemical characterizations of the materials with structural investigations of the photoelectrode thin films by means of AFM and GIWAXS. Finally, in-vitro experiments we demonstrate the biocompatibility of the materials and their ability to increase inter-cellular ROS formation. The systematic comparison allows us to determine relations between physical-chemical properties and photoelectrochemical performances of importance for such novel optoelectronic interfaces.

### 3.3.3 Results

We characterize the oxygen reduction properties of p-type organic semiconducting with photoelectrode samples that were prepared by spin coating solutions of P3HT, PTB7 or PBDB-T

polymer in chlorobenzene onto ITO covered glass slides. Conditions were optimized to obtain thin films of 50 nm thickness for all polymers. The Photoelectrochemical Cell (PEC) setup used to perform the measurements is introduced in **Figure 1a**. The active area of the photoelectrode in contact with electrolyte (PBS – 137mM NaCl, 3mM KCl, 10mM Phosphate buffer, pH 7.4) is confined by a PDMS O-ring and the same area is illuminated from the electrolyte side. The photoelectrode is connected as the working electrode to a potentiostat and a Pt-wire and an Ag|AgCl|KCl (3M) electrode are used as counter and reference electrode, respectively. Figure 2b shows typical photocurrent transients obtained with the P3HT photoelectrode when measured in ambient air and after oxygen removal by fluxing $N_2$ for 60 minutes. Upon illumination a cathodic current is observed that starts with a peak and then settles within a few milliseconds to a relatively constant level. The absence of oxygen causes a significant reduction in current and confirms the central role of oxygen in the generation of photocurrent in this class of materials. The remaining photocurrent intensity is attributed to $H^+$ reduction to gaseous $H_2$.

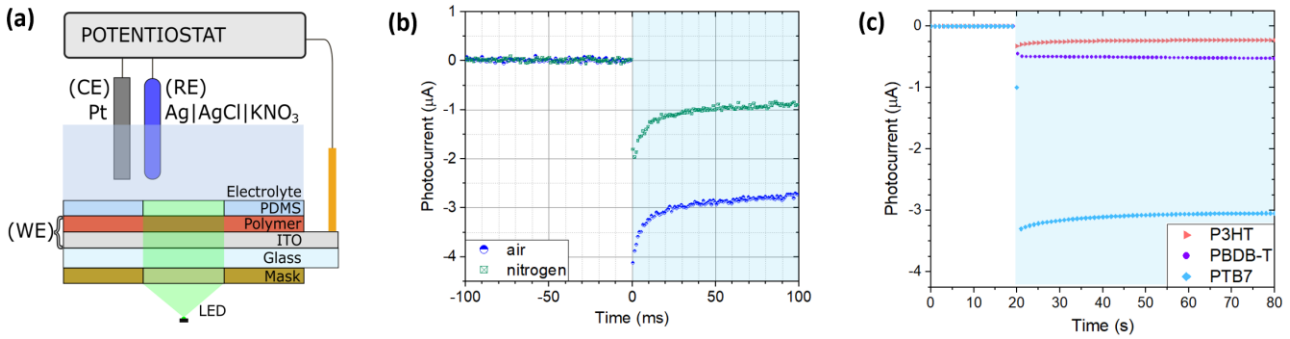


***Figure 1.*** *Photofaradaic transients produced by p-type organic semiconductor photoelectrodes. (a) Scheme of the photoelectrochemical cell. (b) Comparison between the photocurrent transients of a 50nm P3HT thin-film illuminated with a 20mW/cm$^2$ 470nm LED in presence of ambient air and after 60min of nitrogen. (c) Comparison of photocurrent transient generated by photoelectrodes made with different p-type organic semiconductor thin films. Light intensity is 110mW/cm$^2$. Wavelength was chosen close to polymer absorption peak (530nm for P3HT and PBDB-T and 660nm for PTB7). All transients were recorded at open circuit potential as determined in dark.*

Figure 1c compares the long-term Faradaic photocurrent obtained with the different semiconductors in aerated electrolytes. Since the absorption spectra of the compared materials are different, two monochromatic LED were chosen to have comparable absorption coefficients, such as 530nm/2.35eV for P3HT and PBDB-T and 660nm/1.88eV for PTB7 (see **Table 1**). The biomedical application of such thin films as photoelectrodes is motivated by the wireless operation and hence without ground connection inside the biological tissue. Accordingly, we carried out the photocurrent experiments at open circuit potential (OCP) as determined in dark condition at equilibrium as listed in Table 1. We note that such a hypothesized ungrounded condition, would cause the accumulation of positive charge in the polymer during photocathodic activity and it would slow down further photoconversion. Hence the photocurrent values measured at OCP dark provide an upper limit for the polymers' performance. In these conditions, PTB7 outperforms the other polymers in photocurrent and exceeds by 5 times the photocurrent per absorbed mW of PBDB-T and approximately 10 times the one of P3HT. Detailed plateau values are reported in Table 1.

Next, we investigate the spectral properties of the photoelectrochemical current and compare with absorption spectroscopy. The near-infrared window (also known as optical window) defines the range of wavelength where light has its maximum depth of penetration in living tissue, and spans between 625nm and 1315nm, which corresponds to energies between 0.95eV and 2eV. In this respect, the absorption spectra in **Figure 2a** identify PTB7 as the most suitable material for in-vivo applications. The PTB7 absorption peak fits perfectly into the transparency window thus minimizing the energy losses in in-vivo applications due to unspecific tissue dispersion. Figure 2a also shows the comparison between absorption and photocurrent spectra. All the materials show a good agreement between the two curves, especially close to the band-gap energy, suggesting that photocurrent is generated through a mechanism based on HOMO-LUMO excitation in the bulk, exciton generation and separation into free carriers and ultimately transfer of free carriers onto electrochemical species. All the materials show an enhanced photogeneration yield in the supra-bandgap energy probably due to an increased exciton generation rate caused both by optical interference inside the film as well as a higher polaron pair formation efficiency due to hot excitons.[187]

| | LED wavelength | Absorbance (at LED wavelength) | OCP Dark | Max OCP Illuminated | Photocurrent at OCP dark | $H_2O_2$ generation EQE [x$10^{-6}$] |
|---|---|---|---|---|---|---|
| **P3HT** | 530 nm | 0,24 ± 0,01 | + 0,12 V | + 0,35 V | 0.23 μA | 4,05 ± 0,67 |
| **PTB7** | 660 nm | 0,37 ± 0,03 | + 0,17 V | + 0,44 V | 3.04 μA | 16,75 ± 2,29 |
| **PBDB-T** | 530 nm | 0,31 ± 0,02 | + 0,24 V | + 0,54 V | 0.54 μA | 3,31 ± 0,54 |

***Table 1.*** *Data acquired with 50nm organic semiconductor thin films deposited on ITO photoelectrodes, illuminated area = 1cm$^2$, 110mW/cm$^2$ LED light source, PBS electrolyte. Photocurrent (PC) and $H_2O_2$ generation are measured at the open circuit potential measured in dark conditions (OCP Dark). The hydrogen peroxide generation experiment lasted 60 minutes. The voltages are referred to Ag|AgCl 3.0M reference electrode.*

In addition to the photoelectrochemical current characterization it is crucial to determine the efficiency of the electrochemical reduction reaction. For organic semiconductors, a four-electron reduction process is very unlikely to be efficient[188] and instead the ultimate product of ROS generation is $H_2O_2$. Here we quantify the amount of generated $H_2O_2$ in PBS by using the HRP-TMB (Horseradish Peroxidase–3,3',5,5'-tetramethylbenzidine) assay.[189–192] The hydrogen peroxide photoproduction yield experiment was performed by filling the PEC cell with 14 ml of electrolyte, operating the photoelectrode in potentiostatic mode at OCP dark and illuminating from the electrolyte side with a 110mW/cm$^2$ LED for 60 minutes. The photocurrent was monitored throughout the whole experiment duration. Based on the acquired data, we prepared **Figure 2b** that shows the External Quantum Efficiencies (EQE) measured in the form of electron per incident photon as well as $H_2O_2$ molecule produced per incident photon for the three materials. The total charge is calculated through the integral over the 60 minutes experiment. **Figure 2c** depicts instead the Faraday efficiency determined as the ratio between measured photoelectrons and revealed hydrogen peroxide molecules. For all three materials a value of just above 3 to 1 is observed. For each $H_2O_2$ molecule, 2 electrons are needed during the oxygen reduction. Accordingly, approximately $\frac{2}{3}$ of the photocurrent involves $O_2$ reduction while $\frac{1}{3}$ involves other photoreductions such as HER. This ratio strongly resembles the one initially observed in the photocurrent experiment with and without oxygen (Figure 1b). The electrons that make the ratio exceed the 3-to-1 exact proportion can be reasonably ascribed to the further reduction of the $H_2O_2$ in solution to $H_2O$ molecules[193]. As the photoelectrochemical

conversion yield is approximately the same for all the polymers, the peroxide generation EQE trend is reflected in the photocurrent EQE trend. As a result, PTB7 outperforms both P3HT and PBDB-T with a roughly fourfold higher photon to peroxide conversion efficiency. We note that the measured photocurrent is only an effective current and does not provide insight on different contributions related to photoreduction, back electron transfer or other electrochemical processes. Similarly, the measured hydrogen peroxide yield must be considered lower limit of the real value as it does not account for $H_2O_2$ that is further converted to $H_2O$[193] at the WE, that oxidize the polymer[49], or that reverts to $O_2$ in the presence of metallic impurities or catalytic sites[194]. The $H_2O_2$ photoproduction measured for PTB7, in terms of moles per irradiated mW, is noteworthy also compared with other conjugated polymers that can be found in literature such as TPT polymers[195] or PQTEE-COP[196].

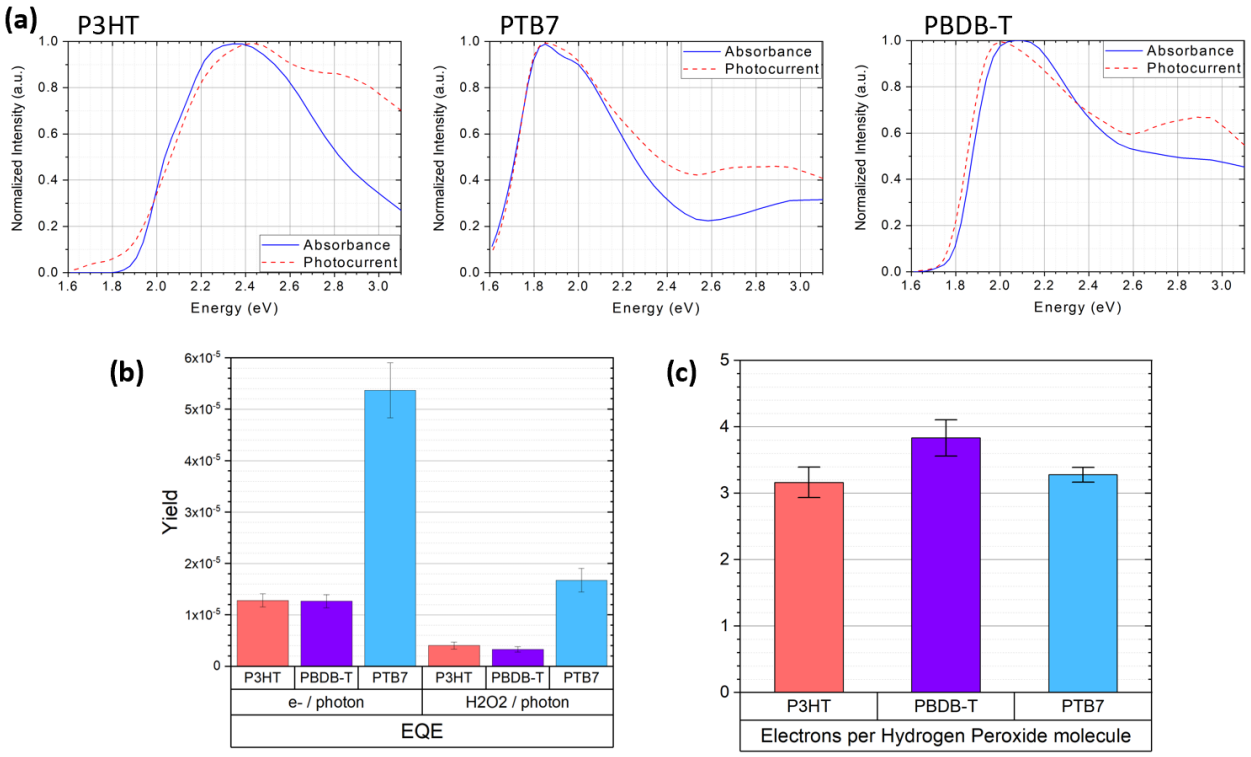


***Figure 2.*** *Spectroscopy and efficiency of photocathodic current: (a) Normalized absorption and photoelectrochemical current spectra of the three different photoelectrode materials; (b) External Quantum Efficiency (EQE) comparison of the three studied polymers, illuminated for 1 hour with a near band-gap LED (530nm for P3HT and PBDB-T and 660nm for PTB7) at an irradiance of 110mW/cm$^2$; (c) ratio between the net charge passed through the WE during the latter experiment and the concentration of $H_2O_2$ measured in water.*

In the following we perform microscopic analysis of the different photoelectrodes in order to understand why PTB7 is a better oxygen photoreducing polymer. **Figure 3a** compares the surface morphology of the three photoelectrodes as measured by Atomic Force Microscopy. All the films show a low roughness as expected for a spin cast film, with an $R_a$ of 1.8nm for P3HT, 1.3nm for PTB7 and 1.7nm for PBDB-T. Also, the observed correlation lengths are similar in the three height maps. Therefore, we exclude that increased surface roughness or porosity of the material could be a reason to explain improved performance in PTB7.

Another key factor to evaluate photoelectrochemical performance regards the energy levels in the three materials. By combining KPFM measurements with the photocurrent spectra and literature data, we construct the energy level diagrams of the ITO/p-type polymer junction as described in the following. KPFM maps as obtained in darkness under ambient conditions on the photoelectrode surfaces are shown in **Figure 3b**. All three materials show a narrow distribution of surface potential (rms = 24.1±0.2V, 19.8±0.1V and 18.9±0.1V for P3HT, PBDB-T and PTB7 respectively) (**Figure 3c**) and no significant correlation with the height map is present. From the average value of surface potential, we determine the shift in vacuum level across the ITO/semiconductor junction by subtracting the average value measured on the pure ITO surface as reference value. With the shift values of +0.32V, +0.30V and +0.10V we initiate the construction of the energy level diagram in Fig. 3d. The offset between vacuum level and HOMO level is taken for the three polymers from literature as determined by UPS measurements[172,173]. The position of the LUMO-level is then determined by the bandgap as measured with absorption spectroscopy (1.88eV, 1.60eV and 1.8eV). It must be stressed on the one hand that the LUMO levels thus obtained don't take into account band bending and surface levels, and on the other hand that the free electrons that participates to ORR are sit at lower energies owing to polaron binding energy. Finally, the Fermi-level through the junction is given by the work function of the underlying ITO layer and was determined by KPFM measurements (WF = 4.9 eV). The completed energy level diagram allows us to make two relevant observations for the photoelectrochemical behavior of the p-type polymers: First, all materials align energetically in the junction to produce a Fermi-level that shows an offset of 0.53±0.02 eV above the HOMO level. Accordingly, all three polymers have an excess of positive free carriers. The similar offset energy in PTB7 and PBDB-T points to a polaronic level that is similar in energy, while the lower offset in P3HT can be ascribed to the alignment with the bipolaronic level[197]. Second, all the LUMO levels are higher than the typical energy level attributable to the effective one-electron oxygen reduction in

water ($O_2/O_2^{-\bullet}$=4.1eV, λ=0.4 eV [47,145]), suggesting a good superimposition between the negative polaron and the redox couple densities of states. Besides, the effective energy of this redox couple could be lower due to the concentration balance of the two participants at equilibrium. Accordingly, we conclude that the energy-levels difference in the three p-type materials is not enough by itself to explain such a higher efficiency in PTB7 together with such a small difference between P3HT and PBDB-T.

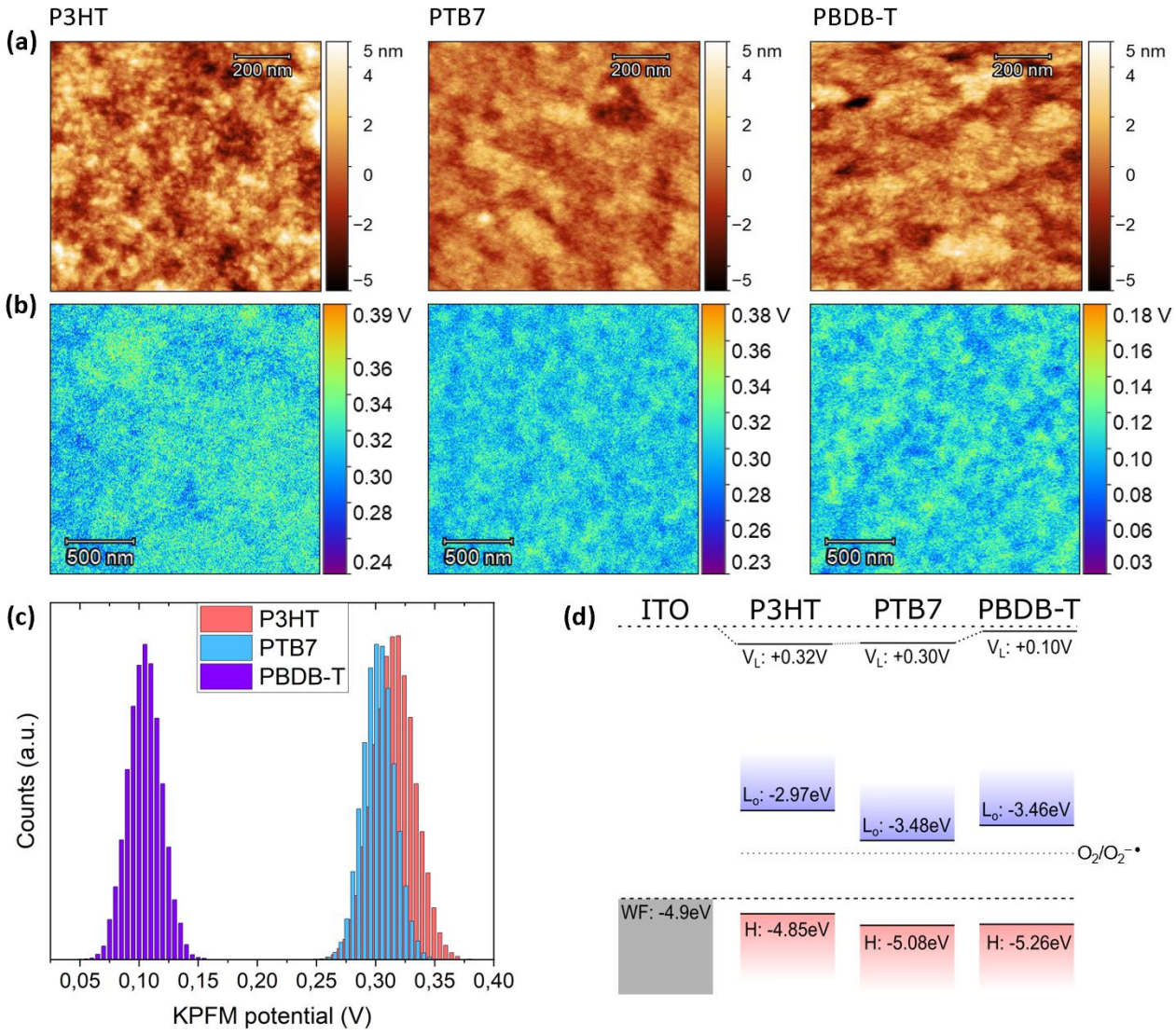


***Figure 3.*** *Microstructural and energic investigations on photoelectrodes by Kelvin Probe Force Microscopy (KPFM): (a) Height maps show that all polymeric films exhibit low roughness, with an Rq < 2nm. (b) KPFM surface potential maps and histograms (c) reveal a narrow distribution of*

*potential on all surfaces and a small, but significant offset in PTB7. (d) Energy level diagram of the ITO/semiconducting polymer junction for the three different polymers. The levels are determined from the KPFM data, the photocurrent spectra and literature values on HOMO energies referred to the Vacuum level. The diagram does not account for band bending and polaron binding energies.*

As surface morphology and energy levels do not provide significant differences between the three polymer photoelectrodes, we continue our inquiry with investigations of the thin film microstructures with 2D GIWAXS. **Figure 4** shows the 2D intensity maps and corresponding intensity profiles for the in-plane and out-of-plane directions to extract information about the degree of order and the polymer chain orientation with respect to electrochemical interface. The distinguished patterns show that P3HT is the material with the higher degree of crystallinity, followed by PTB7 and PBDB-T. The peaks at lower q, between 3 and 12nm$^{-1}$, are attributed to the interchain ordering reflection and its harmonics. Structures present at q higher than 15nm$^{-1}$ reveal the π-π stacking in the semiconducting polymers. Importantly, the comparison between the GIWAXS in-plane and out-of-plane profiles provides information on the preferential orientation of the π -systems as illustrated in **Figure 4c.**

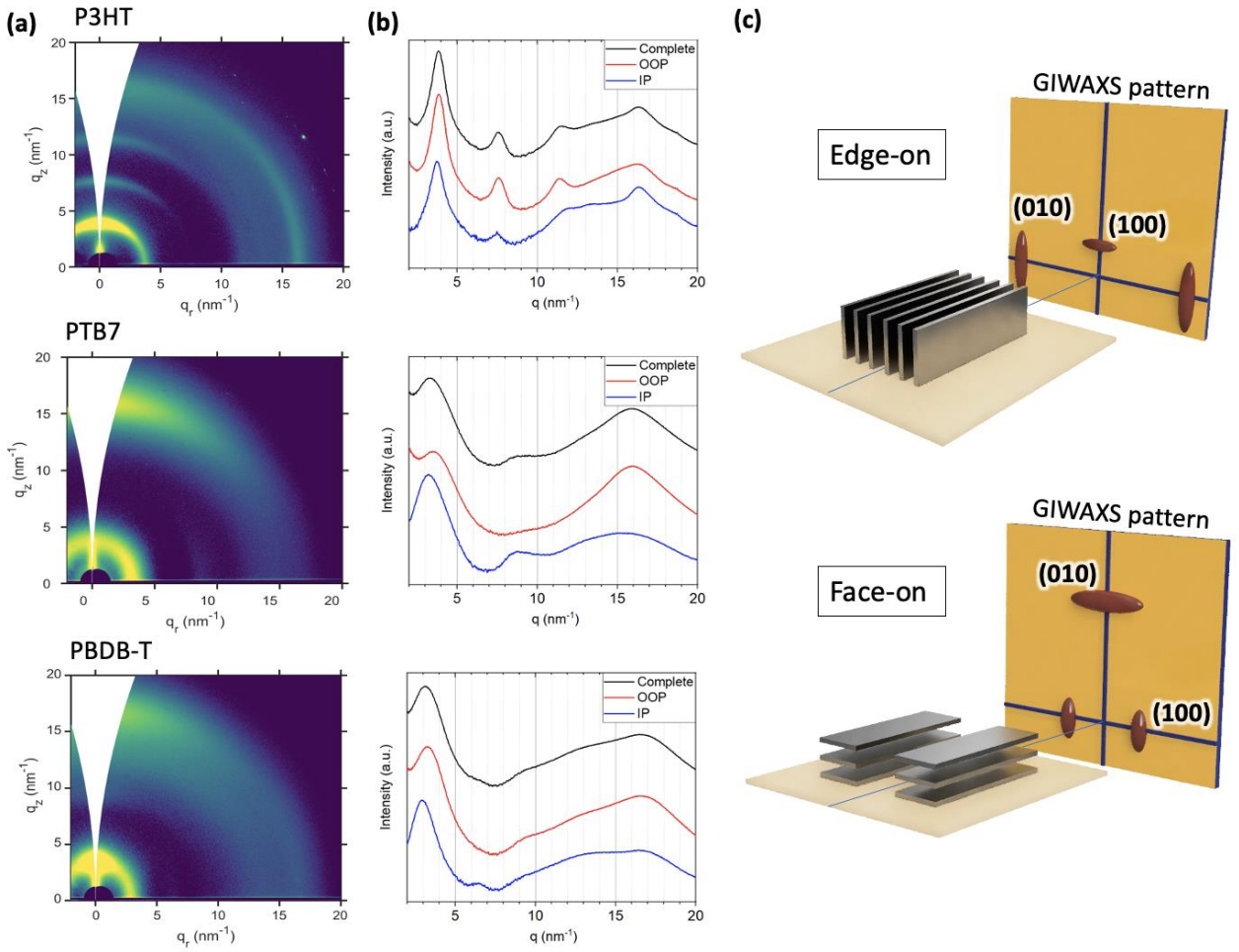


***Figure 4.*** *Microstructural investigation of polymer thin films in photoelectrodes with 2D GIWAXS (a) and corresponding in-plane (IP) and out-of-plane (OOP) linecuts (b). The data shows that P3HT has a higher degree of order, and some oriented crystallites are visible, PTB7 has a mostly an amorphous behavior and a short-range order, and PBDB-T even more. Face-on and edge-on orientations of the polymer chains and their relative GIWAXS pattern are shown in (c). We attribute the edge-on configuration to P3HT while PTB7 has a face-on configuration.*

In P3HT the interference pattern assigned to π-π stacking appears more pronounced in the in-plane direction whereas lower q interchain interactions appear stronger in the out-of-plane direction. This finding points to an edge-on configuration in the investigated P3HT photoelectrodes and agrees with typical structures observed in P3HT thin films. In contrast PTB7 shows the opposite behavior of the GIWAXs pattern even though peaks are less pronounced, and the material has an overall lower crystallinity. Accordingly, we assign the face-on configuration to PTB7. Finally, in PBDB-T no clear

assignment can be made and the pattern is almost symmetric pointing to a pronounced amorphous structure with only small crystalline domains. We propose to relate the characteristic differences in chain orientation to the photoelectrochemical behavior. In the edge-on configuration, as present in P3HT, electron transfer to acceptors beyond the interface must occur across a layer of aliphatic side chains. Such chains have a length of approximately 8Å and hence they constitute a transport barrier. In contrast, in a face on configuration, crystallites expose the pi-system directly to the aqueous interface and to oxygen acceptor states. Therefore, a faster electron transfer is hypothesized in PTB7. We note that in addition to these kinetic arguments on electron transfer, differences in polymer orientation impact also on the surface polarity, dielectric induced stabilization of charge-transfer states[198] and the stabilization of intermediate species in the electrochemical reactions which could further impact on overall efficiency.

In the final part of our work, we test if the findings on the photoelectrochemical properties of the semiconducting polymers can be translated to in-vitro experiments with cells. For this purpose, we cultured Human Umbilical Vein Endothelial Cells (HUVEC) on photoelectrode surfaces while subjecting them to an illumination protocol. To optimize cell-culture experiments, all samples were sterilized with a 2h long thermal treatment at 120°C and a layer of Fibronectin was deposited on the surface to promote cell adhesion. P3HT and PTB7 photoelectrodes were illuminated at a power density of 110mW/cm$^2$ for 3 minutes with a 530nm and a 660nm LED. On PBDB-T photoelectrodes, the same illumination caused cell stress and cell detachment. Accordingly, we reduced the illumination intensity to 2 mW/cm$^2$ keeping 3 minutes of illumination duration with a 530nm LED to maintain normal cellular behavior during illumination. The causes for this phenomenon are unknown and need further investigation. With this illumination protocol we quantified cell viability with the AlamarBlue assay at 24 (immediately after illumination protocol), 72 and 168h from the cell deposition in both the illuminated polymer and controls samples. The AlamarBlue fluorescence signal is an indicator of the metabolic activity inside the cells. In **Figure 5** a clear increase of the fluorescence with time can be observed for all the samples regardless from the presence or absence of the polymer and of the illumination. This means that despite the presence of the polymer photoelectrodes and their generation of ROS, the electrodes are biocompatible and ROS concentrations remain within a non-toxic range and do not affect cellular proliferation.

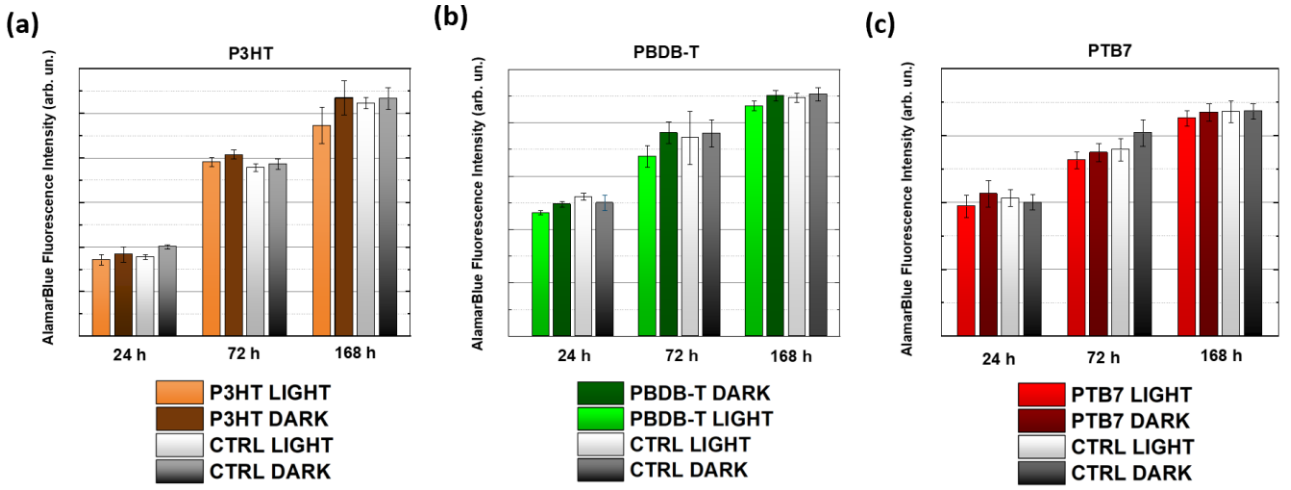


***Figure 5.*** *AlamarBlue fluorescence intensity is proportional to the mitochondrial activity inside cells and is representative of cells vitality and proliferation. Here we compare P3HT (a), PBDB-T (b) and PTB7 (c) data acquired after 24, 48 and 168 hours after incubation, over multiple sample areas and on three experiment replicates each.*

Next, the ROS production was determined with fluorescent microscopy using the $H_2$-DCF-DA assay[199]. As control samples we tested in parallel ITO samples without polymer and both ITO and ITO/polymer samples kept all the time in darkness. **Figure 6** shows the results from fluorescence microscopy performed after the illumination protocol. Average fluorescence values were determined on cell bodies as shown in Fig.6a for the case of P3HT. The diagrams in Fig.6b report the averaged fluorescence values normalized by the value measured on the ITO control kept in darkness. Comparison of the photoelectrodes with the different control samples clearly demonstrates ROS generation inside cell bodies triggered by the illumination. Quantitative comparison indicates that the increase in intracellular ROS concentration is similar for all the polymers. Nevertheless, it must be recalled that PBDB-T is illuminated by 55 times lower power density than the others. The improved efficiency of PTB7 in oxygen reduction at OCP is thus not directly translated to the in-vitro experiment. However, we note that such fluorescence assays have to be interpreted as a qualitative test and hardly permit precise quantitative analysis. In addition, the illumination experiment is performed with floating photoelectrodes, hence the electronic potential is not under control in the experiment, and this could impact on conversion efficiency.

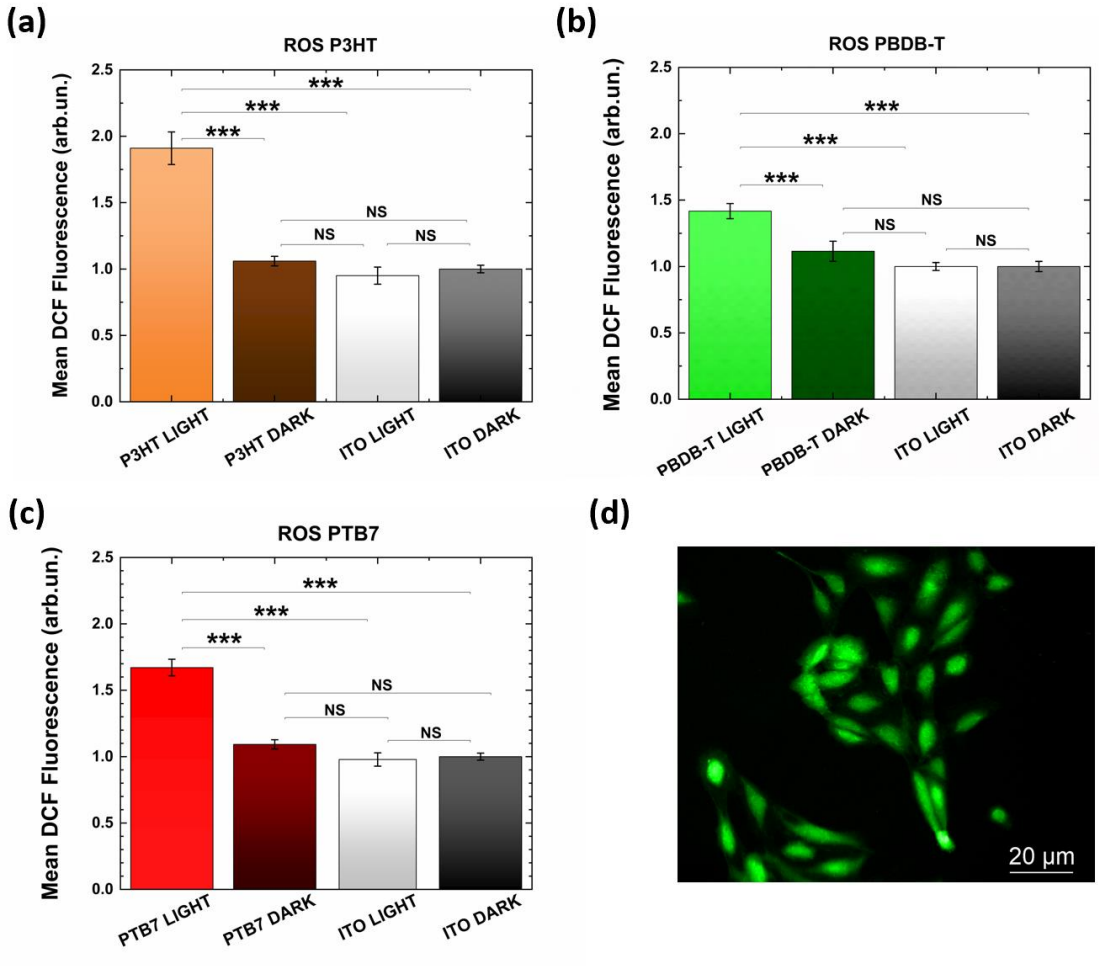


***Figure 5.*** *Mean DCF fluorescence represents the fluorescence intensity of the ROS-sensitive DCF probe internalized within HUVECs plated on ITO and ITO/P3HT, PBDB-T, PTB7 substrates, in light and dark conditions. In the histograms are compared the intracellular ROS observed for cells plated over P3HT (a), PBDB-T (b), and PTB7 (c). In (d) a representative fluorescence image of HUVECs plated over PTB7 as they appear after the illumination protocol. Data were compared using the Anova test 2-ways, with Bonferroni correction (0.05 significance level). * $p < 0.05$, ** $p < 0.01$, *** $p < 0.001$.*

### 3.3.4 Conclusion

In this work we present a comprehensive characterization of three p-type semiconducting polymers, namely P3HT, PTB7 and PBDB-T, as electrode materials for the photoelectrochemical production of reactive oxygen species (ROS). ROS generation impacts on cellular messaging pathways[166,167] and hence organic semiconductor photoelectrodes enable a new transduction method to impact on cellular phenotype with optical, wireless control. Our study aims to identify the relevant material properties for such an application by comparing different p-type semiconductors. We find that all three tested materials exhibit photocathodic current generation due to oxygen reduction processes. Interestingly, PTB7 outperformed the other polymers in different examined aspects. Its maximum in optical absorbance and photoelectrochemical current generation is centered in the optical transparency window of biological tissue. In addition, under the employed conditions, PTB7 photocurrent and $H_2O_2$ generation yields are more than 5 times larger than those shown by the other materials. We attribute a major contribution to this finding to the face-on configuration of the pi-orbital system of the polymer backbone as investigated by GIWAXS. In contrast, P3HT and PBDB-T show more edge-on or amorphous configurations, respectively. These are associated with less efficient electron transfer across the semiconductor/water interface due to barrier properties of aliphatic side chains. The spectroscopic experiments combined with Kelvin-Probe force microscopy allow us to propose the energy level diagrams for the ITO/semiconductor junction for the three materials and we discuss its relevance for the oxygen reduction reaction. Overall, the three materials show comparable energy levels confirming that the observed differences in photoreduction efficiency are related to proximity effects and kinetic phenomena such as electron transport to acceptor sites. Finally, we demonstrate that all three polymer photoelectrodes are biocompatible and induce significant ROS production inside HUVEC cells in in-vitro experiments within a range that is not toxic. To conclude, our results provide comprehensive physicochemical guidelines for the development of organic photoelectrodes with oxygen reduction properties and provide a useful foundation for their implementation into new photoactive biocompatible devices.

The studied polymers may not have outstanding photoconversion yields compared to other polymers in the literature, but they have several characteristics that make them a good fit for the intended in-vivo application. While most literature results focus on the $H_2O_2$ quantum yield at optimal electrical potential, for wireless operativity the potential in electrically floating conditions is determined by

materials and illumination conditions. While polymers such as polyacetylene, polythiophene, and triple-bonded carbon-containing chains have the right energy for oxygen reduction, their optical bandgap does not allow for adequate light penetration.[200] Some alternatives, such as eumelanin-covered PET films[201] or TMP[202], have demonstrated a good current density, but they require a sacrificial reagent, which is not suitable for the physiological environment. Although other studies have examined polymers for ROS production targeting $^1O_2$ generation capability[195], our goal is to activate TRPV-1 channels directly through $H_2O_2$, which can be generated either via direct 2-electron reduction or from 1-electron oxygen reduction to $O_2^-$.

### 3.3.5 Methods

#### Materials and sample preparation

Photoelectrodes are made of a thin polymeric organic semiconductor deposited by spin-coating on Indium-Tin-Oxide (ITO) coated glass slide (Ossila). The p-type semiconductors rr-P3HT (Ossila), PTB7(Sigma Aldrich) and PBDB-T (Sigma Aldrich) were dissolved in Chlorobenzene at 80°C at a concentration of 10mg/ml and spin-coated at 1000rpm for 60s. After deposition the samples were annealed at 100°C for 10 minutes. Polymer film thickness of the prepared samples amounted to 50nm as determined by AFM.

#### Photocurrent and photovoltage spectroscopy, electrochemical impedance measurements

The photoelectrode's active surface was exposed to PBS electrolyte adjusted in pH to mimic Krebs-Ringer HEPES buffer (0.01M phosphate buffer, 0.137M NaCl, pH 7.2 at 25°C). By mounting the photoelectrode in a dedicated cell only the semiconducting layer is exposed to the electrolyte, while the buried ITO surface and the electrical contacts remain separated via a PDMS O-ring. The cell allows the exposition to the illumination from either the ITO side or the solution side, the latter through a quartz window. In a three-electrode setup the photoelectrode was operated as the working electrode. An Ag|AgCl (3M KCl) reference electrode was used in combination with a Pt counter electrode. In spectroscopic measurements the monochromatic illumination of the photoelectrode at a defined wavelength was achieved with a Xenon lamp combined with a monochromator (Cornerstone

260). The amplified current or photovoltage signal was filtered and digitized with a lock-in amplifier (Zurich Instruments) connected to the monitoring output of the potentiostat (Metrohm PGSTAT204). The potentiostat was also used for impedance spectroscopy measurements. For transient measurements the monochromated Xenon lamp light was replaced with monochromatic LEDs (Thorlabs M530L4) driven by a source-measure unit (Thorlabs DC2200).

## Atomic Force Microscopy (AFM) and Kelvin-Probe Force Microscopy (KPFM)

Scanning Probe Microscopies were carried out using a Park Instruments NX10 system using NSC36 Cr-Au coated probes (MikroMasch). For KPFM we use amplitude modulation mode at 17 kHz. In order to carry out measurements in illuminated conditions a custom sample holder was built. The illumination was provided by a monochromatic LEDs (Wurth Elektronik) placed beneath the glass surface, driven by a source-measure unit (Keysight B2912A).

## Absorption spectroscopy

Absorption spectra were recorded on a Shimadzu UV-2550 spectrometer equipped with a film adapter, 300-800nm spectral range, resolution 0.5nm, 10nm/s scan speed.

## Grazing Incidence Wide Angle X-ray Spectroscopy (GIWAXS)

Grazing-Incidence Wide-Angle X-ray Scattering experiments (GIWAXS) were performed at ALBA synchrotron, BL-11 (NCD-SWEET). The X-ray beam wavelength was set at $\lambda = 0.1$ nm. GIWAXS patterns were collected by a LX255-HS 2D (Rayonix) area detector, placed at 11 cm from the sample.

## Hydrogen Peroxide determination

The $H_2O_2$ concentration was evaluated using Horseradish Peroxidase|3,3′,5,5′-Tetramethylbenzidine (HRP-TMB) assay. Solution used for the assay was freshly prepared by mixing in the following sequence: 10µL hydrochloric acid solution (HCl in water 1 M) to adjust the pH for the assay, 2µL horseradish peroxidase solution (HRP in milliQ water, 100µg/mL) and 10µL 3,3',5,5'-tetramethylbenzidine solution (TMB in THF, 10mg/mL) in 1978 µL sample aliquot.

## Cell culture maintenance

HUVECs were purchased from PromoCell and grown in endothelial cell basal medium (PromoCell), supplemented with Endothelial cell GM 2 supplement pack (PromoCell). Cells were kept in T-75 culture flasks coated with 0.2% gelatin and maintained in incubator at 37°C in a humidified atmosphere with 5% $CO_2$. For the experiments, only HUVECs at passage < 7 were employed. After reaching 80-90% of confluence, cells were detached by incubation with 0.5% trypsin-0.2% EDTA (Sigma Aldrich) for 5 min and then plated for experiments. To promote cell adhesion, a layer of 1 mg/ml fibronectin (from bovine plasma, Sigma Aldrich) in phosphate buffer saline (PBS, Sigma Aldrich) was deposited on the surface of the samples and incubated for 30 min. After aspirating the fibronectin with PBS, cells were plated onto samples and cultured into 12well plates.

## AlamarBlue cell viability assay

HUVECs were seeded on polymer and ITO samples in 12 well plates at about 20000 cells/well density. Cell proliferation was evaluated after 24, 48, 168 h after plating in 2 biological replicates. To this aim, AlamarBlue cell reagent was added at a volume concentration of 1:10 to the cell culture.

In principle, the AlamarBlue molecule, resazurin, is a non-fluorescent molecule that is reduced to a fluorescent compound (resorufin) by the mitochondrial respiratory chain in live cells. In this way, the amount of resorufin produced is directly proportional to the quantity of living cells.

Three aliquots of culture media for each condition were placed in a black 96-well microplate and the fluorescence of the AlamarBlue compound was acquired by a plate reader (TECAN Spark 10M Plate Reader) with an excitation/emission wavelength of 540/600 nm. The procedure was repeated at each time point, rinsing, and replacing the AlamarBlue compound with fresh medium after each measurement.

## ROS determination in HUVEC cells

2',7'-dichlorodihydrofluorescein diacetate ($H_2$DCF-DA, Sigma-Aldrich) was employed for intracellular ROS detection. HUVECs were seeded on polymer and control substrates and treated continuously for 3 min with Thorlabs LEDs (530nm @110 mW/cm$^2$ for P3HT; 530nm @2mW/cm$^2$ for PDBD-T; 660nm @10mW/cm$^2$ for PTB7). Immediately after the end of the illumination protocol, cell cultures were incubated with 10 μM $H_2$DCF-DA in KRH for 30min, at 37°C with 5% $CO_2$. After

incubation, the fluorescence of the probe was recorded (excitation/emission wavelengths, 490/520nm, integration time 400ms, 100MHz, binning 1) with a 20X objective on an upright fluorescence microscope (Olympus BX63).

Variation of fluorescence intensity was evaluated over regions of interest covering single-cell areas, and reported values represent the average over multiple cells and different samples.

Image processing was carried out with ImageJ and subsequently analyzed with Origin 2020.

Reported results have been mediated over 3 biological replicates, obtaining a set of at least 1200 cells and 9 samples for each condition.

Data were compared using the Anova test 2-ways, with Bonferroni correction (0.05 significance level). * $p < 0.05$, ** $p < 0.01$, *** $p < 0.001$. Error bars represent the standard error of the mean.

## 3.4 Photovoltage Generation at p-Type Semiconducting Polymer/Electrolyte Interfaces

*Luca Bondi, Maria Rosa Antognazza, Beatrice Fraboni, Tobias Cramer*

### 3.4.1 Abstract

P-type organic semiconductors are gaining interest both as phototransducer material for optically controlled bioelectronics as well as photocathode material for oxygen reduction reactions. Understanding the different competing optoelectronic phenomena arising from the direct interface between the organic semiconductor and an aqueous electrolyte is of central importance in the development of future devices. Here we perform systematic transient and spectroscopic photovoltage measurements on P3HT and PBDB-T thin films in contact with phosphate buffered saline electrolyte. To identify the role of the electrolyte and the impact of electrochemical reactions, we compare the measurements to intrinsic photovoltage generation as observed in capacitively coupled photoelectrodes in the absence of electrolyte. To explain the large observed photovoltages in water and their dependence on light intensity, we develop a simple analytical model based on photoactivated forward and backward charge transfer across the organic semiconductor/water interface. The model captures nicely the different experimental observations, and its fit parameters agree with values obtained by chronoamperometric measurements and electrochemical impedance spectroscopy. The findings are of particular relevance to understand wireless, optically triggered bioelectronic transduction as achieved with p-type organic semiconductor in the form of transducer patches or micro- and nanoparticles in contact with biological cells.

### 3.4.2 Introduction

Photoelectrochemical reactions at organic semiconductor (OS) interfaces are of interest for a range of recent applications such as solar energy conversion with organic photoelectrodes[68,200,203–205] or organic photocapacitors[206] as well as organic optobioelectronic interfaces[42,43,207]. OS have advantageous properties for such applications due to their facile processing, their tunability with organic chemistry, biocompatibility and high absorption coefficients associated to the direct band

gap.[205] Numerous OS already exist with a wide range of energy levels for valence and conduction band and materials can further be optimized to align energetically with redox levels of interest.[208] In addition, several small molecule or polymeric semiconductors have been identified that match the electrochemical window for stable operation in water as electrolyte.[209] Photoelectrochemical investigations have demonstrated that OS often show photocathodic behavior in which photoactivated electrons are transferred from the conduction band to oxygen, protons or other acceptor states.[210] In the presence of suitable donors also photoanodic reactions become observable with electron transport into the valence band of the OS.[205] The measurement of open circuit photovoltage generation at such electrochemical interfaces during illumination provides a valuable characterization technique. It can provide information on the energy differences between OS and redox states. In addition, transient photovoltage measurements provide a means to assess recombination processes. However, the quantitative analysis of these measurements is often complicated and the theoretical descriptions developed for solid state photovoltaics cannot be easily translated as photovoltage can be generated at different interfaces relying on electronic and electrochemical processes.[48,52]

Beside these general considerations, photovoltage generation is of practical relevance for photoelectrochemical applications operating in an electrically floating configuration. In such situations, no wire is connected to set the potential with respect to the surrounding electrolyte and the Fermi level in the OS is shifting with the photogeneration of charge in analogy to an open-circuit configuration. Examples for floating photochemical systems are nano- or microparticles or implanted thin-film photoelectrodes for biomedical applications.[207] Particularly the latter have gained recent attention with demonstrations of optically triggered stimulation of retinal neurons[1,3,30,31,53,59,211,212] or peripheral nerves[62,155] as well as optically controlled tissue regeneration processes.[6,7,9] In these photoactivated biotransducers, the illuminated OS generates a physico-chemical stimulus that impacts on cellular messaging. Possible transduction pathways include the local increase in temperature, the generation of a transient electric field due to photovoltage generation or the production of reactive oxygen species and $H_2O_2$ that directly interact with cellular components.[43] Which one of these pathways is relevant depends on the photoelectrode's architecture, the OS energy-levels and light-intensity.[47] In contrast to invasively wired microelectrode-based bioelectronic interfaces, organic photoelectrodes offer the advantage to be operated purely optically when responsive in the tissue transparency window. This wireless configuration reduces the invasiveness of the interface but puts the electrode in a floating configuration where the photovoltage build-up

impacts on the physico-chemical transduction pathway. Understanding the generation kinetics of such photovoltage under physiological conditions is relevant to optimize materials and device architecture for future applications in organic optobioelectronic.

Polythiophenes are a class of semiconducting polymers that has been widely investigated for photovoltaic applications and raised also interest for photoelectrochemical applications. The main representative of this class of polymers is poly(3-hexylthiophene-2,5-diyl) (P3HT) due to its relatively easy synthesis, its good chemical stability in water and its strong absorption in the visible spectrum. The density of states classifies P3HT as a p-type semiconductor and p-type doping occurs under atmospheric conditions easily due to oxygen incorporation. P3HT based photoelectrodes as well as P3HT based nanoparticles were recently demonstrated as effective opto-bioelectronic interfaces to restore retinal functionality or to control cell-regeneration processes.[50,51] P3HT based photoelectrodes show photocathodic behavior in water in which protons or ambient oxygen act as electron acceptors. Accordingly, formation of a positive photovoltage is observed that depends on pH and oxygen concentration. Recent work addresses photovoltage transients in P3HT/water interfaces with a numerically solved drift-diffusion model and concludes from the modelling that important contributions occur (i) inside the semiconductor due the build-up of a polarized space charge and (ii) at the OS/water interface due to the electrochemical charge transfer.[48] Surface photovoltage measurements on P3HT samples not in contact with electrolyte could further demonstrate that in addition to photogenerated free carriers also polarized charge transfer states inside the OS film contribute to the photovoltage signal.[44]

Here our objective is to identify the main mechanism that leads to the generation of the large photovoltages observed in p-type organic semiconductor/water interfaces under physiologic conditions as relevant for biotransducers. To this end we perform transient and spectroscopic photovoltage measurements on p-type polymer samples deposited on ITO. We test rr-P3HT as well as PBDB-T as semiconductor materials. Both materials are biocompatible, stable in water and widely employed in OPV. They distinguish however in their microstructure and density of states: PBDB-T has a higher glass transition, a more amorphous structure and features a smaller bandgap than P3HT.[184] With the results we identify an analytical model based on forward and backward electron transfer reactions across the OS/water interface to describe the transient phenomena as well as its dependence on light intensity. We verify the model by comparing its fit parameters to values obtained by independent chronoamperometric measurements and electrochemical impedance spectroscopy.

We conclude by discussing the implications of the findings for optobioelectronic transduction pathways.

### 3.4.3 Results and discussion

#### Experimental characterization of photovoltage generation

In our research we measure the photovoltage transients generated in the p-type semiconducting polymer thin films of P3HT or PBDB-T deposited on ITO substrates. In order to be comparable to the physiological conditions present in biological application scenarios, we use aerated phosphate buffered saline solution (0.01M phosphate buffer, 0.137M NaCl, pH 7.4, 6.2g/l $O_2$ at 25°C) as electrolyte and compare our results to photovoltage measurements obtained without electrolyte in air. Both measurement configurations are shown in Figure 1a. In the presence of electrolyte, we use an Ag|AgCl reference electrode. In absence of electrolyte, a capacitively coupled ITO covered glass slide is used and the gap between the semiconducting layer and the counter electrode is controlled by a porous spacer to create a 30µm thick air gap. In both cases a high impedance differential amplifier (>100M□) conditions the photovoltage signal prior to data acquisition. According to our sign convention, a positive photovoltage is attributed to photocathodic behavior with positive charge accumulating at the photoelectrode side.

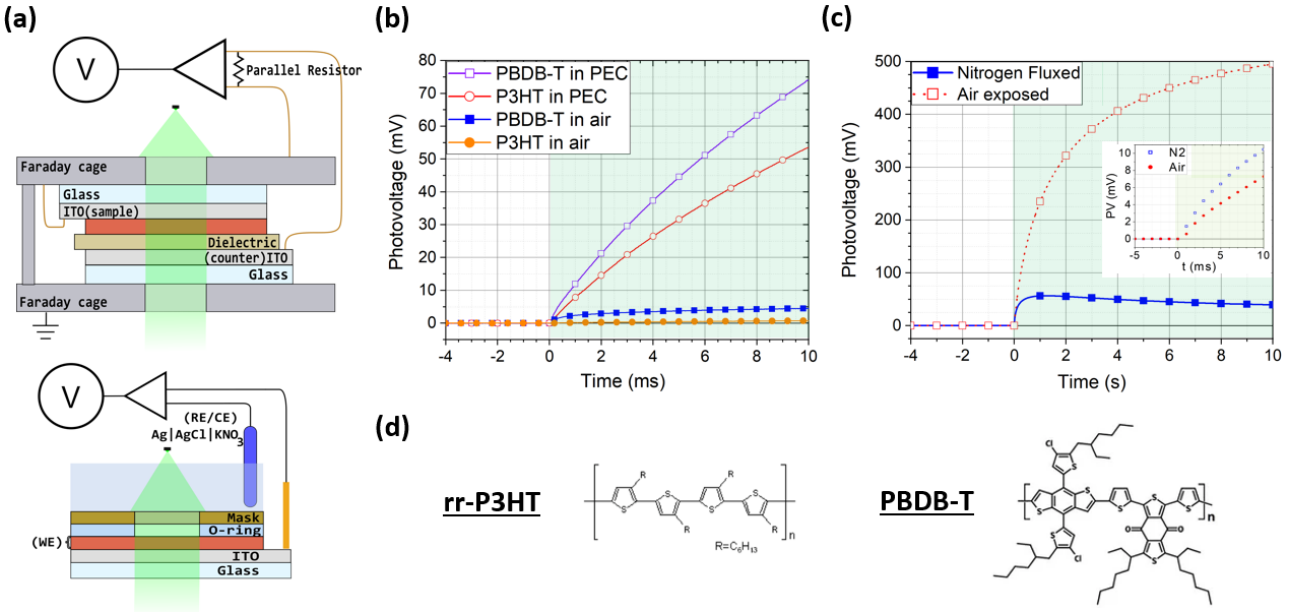


***Figure 1.*** *Experimental measurement of photovoltage: (a) scheme showing photovoltage experiment conducted in absence and presence of PBS electrolyte. (b) Comparison of transient photovoltage measurements on P3HT and PBDB-T photoelectrodes. (c) Photovoltage transient of P3HT measured in PBS electrolyte in presence and absence of oxygen. Inset: initial photovoltage build-up. (d) chemical structures of thiophene-based, organic p-type semiconductive polymers investigated in this paper: (sx) rr-P3HT, (dx) PBDB-T.*

Figure 1b and c compare the photovoltage transients of P3HT and PBDB-T based photoelectrodes measured in presence and absence of PBS electrolyte. These transients were generated by illuminating for 10ms the photoelectrode with monochromatic light at 450nm with 110mW/cm$^2$ light intensity. The photoelectrodes were illuminated through the electrolyte or through the air gap, thus hitting the OSC first and the ITO after. In the presence of electrolyte, large positive photovoltages of several hundred millivolts build-up in a slow process lasting several seconds (Figure 1c). Photovoltages acquired in the absence of electrolyte show very different transients: the signals stabilize within a few milliseconds and reach values that are two-orders of magnitude lower. Both, in electrolyte and in air the photoelectrodes accumulate positive charge assigned to photocathodic behavior. The measurements presented in Figure 1c demonstrate further that the large photovoltage in electrolyte only builds up when oxygen is present. This finding points to the important role of redox – reactions with oxygen as electron acceptor in photovoltage build-up. Photoelectrochemical

reduction of oxygen to reactive oxygen species and ultimately $H_2O_2$ are well characterized for p-type semiconducting polymers such as P3HT operated in ambient conditions.[52,160,213–224] In the absence of oxygen smaller photovoltages are observed that still exceed the ones measured in air. The effect is attributed to protons as acceptor states reacting with small probabilities to hydrogen as this reaction is kinetically very hindered.

To further inquire on the energetic states involved in photovoltage generation we performed spectroscopic measurements. The findings are shown in Figure 2 where the two photovoltage spectra (with and without electrolyte) are compared to the electrochemical photocurrent spectra and to the absorption spectra. For both materials we find that the onsets of photovoltage and photocurrent generation match the shape of the absorption spectra. This finding demonstrates that optical excitations exceeding the optical bandgap lead to photovoltage generation. Deviations from the absorption spectra at higher energies are attributed to the impact of the wavelength on the generation profile in the semiconductor. The glass-ITO-OS-water layered structure gives rise to internal reflections and interference effects that lead to a non-exponential distribution of excitons inside the semiconducting layer. Depending on the generation profile at a particular wavelength/energy, this effect can increase or decrease the formation of free charges at the OS/electrolyte interface. This in turn drives more photoelectrochemical reactions shifting the maximum of photovoltage or photocurrent in energy with respect to the absorption spectra. Furthermore, P3HT shows an additional wavelength dependency due to its free-charge generation mechanism.[225]

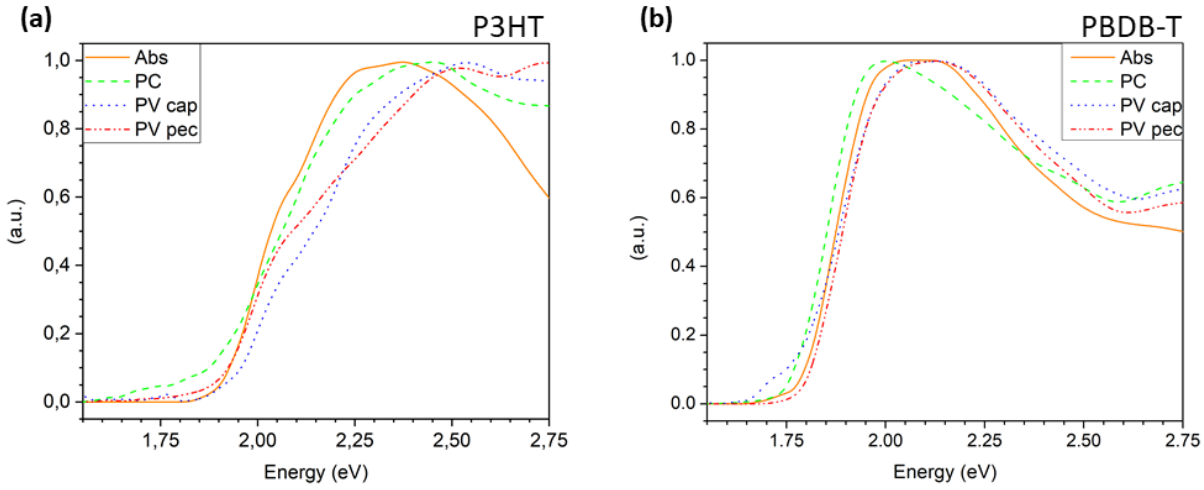


***Figure 2.*** *Comparison of absorption, photocurrent and photovoltage spectroscopy for P3HT (a) and PBDB-T (b) photoelectrodes.*

## Analytical model for photovoltage generation at the semiconductor/ electrolyte interface

From these findings we can derive a first, simplified interpretation of the photovoltage generation in p-type semiconductor photoelectrodes. Independent of the presence of electrolyte, photogenerated excitons are rapidly formed during illumination but dissociate only at very low quantum yields into free carriers. The low quantum yield is caused by the low dielectric constant of organic semiconductors and by the absence of internal electric fields and related band bending. The ITO substrate has its Fermi level positioned in the bandgap of the semiconductor and acts as acceptor for electrons as well as for hole charges[52]. In addition, the aliphatic side-chains of the semiconductor generate external interfaces that have only a minor defect concentration and are free of dangling bonds or trapped surface charges. Accordingly, only a low photovoltage (< 2 mV) is observed in the absence of electrolyte. As the effective origin of this small signal, different effects are discussed in the literature. Contributions could come from small electric fields nevertheless present at the external thin film interfaces or at internal interfaces between crystallites and amorphous regions.[44] However, in our opinion the important contribution comes from the differences in mobility of positive and negative carriers as shown by drift-diffusion simulations.[48] Oxygen related traps cause immediate trapping of negative carriers in thiophene based polymers and hence the distribution of negative charge is fixed to the optical absorption profile in the thin film. Instead, positive hole carriers remain mobile and diffuse through the film towards the ITO electrode when illumination arrives from the external surface as in our experiments. Consequently, a small positive polarization occurs at the ITO side of the photoelectrode as measured in our experiments. The timescale of this photovoltage build-up and its recombination is fast in thin films as only electronic processes are involved.

The presence of the aqueous electrolyte changes completely the photovoltage response as now photoelectrochemical processes play an important role. Figure 4 shows a basic scheme with the relevant energy levels for the materials and electrochemical reactions present at the photoelectrode/electrolyte interface. The incisive process is the transfer of free electrons onto oxygen acceptor states, present in the electrolyte. The energy-level for the one-electron transfer to oxygen depends on the hydration of the molecule and the local concentration of the reduced form but can be taken to be > 4.1 eV[47] and hence electrons in the p-type polymers conduction band have a strong enough driving force for transfer. With the transfer of electrons across the interface, hole charges

accumulate in the semiconducting thin film and negative ionic charges in the electrolyte. The formation of this space charge layer during illumination irreversibly enhances the wettability of the interface.[160,226,227] The shift in vacuum level caused by the charge accumulation at the semiconductor/electrolyte interface progressively reduces the driving force for the aforementioned electron transfer and increases the driving force for redox reactions in the opposite direction. At a certain photovoltage, forward and backward electron transfer counterbalance and the photoelectrode reaches a stable photovoltage $V_{p,0}$ as indicated in Figure 4b. Here we note that the dynamic equilibrium at photovoltage saturation can still require mass transport to the interface to maintain a constant concentration of participating redox states. Accordingly, in case of mass transport limitations, variations in photovoltage saturation level can still occur on longer time scales and depend on the photoelectrode and measurement cell geometry.

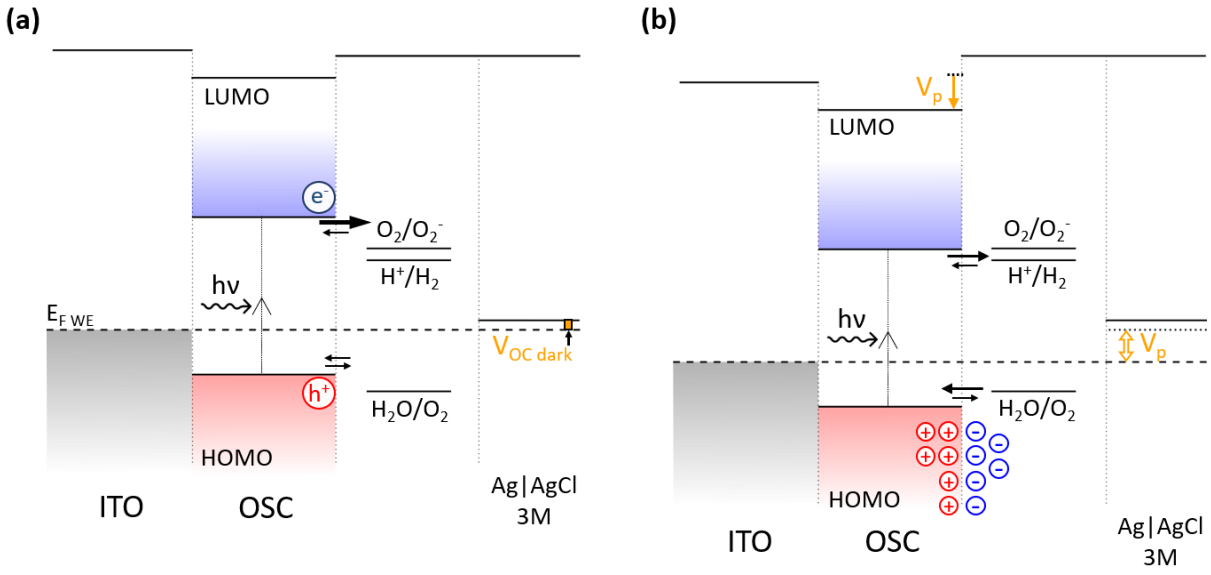


***Figure 3.*** *Energy diagrams explaining initial photovoltage generation and saturation: (a) Upon illumination electrons are transferred from the HOMO level onto oxygen acceptor state in the electrolyte. Therefore, an interfacial double layer builds up. The acceptor level rises in energy, further transfer of excited electrons becomes unlikely. Instead, electron transfer in the opposite direction has increased driving force.*

Based on this interpretation we derive in the following an analytical description of the photovoltage generation in OS/electrolyte interfaces as determined by the electrochemical processes. First, we note that the photovoltage $V_p$ is directly related to the charge $q$ that accumulates across the OS/electrolyte interface. The capacitance $C_H$=$q/V_p$ storing the charge depends on the localization of the charge in the OS and on the capacitance of the ionic Debye-Helmholtz layer. Accordingly, assuming a constant capacity, we can define the rate of photovoltage build-up as:

$$\frac{dV_p}{dt} = \frac{d(q(t)/C)}{dt} = \frac{I_F(t)}{C_H} \qquad [1]$$

where $I_F(t)$ is the net photocurrent passing through the interface. As it is a faradic current, it is expressed as the sum of several possible forward and backward electron transfer reactions:

$$I_F(t) = \frac{dq}{dt} = \frac{d(p-n)}{dt} = nk_{ET,f1} - pk_{ET,b1} - \cdots \qquad [2]$$

Here the important forward reaction is the transfer of electrons onto oxygen acceptor states described with rate constant $k_{ET,f}$ and directly proportional to the amount of photogenerated electronic carriers $n$. In the opposite direction, transfer of electrons from donor sites onto the OS is relevant to fill hole states with concentration $p$. Several processes can be considered for this direction: re-oxidation of intermediate ROS species from oxygen reduction reaction, oxidative processes against the polymer side-chains or water oxidation. All contributions depend strongly on the voltage of the photoelectrode that controls the energetic alignment between donors and acceptors states. The overall faradaic current is then produced as the sum of all relevant processes. To derive an analytic expression, we assume for each process a Tafel equation that shows an exponential dependence on the voltage difference between related energy levels. In addition, we note that in the photovoltage experiments only small amounts of faradic processes occur at the OS/electrolyte interface and hence we assume that concentrations of participating electronic or chemical species remain constant. Considering only one relevant forward and one relevant backward electron transfer process we obtain (for details see appendix):

$$I_F = I_{f,0}\exp\left[\alpha_f\left(V_p - V_f\right)\right] - I_{b,0}\exp\left[-\alpha_b\left(V_p - V_b\right)\right] = 2\,I_0\sinh\left(\alpha\left(V_p - V_{p,0}\right)\right) \qquad [3]$$

Here $V_f$ and $V_b$ are the energy levels associated to the electrochemical processes. We further simplify without loss of generality by setting the charge transfer coefficients for forward and backward reaction equal: $\alpha_F = \alpha_B = \alpha$. The coefficient $\alpha$ is of the form $\alpha = \frac{\beta ne}{k_b T}$ where $\beta$ is the barrier

symmetry coefficient, n is the number of electrons involved in the reaction, F is the Faraday constant, $R$ is the ideal gas constant and T is the temperature. We call the parameter $I_0$ the effective exchange current and its value is $I_0 = \sqrt{I_{f,0} I_{b,0} \exp[\alpha(V_b - V_f)]}$. The voltage $V_{p,0}$ now denotes the saturation photovoltage.

The combination of equations [1]-[3] leads to a differential equation that can be solved analytically. The boundary conditions are set by starting the photovoltage experiment at short circuit condition ($t = 0 \rightarrow V_p = 0$) and we obtain:

$$V_p(t) = V_{p,0} - \frac{2}{\alpha} \operatorname{atanh}\left\{\exp\left\{-2\alpha \frac{I_0}{C_H} t\right\} \tanh\left(-\frac{\alpha}{2} V_{p,0}\right)\right\} \qquad [4]$$

The equation describes the transient of the photovoltage build-up. As important fit parameters it contains the effective exchange current $I_0$, the saturation photovoltage $V_{p,0}$, the capacitance of the OS/electrolyte interface C and the charge transfer coefficient alpha. The dependence on light intensity can be made explicit in equation [4] by considering parameters $V_{p,0}$ and $I_{F,0}$ (see appendix and results below).

In the following we test the analytical model on photovoltage transient measurements performed on short and longer timescales and with varying light intensity. Figure 5a shows a 60-second-long photovoltage transient of a 40nm thick P3HT film under blue illumination. Equation 4 provides an excellent fit to the data obtaining parameters $\frac{I_0}{C_H} = (17.7 \pm 0.1)\ mV s^{-1}$, $V_{p,0} = (520 \pm 1)\ mV$ and $\beta n = (0.172 \pm 0.001)$. The model reproduces the transient over the whole illumination period and as the inset reports also the excellent fit at shorter time scales.

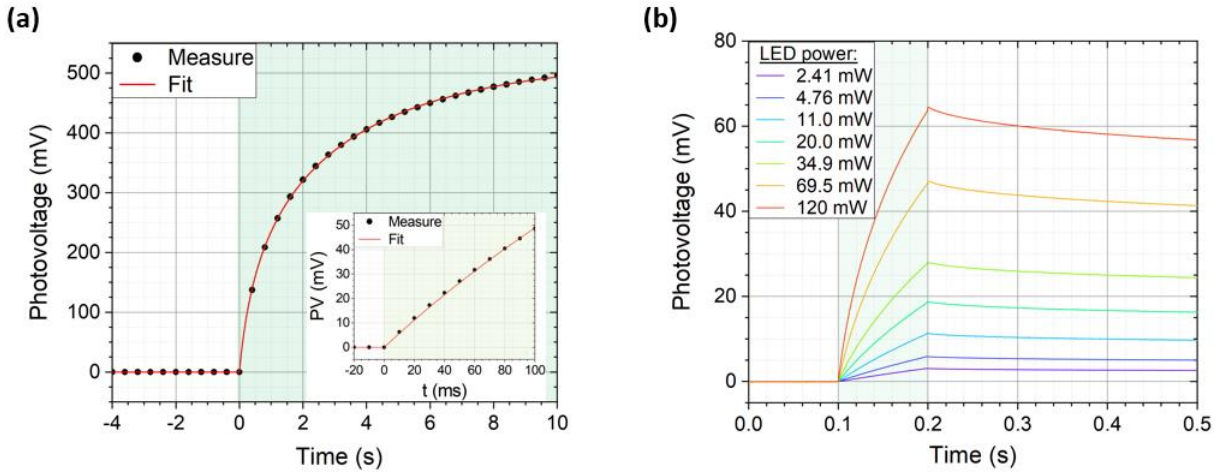


***Figure 4.*** *Photovoltage transients recorded in the presence of aeriated PBS electrolyte and fit to model (a) of a P3HT photoelectrode illuminated for 10 sec with 530nm 110mWcm$^{-2}$ green LED. (b) P3HT photoelectrodes illuminated for 100ms at varying light intensities (from 2.41mW/cm$^2$ to 120mW/cm$^2$) and following photovoltage drop-down.*

Photovoltage transients with shorter illumination time (100ms) are reported in Figure 4b. In the shown experiments, the light intensity was varied from 2.41mW/cm$^2$ to 120mW/cm$^2$ and this caused a significant change in the amount of photovoltage build-up and also in the shape of the transient. The figure reports also the slow recombination of the photovoltage after illumination. According to our model the initial slope of the photovoltage transient is dependent on two important contributions: First, the faradic current $I_{F,0}$ passing through the OS/water interface at the start of the illumination. At this initial condition, photovoltage is distant from saturation and only the forward transfer of electrons from the conduction band to oxygen acceptor states is relevant. The current can be directly measured by performing a chronoamperometric measurement with the voltage fixed at $V_{OC,dark}$ with a potentiostat and the same illumination conditions:

$$\left(\frac{dV_p}{dt}\right)_{t=0} = \frac{nk_{ET,f}(V_p=V_{OC,dark})}{C_H} \approx -\frac{I_{F,0}}{C_H} \qquad [4]$$

Second, the capacitance $C_H$ in the denominator limits the slope of photovoltage build-up.

The parameters $I_F$ and $C_H$ in equation [5] can be determined directly with experimental methods and thus provide a method to verify our assumptions. Figure 5a shows the impedance spectra of the P3HT electrode at $V_{OC,dark}$, under the same illumination conditions as in the transients (530nm,

$110\text{mWcm}^{-2}$) and the relative fit to the equivalent circuit model depicted in Figure 6b. The experimental spectra demonstrate the capacitive behavior of the photoelectrode at high frequencies while at low frequencies the faradaic behavior dominates. In order to fit the wider phase peak at ca. 100Hz and the second peak at higher frequencies giving rise to a shoulder at ca. 10kHz we have to include two different capacitances. The smaller capacitance corresponds to the ITO/semiconductor interface. From the model fit we obtain a value of $C_S$ = 246±15 nF/cm$^2$. The second capacitance, $C_H$, regards the charged double layer forming at the OS/electrolyte interface and a value of $C_H$ = 548±26 nF/cm$^2$ is obtained. The two different interfaces distinguish strongly in their charge injection resistances in parallel to the capacitors: $R_{inj}$ = 122 Ω and $R_{ET}$= 109 kΩ. For the electrolyte resistance we find $R_{el}$= 56 Ω. The internal resistance of the P3HT semiconducting layer is too small to be measured for a 50 nm thick film. With the same illumination conditions, we measure the faradaic photocurrent $I_{F,0}$ as shown in Figure 6c. After a small initial transient, the current stabilizes at a value of $I_{F,0}$= -0.825±0.002 µA. The two values yield a slope of $(dV_p/dt)_{calc}$= 1.51±0.08 V/s which compares very well to the experimentally obtained slope of the photovoltage transient of $dV_p/dt$ =1.65±0.15 V/s confirming our model.

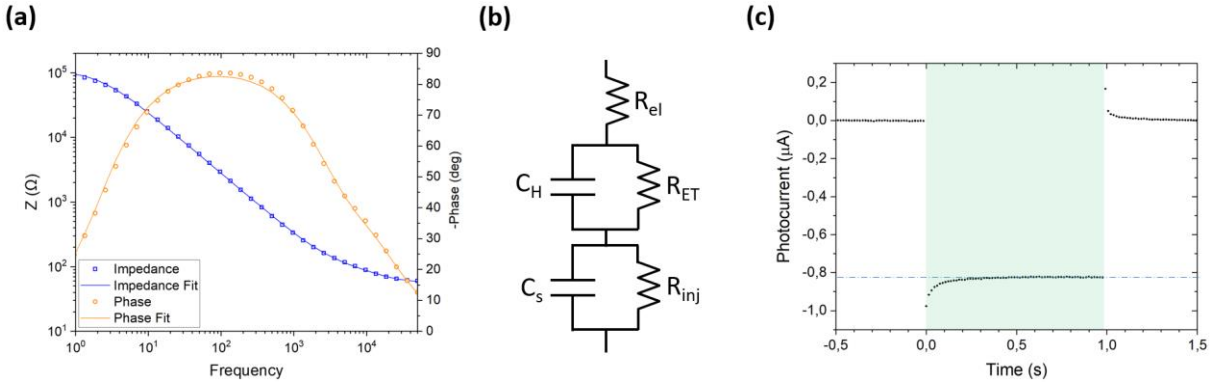


***Figure 5.*** *Understanding of transient photovoltage measurements: (a) impedance spectra of P3HT photoelectrode under 530nm 110mWcm$^{-2}$ illumination, (b) equivalent circuit of the photoelectrode, (c) transient photocurrent generation.*

Next, we test if our model is also in agreement with the effect of light intensity on photovoltage transients. The relevant parameter that changes with light intensity is the concentration of free

electrons *n* introduced in equation [2]. The hole concentration *p* is considered to be constant, as its value is given by the amount of doping in the p-type material and the small variations due to exciton separation are not expected to have a significant impact. Following a spontaneous exciton separation mechanism with monomolecular or trap assisted recombination we can assume that *n* is proportional to light intensity *P*. Accordingly we expect with a linear increase of the initial photovoltage generation rate as $\frac{dV}{dt} \approx \frac{I_{F,0}}{C} \propto n \propto P$. The data shown in Figure 6a confirms this assumption for light intensities varying of 2 orders of magnitude.

In addition to the initial photovoltage generation rate also the saturation photovoltage $V_{p,0}$ changes with light intensity as demonstrated in the appendix:

$$V_{p,0} = \frac{1}{2\alpha} ln(\beta P) \qquad [6]$$

We note that such a logarithmic dependence of open circuit photovoltage is typically observed for solar cells, inorganic photoelectrodes [228] or dye-sensitized solar cells [229]. Usually, the process is explained by electronic recombination currents and related charge distribution effects happening across the p/n junction. In our case, the effect is completely based on photoelectrochemical reactions and their back reactions. All properties of the charge generation in the semiconductor are included in the proportionality constant b. An important assumption of equation [6] is that the back-electron transfer reaction that leads to charge recombination is not directly influenced by light intensity. We probe this hypothesis by analyzing the photovoltage recombination rates obtained after switching off the illumination (data shown in Fig.4b). From the photovoltage decrease in darkness after illumination we calculate the recombination current by $I_{F,dark} = C_H \frac{dV_p}{dt}\Big|_{0,\ dark}$ where *t=0* here is considered the light switch-off moment. Its dependence on voltage is defined in analogy to equation [3] as

$$I_{F,dark} = 2\, I_{0,dark} \sinh\left[\alpha\kappa\left(V_p - V_{OC,dark}\right)\right] \qquad [7]$$

Where $\kappa = \frac{e}{k_b T}$ We test this equation by plotting the measured $I_{F,dark}$ against the value of the hyperbolic sine function as shown in figure 6b. Each data point was obtained for a different light intensity varying almost two orders of magnitude. All data points fall on a straight line with intercept zero confirming equation [7] and justifying the assumptions. From the slope we obtain

$I_{0,dark}$= 36.9±1.0 .

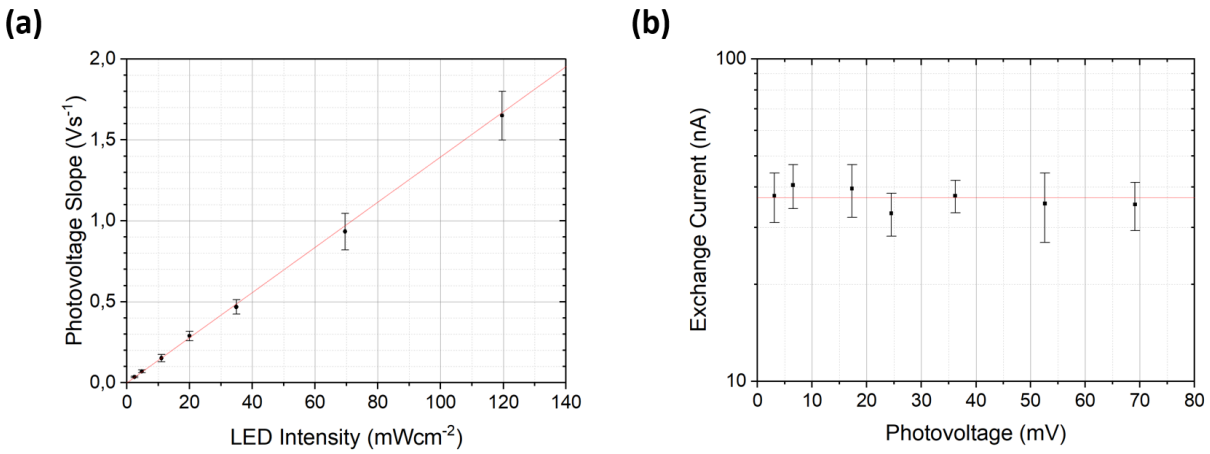


***Figure 6.*** *Analysis of photovoltage generation and recombination: (a) initial time derivative of photovoltage at different light intensities, (b) recombination exchange current term measured after switching off the illumination of varying intensities.*

## Relevance for organic optobioelectronic interfaces

Our findings on photovoltage generation allow us to discuss some relevant opportunities and limitations for future optically controlled interfaces with biological cells. In contrast to wired solar cells and photoelectrodes employed in energy applications, photovoltage generation is crucial in these biomedical applications as bioelectronic photoelectrodes are usually operated in an electrically floating condition. To reduce invasiveness, no wire is attached to remove charges that build-up during illumination or more precisely to set the working potential of the photoelectrode with respect to the surrounding bath. In approaches that rely on semiconducting nanoparticles, such a floating condition cannot be avoided. Accordingly, these nanoparticles or floating photoelectrodes made with p-type polymers charge positively under illumination.

The charging mechanism provides a potential transduction pathway to optically impact on the membrane potential of cells. However, with respect to biological systems, timescales at which p-type polymer electrodes charge positively are slow. The reasons for the slow response are on the one hand the small quantum-efficiency of charge carrier generation and on the other hand the large interfacial capacitance that needs to be charged. Both, charge generation as well as capacitance are proportional to the area of the semiconductor/electrolyte interface and hence changing size or introducing

increased surface roughness with microstructures is expected to have only small effects on timescales. Even though large photovoltages exceeding hundreds of millivolts are realistic for p-type semiconductors, its slow build-up makes the transduction to biological cells difficult as ions screen the emerging electric field attenuating its effect before it reaches a cellular membrane. Only direct interaction between the hydrophobic cell membrane and the p-type photoelectrode or particle with a large sealing resistance could inhibit ion-migration and related screening of the electrostatic interaction.

An alternative transduction pathway relies on the photogeneration of ROS and $H_2O_2$ at the p-type semiconductor surface. Our model allows to quantify the faradaic current that gives rise to the reduced oxygen species in floating nanoparticles or photoelectrodes. The photovoltage generation causes a significant reduction in the formation rate and when a steady state with constant photovoltage is reached, the amount of generated reduced species is determined by the slower back-electron transfer $I_{F,dark}$. Accordingly, in order to warrant efficient ROS generation in biological photoelectrodes operated wirelessly, it is not sufficient to just consider the quantum yield of exciton separation into free carriers, but one also has to optimize the back-electron transfer reaction in order to avoid excessive photovoltage build-up.

### 3.4.4 Conclusion

In this work we analyze how p-type organic photoelectrodes can generate large open-circuit photovoltages once they are in contact with electrolyte. For example, photoelectrodes made with thin films of P3HT or PBDB-T we find that oxygen becomes the crucial acceptor for the transfer of photogenerated free electrons from the conduction band. Remaining free hole carriers accumulate in the organic semiconducting layer giving rise to the large positive voltages that are measured. In contrast, photovoltage generated in the absence of electrolyte and electrochemical reactions is much smaller and generates on a much faster timescale following a purely electronic mechanism. To understand the photovoltage transients of the materials in contact with electrolyte we develop a simplified analytical model, that includes forward and backward electron transfer reactions at the semiconductor/electrolyte interface as well as an interfacial capacitance that gets charged by the photogenerated carriers. The resulting function fits perfectly the photovoltage transients confirming

the reliability of the initial assumptions. Furthermore, the function correctly describes the dependence on light intensity. The obtained parameters on photofaradaic current values and interfacial capacitance are compared to direct measurements with chronoamperometric measurements and electrochemical impedance spectroscopy with excellent agreement.

We think that being able to ascribe the electrical properties of the device to the energetics of the involved chemical substances is of significant importance for the development of future photoelectrochemical transductors. The development of an effective model has made it possible to predict the behavior of the system in open circuit conditions. We have also seen how the photovoltage generation is directly influenced by the alignment between the polymer orbitals and the acceptor molecules in water. This phenomenon can be exploited to gain higher photocurrents and to select a particular target acceptor. Moreover, we extracted important parameters such as the photovoltage dependence from the illumination intensity, and the photoreducing and back-electron transfer currents dependence on the photoelectrode potential. These can be used to identify which material and which illumination protocol best fit a specific purpose in floating conditions. We are currently employing these results to develop floating photoelectrodes thin films and suitable organic nanoparticles capable to trigger regenerative biological responses in human hearts. The results presented in this paper will be guidelines to achieve the desired photofaradaic behavior and to achieve photovoltages that are non-harmful for the cells.

## 3.4.5 Methods

### Materials and sample preparation

Photoelectrodes are made of a thin polymeric organic semiconductor deposited by spin-coating on a fully oxidized Indium-Tin-Oxide (ITO) coated glass slide. The p-type semiconductors rr-P3HT and PBDB-T, both thiophene-ring based polymers, are depicted in Figure 1. Materials were purchased from Ossila and Sigma Aldrich. The polymers were dissolved in Chlorobenzene at 80°C and spin-coated at 1000rpm for 60s. The solution concentration was varied to control the thickness. After deposition, the samples were annealed at 100°C for 10 minutes in order to get rid of residual solvent and to relax the internal strain.

## Photocurrent and photovoltage spectroscopy, electrochemical impedance measurements

Photoelectrochemical measurements were done in the setup schematized in Figure 1s. The photoelectrode's active surface was exposed to PBS electrolyte (0.01M phosphate buffer, 0.137M NaCl, pH 7.4 at 25°C). By mounting the photoelectrode in a dedicated cell, only the semiconducting layer is exposed to the electrolyte, while the buried ITO surface and the electrical contacts remain separated via a PDMS O-ring. The cell allows the exposition to the illumination from either the ITO side or the solution side, the latter through a quartz window. In a three-electrode setup the photoelectrode was operated as the working electrode. An Ag|AgCl (3M KCl) reference electrode was used in combination with a Pt counter electrode. In spectroscopic measurements the monochromatic illumination of the photoelectrode at a defined wavelength was achieved with a Xenon lamp combined with a monochromator (Cornerstone 260). The amplified current or photovoltage signal was filtered and digitized with a lock-in amplifier (Stanford Instruments) connected to the monitoring output of the potentiostat (Metrohm PGSTAT204) for photocurrent measurement or directly to the voltage amplifier (Femto DLPVA-100-F-D) for photovoltage measurements. The potentiostat was also used for impedance spectroscopy measurements. For transient measurements the monochromated Xenon lamp light was replaced with monochromatic LEDs (Wurth Elektronik) driven by a source-measure unit (Keysight B2912A).

## Capacitive coupling setup for photovoltage analysis in absence of electrolyte

We introduce a novel simple setup built to measure photovoltage transients generated in absence of electrolyte. The signal is collected through capacitive coupling between the photoactive material and an ITO counter electrode. The main structure is composed of a metallic faraday cage with a central hole on two opposite sides to let the light pass though. In the path of light is placed a structure composed of the polymer thin film separated from an ITO counter electrode through a 30µm thick insulating film. This sandwich structure can be assimilated to a planar capacitor in series with a photo-actuated voltage generator.

## 3.5 Supporting information

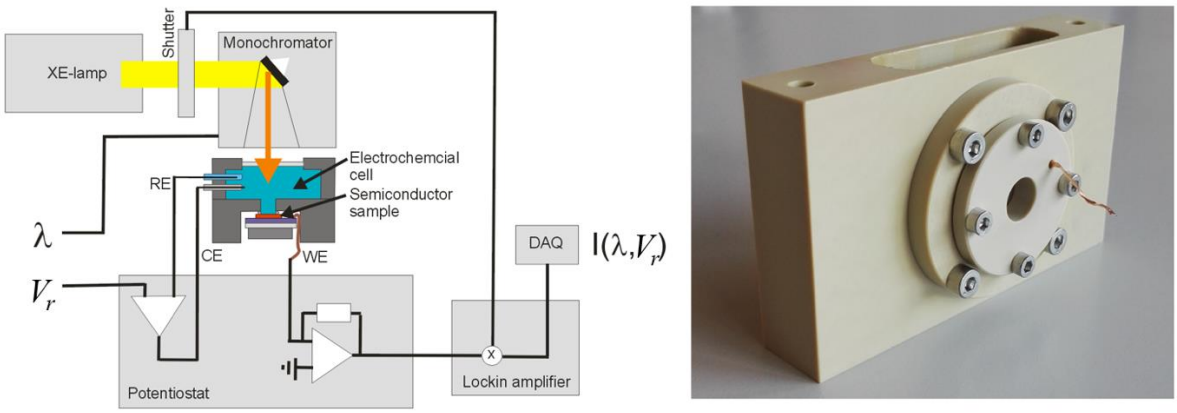


***Figure s1.*** *Experimental setup for the characterization of electrochemical processes at the semiconductor liquid interface. (a) diagram of the illumination system, measurement cell and electronic equipment allowing to measure photocurrent I as a function of wavelength □ and photoelectrode potential $V_r$. (b) photograph of the measurement cell, which puts the organic semiconductor interface in contact with the electrolyte while isolating the ITO back contact.*

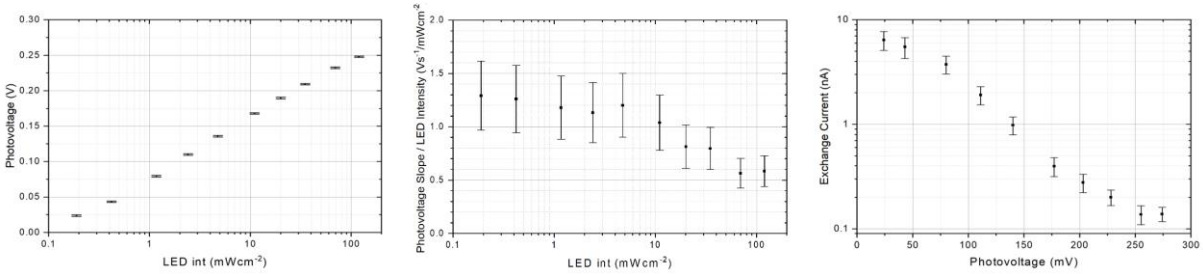


***Figure s2.*** *Photoelectronic characterization of the photovoltage transients: (a) maximum photovoltage built up by PBDB-T photoelectrode under 100ms 530nm 110mWcm$^{-2}$ illumination, (b) initial photovoltage slope at OCP dark, (c) recombination exchange current term calculated from a simplified Butler-Volmer model.*

**S3.**

The derivation starts with the expression of the faradic current as a sum of different electrochemical processes described by Tafel equations:

$$I_F = I_{f,0}\exp\left[-\alpha_f\left(V_p - V_f\right)\right] - I_{b,0}\exp\left[\alpha_b\left(V_p - V_b\right)\right] \quad \text{[SE1]}$$

In which Vp is the photovoltage and Vb and Vf characterize the voltage levels of the individual forward and backward electrochemical reactions.

By introducing $I_{f,01} = I_{f,0}\exp\left(\alpha_f V_f\right)$ and $I_{b,01} = I_{b,0}\exp(-\alpha_b V_b)$we obtain:

$$I_F = I_{f,01}\exp\left(-\alpha_f V_p\right) - I_{b,01}\exp(\alpha_b V_p) \quad \text{[SE2]}$$

When open circuit photovoltage is reached we introduce the condition $V_p = V_{p,0}$ and then the faradic current is 0: $I_F = 0$. In the following we derive the expression that determines Vp,0:

$$0 = I_{f,01}\exp\left(-\alpha_f V_{p,0}\right) - I_{b,01}\exp(\alpha_b V_{p,0}) \quad \text{[SE3]}$$

$$I_{f,01}\exp\left(-\alpha_f V_{p,0}\right) = I_{b,01}\exp(\alpha_b V_{p,0}) \quad \text{[SE4]}$$

$$I_{f,01}\exp\left(-\alpha_f V_{p,0}\right)\exp\left(\alpha_f V_{p,0}\right) = I_{b,01}\exp\left(\alpha_b V_{p,0}\right)\exp\left(\alpha_f V_{p,0}\right) \quad \text{[SE5]}$$

$$I_{f,01}\exp\left(-\alpha_f V_{p,0}+\alpha_f V_{p,0}\right) = I_{b,01}\exp\left(\alpha_b V_{p,0} + \alpha_f V_{p,0}\right) \quad \text{[SE6]}$$

$$I_{f,01} = I_{b,01}\exp\left(V_{p,0}\left(\alpha_b + \alpha_f\right)\right) \quad \text{[SE7]}$$

$$V_{p,0} = \frac{1}{\alpha_f+\alpha_b} ln\left(\frac{I_{f,01}}{I_{b,01}}\right) \quad \text{[SE8]}$$

Equation [6] allows to calculate the saturation photovoltage $V_{p,0}$. We can introduce the light intensity by introducing that the electronic carrier concentration is proportional to the light intensity:

$$I_{f,01} \sim n \sim P$$

The backward reaction does not depend on light intensity as the hole concentration is large also in darkness due to doping of the p-type semiconductor. The small variation in p due to photogeneration

does not have an effect. Accordingly we obtain a logarithmic dependence of photovoltage saturation on light intensity.

The introduction of equation [SE8] into equation [SE2] allows further simplifications:

$$I_F = I_{f,01}\exp\left(-\alpha_f V_{p,0}\right)\exp\left[-\alpha_f\left(V_p - V_{p,0}\right)\right] - I_{b,01}\exp(\alpha_b V_{p,0})\exp\left[\alpha_b(V_p - V_{p,0})\right] \quad \text{[SE9]}$$

$$I_F = I_{f,01}\left(\frac{I_{f,01}}{I_{b,01}}\right)^{-\frac{\alpha_f}{\alpha_f+\alpha_b}} e^{[-\alpha_f(V_p - V_{p,0})]} - I_{b,01}\left(\frac{I_{f,01}}{I_{b,01}}\right)^{\frac{\alpha_b}{\alpha_f+\alpha_b}} e^{[\alpha_b(V_p - V_{p,0})]} \quad \text{[SE10]}$$

$$I_F = I_{f,01}^{\frac{\alpha_b}{\alpha_f+\alpha_b}} I_{b,01}^{\frac{\alpha_f}{\alpha_f+\alpha_b}} e^{[-\alpha_f(V_p - V_{p,0})]} - I_{f,01}^{\frac{\alpha_b}{\alpha_f+\alpha_b}} I_{b,01}^{\frac{\alpha_f}{\alpha_f+\alpha_b}} e^{[\alpha_b(V_p - V_{p,0})]} \quad \text{[SE11]}$$

If we set $\alpha_f = \alpha_b$ and we call it $\alpha$ :

$$I_F = \sqrt{I_{f,01}I_{b,01}}\left(e^{[-\alpha(V_p - V_{p,0})]} - e^{[\alpha(V_p - V_{p,0})]}\right) = 2\sqrt{I_{f,01}I_{b,01}}\sinh\left(\alpha\left(V_p - V_{p,0}\right)\right) \quad \text{[SE12]}$$

**S4.**

We performed an experiment where a 110mWcm$^{-2}$ 530nm LED illumination was shined for 60 minutes over an electrically floating PBDB-T thin-film in the PEC cell. An aliquot of the electrolyte was then collected and its $H_2O_2$ content was evaluated through HRP-TMB assay. Given the long illumination interval, and the photovoltage transient shown by the material, we can safely approximate the behavior as if it was at maximum photovoltage for all the illumination period.
Since at maximum photovoltage the net current is zero, the forward and back electron transfer should be equal in modulus. At that potential we can infer that all the forward electron transfer comes from LUMO, and the back-electron transfer comes from HOMO. From the exchange current we can calculate the LUMO current in floating conditions at long times (long enough to reach the stable photovoltage: >1minute). By multiplying this current for the $H_2O_2$ generation experiment duration, we get to know the total charge that has faradaically flowed through the electrode. By multiplying this charge for the electron-to-$H_2O_2$ conversion efficiency we should be able to obtain the number of $H_2O_2$ moles produced, which divided by the electrolyte volume will give a good estimate for the $H_2O_2$ concentration in water:

$$C_{H_2O_2} = \frac{n}{V} = \frac{1}{V}\frac{q}{F}k_{eff} = \frac{1}{V}\frac{I_{OC}\,t}{F}k_{eff} = \frac{\mathrm{I}_0 t}{V}\frac{2\sinh\left(0.5\frac{F}{RT}\left(V_p - V_{OC_{dark}}\right)\right)}{F}k_{eff} \quad \text{[SE13]}$$

Where $n$ is the number of moles, $V$ is the volume of electrolyte in the cell, $F$ the Faraday constant, $q$ the electron charge, $k_{eff}$ the electron-to-$H_2O_2$ conversion efficiency, $I_{OC}$ the estimated open circuit current, $I_0$ the calculated exchange current of the recombination current, $t$ the duration of the experiment, $R$ the ideal gas constant, $T$ the temperature, $V_p$ the maximum photovoltage and $V_{OC,dark}$ the open circuit voltage in dark.

The experimental $H_2O_2$ concentration produced by a floating PBDB-T electrode in PBS after 60 minutes lays between the error bars of this value, thus validating the hypotheses made so far.

# 3.6 Photoactive Polymeric Nanoparticles for in-loco Hydrogen Peroxide Photoproduction

*Luca Bondi, Gabriele Tullii, Maria Rosa Antognazza, Camilla Marzuoli, Tobias Cramer*

## 3.6.1 Introduction

Recently, Antognazza's group demonstrated first evidences for optical control of tissue regeneration through a novel approach based on to the use of light responsive semiconducting polymers.[9,10,51,54,230] They observed the controlled growth of the tubular assembly in endothelial colony-forming cells (ECFCs), mediated by photoexcitation of the functional material regioregular poly(3-hexylthiophene) (rr-P3HT) in form of thin films.[7,10,11,231] However, the use of rr-P3HT thin films, while fully compliant with *in vitro* cell cultures, is limited for *in vivo* applications, for a number of reasons: (i) rr-P3HT thin film optical absorption is located in the green part of the spectral range and therefore misaligned with the physiological spectral window; (ii) thin films, though greatly conformable, require surgical implantation; (iii) they are only able to generate reactive oxygen species (ROS) and strong electric field outside the cell membrane and rely on the diffusion of generated messengers through the cell membrane.

Organic semiconducting nanoparticles (NPs) could represent an alternative to thin films. Prototypical rr-P3HT nanoparticles have already been demonstrated to efficiently generate reactive oxygen species (ROS) upon visible light excitation, without affecting cell viability.[51] Interestingly, light-activated ROS generation deterministically triggers modulation of intracellular calcium ion flux, successfully controlled at the single cell level.[51] NPs with the correct size distribution are also able to penetrate the cell membrane and accumulate in the cytosol allowing a spatially more targeted approach.

Following our previous work on p-type polymeric thin-films, we make a step forward towards all these three targets by studying two alternative low band-gap conjugated polymers, commonly employed in high performance organic solar cells,[185,232] namely (Poly[(2,6-(4,8-bis(5-(2-ethylhexyl)thiophen-2-yl)-benzo[1,2-b:4,5-b']dithiophene))-alt-(5,5-(1',3'-di-2-thienyl-5',7'-bis(2-ethylhexyl)benzo [1',2'-c:4',5'-c']dithiophene-4,8-dione)] (PBDB-T) and (Poly[[4,8-bis[(2-ethylhexyl)oxy]benzo[1,2-b:4,5-b']dithiophene-2,6-diyl][3-fluoro-2-[(2-ethylhexyl)carbonyl]thieno

[3,4-b]thiophenediyl]] (PTB7). Both materials are characterized by a strong red-light absorption falling in the physiological transparency window.

Nanoparticles are frequently defined as solid, colloidal particles in the range 10–1000nm.[233,234] Several methods to prepare polymer NPs by dispersing preformed polymers have already been developed and successfully utilized, namely: Solvent evaporation (microemulsion method), nanoprecipitation, salting-out, dialysis, and supercritical fluid technology.[235] The physics behind these processes has already been widely investigated.[80] In the case of the polymers of interest, the first two methods offer a simple pathway to NPs preparation. Moreover, these methods work well with the use of surfactants,[235] which are useful to stabilize them in the high ionic strength biological mediums in which they are meant to be employed. In solvent evaporation, polymer solutions are prepared in volatile solvents, and emulsions are formulated. The emulsion is converted into a nanoparticle suspension on evaporation of the solvent for the polymer, which is allowed to diffuse through the continuous phase of the emulsion.[236] Flash nanoprecipitation is based on the interfacial deposition of a polymer after displacement of a semipolar solvent, miscible with water, from a lipophilic solution. Rapid diffusion of the solvent into non-solvent phase results in the decrease of interfacial tension between the two phases, which increases the surface area and leads to the formation of small droplets of organic solvent.[237,238] We chose nanoprecipitation because of its simplicity, reproducibility[239] and the fact that in contrast to microemulsion it is less likely the coalescence of nanodroplets which may affect the final particle size and morphology.[235,240] Depending on polymer concentration and the organic-to-surfactant ratio it is possible to tune the nanoparticle size and covering.[241]

In this work, we process the materials in the form of nanoparticles (NPs) exploring diverse preparation conditions and how they impact on the optical, physical and photoelectrochemical performances. We built an AFM stage for KPFM measurements under illumination to probe the changes in surface voltage induced by light. Since NPs are a microscopic entity which behave as electrically floating device, every macroscopic instrument used to probe them cannot be contacted in a continuous way, otherwise their properties could be perturbed in multiple ways: Fermi level shifting, dipole formation, new contact capacities and so on. In order to get around these limitations, we developed a novel experimental technique to spectroscopically probe the charge accumulation in photoactive NPs following light-induced photoelectrochemical processes, through their sub-millisecond electrical discharge. Furthermore, we demonstrate that there are no adverse responses to

administration and internalization in Human umbilical vein endothelial cells (HUVECs), widely employed as a valuable model for the study of the endothelium function.[242]

### 3.6.2 Results

The polymer nanoparticles (NPs) dispersions are prepared by the flash nanoprecipitation method as shown in **Figure 1**. Since the NPs are designed to operate in the biological environment, they should be able to withstand high ionic strength mediums. In order to enhance the stability of the colloid within the ionic medium, an amphiphilic triblock copolymer surfactant, Pluronic F127, is added in the process. Pluronic block copolymers have been widely used to enhance biocompatibility, water-solubility and stability of drug delivery systems, up conversion NPs and innovative nanocarriers.[81,235,243] In particular, Pluronic F127 was successfully employed for the fabrication of stable water dispersions of carbon nanomaterials and conjugated polymer NPs, including PTB7 NPs.

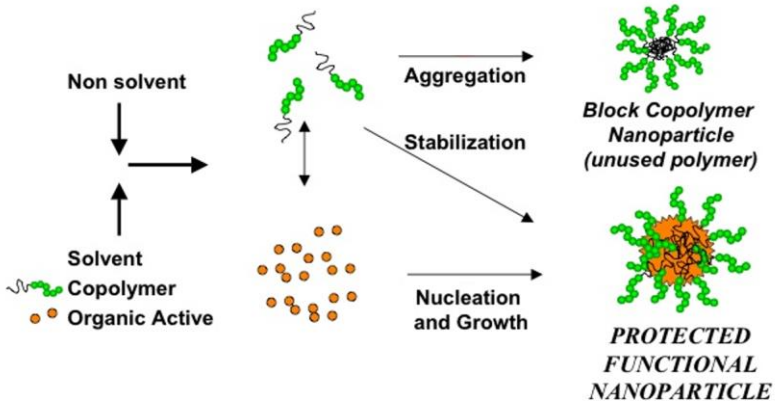


***Figure 1.*** *Flash nanoprecipitation method used to prepare the NPs. The polymeric semiconductor is dissolved in Tetrahydrofuran (THF), eventually with Pluronic F127. Polymeric solution is injected into water, which is non-solvent for the polymer and soluble in THF, to form a nanoparticle colloid. This colloid is put under slow stirring (~300rpm) at 40°C in order to let THF evaporate.*

The flash nanoprecipitation method involves mixing the organic active material which will form the NPs in a suitable solvent at high temperature. In the same solution the nanoparticle-protecting agent can be added. This solution must then be rapidly injected in a liquid which is a non-solvent for the

polymers while showing good solubility with the polymers' solvent. The non-solvent must be under strong stirring (>1000rpm) in order to create micromixing conditions. We have used ultrapure MilliQ water as well as various Phosphate Buffered Saline (PBS) solution concentrations as non-solvent. A protocol optimized by our collaborators suggest keeping the same temperature in the solution and in water in order to avoid thermal gradients and promote a smaller and more monodispersed size of the NPs. After the solution injection and the NPs colloid formation, the latter is kept under slow stirring conditions (<400rpm) at 40°C in order to let THF evaporate. The supernatant is separated via centrifugation and removed, and the clean nanoparticle colloid is eventually dialyzed in order to get rid of ions and part of the unreacted Pluronic F127.

The NPs were then analyzed structurally through non-contact Atomic Force Microscopy (nc-AFM) and Transmission Electron Microscopy (TEM), performed by UPV/EHU's scientists in San Sebastián, as shown in **Figure 2**. Both the techniques show approximately spherical NPs with no particular features in the range of diameters of 100-200nm. The comparison between NPs synthesized in the absence (**Figure 2a**) and in the presence (**Figure 2b**) of Pluronic F127 shows that even after multiple dialyses, performed before deposition on substrates as in the protocols for microscopy imaging, residues remain when Pluronic F127 is used, as it can be seen by the filaments observable between nanoparticles in Figures 2b. It can be seen that this excess copolymer forms filaments and networks when the suspending water evaporates during the deposition on the substrate for TEM or AFM investigations. From careful observation we can also see that when the colloid with Pluronic is deposited, clusters of NPs form, separated from each other and protected from the environment by Pluronic F127. It must be stressed however that during the evaporation of water the concentration of the sol increases progressively, thus promoting clustering and aggregation.

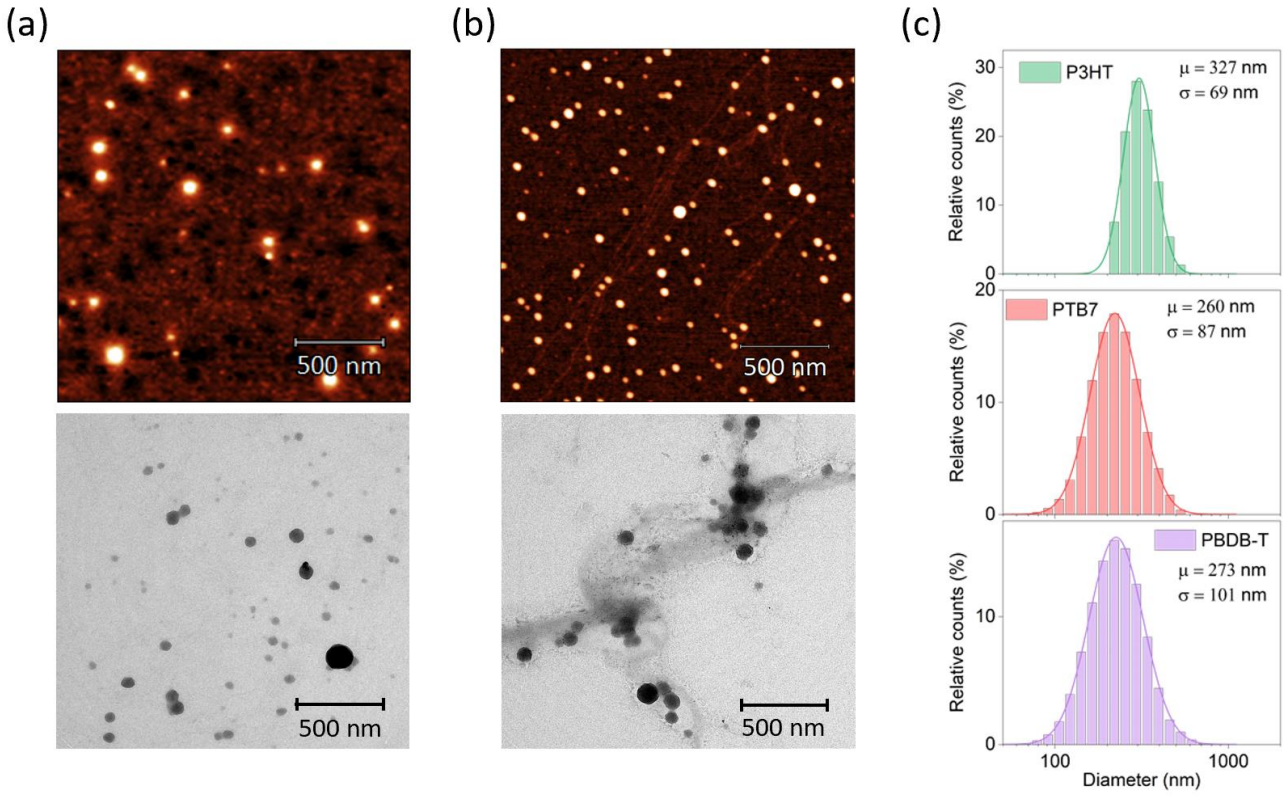


***Figure 2.*** *NPs non-contact AFM topology images (top) and TEM images (bottom) of NPs without (a) and with (b) Pluronic F127 (performed by scientist at UPV/EHU at D. Mecerreyes' group). In both the images with Pluronic we can distinguish the excess of this material depositing over the substrate forming networks between particles. In (c) we show the Dynamic Light Scattering (DLS) data acquired from nanoparticles dispersions produced using PBS. From the gaussian fit we can extract the average hydrodynamic diameter of the NPs and its relative standard deviation.*

In **Figure 2c** we show the Dynamic Light Scattering (DLS) analysis of the dispersions. In semi-logarithmic scale, a Gaussian distribution perfectly fits the histogram. From the fit we extract the hydrodynamic diameter of the NPs and the relative dispersity in the form of the gaussian's standard deviation. These parameters are important to predict whether the material and the nanoprecipitation protocol used are suitable for the production of NPs with a small enough size to enter the target cell. In the case of our study, a soft limit is set at 400nm and depends on the chemical nature of the polymeric material and the protective shell employed.

By comparing diameters extracted from TEM with the hydrodynamic diameters from DLS we observe almost a two-fold increase in the latter compared to the former. The hydrodynamic diameter, or more precisely the Stokes diameter in our case, refers to the equivalent diameter of a hard sphere that diffuses at the same rate as the observed particles. This means that either the Pluronic forms a shell with a thickness comparable with the nanoparticle's radius, or it interacts with the surroundings in such a way that the diffusion is slowed down significantly. The first case can be excluded due to the Pluronic ratio used for the synthesis. The second case can be either caused by the interaction with water or by the interaction of the Pluronic shell with other Pluronic molecules. These, in turn, can be either those dissolved in water or other nanoparticles' shells.

By comparing the NPs synthesized in MilliQ water with those synthesized in different PBS concentrations, the size analysis highlights a neat increase in size by increasing the ionic strength of the non-solvent medium. Additional experiments were done using NaCl in place of PBS to assess if the observed increase was in fact due to the ionic strength or to the presence of phosphate ions. These experiments show accordance between the diameters of NPs obtained using PBS and those obtained with NaCl solution with the same NaCl concentrations, thus corroborating the initial argument.

In conclusion, apart from macroscopic aggregates, all the analyzed NPs distributions shown sizes within the aforementioned upper limit for cellular uptake.

In order to assess the stability of the dispersions we observed the z-potential of the nanoparticles. The z-potential is a measure of the electric potential measured at slipping plane of the NPs and is a good estimator for the dispersion stability toward aggregation. The higher is the modulus of this potential, the higher is the repulsion between nanoparticles and hence the lower is the tendency to aggregate.

The measure of the NPs in PBS shown a very low z-potential, which can be justified by the shielding effect due to the high ionic concentration in the solution. Independently of the Pluronic concentration, the z-potential of the NPs in PBS was lower than 10mW, meaning very low stability toward aggregation. This instability could also be seen in DLS through the progressive increase in the mean value and standard deviation of the measured hydrodynamic radii.

| | MilliQ water | | Phosphate Buffer Saline, Dialyzed | | |
|---|---|---|---|---|---|
| | 0:1 (no Pluronic) | 1:9 Pluronic | 1:50 Pluronic | 1:18 Pluronic | 1:9 Pluronic |
| P3HT | -41 mV | -38,2 mV | -23,6 mV | -25,6 mV | -29,9 mV |
| PTB7 | -44 mV | -36,4 mV | -34,3 mV | -36,8 mV | -24,7 mV |
| PBDB-T | -37 mV | -33,2 mV | -30,7 mV | -20,3 mV | -29,9 mV |

***Table 1.*** *Z-Potential measured for different water salinities and different Pluronic content to assess the stability of the nanoparticles. In the Pluronic content field, the ratio is expressed in terms of Pluronic: Polymer mass ratio. The PBS synthesized NPs were dialyzed 3 times for 2 days in order to lower the ionic strength of the medium.*

In **Table 1** are listed the z-potentials for all the studied materials, synthesized both in MilliQ and in PBS with different Polymer : Pluronic ratios. We can see that the materials in MilliQ water have the highest moduli, all falling within the stability range (>|30|mW). We can also observe that the presence of the Pluronic shell results in a lower potential. This can be explained by the fact that the presence of Pluronic on the surface of the NP moves further away the slipping plane which results in a higher shielding of the charge. On the other hand, there is no clear dependency of the z-potential from the Pluronic content in NPs synthesized in PBS. All these NPs fall nevertheless in a range of acceptable stability (20mV<|Z|<30mV). The material which shown an overall higher potential is PTB7, suggesting it could be the most stable in the majority of cases.

Even though low Pluronic content shows a higher z-potential, in the presence of this protecting polymer the stability of the colloid is also given by the non-sticking character of it. This results in a non-direct correlation between the potential and the long-term stability. All the following studies are then referred to NPs synthesized with a Pluronic-to-polymer ratio of 9:1 since it was the standard optimized by the group for long-term stability.

In **Figure 3a** we show the comparison between the absorption spectra of the polymers nanoprecipitated in MilliQ and in PBS. In P3HT three main vibronic peaks are visible in both cases at approximately 610nm, 560nm and 510nm. The energy of the peaks slightly redshifts with

increasing ionic strength of the non-solvent aqueous medium. The intensity ratio of these peaks changes considerably from one to the other conditions, with an overall absorption which results redshifted for the PBS case. We note that in P3HT the spectrum of NPs synthesized in MilliQ water is comparable with the thin-film absorption spectrum, while the PBS one resembles the reflection spectrum of the thin-films. PBDB-T shows approximately the same spectra in the two conditions with the absorption peak redshifted of 20nm. PTB7-MilliQ shows an absorption peak at 610nm and a shoulder at 665nm, while PTB7-PBS have one absorption peak at 700nm and a shoulder at 610nm. This result suggests the coexistence of a vibronic band at 610nm with a different contribution to the total absorption, while we cannot conclude anything about the feature at lower energies.

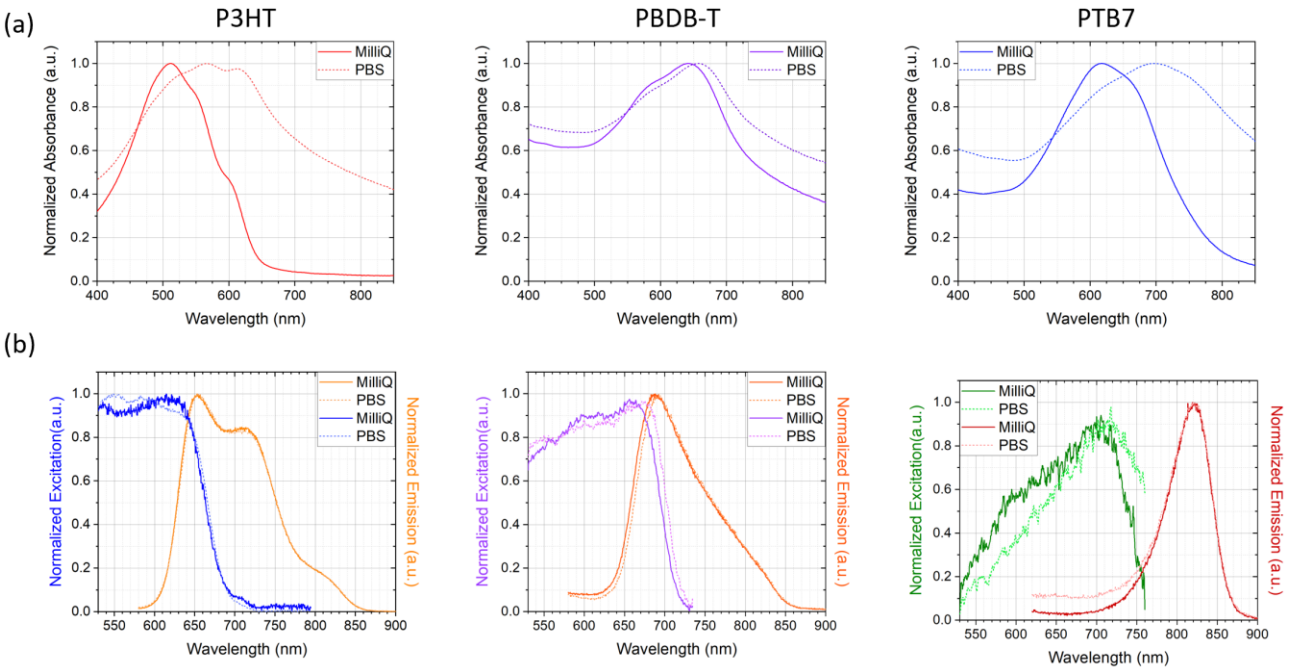


***Figure 3.*** *In (a) we show the absorption spectra of NPs synthesized with the three studied materials both in presence of PBS and in pure MilliQ water. These spectra should be compared with the Excitation (left axes) and Emission spectra (right axes) relative to the same nanoparticles shown underneath in (b).*

Together with the fact that the normalized excitation and emission spectra of P3HT is the same in both the conditions as shown in **Figure 3b**, suggest that the energetics of the bands does not change significantly. Excitation spectra of PBDB-T on the other hand replicate the same small shift observed in absorption thus implying an effective shift in the energetics of the polymers' bulk. Finally, despite the small difference in the shapes of photoluminescence curves of PTB7, the excitation peaks are almost superimposable for the two NPs synthesis conditions whereas even though the absorption peaks differ of just less than 100nm. Nevertheless, in PTB7-MilliQ excitation spectrum there are both a peak at 700nm and a shoulder at 610nm which disappear in PTB7-PBS. These same features are found in the absorption spectra, suggesting the existence of the 700nm state in both the NPs despite it is not distinguishable in PTB7-MilliQ. In Figure 3b we observe a small stokes shift in P3HT (100meV) and PBDB-T (70meV MilliQ, 40meV PBS) while in PTB7 it is larger (230meV MilliQ, 210meV). Lastly, it can be noted that there is a net increase in all the NPs absorption spectra at energies both higher and lower than the absorption peaks when the employed aqueous non-solvent is PBS. This can be attributed to the higher Mie scattering as a result of the larger NPs average size and distribution.

From Bossio's paper[51] we know that P3HT NPs induce ROS generation inside living cells. At first, we assume the same optoelectrochemical behavior as observed in thin film allowing for the possibility of some deviation. In order to evaluate the photoelectrochemical activity of the nanoparticles in absence of an electrolyte we deposit them over an ITO film and measure the KPFM potential difference between dark and illuminated conditions. The illumination is performed through a 530nm, 30mWcm$^{-2}$ LED placed underneath the ITO covered glass slide. The wavelength chosen is the best trade-off between the absorption of the materials, with an energy higher than all the energy gaps and a good absorption coefficient. The illumination intensity is the maximum experimental value that allows a stable scan without excessive substrate thermal drift. In order to best access the polymers' properties, we investigated the NPs without Pluronic shielding. Since there is no surfactant protection, the NPs used are nanoprecipitated only in MilliQ water. **Figure 4a** shows the morphology of the selected NPs and the relative KPFM image in dark conditions. We observe that the potential distribution is not uniform. This suggests surface polarization possibly due to surface oxidation, structural inhomogeneity, ions coordinated during the colloidal phase, static charge that is unable to completely discharge because of low conductivity of the polymers or other spurious phenomena.

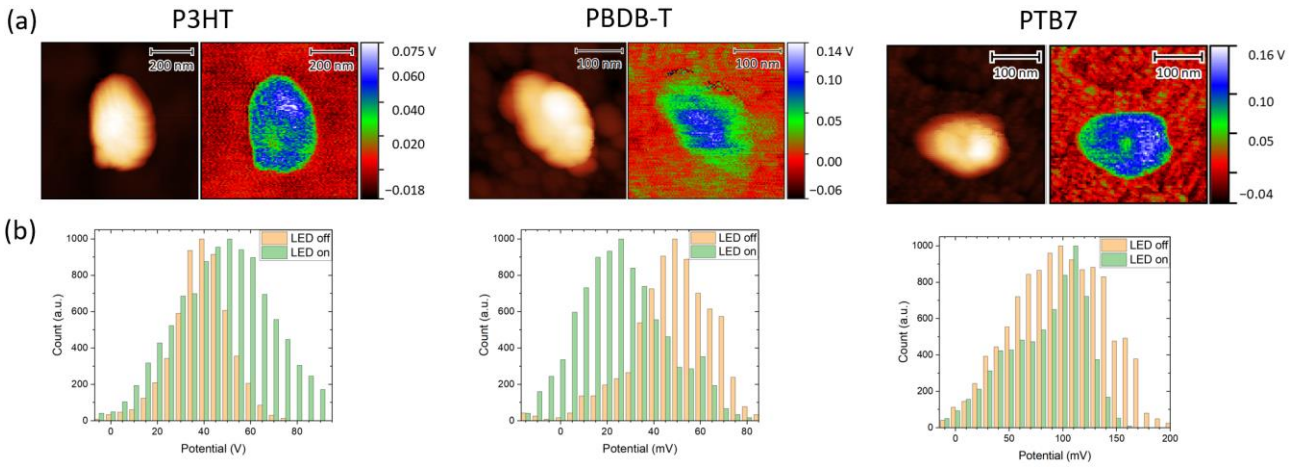


***Figure 4.*** *(a) Nanoparticles KPFM imaging in dark conditions and relative AFM morphology. From the left, the nanoparticles show an average KPFM signal of (40.0 ± 17.3)mV , (50.8 ± 21.6)mV and (95.2 ± 65.1)mV. KPFM potential measured in dark conditions and after 60 seconds of 30mWcm$^{-2}$ 530nm highlights are compared: PTB7 show no significant difference in the potential distribution over the NP with P>0.05, whereas P3HT and PBDB-T undergo a significative potential change with P<0.005).*

In order to compare the KPFM potential of the nanoparticles before and after illumination, in the first we set a threshold value to determine the boundary between ITO and the NP and we pixelate the latter. Then we bin the potential scale, and we create histograms with the entries. The histograms can be fit with gaussian curves from which we can extract the means and the variances. In **Figure 4b** we compare these histograms in dark and illuminated conditions for all the materials. P3HT shows μ=(40.0 ± 17.3)mV and (49.0 ± 31.3)mV, PTB7 shows μ=(50.8 ± 21.6)mV and (23.9 ± 26.4)mV, and PTB7 shows (95.2 ± 65.1)mV and (91.1 ± 52.0)mV. By requesting a 5% confidence for statistical significance, these data lead to a KPFM potential difference of means of: (9.0 ± 1.0)mV for P3HT, -(27.0 ± 1.5)mV for PBDB-T and -(4.0 ± 5.2)mV for PTB7. With these data we observe no significative difference in the PTB7 distributions with $P_{PTB7} > 0.05$, whereas the other materials show significative difference with $P_{P3HT} < 0.005$ and $P_{PBDB\text{-}T} < 0.005$.

Also, in the case of a significative difference, the photoinduced voltage difference observed is in line with the data on films in absence of electrolyte and are orders of magnitude lower than those observed on films in contact with an electrolyte. Moreover, the sign of the KPFM difference is positive for

P3HT and negative for PBDB-T. Provided that more studies need to be performed to establish the nature of these signals, we discard the possibility that they influence in some way the behavior in electrolyte and in-vitro. We speculate that they are produced mainly from the discharge of static charges during illumination given the photoconductivity of these materials and possibly from the reduction of humidity present in water.

In this context we assume the same behavior for thin-films in electrically floating conditions and nanoparticles when exposed to electrolyte. As discussed in the previous chapter, photon absorption leads to the reduction of acceptor molecules in water, mainly oxygen and secondarily hydroxonium ion, and in floating device to the accumulation of positive charges in the polymer. In order to validate this assumption, we performed the experiment shown in **Figure 5**.

The experiment consists in the measurement of the current produced by the discharge of illuminated NPs on an ITO surface placed in contact with the suspension. The setup of the experiment is composed by a PDMS cell filled with the NPs dispersion with a 2.8cm$^2$ ITO working electrode (WE) on one side which closes the circuit with an Ag|AgCl wire Reference/Counter electrode (RE/CE). Although the nanoparticle's discharge probability is intrinsically negligible on the RE given the thermodynamics of the charge transfer from the polymer to the AgCl, in order to minimize the possibility of electron transfer on exposed silver, precautions were taken: the chloride deposition was performed electrochemically with a small current in order to have a more uniform coating and the area of the counter electrode was minimized to 0.5cm$^2$. The wire resistance was still low enough not to disturb the discharge of the nanoparticles since a resistance of the order of the tens of kΩ with the expected current of the order of hundreds nA will result in a potential drop of the order of the mV. This magnitude is not significative compared to the energy difference between the positive polaron level in the semiconductor where the positive charges are accumulated and the Fermi level of the WE where the charges will be transferred during the discharge event.

As described in **Figure 5a** the light absorption cause charge accumulation in the nanoparticle which results in a shift of the vacuum level and hence of the energy levels. Keeping the illumination on, eventually the reduction photocurrent from the NP is completely balanced from the back-electron transfer and the photovoltage reach an equilibrium state. The NP is surrounded by negative ions in order to reach charge neutrality, so the overall NP-diffuse double layer system is neutral. Being so, the NPs move in the aqueous phase following a Brownian motion. Because of the motion, some NPs will eventually reach and impact on the ITO WE. During the impact, the distance between the

nanoparticle's surface and the ITO surface are close enough to allow charge transfer (CT) processes. If the Fermi level of the WE is higher than the energy barrier for CT we expect it to happen. If the energy difference is even higher than the nanoparticle's rest Fermi level in dark conditions, we expect it to potentially totally discharge if it spend enough time near the ITO surface. In our system is contemplated the possibility to apply a bias between the WE and the RE in order to shift the Fermi level of the former.

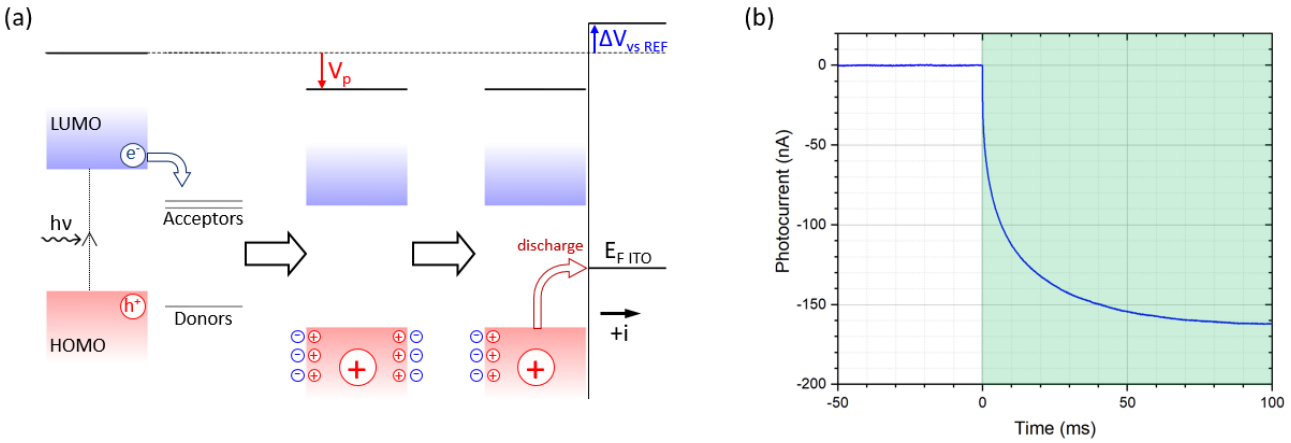


***Figure 5.*** *In (a) we show the energetics of the complete charge/discharge cycle of an illuminated nanoparticle dispersed in water. When the light is absorbed, electrons are promoted to excited states and can reduce acceptors in water, thus leaving a net positive charge in the nanoparticle. By charging electrically, the energy levels shift downwards and reach an equilibrium potential if continuously illuminated. Driven by Brownian motion the NP eventually reach the ITO electrode. If the energetics is favorable, the electrode will reduce the nanoparticle thereby discharging it. Because of the time constant of the amplifier-electrode system, the discharge events are integrated and can be measured as a macroscopic current transient. Here is shown the current as a function of time (b) measured for a P3HT dispersion illuminated by a 130mWcm$^{-2}$ 530nm LED source with no applied bias.*

The electric circuit model of our acquisition setup can be approximated to be composed by $C_{ITO}$ in series with $R_{liquid\ phase}$ and $R_{RE}$. If the time constant is significantly larger than the sum between the discharge duration and the average time between two discharges, the circuit behaves as a current integrator. We therefore expect to lose the single peaks resolution and to see a growing current with

a $\left(1 - e^{-\frac{t}{\tau}}\right)$ behavior as a first order approximation. Deviations from this behavior are expected when long enough acquisition durations are employed due to multiple factors such as: depletion of oxygen dissolved in water, $Cl^-$ concentration variations caused by Ag|AgCl operation, convection motions in water and non-uniformity of charge density in the proximity of the electrode given by the charge-discharge dynamics.

We tested this hypothesis by illuminating with a 530nm 130mW/cm$^2$ LED source the cell containing the NPs dispersion and acquiring the current as a function of time. We then subtracted the blank signal consisting of the same experiment performed with only water. The experiment confirmed our initial guess as shown in **Figure 5b**. The sign of the current is consistent with a reducing current flowing from the WE to the suspension.

We exploited this to explore the spectral response of the NPs photovoltage generation. To do so we illuminated the setup using a chopped and monochromated light from a Xenon lamp and acquiring the signal through a lock-in amplifier.

The amplitude of the current is correlated to different properties of the solution and the NPs such as the number of NPs in solution, the quantum efficiency of the photoelectrochemical process and the charge storage capacity of the NPs. In addition also the ratio between the RC time constant of the circuit and the chopping frequency will determine the maximum measured current. Since we are interested in the normalized spectra, the absolute value of the current is not relevant. The chopping frequency has hence been optimized matching the lowest noise (the higher the frequency, the better) with the highest current modulus (the lower the frequency, the better).

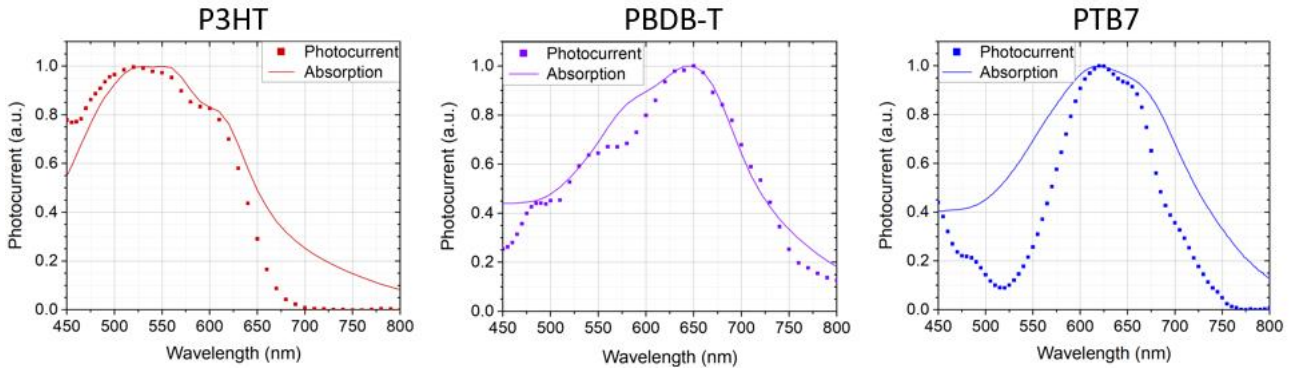


***Figure 6.*** *Comparison between NPs absorption spectra and their photoelectrochemical current spectra. The photocurrent is generated through the discharge of photocharged NPs over an ITO electrode.*

**Figure 6** shows the photoelectrochemical current spectra for P3HT, PBDB-T and PTB7 NPs, at 1:9 Pluronic:Polymer relative mass concentration. The photocurrent spectra are very similar to the optical absorption spectra, indicating a symbatic-like behavior. Similar spectra are also observed in photoelectrochemical current spectra of thin-films made of these materials. Accordingly absorbed photons contribute equally to the photocurrent generation, independent on their energy. We hence exclude a significant contribution of defect states or interfacial energy levels to the process. Instead, the photoelectrochemical activity relies on bulk optical bandgap absorption leading to exciton formation, thermalization and subsequent dissociation into free charge carriers in the NPs. Free electronic carriers participate in the electrochemical reduction of oxygen in the solution leading to ROS formation.

The findings are in line with previous results obtained with P3HT NPs, and demonstrate the occurrence of photo-electrochemical reactions at the polymer/buffer interface of NPs, mostly leading to oxygen reduction processes and to the formation of ROS species, all virtually ending up in hydrogen peroxide formation at timescales > 1 s.

In biological tissue, intracellular and extracellular $H_2O_2$ concentration represent a powerful signaling event for the modulation of angiogenic processes. The possibility to modulate it on demand and over different orders of magnitude, through touchless optical excitation of smart nanomaterials, may open the path to interesting therapeutic applications. Thus, Antognazza's group (our partners at IIT-CNST) investigated the interactions between polymer NPs and endothelial cells.

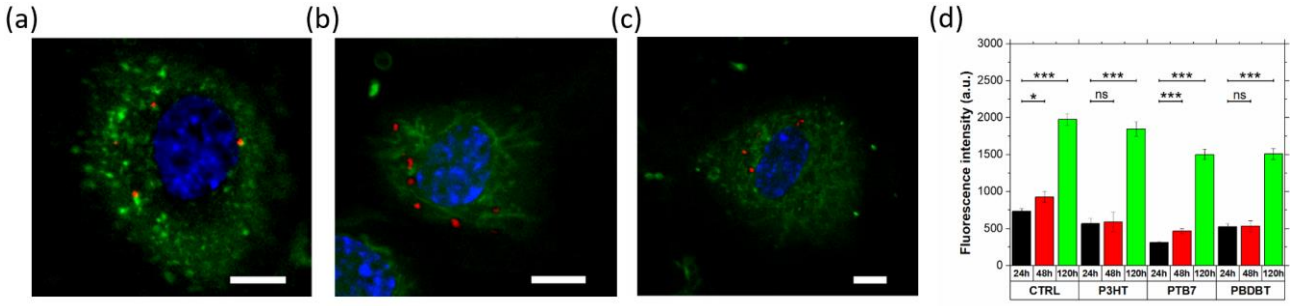


***Figure 7.*** *Representative confocal images depicting HUVEC cells loaded with P3HT (a), PBDB-T (b) and PTB7 (c) NPs acquired at a z plane correspondent to the cell inner part. Cells are stained with Cell mask green (membrane, green) and Hoechst 33342 (nuclei, blue), NPs fluorescence emission is in red. Scale bars, 5 µm. Viability of HUVECs (d), incubated with the different NPs, evaluated as the fluorescence of the reduced form of the AlamarBlue cell viability reagent. Data were compared using the nonparametric Mann-Whitney U-test (0.05 significance level). *p < 0.05, ***p < 0.001. Error bars represent the standard error of the mean ($\sigma_{mean}$). (performed by Antognazza's group at IIT-CNST)*

Human Umbilical Vein Endothelial Cells (HUVECs) were selected as a valuable model, largely accepted in literature for the study of the main biological pathways involved in endothelium function, including normal and neoplastic proliferation, migration, and angiogenesis, as well as for the development of therapies against cancer and cardiovascular diseases.

The viability and proliferation of HUVECs treated with NPs is assessed by using the AlamarBlue assay at three different time points (**Figure 7d**). By adopting a conservative approach, the concentration is fixed at 20 ug $mL^{-1}$. Data show that the cell metabolic activity is preserved in the presence of all considered NPs, up to 120 hours after plating. Interestingly, one should notice a higher proliferation increase, in percentage, between 24 and 120 hours after plating in the case of HUVECs treated with NPs (+226% for P3HT, +187% for PBDB-T and +384% for PTB7) in comparison to the untreated ones (CTRL, +169%).

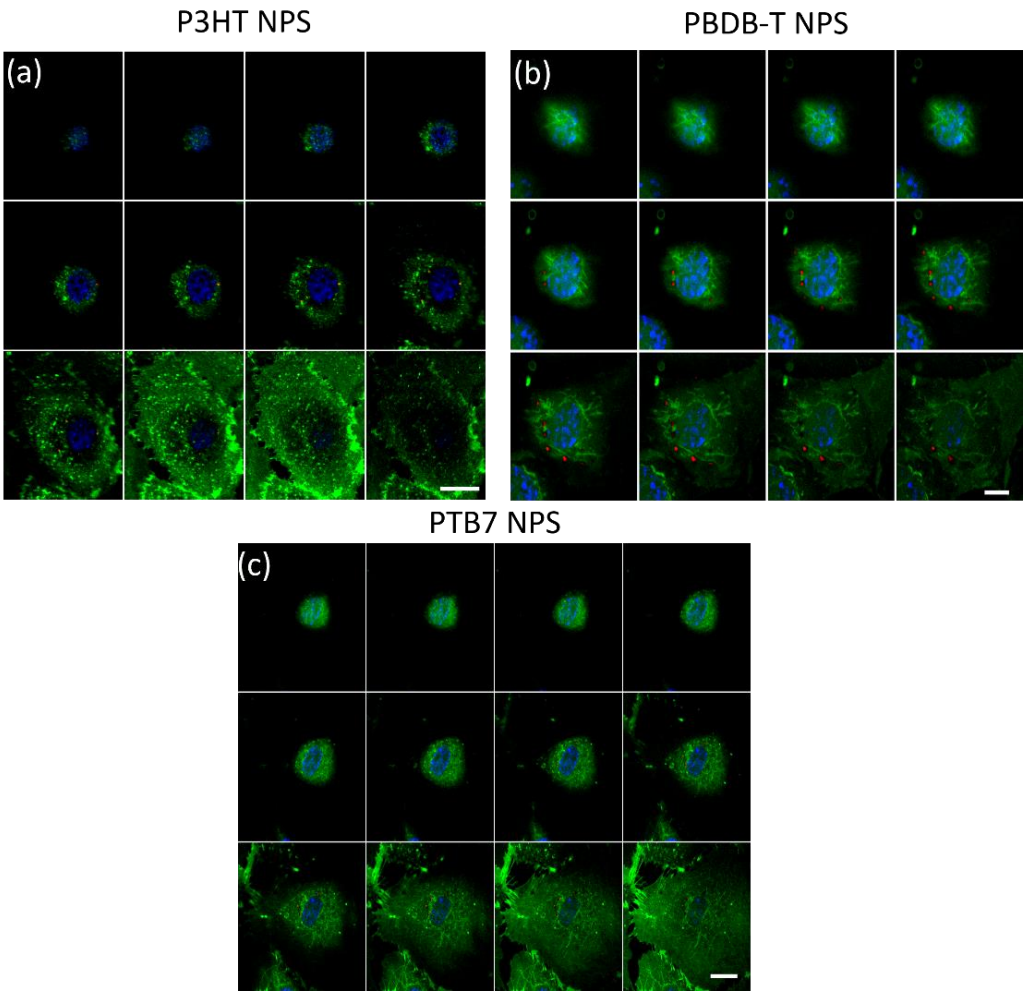


***Figure 8.*** *Confocal optical sections depicting HUVEC cells treated with P3HT, PBDB-T and PTB7 NPs. Cells are stained with Cell mask green (membrane, green) and Hoechst 33342 (nuclei, blue), NPs emission is depicted in red. Focal planes are acquired from the top interface with the extracellular bath (upper left) to the bottom of the cells (lower right). Scale bars are 5 µm as a refence. (performed by Antognazza's group at IIT-CNST)*

Moreover, our partners at IIT-CNST investigated the capability of NPs to internalize within the intracellular environment, by means of confocal microscopy (**Figure 7a-c**). The most critical parameters governing the capability of NPs to cross the plasma membrane and to internalize within the cell cytosol are the shape, the size, and the z-potential. TEM, DLS and z-potential measurements (**Figure 2, Table 1**) demonstrated that there are no appreciable differences among the three considered NPs. Based on these data, no sizable difference in internalization process is expected.

### 3.6.3 Conclusions

In this work we present a comprehensive characterization of p-type semiconducting polymeric NPs as nanophototransducers for future in-vivo reactive oxygen species (ROS) production. ROS generation impacts on cellular messaging pathways and hence organic semiconductive NPs enable a new transduction method to impact on cellular phenotype with optical, wireless control. We report the study on flash nanoprecipitated NPs made of the three photoactive polymers P3HT, PBDB-T and PTB7. Studies were performed to explore the influence on the energetics of the NPs and the stability of the colloid when different aqueous antisolvent ionic strength is employed. Moreover, different polymer-to-surfactant mass ratios were screened. Our study aims to characterize the nanoparticles' morphology, energetics, stability and photogeneration capability.

We find that all three tested materials exhibit photocathodic current generation due to reduction of acceptor molecules in water and charge positively when illuminated. All NPs fall within the dimensional limits for cell internalization and with confocal imaging it was verified for HUVECs used for in-vitro experiments.

Nanoparticles flash nanoprecipitated in PBS show a larger radius than the same material ones precipitated in MilliQ thanks to a kinetic and structural effect of NaCl on the NPs formation process. In the presence of Pluronic F127 as a surfactant, the nanoparticles' radii evaluated from AFM and TEM differs significantly from the one measured through DLS, thus suggesting that the mobility and the perceived environment viscosity are considerably influenced. On the other hand, its presence enhances the stability and does not affect the internalization capabilities while lowering the z-potential. This is likely due to a distancing of the slipping plane from the polymer surface accommodating more counter-ions within the hydrodynamic radius.

We found significative differences in the absorption spectra of the NPs precipitated in MilliQ water and those precipitated in PBS which are not reflected in an appreciable change in excitation and emission spectra, whereas no new peaks appear. This suggests that the first are either due to a change in reflectivity or in the different contribution of non-radiative states. A new experiment was developed to study the photovoltage build-up of the NPs when dispersed in an aqueous medium. After proving the efficacy of the method with a single wavelength, the same experiment was repeated by scanning the light source through the visible spectrum to evaluate the relation between photoelectrochemical

capabilities and incident wavelength. By comparing the spectra obtained with this method using NPs without surfactant with the relative absorption spectra we highlight the perfect superimposability of the peaks and a good superimposability of the remainder. We conclude that absorbed photons contribute equally to the photocurrent generation, independent on their energy.

Finally, it has been demonstrated that all three polymer photoelectrodes are internalized inside the cell membrane but remain outside the nucleus. In addition, all the materials are biocompatible and induce HUVEC cells proliferation in in-vitro experiments. Interestingly, PTB7 outperformed the other polymers in different examined aspects. Its excitation spectrum extends in the optical transparency window of biological tissue, its z-potential is overall the more negative and the average NPs size is the smallest. To conclude, our results provide comprehensive physicochemical characterization of two new material alternative to P3HT for phototransducting nanoparticles, namely PBDB-T and PTB7, both nanoprecipitated in a low and in a high ionic strength aqueous medium and explore the use of Pluronic F127 as an antiaggregant and its effects on the performances of these NPs.

## 3.6.4 Methods

### Materials

Regioregular P3HT (Sigma-Aldrich) with a molecular weight ($M_w$) of 115-135 kDa was purchased from Sigma-Aldrich. PTB7 was purchased from Ossila, batch M216, $M_w$=78 kDa. PBDB-T was purchased from Ossila, batch M1002, $M_w$=70 kDa, and from Sigma-Aldrich, batch 901099, $M_w$=70 kDa. Pluronic F127 was purchased from Sigma-Aldrich (powder, BioReagent). Phosphate Buffered Saline (PBS) and Resazurine (AlamarBlue assay) were purchased from Sigma-Aldrich.

### Flash Nanoprecipitation

The nanoparticles of conjugated polymers were prepared by flash nanoprecipitation, summarized in Figure 1. Firstly, the conjugated polymer and, if needed, Pluronic F127 are dissolved together in tetrahydrofuran (THF) at a concentration of 1 mg·mL$^{-1}$. We initially considered four mass relative composition between Pluronic and the conjugated polymer (0:1 i.e. no Pluronic, 1:50, 1:18 or 1:9). The solutions are kept stirring at 60°C until completely dissolved (approximately 1 hour). Then, 1 mL of the organic solution is injected into 10 mL of MilliQ water or PBS solution (1x) under intense

stirring (>1200 rpm). Since the nanoprecipitation is almost immediately achieved, after 10 seconds the dispersion is placed into a beaker and kept stirring at 40°C until complete evaporation of the THF. Finally, the dispersion is centrifuged at 500 rpm for 5 minutes to separate the remaining fraction of aggregates. For samples prepared using PBS, dialysis procedure was carried out by using Visking membranes (Visking DTV by Medicell Int Ltd. Cut-off range 12-14 $kg \cdot mol^{-1}$ with diameters of 25.5 mm) to lower the ionic strength of the medium and enhance the stability of the colloid. The dialysis tubing was kept in stirring ultrapure MilliQ water at room temperature for three days, changing the water periodically. The dispersion is finally stored at 4°C in dark conditions to avoid aggregation.

In the case of use for in-vitro experiment, the dispersions are lyophilized using a freeze-dryer (Telstar ®) at -83ºC and a pressure of 0.2 mbar during 48 hours for two reasons: to minimize the presence of pathogenic agents and to re-disperse the nanoparticles at a proper concentration of polymer mass in water. Then, the NPs are dispersed in Endothelial cell medium, enriched with 100 mg $ml^{-1}$ penicillin and 100 mg $ml^{-1}$ streptomycin, at a concentration of 40μg $mL^{-1}$ in sterile conditions. This dispersion is finally diluted in the cell culture wells employed for the experiments at the chosen final concentration.

## AFM and KPFM

Scanning Probe Microscopies were carried out using a Park Instruments NX10 system using NSC36 Cr-Au coated probes (MikroMasch). For KPFM we use amplitude modulation mode at 17 kHz. In order to carry out measurements in illuminated conditions a custom sample holder was built. The illumination was provided by a monochromatic LEDs (Wurth Elektronik) placed beneath the glass surface, driven by a source-measure unit (Keysight B2912A).

## TEM

TEM measurements were performed on a TECNAI G2 20 TWIN operated at 200 kV and equipped with LaB6 filament. Samples were prepared by casting a droplet of the dispersion onto a TEM cooper grid (300 Mesh) covered by a pure carbon film and dried at ambient temperature. The grid was glow discharged before putting the drop of suspension.

## DLS and z-Potential

DLS and z-potential measurements were performed with a Malvern Zetasizer Nano-ZS 90 (Malvern, UK) equipped with a He-Ne laser (($\lambda$ = 633 nm) under scattering angle of 173°. Samples were prepared by pouring the dispersion into disposable folded cuvettes in the case of DLS and into DTS1070 cells in the case of z-potential measurements.

## Spectrofluorimetry

Absorption, Excitation and Emission spectra were measured on a Lambda 950 UV/Vis/NIR spectrometer (Perkin Elmer) using 4ml disposable plastic cuvettes. The scanning speed was adjusted case by case in order to obtain a clean signal. When measuring the absorption spectra, solution have been diluted at needs in order to keep the absorbance lower than the value of 1.5A to get a linear response over the whole spectral band.

## Photoelectrochemical Cell

We introduce a novel simple setup built to measure the current generated by the discharge of photocharged NPs over a fixed area. The main structure is composed of a metallic faraday cage with a central hole on two opposite sides to let the light pass though. In the path of light is placed a structure composed of a PDMS cell filled with the NPs dispersion with a 2.8cm$^2$ ITO working electrode (WE) on one side, a glass slide on the other side, and an AgCl covered Ag wire as Reference/Counter electrode (RE/CE) to close the circuit. The cell allows the exposition to the illumination from either the ITO side or the solution side, the latter through a glass window. In spectroscopic measurements the monochromatic illumination of the photoelectrode at a defined wavelength was achieved with a Xenon lamp combined with a monochromator (Cornerstone 260). The amplified current signal was filtered and digitized with a lock-in amplifier (Zurich Instruments). For transient measurements the monochromated Xenon lamp light was replaced with monochromatic LEDs (Thorlabs M530L4) driven by a source-measure unit (Thorlabs DC2200).

## Cell culture of Human Umbilical Vein Endothelial cells (HUVECs)

HUVECs cell lines were purchased from PromoCell. The cells were grown on culture flasks coated with 0.2% gelatin in Endothelial cell medium (Endothelial cell basal medium 2, PromoCell), enriched

with Endothelial cell GM 2 supplement pack (PromoCell), and maintained at 37°C, 5% $CO_2$. For the experiments, only HUVECs at passage < 7 were employed.

For all experiments, HUVECs were plated on glass slides at $7\times10^3$ cells/cm$^2$ density and after 3h from plating the cells were incubated with the different NPs at 20μg mL$^{-1}$ concentration for 20h. The NPs-treated samples were rinsed with KRH to remove non-internalized NPs at the beginning of each measurement. HUVECs plated on glass slides without NPs were used as control condition (CTRL).

## AlamarBlue viability assay

HUVECs were plated in 12 wells plates by employing cell growth medium without phenol red. Cell proliferation was evaluated 24, 48, and 120 h after incubation. Prior to measurements at each time point, the growing medium was replaced with fresh medium containing 100 mg mL$^{-1}$ of AlamarBlue (Thermo-Fisher). The AlamarBlue reagent is based on the Resazurin, a cell-permeable non-fluorescent compound that upon entering living cells is reduced to the highly fluorescent Resorufin. The fluorescence of the latter is thus an indicator of the viability and proliferation of cells. The samples were incubated for 3h at 37 °C, 5% $CO_2$, in the dark. Then, three aliquots of culture media (100μL) were placed in black 96-well microplates and their fluorescence was acquired using a TECAN Spark microplate reader (excitation wavelength: 530 nm, emission acquired at 590 nm).

## Confocal imaging

Cell membrane and nuclei are stained, respectively, by Cell Mask Green (Thermo-Fisher, exc/em wavelength, 522/535 nm) and HOECHST (Thermo Fisher, exc/em, 350/461 nm). Z-stacks were acquired with an upright microscope (Olympus BX63), equipped with a 60X water immersion objective, a spinning disk confocal module (X-Light V2 spinning disk module from Crest Optics), and a sCMOS Camera (Prime BSI, Teledyne Photometrics; Tucson, Arizona, USA). The system, comprising LED and laser light sources (Spectra III and Celesta, from Lumencor) was assembled by Crisel Instruments. Excitation/emission wavelengths were 530/660 nm for P3HT NPs and 660/750 nm for PTB7 and PBDB-T NPs. The experiments were carried out at room temperature and by employing a Krebs Ringer's (KRH) extracellular solution (mM): 135 NaCl, 5.4 KCl, 1.8 $CaCl_2$, 1 $MgCl_2$, 5 HEPES, 10 Glucose, pH adjusted to 7.4 with NaOH. Images were processed with ImageJ.

## 3.7 Porous rra-P3HT Thin-film Photoelectrochemical Response Characterization

### 3.7.1 Introduction

Recently it has been demonstrated that even a single layer of p-type polymer such as P3HT can build-up photovoltage due to photoelectrochemical reactions.[48,160] A relevant pathway to stimulate cells relies on semiconductor photo-electrochemistry. Here excited charge carriers transfer through the semiconductor/water interface and cause oxidation or reduction reactions in the biological system. Such photofaradaic processes have to be tuned to generate electrochemical messenger molecules that impact on cellular processes.[43] We note that an organic semiconductor device in direct contact with the aqueous electrolyte can follow both stimulation mechanisms, photocapacitive as well as photofaradic.[47] Which one of the two prevails depends on the semiconductor energy levels and their alignment with redox species as well as kinetic barriers for electron transfer. Both processes start under illumination by the generation of localized excitons and their subsequent dissociation into free carriers occurring at interfacial electric fields or spontaneously.[48]

In the case of p-type polymers such as P3HT or PEDOT the typical acceptor molecule taking free electrons is oxygen as it is always present in biological conditions.[49,142,160,163] The oxygen reduction reaction (ORR) generates $H_2O_2$ on organic semiconductor surfaces and other intermediate ROS species.[49,164] Importantly, the ORR products are known to act as messenger substances with impact on cell homeostasis, cell metabolism and regenerative processes. The photofaradaic generation of ROS species has been employed through the use of organic semiconductor thin films as well as injectable nanoparticles and was demonstrated to be effective in stimulating cardiac cell regeneration.[30,57–60,165] The detailed mechanism of the photofaradaic transduction chain depends on the physico-chemical interactions occurring at the interface with the cellular medium[43,47] and between the ROS and the particular cell line[166]. Steady state physiological flux of $H_2O_2$ to specific protein targets leads to reversible oxidation, altering protein activity, localization and interactions.[167] This contributes to adaptation of various processes in cells and organs, including cell proliferation, differentiation, migration and angiogenesis[168–170]. Overall, physiological targets of ROS serve as redox switches in signal transduction acting in response to stressors or external perturbations[167].

Most of the studies were conducted on single-polymer photoelectrodes and relied on the use of regioregular poly-3-Hexylthiophene (rr-P3HT), a semicrystalline polymer with a low glass transition temperature ($T_g \approx T_{amb}$) and a noticeable chain mobility[171]. This material has recently been under the spotlight as an effective photocathode for triggering cell differentiation pathways through the production of Reactive Oxygen Species (ROS).[50,51]

The aim of the study is to develop a new generation of porous thin films for biological applications to enhance the surface area exposed to the electrolyte. This will result in a higher interfacial capacitance, more acceptor molecules in contact with the semiconductor and a higher contact area for the cells to adhere with, favoring their photo-stimulation for the next in vitro and in vivo studies.

For such purpose, the large band-gap regiorandom poly-3-hexyltiophene rra-P3HT was selected as conjugated polymer and polylactic acid (PLA) as a hydrolysable polyester approved by the Food and Drug Administration (FDA). In a first step, graft copolymers of P3HT and PLA, P3HT-g-PLA, were synthesized by chemical oxidative polymerization of 3-hexyltiophene and α-EDOT-PLA macromonomer. Several graft copolymers with different PLA percentages were synthesized by modulating the ratio between both monomers in the polymerization reaction. Then, non-porous thin films were fabricated by spin coating of those P3HT-g-PLA copolymers over ITO-glass substrates. Subsequently, porous thin films were obtained by the hydrolysis of PLA in presence of a sodium hydroxide (NaOH) solution. Thin films with different pore sizes were obtained depending on the PLA proportion on the graft copolymers, P3HT-g-PLA.

We performed photocurrent studies to identify the materials with the highest PEC efficiency, leading to non-toxic production of Reactive Oxygen Species (ROS), in a biological-like environment. Based on in depth characterization of the optical, microscopy, electrical and electrochemical properties of the above-mentioned materials in form of thin films exposed to an electrolyte, we investigated the phototransduction performances in light-activated redox processes occurring at the polymer surface. This same surface will be the one in close proximity to the living cell membrane in in-vitro experiments and in-vivo conditions. Cell viability was then evaluated in HUVECs both in dark an in illuminated conditions, and the efficacy in ROS production was considered for both porous and non-porous materials. Taking into account that the photo-electrochemical processes highly influence the angiogenesis activity in endothelial cells and modulate the intracellular Ca2+ concentration in cardiac and endothelial cell models[6,7,9,10,51], the ability of those porous P3HT-based films to generate Reactive

Oxygen Species (ROS) upon illumination in extracellular-like conditions will be evaluated and primarily considered as a key parameter to guide the selection of the most promising pore size film.

### 3.7.2 Results

This study deals with the optimization of thin films devices for the enhancement of the phototransduction processes occurring at the interface between the light sensitive organic semiconductor and the living cell. These processes may be categorized in three types, i.e., photothermal (PT), photoelectrical (PE) and photoelectrochemical (PEC) transduction. We demonstrated that the PEC processes represent the most effective mechanism to modulate the activity of endothelial and cardiac cells, cellular models of interest in our studies. In particular, we found that PEC reactions highly influence the angiogenesis activity in endothelial cells and modulate the intracellular $Ca^{2+}$ concentration in cardiac and endothelial cell models. In light of this, we developed porous thin films, in order to enhance the surface area in contact with cells and hence the efficacy of PEC processes induced by photo-stimulation. The material synthesis for this new generation of devices, based on graft copolymers of regiorandom poly-3-hexyltiophene (rra-P3HT) and polylactic acid (PLA), P3HT-g-PLA**,** is discussed in the Methods section.

Firstly, non-porous thin films were prepared by spin coating of the previously synthesized graft copolymers P3HT-*g*-PLA, dissolved in chlorobenzene, over ITO-glass substrates. As control, EDOT-PLA macromonomer and P3HT homopolymer, dissolved in chlorobenzene, were also deposited on ITO-glass substrates. The surface morphology of these films was analyzed by Atomic Force Microscopy (AFM) (**Figure 1a**).

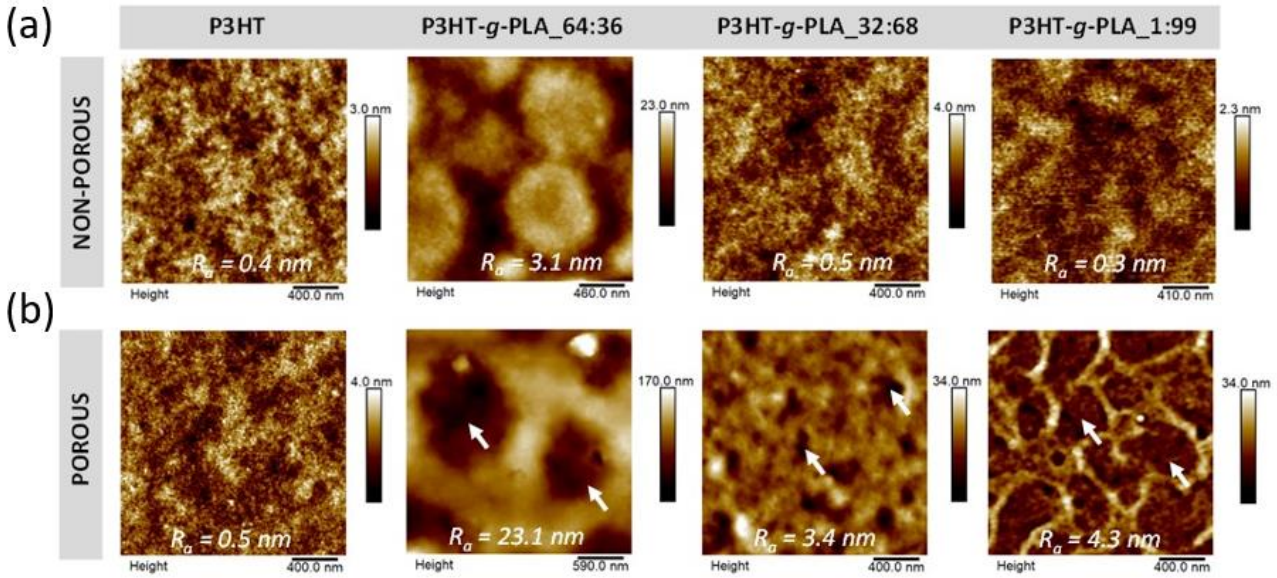


***Figure 1.*** *AFM images of: (a) non-porous films prepared by spin coating of a chlorobenzene solution of EDOT-PLA macromonomer, P3HT homopolymer, and graft copolymers P3HT-g-PLA, and (b) porous films obtained after PLA hydrolysis in contact with NaOH. Arrows show the pores formed.*

The P3HT films shows a homogenous morphology with a low average surface roughness ($R_a$) of 0.4 nm. Similar morphologies are observed in the case of graft copolymers P3HT-*g*-PLA_32:68 and P3HT-*g*-PLA_1:99. The graft copolymer with the lowest PLA percentage, P3HT-*g*-PLA_64:36, exhibits a different morphology with the formation of spherulites probably due to the different packaging of the P3HT chains during the film formation. In a second step porous thin films were obtained by hydrolysis of PLA in presence of a NaOH solution (**Figure 1b**). In that case, EDOT-PLA film is totally degraded, and the characteristic morphology of ITO is observed, whereas in the case of P3HT films the morphology remains unaltered showing the same $R_a$, as expected because P3HT is not degraded in presence of NaOH. Thus, in the case of P3HT-*g*-PLA films a different morphology is detected in comparison with the homologous P3HT-*g*-PLA films shown in Figure 3A. The surface roughness is increases and pores with different sizes are observed as consequence of the hydrolysis of PLA present in those films. The thickness of these films was also measured by AFM through the scratching of the films.

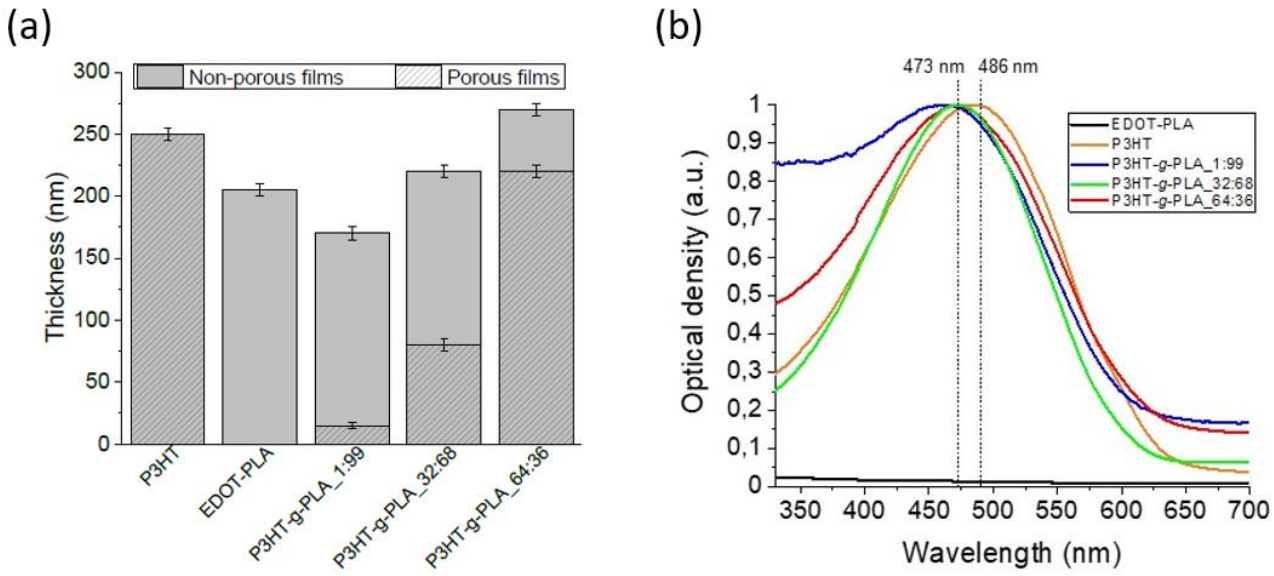


***Figure 2.*** *(a) Thickness of the films before and after hydrolysis determined by AFM. (b) comparison between the normalized UV-vis absorption spectra of pure P3HT thin-film, the three compositions of porous P3HT-g-PLA and EDOT-PLA only. A small blue shift (13nm) can be appreciated from P3HT to porous P3HT.*

The non-porous films show a thickness between 170 and 210 nm (**Figure 2a**). After PLA hydrolysis, as expected P3HT films thickness does not decrease in the case of P3HT films, whereas PLA films are totally degraded. Regarding P3HT-*g*-PLA films, there is a direct proportionality between the thickness and the PLA content of the graft copolymers (**Figure 2a**).

The optical absorption of the films was determined by UV-vis spectrophotometry (**Figure 2b**). P3HT spectrum shows a single absorption peak at 486 nm due to the π-π* electronic transition of P3HT chains in a flexible random-coil conformation. In the case of films prepared with the graft copolymers, P3HT-*g*-PLA, the absorption maxima are slightly blue-shifted towards 473 nm, which is indicative of a less strong aggregation between polymeric backbones, probably due to increased torsional twisting. The optical absorption region shown is in the same range than the rr-P3HT, therefore the films reported here can be excited using the 530 nm LED source used for previous thin films.

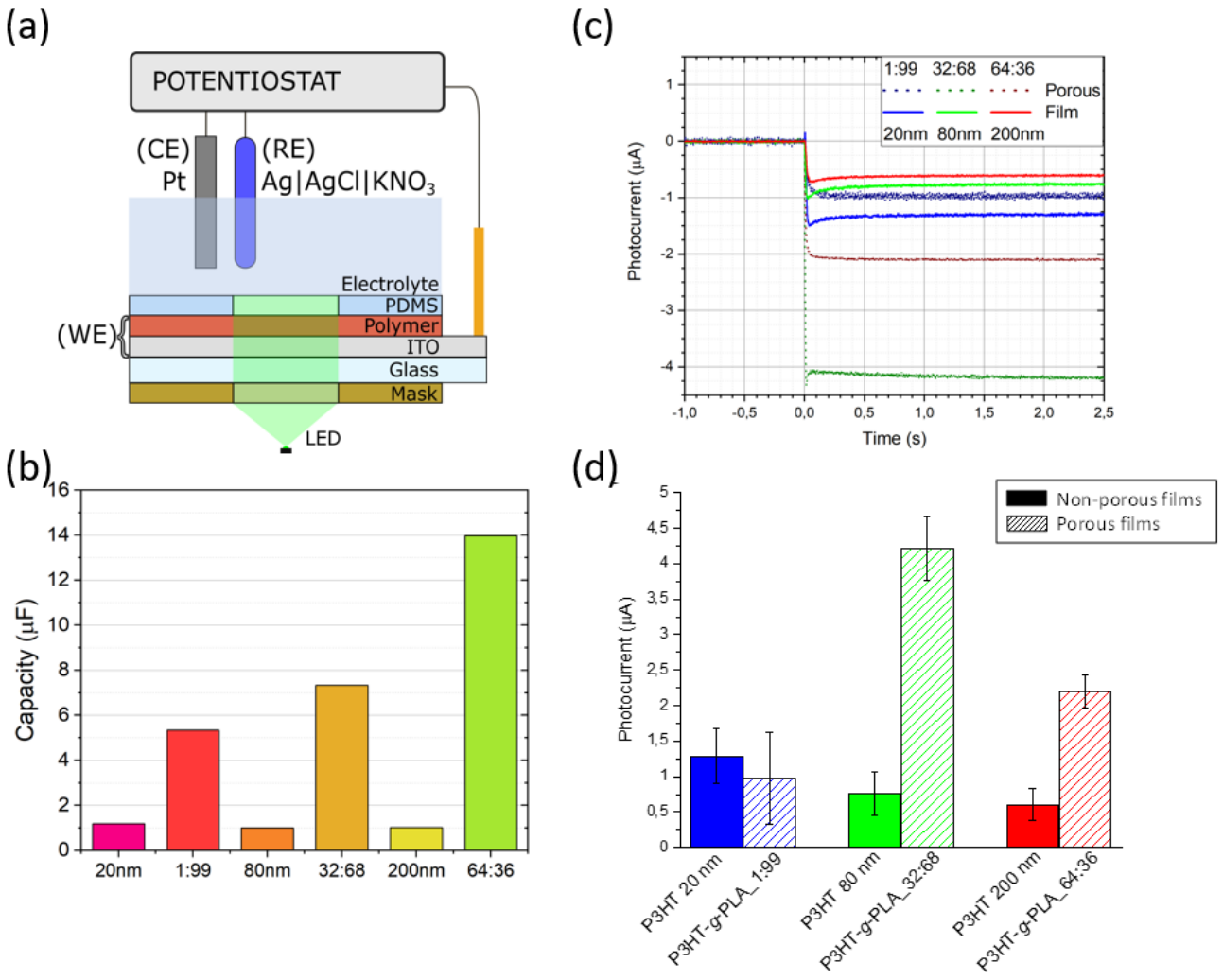


***Figure 3.*** *(a) Scheme of the photoelectrochemical cell. (b) Capacity at the P3HT-PBS interface extracted from the electrochemical circle fit of the electrochemical impedance spectra. Increasing the thickness of thin film does not affect the capacity value in nonporous thin-films while it increases it in porous materials. (c) Photocurrent curves of non-porous P3HT films with different thickness and porous films made of P3HT-g-PLA_1:99 (blue dots), P3HT-g-PLA_32:68 (green dots), and P3HT-g-PLA_64:36 (red dots) when irradiated with a LED at 110 mW and 530 nm. (d) Photocurrent values after 1-second laser irradiation: full bars refer to non-porous and striped bars to porous thin-films.*

The Photoelectrochemical Cell (PEC) setup used to perform the measurements is introduced in **Figure 3a**. The active area of the photoelectrode in contact with electrolyte (PBS – 137mM NaCl, 3mM KCl, 10mM Phosphate buffer, pH 7.4) is confined by a PDMS O-ring and the same area is

illuminated from the electrolyte side. The photoelectrode is connected as the working electrode to a potentiostat and a Pt-wire and an Ag|AgCl|KCl (3M) electrode are used as counter and reference electrode, respectively. **Figure 3b** shows photocurrent transients obtained with both porous and non-porous P3HT photoelectrodes by irradiating the films with a 530nm 110mWcm$^{-2}$ LED. Upon illumination a cathodic current is observed that starts with a peak and then settles within a few tenth of a second to a relatively constant level.

To compare the data with the non-porous reference material (pure P3HT), variation in layer thickness have to be considered. We observe that the copolymers with higher PLA content result in thinner layers after hydrolysis. Accordingly, we prepared reference photoelectrodes with pure P3HT of comparable thickness (20 nm, 80 nm, and 200nm). The photocurrent of pure P3HT films decreases from 1.3 µA to 0.6 µA as the film thickness increases from 80 nm to 200 nm (**Figure 3d**).

Interestingly, in the case of porous films, fabricated starting from copolymers with 36 and 68 % of PLA (P3HT-*g*-PLA_64:36 and P3HT-*g*-PLA_32:68) an enhancement of the photocurrent intensity of about 2 and 4 times is achieved, respectively, as compared to the values obtained using non-porous P3HT films of the same thickness (**Figure 3d**). This achievement could be attributed to the higher surface area exposed to the electrolyte. On the other hand, the low performance associated to the devices obtained using the higher percentage of PLA (99%, P3HT-g-PLA_1:99) may be due to the limited quantity of P3HT semiconductor present in the structure after PLA hydrolysis. In this case the pores are so wide that just a little fraction of P3HT forms the film whereas the remaining area of the photoelectrode is composed by ITO in direct contact with water. As a consequence, also the quantity of absorbed light is very small compared to the other sample, and the amount of photogenerated excitons and free charges available for photoreduction is smaller.

To get insight on the capacitive behavior of the photoelectrode, under the same illumination conditions as in the photocurrent experiment, we perform electrochemical impedance spectroscopy. From the electrochemical circle fit of the Bode diagram of the impedances we can extract the capacity associated to the low-frequency side of the spectrum. From previous works, we can confidently assign it to the capacitance of the interface between the semiconductor and the electrolyte.

**Figure 3b** shows the comparison between the capacities of all the P3HT thin-films at the open circuit potential. Predictably, since all the non-porous thin film have the same surface area in contact with water, the capacity is the same within the range of experimental uncertainties. On the other hand, the

capacity in porous thin-films grows with growing thickness suggesting a higher total surface area. The non-coincidence between the highest surface electrode and the highest performing electrode can be attributed to the fact that despite the higher contact with the electrolyte, the contribution of the light excitation decays with penetration giving an overall lower photocurrent.

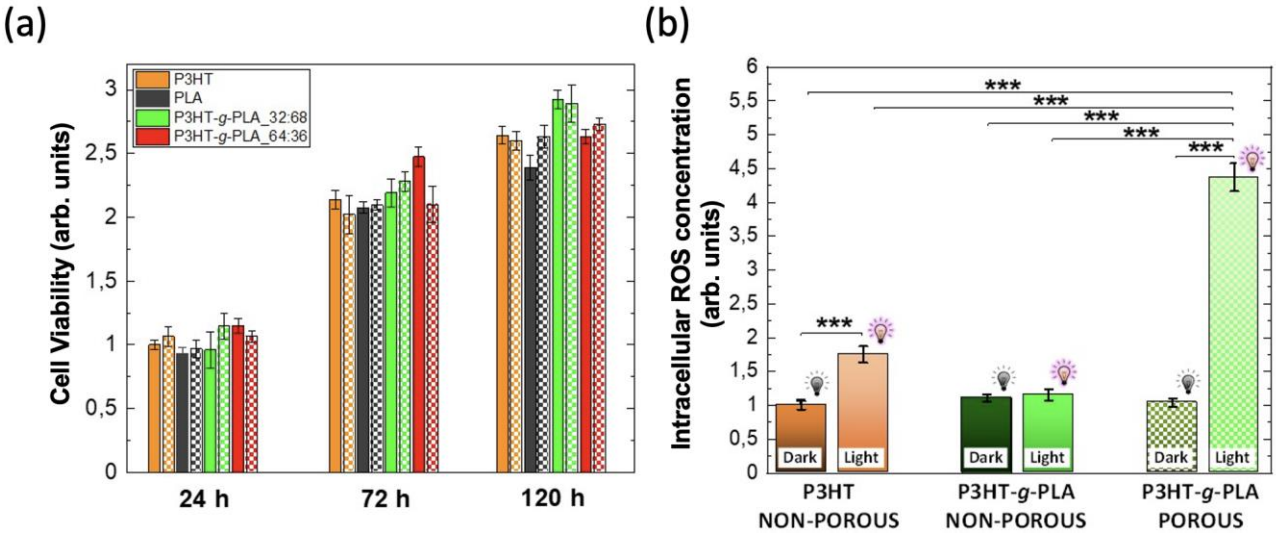


**Figure 4.** *Viability of HUVECs (a), incubated with the different samples, evaluated as the fluorescence of the reduced form of the AlamarBlue cell viability reagent. Error bars represent the standard error of the mean ($\sigma_{mean}$). (b) Mean DCF fluorescence, representative of ROS intracellular presence, within HUVECs plated on pristine P3HT, P3HT-g-PLA block copolymer, and porous P3HT substrates, in light and dark conditions. Data were compared using the nonparametric Mann-Whitney U-test (0.05 significance level). *p < 0.05, ***p < 0.001. (performed by Antognazza's group at IIT-CNST)*

In the final part of our work, we test the impact of these materials on the cell viability of Human Umbilical Vein Endothelial Cells (HUVEC) cultured on photoelectrode surfaces. We investigated them both in full dark conditions and while subjecting them to an illumination protocol. Since very low photoelectrochemical activity was registered in P3HT-g-PLA 1:99, it was not interesting for further studied and it was not evaluated on in-vitro conditions. To optimize cell-culture experiments, all samples were sterilized with a 2h long thermal treatment at 120°C and a layer of Fibronectin was deposited on the surface to promote cell adhesion. Photoelectrodes were illuminated at a power

density of 110mW/cm$^2$ for 3 minutes with a 530nm LED after 3h cell incubation. With this illumination protocol we quantified cell viability with the AlamarBlue assay at 24, 72 and 168h from the cell deposition in both the illuminated polymer and controls samples. The AlamarBlue fluorescence signal is an indicator of the metabolic activity inside the cells. In **Figure 4a** a clear increase of the fluorescence with time can be observed for all the samples regardless from the presence or absence of the polymer and of the illumination. This means that despite the presence of the polymer photoelectrodes and their generation of ROS, the electrodes are biocompatible and ROS concentrations remain within a non-toxic range and do not affect cellular proliferation.

Next, the ROS production was determined with fluorescent microscopy using the $H_2$-DCF-DA assay[199]. As control samples we tested in parallel P3HT samples and the highest photocurrent performing P3HT-g-PLA 32:68 copolymers both hydrolyzed and non-hydrolyzed, both kept all the time in darkness and illuminated with the same protocol as in viability assays. **Figure 4b** shows the results from fluorescence microscopy performed after the illumination protocol. Average fluorescence values were determined on cell bodies. The diagrams report the averaged fluorescence values normalized by the value measured on the non-porous P3HT control kept in darkness. Comparison of the photoelectrodes with the different control samples clearly demonstrates ROS generation inside cell bodies triggered by the illumination in P3HT and porous P3HT, while non-significative intracellular ROS production was measured in the block copolymer sample. Quantitative comparison indicates that the increase in intracellular ROS concentration can be found in the porous samples. The improved efficiency of porous polymers in oxygen reduction at OCP is thus directly translated to the in-vitro experiment. Is worth of mention that the illumination experiment is performed with floating photoelectrodes, hence the electronic potential is not under control in the experiment, and this could impact on conversion efficiency.

## 3.7.3 Conclusions

In this work, we have reported the synthesis of a new generation of semiconducting polymer materials with enhanced photoelectrochemical properties to be employed in the context of ROS production for cell stimulation. Three different graft copolymers made of rra-P3HT and PLA, P3HT-*g*-PLA_1:99, P3HT-*g*-PLA_32:68, and P3HT-*g*-PLA_64:36, have been synthesized by chemical oxidative

polymerization, tuning the ratio between 3HT monomer and EDOT-PLA macromonomer in the feed. Then, the graft copolymers were employed for the fabrication of porous thin films by a two-steps process. In the first step, thin films were obtained by spin coating over ITO-glass substrates. Then, the porosity was induced by PLA hydrolysis in presence of NaOH leading to porous thin films as confirmed by AFM. The films fabricated with the graft copolymers, P3HT-*g*-PLA, exhibited similar optical absorption spectra but enhanced absorption coefficients as compared to rr-P3HT films. In addition, porous materials showed an increased capacitance as compared to non-porous thin-films, thanks to the higher surface area exposed to the electrolyte. This could be exploited for the optimization of illumination patterns when using floating devices. Porous P3HT also showed a fourfold increase in photocurrent, which likewise results from the increased surface area. These results, when translated to in vivo devices, allow for the need of a lower illumination intensity which can be beneficial for the overall device architecture and will lower the invasiveness. The effect is expected to improve the performances in optical modulation of intracellular ROS and hence provides a promising improvement in device architecture for in vitro and in vivo models. Finally, we demonstrated that the devices do not negatively alter the cell viability and neither it does their exposition to a strong light source, even though this last occurrence induce a higher intracellular ROS production when compared to flat rr-P3HT thin films.

## 3.7.4 Methods

### Synthesis of the P3HT-g-PLA copolymer

In a first step, the α-EDOT-PLA macromonomer was synthesized by ring-opening polymerization (ROP) using 3,4-ethylenedioxythiophene(EDOT)-methanol (EDOT-methanol) as chain initiator of L-lactide polymerization (**Figure 5a**). The ROP was carried out in bulk using an organocatalyst formed by a mixture of methanesulfonic acid (MSA) and 4-dimethylaminopyridine (DMAP) in a ratio 1:1.29, and a 90% conversion was reached after 2 hours reaction at 130°C. Then, P3HT-*g*-PLA copolymers were synthesized by chemical oxidative copolymerization of 3-hexylthiophene and the previously synthesized α-EDOT-PLA macromonomer using $FeCl_3$ as oxidant agent (**Figure 5b**).

P3HT-*g*-PLA copolymers with different PLA percentages, 11%, 36%, 68%, and 99%, were synthesized by varying the 3HT:PLA ratio in the reaction feed and named as P3HT-*g*-PLA_89:11,

P3HT-*g*-PLA_64:36, P3HT-*g*-PLA_32:68, and P3HT-*g*-PLA_1:99 respectively. Yields higher than 45% were obtained in all cases.

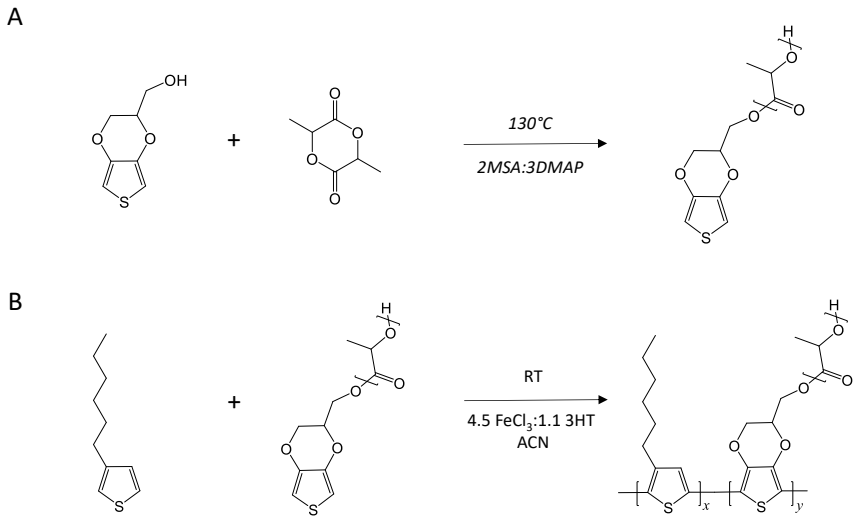


***Figure 5.*** *Chemical routes employed to synthesize: (A) EDOT-PLA macromonomer by ROP and (B) P3HT-g-PLA copolymers by chemical oxidative polymerization.*

## Thin-film preparation and hydrolysis

These P3HT-*g*-PLA copolymers were used to manufacture porous thin films in a two-steps process (**Figure 6**): (*i*) preparation of non-porous films by spin coating different solutions of P3HT, EDOT-PLA, P3HT-*g*-PLA_1:99, P3HT-*g*-PLA_32:68, and P3HT-*g*-PLA_64:36 in chlorobenzene over ITO-glass substrates; (*ii*) hydrolysis of PLA by immersing the films in NaOH 1M for 4 hours.

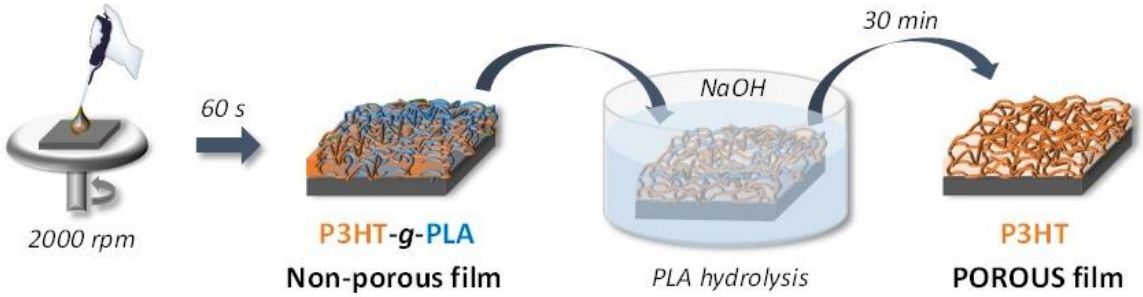


***Figure 6.*** *Schematic representation of the two-steps process followed to obtain porous thin films by spin-coating of the copolymers P3HT-g-PLA dissolved in chlorobenzene, and subsequent PLA hydrolysis in contact with NaOH.*

## Atomic Force Microscopy (AFM)

Atomic Force Microscopy (AFM) studies were performed on a Nanoscope IV of Digital Instrument. Experiments were operated under non-contact topology mode in air at ambient conditions.

## Absorption spectroscopy

Absorption spectra were recorded on a Shimadzu UV-2550 spectrometer equipped with a film adapter, 300-800nm spectral range, resolution 0.5nm, 10nm/s scan speed.

## Photocurrent transients and Electrochemical impedance measurements

The photoelectrode's active surface was exposed to PBS electrolyte. By mounting the photoelectrode in a dedicated cell only the semiconducting layer is exposed to the electrolyte, while the buried ITO surface and the electrical contacts remain separated via a PDMS O-ring. The cell allows the exposition to the illumination from either the ITO side or the solution side, the latter through a quartz window. In a three-electrode setup the photoelectrode was operated as the working electrode. An Ag|AgCl (3M KCl) reference electrode was used in combination with a Pt counter electrode. For transient measurements the monochromatic LEDs (Thorlabs M530L4) was driven by a source-measure unit (Thorlabs DC2200).The amplified current or photovoltage signal was filtered and digitized with a lock-in amplifier (Zurich Instruments) connected to the monitoring output of the potentiostat (Metrohm PGSTAT204). The potentiostat was also used for impedance spectroscopy measurements.

## Cell culture maintenance

HUVECs were purchased from PromoCell and grown in endothelial cell basal medium (PromoCell), supplemented with Endothelial cell GM 2 supplement pack (PromoCell). Cells were kept in T-75 culture flasks coated with 0.2% gelatin and maintained in incubator (37°C, humidified atmosphere, 5% $CO_2$). For the experiments, only HUVECs at passage < 7 were employed. After reaching 80-90% confluence, cells were detached with 0.5% trypsin-0.2% EDTA (Sigma Aldrich) for 5 min and plated for experiments. To promote adhesion, a 1 mg/ml fibronectin layer (from bovine plasma, Sigma Aldrich) in PBS (Sigma Aldrich) was deposited on the surface of the samples and incubated for 30 min. After aspirating fibronectin and PBS, cells were plated and cultured into 12well plates.

## AlamarBlue cell viability assay

HUVECs were seeded on polymer and ITO samples in 12 well plates at about 20000 cells/well density. Cell proliferation was evaluated after 24, 48, 168 h after plating in 2 biological replicates. To this aim, AlamarBlue cell reagent was added at a volume concentration of 1:10 to the cell culture.

In principle, the AlamarBlue molecule, resazurin, is a non-fluorescent molecule that is reduced to a fluorescent compound (resorufin) by the mitochondrial respiratory chain in live cells. In this way, the amount of resorufin produced is directly proportional to the quantity of living cells.

Three aliquots of culture media for each condition were placed in a black 96-well microplate and the fluorescence of the AlamarBlue compound was acquired by a plate reader (TECAN Spark 10M Plate Reader) with an excitation/emission wavelength of 540/600 nm. The procedure was repeated at each time point, rinsing, and replacing the AlamarBlue compound with fresh medium after each measurement.

## ROS determination in HUVEC cells

2',7'-dichlorodihydrofluorescein diacetate ($H_2$DCF-DA, Sigma-Aldrich) was employed for intracellular ROS detection. HUVECs were seeded on polymer and control substrates and treated continuously for 3 min with Thorlabs LEDs (530 nm @110 mW/cm$^2$ for P3HT; 530nm @2mW/cm$^2$ for PDBD-T; 660nm @10mW/cm$^2$ for PTB7). Immediately after the end of the illumination protocol, cell cultures were incubated with 10 μM $H_2$DCF-DA in KRH for 30 min, at 37°C with 5% $CO_2$. After incubation, the fluorescence of the probe was recorded (excitation/emission wavelengths, 490/520nm; integration time 400ms, 100MHz, binning 1) with a 20X objective on an upright microscope (Olympus equipped with a Teledyne Photometrics Camera).

Variation of fluorescence intensity was evaluated over regions of interest covering single-cell areas, and reported values represent the average over multiple cells and different samples.

Image processing was carried out with ImageJ and subsequently analyzed with Origin 2020.

Reported results have been mediated over 3 biological replicates, obtaining a set of at least 1200 cells and 9 samples for each condition.

Data were compared using the Anova test 2-ways, with Bonferroni correction (0.05 significance level). * $p < 0.05$, ** $p < 0.01$, *** $p < 0.001$. Error bars represent the standard error of the mean.

# 4 Conclusions

In this thesis, an extensive characterization of organic photocathodes as bioelectronic phototransducers is presented, with the focus on wireless phototransducers. In the bioelectronic context the primary means of communication are chemical signaling and, in the case of excitable cells, action potentials. Therefore, depending on the application, both the photofaradaic and the photocapacitive mechanism are of interest. The first is referred to the light-induced oxidoreduction of donor or acceptor molecules present in water and could be used to generate chemical species able to trigger a biological pathway in the targeted cells. The second is referred to light-induced displacement currents that through capacitive coupling to excitable cell can depolarize or hyperpolarize them and trigger an action potential. By being able to predict how a material or a device will behave during optical excitation is fundamental for the comprehension and the future development of next generation biocompatible photoelectrochemical transducers. The study was conducted on organic molecular heterojunction thin-film structures as well as on p-type homopolymers, the latter being either in the form of thin-films or of nanoparticles. The aim is to understand which are the energetic, structural, and kinetic factors that affect the response to light, how they can be optimized for the desired purpose, and how they can be combined in a model able to explain and predict the behavior when these materials are used in an electrically floating device.

To achieve this, we started our study by investigating the $H_2$Pc/PTCDI organic heterojunction, which has already been proposed as a retina prothesis. I proposed this system as the starting point for this dissertation because the region of charge generation at the planar p/n junction is clearly separated from the organic semiconductor/water interface, where photoelectrochemical processes occur. Being so, the charge photogeneration problem can be isolated both analytically and experimentally. Throughout this study, electrochemical impedance spectroscopy, KPFM and photocurrent spectroscopy are used to determine basic properties of the heterojunction/electrolyte interface such as photovoltage, capacitive couplings and charge transfer resistance. These findings are combined to develop an equivalent circuit model which agrees quantitatively with the photocurrent transients. Importantly, the model correctly describes the transition from faradaic photocurrents observed at negative photoelectrode potentials towards a capacitive behavior at positive potentials. The model can explain the effect by the resulting energy shift of the semiconductors' states, which makes the

charge transfer of the photoexcited electron to acceptor states in the aqueous electrolyte increasingly unfavorable. Accordingly, the electronic carriers accumulate instead in the conduction band of the n-type semiconductor and interact only electrostatically with the electrolyte generating an ionic displacement current. The value of the model is demonstrated, by using it to simulate the response of p/n-junction photoelectrodes operated in floating conditions, as occurs in artificial retina applications. By starting from a negative potential, the simulation shows that since a cathodic current is developed during illumination, the photoelectrode charge positively and shifts to the photocapacitive regime by itself. The energetic alignment between the semiconductor and the donor and acceptor molecules in the electrolyte drives the photoelectrochemical behavior of the device, and with the developed model we show which parameters and properties needs to be tuned to achieve a specific behavior and optimize the performances.

In the next work I carried out a comprehensive characterization of three p-type semiconducting polymers, namely rr-P3HT, PTB7 and PBDB-T, as thin-film photoelectrode materials. Here I was interested in the factors affecting the photofaradaic yield of reactive oxygen species (ROS) photoproduction in electrically floating conditions for in-vivo applications. I found that the photocathodic current generation is mainly driven by oxygen reduction processes in all the tested materials. For all the materials, absorption and photocurrent spectra are superimposable, suggesting that the photocurrent follows the bulk exciton formation. PTB7 immediately demonstrated very appealing characteristics. First, its maximum optical absorbance and thus photoelectrochemical current generation are centered in the optical transparency window of biological tissue. Under the employed conditions, PTB7 photocurrent and $H_2O_2$ generation yields are more than 5 times larger than those shown by the other materials. GIWAXS investigation suggested a face-on configuration of the π-orbital system of this polymer backbone, while in contrast P3HT and PBDB-T show more edge-on or amorphous configurations, respectively. These last configurations are associated with a longer distance between the conduction band electron density and the electrolyte due to hydrophobic properties of the aliphatic side chains. A longer distance then results in a less efficient electron transfer across this interface, and this impacts significantly in the photofaradaic yield. The spectroscopic experiments combined with KPFM are combined to develop the energy level diagrams for the ITO/SC junction for these materials. Overall, the three materials show comparable energy levels confirming that the observed differences in photoreduction efficiency can be related to proximity effects and kinetic phenomena such as electron transport to acceptor sites, charge generation

mechanisms, and oxygen photoreduction efficiency. The biocompatibility of all these polymers is attested through AlamarBlue assay both in dark and after illumination protocols. Finally, ROS production inside HUVEC cells plated over electrically floating thin-film photoelectrodes is proved to be effective and within a range that is not toxic.

Aiming at single polymer wireless photocathodes, and knowing the influence of the energetic alignment between the device and the surrounding aqueous environment, the next question addressed in this thesis is how the photovoltage evolves in time, given a specific set of material and device properties. To study this question, I measured in p-type organic semiconductor photoelectrodes the transients of photovoltage generation under varying conditions: (i) in the presence/absence of an electrolyte (ii) in the presence/absence of oxygen and (iii) in different p-type organic semiconductors. To do so, I developed a capacitively coupled setup with a sensitivity in the scale of μV and able to operate with bandwidth up to 100kHz, in order to perform photovoltage analysis in absence of water. Interestingly the photovoltage spectra with and without electrolyte are superimposable both, with the photocurrent as well as absorption spectra. This clearly indicates that the main photogeneration processes is the same in all conditions, but differing in intensity. Following the energetic data from the previously reported research, I developed a simple analytical model for the system which is able to explain the large observed photovoltages (exceeding in some case 500mV) in the presence of an electrolyte and oxygen. The model relies on forward and backward electron transfer reactions through the organic semiconductor/electrolyte interface to charge the interfacial capacitor building up photovoltage. The resulting equation fits perfectly the photovoltage transient measurements, thus confirming the validity of the initial assumptions. By combining data from the electrochemical impedance spectroscopy and from photovoltage transients, I was able to identify the double layer capacitance as the location for charge accumulation in electrically floating conditions. Next, I tested photovoltage generation at different light intensities and I observed a linear increase of the initial photovoltage slope with light intensity. This, together with the observation that the recombination current depends on the voltage but does not depend on the illumination intensity, confirms the validity of the proposed mechanism. The model is applied with success in a parallel work to predict the hydrogen peroxide photogeneration from floating photocathodes. We are currently employing these results to develop floating photoelectrodes thin films and suitable organic nanoparticles capable to trigger regenerative biological responses in human hearts.

In the realm of floating photoelectrodes for the in-vivo photogeneration of ROS, nanoparticles are a promising candidate thanks to the lower invasiveness required for their implantation and the higher spatial resolution achievable. Moreover, whereas thin-films can only generate ROS in the extracellular environment, nanoparticles can be internalized thus opening a new scenario by affecting the cellular homeostasis with additional cellular messaging pathways able to impact on the cellular phenotype. Following the LION-HEARTED project, I have focused my attention on flash nanoprecipitated NPs made of the three photoactive polymers already studied in the form of thin-films: rr-P3HT, PBDB-T and PTB7. First, I explored the influence on the energetics of the NPs and the stability of the colloid caused by using different aqueous antisolvent ionic strength during nanoprecipitation. Additionally, different polymer-to-surfactant mass ratios were screened. The study aimed to characterize the nanoparticles' morphology, energetics, stability and photogeneration capability. By means of a custom-built experiment, we find that all three tested materials exhibit photocathodic current generation and consequent positive charge accumulation due to reduction of acceptor molecules in water. The precipitation conditions in the nanoparticle synthesis lead to nanoparticles with size distributions that fit the limits for cell internalization as demonstrated by confocal imaging of the internalization in HUVEC cell line. When PBS is used as antisolvent during precipitation, a larger average radius is measured as compared with those produced in MilliQ. The effect is caused by the NaCl acting on kinetic and structural effects of the nanoparticle formation process. In the presence of Pluronic F127 as a surfactant, the radii evaluated from AFM and TEM differ significantly from those measured via DLS, suggesting that NPs mobility in the colloid is significantly influenced. Despite the z-potential is lowered, likely because of a slipping plane distancing from the polymer surface with the possibility to accommodate more counter-ions within the hydrodynamic radius, its presence enhances the stability and does not affect the internalization capabilities. The absorption spectra of the NPs precipitated in MilliQ and in PBS show clear differences, which are not reflected in an appreciable change in excitation and emission spectra. I concluded that these changes are either caused by a change in the reflectivity or in the different contribution of non-radiative states. Finally, to demonstrate photochemical functionality of the prepared nanoparticles we developed a chronoamperometric measurement scheme done with NP dispersions in PBS. All samples show a photocathodic response in agreement with the thin films. Spectroscopic measurements of the NP photoelectrochemical current agree well with absorption spectra and demonstrate that absorbed photons contribute equally to the photocurrent generation.

Furthermore, in-vitro experiments demonstrate that all the materials have a good biocompatibility both in dark and illuminated conditions. Interestingly, also in nanoparticles PTB7 outperformed the other polymers in different examined aspects: the NP spectrum extends more in the optical transparency window of biological tissue; its z-potential is overall the more negative and the average NPs size is the smallest. We thus provided a comprehensive physicochemical characterization of two new material alternative to P3HT for phototransducting nanoparticles, namely PBDB-T and PTB7, and explore the use of Pluronic F127 as an antiaggregant and its effects on the performances of these NPs.

The last part of my thesis results describes the characterization of porous P3HT thin films as prepared by our project partners in POLYMAT. Three different graft copolymers made of rra-P3HT and PLA, P3HT-*g*-PLA_1:99, P3HT-*g*-PLA_32:68, and P3HT-*g*-PLA_64:36, have been synthesized by chemical oxidative polymerization, tuning the ratio between 3HT monomer and EDOT-PLA macromonomer. After spin-coating the porosity was induced by PLA hydrolysis in presence of NaOH, and it was confirmed through nc-AFM measurements. They exhibit similar optical absorption spectra, but higher absorption coefficients as compared to rr-P3HT films. Increased capacitance is measured for these porous films as compared to the non-porous ones made of either one of the studied polymers. This is easily justifiable by the higher surface area exposed to the electrolyte, which could be also responsible for the fivefold increase in photocurrent measured in flat films with the same thickness and made of the same material. Aiming to in vivo devices, this would allow lower illumination intensities requirements. Finally, also these devices demonstrated no negative effects on cell viability both in dark and illuminated conditions, even though this last occurrence induce a higher intracellular ROS production when compared to flat rr-P3HT thin films.

The aim of these studies is to overcome the limitations of materials used for in-vivo stimulation of biological pathways. In the first chapter, we demonstrated that a planar heterojunction exhibits both photocapacitive and photofaradaic behavior. A simple model is proposed to explain the relationship between material properties and specific behavior, and developed a model to simulate photocurrent and photovoltage response under electrically floating conditions. To achieve predominant photofaradaic behavior targeting ORR over HER, we investigated conjugated donor polymers. Since these materials must be biocompatible and operate wirelessly in in-vivo conditions, low band-gap materials with high absorption coefficients are chosen, without the need for sacrificial molecules or back-electrodes, and with a preferential photofaradaic pathway towards hydrogen peroxide

generation through oxygen photoreduction. These conditions narrowed down the available choices to a small number of conjugated polymers. We then developed a technique to predict voltage based on illumination conditions for thin-film electrodes, which can be applied to other wireless devices, such as micro- and nanoparticles. We also proposed a method to analyze the photocharging behavior of microparticles made with the same polymers used in the thin-films. Finally, we proposed a new synthetic pathway to enhance the photocurrent and capacitance of polymeric thin-films by controlling their porosity.

In conclusion, being able to explain the photoelectrochemical properties of the device with their materials structure and energetics, is of great importance for the development of future wireless phototransductors. The development of an effective model has made it possible to predict the behavior of the system in open circuit conditions. It was demonstrated the correlation between the photovoltage generation dynamics and the energetic alignment of the systems' states with the acceptor molecules in water both for heterojunctions and for organic p-type photocathodes. Important correlations were extracted such as how the photocurrent is influenced by the charge accumulation, how photovoltage depends on the illumination intensity, the structural influence on photovoltage generation and the voltage dependence of the back-electron transfer. All this knowledge can now be transferred to the design and the optimization of novel devices able to target specific acceptors, to be selective on photocapacitive or photofaradaic operation modes and to improve the previously achieved performances. Furthermore, better illumination protocols can be employed which improve the required performance and waste less energy to reach the target.

# 5 Bibliography


1. Airaghi Leccardi, M. J. I. *et al.* Photovoltaic organic interface for neuronal stimulation in the near-infrared. *Commun. Mater.* **1**, 1–13 (2020).
2. Stoppacher, S. *et al.* Modeling external stimulation of excitable cells using a novel light-activated organic semiconductor technology. *Stud. Health Technol. Inform.* **271**, 9–16 (2020).
3. Rand, D. *et al.* Direct Electrical Neurostimulation with Organic Pigment Photocapacitors. *Adv. Mater.* **30**, 1–11 (2018).
4. Schmidt, T. *et al.* Light Stimulation of Neurons on Organic Photocapacitors Induces Action Potentials with Millisecond Precision. *Adv. Mater. Technol.* **7**, (2022).
5. Jakešová, M. *et al.* Optoelectronic control of single cells using organic photocapacitors. *Sci. Adv.* **5**, eaav5265 (2019).
6. Abdel Aziz, I. *et al.* Polythiophene-mediated light modulation of membrane potential and calcium signalling in human adipose-derived stem/stromal cells. *J. Mater. Chem. C* 9823–9833 (2022) doi:10.1039/d2tc01426b.
7. Lodola, F. *et al.* Conjugated polymers optically regulate the fate of endothelial colony-forming cells. *Sci. Adv.* **5**, (2019).
8. Milos, F. *et al.* High Aspect Ratio and Light-Sensitive Micropillars Based on a Semiconducting Polymer Optically Regulate Neuronal Growth. *ACS Appl. Mater. Interfaces* **13**, 23438–23451 (2021).
9. Onorato, G. *et al.* Optical Control of Tissue Regeneration through Photostimulation of Organic Semiconducting Nanoparticles. *Adv. Healthc. Mater.* **11**, 1–13 (2022).
10. Negri, S. *et al.* Conjugated polymers mediate intracellular Ca2+ signals in circulating endothelial colony forming cells through the reactive oxygen species-dependent activation of Transient Receptor Potential Vanilloid 1 (TRPV1). *Cell Calcium* **101**, 102502 (2022).
11. Moccia, F., Negri, S., Faris, P., Ronchi, C. & Lodola, F. Optical excitation of organic semiconductors as a highly selective strategy to induce vascular regeneration and tissue repair. *Vascul. Pharmacol.* **144**, 106998 (2022).
12. Piccolino, M. Luigi Galvani's path to animal electricity. *Comptes Rendus - Biol.* **329**, 303–318 (2006).
13. Hatsopoulos, N. G. & Donoghue, J. P. The science of neural interface systems. *Annu. Rev. Neurosci.* **32**, 249–266 (2009).
14. Anderson, J. M., Rodriguez, A. & Chang, D. T. Foreign body reaction to biomaterials. *Seminars in Immunology* vol. 20 86–100 (2008).
15. Kindermann, M., Schwaab, B., Berg, M. & Fröhlig, G. Longevity of dual chamber pacemakers: Device and patient related determinants. *PACE - Pacing Clin. Electrophysiol.* **24**, 810–815 (2001).
16. Hauser, R. G. The growing mismatch between patient longevity and the service life of implantable cardioverter-defibrillators. *J. Am. Coll. Cardiol.* **45**, 2022–2025 (2005).
17. Li, Y., Li, N., De Oliveira, N. & Wang, S. Implantable bioelectronics toward long-term

stability and sustainability. *Matter* **4**, 1125–1141 (2021).

18. Thimot, J. & Shepard, K. L. Bioelectronic devices: Wirelessly powered implants. *Nat. Biomed. Eng.* **1**, 1–2 (2017).
19. Sanjuan-Alberte, P. *et al.* Wireless Nanobioelectronics for Electrical Intracellular Sensing. *ACS Appl. Nano Mater.* **2**, 6397–6408 (2019).
20. Agarwal, K., Jegadeesan, R., Guo, Y. X. & Thakor, N. V. Wireless Power Transfer Strategies for Implantable Bioelectronics. *IEEE Rev. Biomed. Eng.* **10**, 136–161 (2017).
21. Li, Y. *et al.* Low-level laser therapy induces human umbilical vascular endothelial cell proliferation, migration and tube formation through activating the PI3K/Akt signaling pathway. *Microvasc. Res.* **129**, 103959 (2020).
22. Ghezzi, D. *et al.* A polymer optoelectronic interface restores light sensitivity in blind rat retinas. *Nat. Photonics* **7**, 400–406 (2013).
23. Antognazza, M. R., Aziz, I. A. & Lodola, F. Use of exogenous and endogenous photomediators as efficient ROS modulation tools: Results and perspectives for therapeutic purposes. *Oxid. Med. Cell. Longev.* **2019**, (2019).
24. Antognazza, M. R. *et al.* Characterization of a Polymer-Based, Fully Organic Prosthesis for Implantation into the Subretinal Space of the Rat. *Advanced Healthcare Materials* vol. 5 2271–2282 (2016).
25. Keum, H., Mccormick, M., Liu, P., Zhang, Y. & Omenetto, F. G. Epidermal Electronics. **333**, 838–844 (2011).
26. Kaltenbrunner, M. *et al.* An ultra-lightweight design for imperceptible plastic electronics. *Nature* **499**, 458–463 (2013).
27. Choi, S., Lee, H., Ghaffari, R., Hyeon, T. & Kim, D. H. Recent Advances in Flexible and Stretchable Bio-Electronic Devices Integrated with Nanomaterials. *Adv. Mater.* **28**, 4203–4218 (2016).
28. Lim, H. R. *et al.* Advanced Soft Materials, Sensor Integrations, and Applications of Wearable Flexible Hybrid Electronics in Healthcare, Energy, and Environment. *Adv. Mater.* **32**, 1–43 (2020).
29. Shi, C., Costa, T., Elloian, J., Zhang, Y. & Shepard, K. L. A 0.065-mm3 Monolithically-Integrated Ultrasonic Wireless Sensing Mote for Real-Time Physiological Temperature Monitoring. *IEEE Trans. Biomed. Circuits Syst.* **14**, 412–424 (2020).
30. Ghezzi, D. *et al.* A hybrid bioorganic interface for neuronal photoactivation. *Nat. Commun.* **2**, (2011).
31. Ferlauto, L. *et al.* Design and validation of a foldable and photovoltaic wide-field epiretinal prosthesis. *Nat. Commun.* **9**, 1–15 (2018).
32. Mathieson, K. *et al.* Photovoltaic retinal prosthesis with high pixel density. *Nat. Photonics* **6**, 391–397 (2012).
33. Shmilovitz, D., Ozeri, S., Wang, C. C. & Spivak, B. Noninvasive Control of the Power Transferred to an Implanted Device by an Ultrasonic Transcutaneous Energy Transfer Link. *IEEE Trans. Biomed. Eng.* **61**, 995–1004 (2014).
34. Ozeri, S. & Shmilovitz, D. Ultrasonic transcutaneous energy transfer for powering implanted devices. *Ultrasonics* **50**, 556–566 (2010).

35. Zhou, Y., Liu, C. & Huang, Y. Wireless power transfer for implanted medical application: A review. *Energies* **13**, (2020).

36. Agrawal, D. R. *et al.* Conformal phased surfaces for wireless powering of bioelectronic microdevices. *Nat. Biomed. Eng.* **1**, 1–9 (2017).

37. Smith, A. M., Mancini, M. C. & Nie, S. Bioimaging: Second window for in vivo imaging. *Nat. Nanotechnol.* **4**, 710–711 (2009).

38. Feron, K. *et al.* Organic bioelectronics: Materials and biocompatibility. *Int. J. Mol. Sci.* **19**, (2018).

39. Liu, Q. *et al.* 18% Efficiency organic solar cells. *Sci. Bull.* **65**, 272–275 (2020).

40. Knupfer, M. Exciton binding energies in organic semiconductors. *Appl. Phys. A Mater. Sci. Process.* **77**, 623–626 (2003).

41. Green, M. A. Improved value for the silicon free exciton binding energy. *AIP Adv.* **3**, (2013).

42. Manfredi, G., Colombo, E., Barsotti, J., Benfenati, F. & Lanzani, G. Photochemistry of Organic Retinal Prostheses. *Annu. Rev. Phys. Chem.* **70**, 99–121 (2019).

43. Hopkins, J. *et al.* Photoactive Organic Substrates for Cell Stimulation: Progress and Perspectives. *Adv. Mater. Technol.* **4**, 1–10 (2019).

44. Osterloh, F. E., Holmes, M. A., Chang, L., Moulé, A. J. & Zhao, J. Photochemical charge separation in poly(3-hexylthiophene) (P3HT) films observed with surface photovoltage spectroscopy. *J. Phys. Chem. C* **117**, 26905–26913 (2013).

45. Osterloh, F. E. *et al.* P3HT:PCBM bulk-heterojunctions: Observing interfacial and charge transfer states with surface photovoltage spectroscopy. *J. Phys. Chem. C* **118**, 14723–14731 (2014).

46. Đerek, V., Rand, D., Migliaccio, L., Hanein, Y. & Głowacki, E. D. Untangling Photofaradaic and Photocapacitive Effects in Organic Optoelectronic Stimulation Devices. *Front. Bioeng. Biotechnol.* **8**, 1–8 (2020).

47. Paltrinieri, T. *et al.* Understanding Photocapacitive and Photofaradaic Processes in Organic Semiconductor Photoelectrodes for Optobioelectronics. *Adv. Funct. Mater.* **2010116**, (2021).

48. Chiaravalli, G., Manfredi, G., Sacco, R. & Lanzani, G. Photoelectrochemistry and Drift-Diffusion Simulations in a Polythiophene Film Interfaced with an Electrolyte. *ACS Appl. Mater. Interfaces* **13**, 36595–36604 (2021).

49. Gryszel, M. *et al.* General Observation of Photocatalytic Oxygen Reduction to Hydrogen Peroxide by Organic Semiconductor Thin Films and Colloidal Crystals. *ACS Appl. Mater. Interfaces* **10**, 13253–13257 (2018).

50. Abdel Aziz, I. *et al.* Light-Triggered Electron Transfer between a Conjugated Polymer and Cytochrome C for Optical Modulation of Redox Signaling. *iScience* **23**, 101091 (2020).

51. Bossio, C. *et al.* Photocatalytic activity of polymer nanoparticles modulates intracellular calcium dynamics and reactive oxygen species in HEK-293 cells. *Front. Bioeng. Biotechnol.* **6**, 1–17 (2018).

52. Mosconi, E. *et al.* Surface Polarization Drives Photoinduced Charge Separation at the P3HT/Water Interface. *ACS Energy Lett.* **1**, 454–463 (2016).

53. Maya-Vetencourt, J. F. *et al.* Subretinally injected semiconducting polymer nanoparticles rescue vision in a rat model of retinal dystrophy. *Nat. Nanotechnol.* **15**, 698–708 (2020).

54. Zangoli, M. *et al.* Engineering thiophene-based nanoparticles to induce phototransduction in live cells under illumination. *Nanoscale* **9**, 9202–9209 (2017).

55. Martín, J. *et al.* Poly(3-hexylthiophene) nanowires in porous alumina: Internal structure under confinement. *Soft Matter* **10**, 3335–3346 (2014).

56. Nikić, M. *et al.* Micropyramid structured photo capacitive interfaces. *Nanotechnology* **33**, (2022).

57. Gryszel, M. & Głowacki, E. D. Organic thin film photofaradaic pixels for on-demand electrochemistry in physiological conditions. *Chem. Commun.* **56**, 1705–1708 (2020).

58. Lodola, F., Martino, N., Tullii, G., Lanzani, G. & Antognazza, M. R. Conjugated polymers mediate effective activation of the Mammalian Ion Channel Transient Receptor Potential Vanilloid 1. *Sci. Rep.* **7**, 1–10 (2017).

59. Antognazza, M. R. *et al.* Characterization of a Polymer-Based, Fully Organic Prosthesis for Implantation into the Subretinal Space of the Rat. *Adv. Healthc. Mater.* **5**, 2271–2282 (2016).

60. Bargigia, I. *et al.* The Photophysics of Polythiophene Nanoparticles for Biological Applications. *ChemBioChem* **20**, 532–536 (2019).

61. Yang, K. *et al.* Photoactive poly(3-hexylthiophene) nanoweb for optoelectrical stimulation to enhance neurogenesis of human stem cells. *Theranostics* **7**, 4591–4604 (2017).

62. Donahue, M. *et al.* Wireless optoelectronic devices for vagus nerve stimulation in mice. *J. Neural Eng.* **19**, (2022).

63. Vaquero, S. *et al.* Conjugated polymers for the optical control of the electrical activity of living cells. *J. Mater. Chem. B* **4**, 5272–5283 (2016).

64. Ohashi, M. *et al.* Hydrogen peroxide modulates neuronal excitability and membrane properties in ventral horn neurons of the rat spinal cord. *Neuroscience* **331**, 206–220 (2016).

65. Rudolph, M. & Ratcliff, E. L. Normal and inverted regimes of charge transfer controlled by density of states at polymer electrodes. *Nat. Commun.* **8**, 1–6 (2017).

66. Missey, F. *et al.* Organic electrolytic photocapacitors for stimulation of the mouse somatosensory cortex. *J. Neural Eng.* **18**, 2–3 (2021).

67. Missey, F. *et al.* Laser-Driven Wireless Deep Brain Stimulation using Temporal Interference and Organic Electrolytic Photocapacitors. *Adv. Funct. Mater.* **32**, (2022).

68. Gryszel, M., Markov, A., Vagin, M. & Głowacki, E. D. Organic heterojunction photocathodes for optimized photoelectrochemical hydrogen peroxide production. *J. Mater. Chem. A* **6**, 24709–24716 (2018).

69. Warczak, M., Gryszel, M., Jakešová, M., Derek, V. & Głowacki, E. D. Organic semiconductor perylenetetracarboxylic diimide (PTCDI) electrodes for electrocatalytic reduction of oxygen to hydrogen peroxide. *Chem. Commun.* **54**, 1960–1963 (2018).

70. Vanderroost, M., Ronsse, F., Dewettinck, K. & Pieters, G. Coating processes in fluidised beds: quality control model based on population balance theory. *Commun. Agric. Appl. Biol. Sci.* **73**, 231–235 (2008).

71. Dobrzanski, L. A. & Szindler. Sol gel TiO2 antireflection coatings for silicon solar cells. *J. Achiev. Mater. Manuf. Eng.* **52**, 7–14 (2012).

72. Scriven, L. E. Physics and Applications of DIP Coating and Spin Coating. *MRS Proc.* **121**, 717–729 (1988).

73. Emslie, A. G., Bonner, F. T. & Peck, L. G. Flow of a viscous liquid on a rotating disk. *J. Appl. Phys.* **29**, 858–862 (1958).

74. Wilson, S. K., Hunt, R. & Duffy, B. R. The rate of spreading in spin coating. *J. Fluid Mech.* **413**, 65–88 (2000).

75. Danglad-Flores, J., Eickelmann, S. & Riegler, H. Deposition of polymer films by spin casting: A quantitative analysis. *Chem. Eng. Sci.* **179**, 257–264 (2018).

76. Mirabito, T., Huet, B., Redwing, J. M. & Snyder, D. W. Influence of the Underlying Substrate on the Physical Vapor Deposition of Zn-Phthalocyanine on Graphene. *ACS Omega* **6**, 20598–20610 (2021).

77. Fortunato, E., Barquinha, P. & Martins, R. Oxide semiconductor thin-film transistors: A review of recent advances. *Adv. Mater.* **24**, 2945–2986 (2012).

78. Najim, A. A., Muhi, M. A. H., Gbashi, K. R. & Salih, A. T. Synthesis of Efficient and Effective γ-MnO2/α-Bi2O3/a-Si Solar Cell by Vacuum Thermal Evaporation Technique. *Plasmonics* **13**, 891–895 (2018).

79. Hao, Y., Seo, J. H., Hu, Y., Mao, H. Q. & Mittal, R. Flow physics and mixing quality in a confined impinging jet mixer. *AIP Adv.* **10**, (2020).

80. Horn, D. & Rieger, J. Organic Nanoparticles in Aqueous Phase. *Angew. Chem* **40**, 4330–4361 (2001).

81. D'Addio, S. M. & Prud'homme, R. K. Controlling drug nanoparticle formation by rapid precipitation. *Adv. Drug Deliv. Rev.* **63**, 417–426 (2011).

82. Dormidontova, E. E. Micellization kinetics in block copolymer solutions: scaling model. *Macromolecules* **32**, 7630–7644 (1999).

83. Garrett, J. L. & Munday, J. N. Fast, high-resolution surface potential measurements in air with heterodyne Kelvin probe force microscopy. *Nanotechnology* **27**, (2016).

84. Johnson, E. O. Measurement of minority carrier lifetimes with the surface photovoltage. *J. Appl. Phys.* **28**, 1349–1353 (1957).

85. Munakata, C., Nishimatsu, S., Honma, N. & Yagi, K. Ac Surface Photovoltages in Strongly-Inverted Oxidized P-type sIlicon Wafers. *Jpn. J. Appl. Phys.* **23**, 1451–1461 (1984).

86. Podolian, A., Kozachenko, V., Nadtochiy, A., Borovoy, N. & Korotchenkov, O. Photovoltage transients at fullerene-metal interfaces. *J. Appl. Phys.* **107**, (2010).

87. Bard, A. J. & Faulkner, L. R. Electrochemical Methods: Fundamentals and Applications. (2001).

88. Orazem, M. E. & Tribollet, B. *Electrochemical Impedance Spectroscopy*. (Wiley, 2017).

89. Macdonald, J. R. & Johnson, W. B. Fundamentals of Impedance Spectroscopy. in *Impedance Spectroscopy* 1–26 (John Wiley & Sons, Ltd, 2005). doi:https://doi.org/10.1002/0471716243.ch1.

90. Raistrick, I. D., Franceschetti, D. R. & Macdonald, J. R. Theory. in *Impedance Spectroscopy* 27–128 (John Wiley & Sons, Ltd, 2005). doi:https://doi.org/10.1002/0471716243.ch2.

91. Deleebeeck, L. & Veltzé, S. Electrochemical impedance spectroscopy study of commercial Li-ion phosphate batteries: A metrology perspective. *Int. J. Energy Res.* **44**, 7158–7182 (2020).

92. Bredar, A. R. C., Chown, A. L., Burton, A. R. & Farnum, B. H. Electrochemical Impedance

Spectroscopy of Metal Oxide Electrodes for Energy Applications. *ACS Appl. Energy Mater.* **3**, 66–98 (2020).

93. Xu, Y. *et al.* A review of impedance measurements of whole cells. *Biosens. Bioelectron.* **77**, 824–836 (2016).
94. Sacco, A. Electrochemical impedance spectroscopy: Fundamentals and application in dye-sensitized solar cells. *Renew. Sustain. Energy Rev.* **79**, 814–829 (2017).
95. Bandarenka, A. S. Exploring the interfaces between metal electrodes and aqueous electrolytes with electrochemical impedance spectroscopy. *Analyst* **138**, 5540–5554 (2013).
96. Wang, S. *et al.* Electrochemical impedance spectroscopy. *Nat. Rev. Methods Prim.* **1**, (2021).
97. Mironov, V. *Fundamentals of Scanning Probe Microscopy*. (2014).
98. García, R., Magerle, R. & Perez, R. Nanoscale compositional mapping with gentle forces. *Nat. Mater.* **6**, 405–411 (2007).
99. Rohwerder, M. & Turcu, F. High-resolution Kelvin probe microscopy in corrosion science: Scanning Kelvin probe force microscopy (SKPFM) versus classical scanning Kelvin probe (SKP). *Electrochim. Acta* **53**, 290–299 (2007).
100. Cheran, L. E., Johnstone, S., Sadeghi, S. & Thompson, M. Work-function measurement by high-resolution scanning Kelvin nanoprobe. *Meas. Sci. Technol.* **18**, 567–578 (2007).
101. Surplice, N. A. & D'Arcy, R. J. A critique of the Kelvin method of measuring work functions. *J. Phys. E.* **3**, 477–482 (1970).
102. Wicinski, M., Burgstaller, W. & Hassel, A. W. Lateral resolution in scanning Kelvin probe microscopy. *Corros. Sci.* **104**, 1–8 (2016).
103. Murrey, T. L. *et al.* Anion Exchange Doping: Tuning Equilibrium to Increase Doping Efficiency in Semiconducting Polymers. *J. Phys. Chem. Lett.* **12**, 1284–1289 (2021).
104. Wicinski, M., Burgstaller, W. & Hassel, A. W. Lateral resolution in scanning Kelvin probe microscopy. *Corros. Sci.* **104**, 1–8 (2016).
105. McMurray, H. N. & Williams, G. Probe diameter and probe-specimen distance dependence in the lateral resolution of a scanning Kelvin probe. *J. Appl. Phys.* **91**, 1673–1679 (2002).
106. Müller-Buschbaum, P. Grazing incidence small-angle X-ray scattering: An advanced scattering technique for the investigation of nanostructured polymer films. *Anal. Bioanal. Chem.* **376**, 3–10 (2003).
107. Mahmood, A. & Wang, J. L. A Review of Grazing Incidence Small- and Wide-Angle X-Ray Scattering Techniques for Exploring the Film Morphology of Organic Solar Cells. *Sol. RRL* **4**, 1–39 (2020).
108. Hexemer, A. & Müller-Buschbaum, P. Advanced grazing-incidence techniques for modern soft-matter materials analysis. *IUCrJ* **2**, 106–125 (2015).
109. Ezquerra, T. A., García-Gutiérrez, M., Nogales, A. & Gómez, M. *Applications of Synchrotron Light to Scattering and Diffraction*. *Training & Development Journal* vol. 33 (2009).
110. Patterson, A. L. The scherrer formula for X-ray particle size determination. *Phys. Rev.* **56**, 978–982 (1939).
111. Ameh, E. S. A review of basic crystallography and x-ray diffraction applications. *Int. J. Adv. Manuf. Technol.* **105**, 3289–3302 (2019).

112. Chabinyc, M. L. X-ray Scattering from Films of Semiconducting Polymers. *Polym. Rev.* **48**, 463–492 (2008).

113. Champness, P. E. *Electron Diffraction in the Transmission Electron Microscope*. (Garland Science, 2001). doi:https://doi.org/10.1201/9781003076872.

114. Kirkland, E. J. *Advanced Computing in Electron Microscopy*. (Springer, 2010).

115. Kvaalen, E. Schematic view of imaging and diffraction modes in TEM. https://en.wikipedia.org/wiki/Transmission_electron_microscopy#/media/File:Schematic_view_of_imaging_and_diffraction_modes_in_TEM.tif.

116. Housecroft, C. E. & Constable, E. C. *Chemistry: an introduction to organic, inorganic and physical chemistry*. (2010).

117. CULLIFORD, B. J. & NICKOLLS, L. C. THE BENZIDINE TEST: A CRITICAL REVIEW. *J. Forensic Sci.* **9**, 175–191 (1964).

118. Josephy, D., Eling, T. & Mason, R. The Horseradish Peroxidase-catalyzed Oxidation of 3,5,3',5'- Tetramethylbenzidine. *J. Biol. Chem.* **257**, 3669–3675 (1982).

119. Wojtala, A. *et al. Methods to monitor ROS production by fluorescence microscopy and fluorometry*. *Methods in Enzymology* vol. 542 (Elsevier Inc., 2014).

120. Winterbourn, C. C. The challenges of using fluorescent probes to detect and quantify specific reactive oxygen species in living cells. *Biochim. Biophys. Acta - Gen. Subj.* **1840**, 730–738 (2014).

121. Wardman, P. Fluorescent and luminescent probes for measurement of oxidative and nitrosative species in cells and tissues: Progress, pitfalls, and prospects. *Free Radic. Biol. Med.* **43**, 995–1022 (2007).

122. Kumar, P., Nagarajan, A. & Uchil, P. D. Analysis of cell viability by the alamarblue assay. *Cold Spring Harb. Protoc.* **2018**, 462–464 (2018).

123. Di Maria, F., Lodola, F., Zucchetti, E., Benfenati, F. & Lanzani, G. The evolution of artificial light actuators in living systems: From planar to nanostructured interfaces. *Chem. Soc. Rev.* **47**, 4757–4780 (2018).

124. Feyen, P. *et al.* Light-evoked hyperpolarization and silencing of neurons by conjugated polymers. *Sci. Rep.* **6**, 1–14 (2016).

125. Someya, T., Bao, Z. & Malliaras, G. G. The rise of plastic bioelectronics. *Nature* vol. 540 379–385 (2016).

126. Diao, Y. *et al.* Solution coating of large-area organic semiconductor thin films with aligned single-crystalline domains. *Nat. Mater.* **12**, 665–671 (2013).

127. Xu, J. *et al.* Highly stretchable polymer semiconductor films through the nanoconfinement effect. *Science (80-. ).* **355**, 59–64 (2017).

128. Khodagholy, D. *et al.* NeuroGrid: Recording action potentials from the surface of the brain. *Nat. Neurosci.* **18**, 310–315 (2015).

129. Marzocchi, M. *et al.* Physical and Electrochemical Properties of PEDOT:PSS as a Tool for Controlling Cell Growth. *ACS Appl. Mater. Interfaces* **7**, 17993–18003 (2015).

130. Tonazzini, I. *et al.* Multiscale morphology of organic semiconductor thin films controls the adhesion and viability of human neural cells. *Biophys. J.* **98**, 2804–2812 (2010).

131. Bystrenova, E. *et al.* Neural networks grown on organic semiconductors. *Adv. Funct. Mater.* **18**, 1751–1756 (2008).

132. Cramer, T. *et al.* Water-gated organic field effect transistors-opportunities for biochemical sensing and extracellular signal transduction. *Journal of Materials Chemistry B* vol. 1 3728–3741 (2013).

133. Bobbert, P. A., Sharma, A., Mathijssen, S. G. J., Kemerink, M. & De Leeuw, D. M. Operational stability of organic field-effect transistors. *Adv. Mater.* **24**, 1146–1158 (2012).

134. Proctor, C. M., Rivnay, J. & Malliaras, G. G. Understanding volumetric capacitance in conducting polymers. *J. Polym. Sci. Part B Polym. Phys.* **54**, 1433–1436 (2016).

135. Rivnay, J., Wang, H., Fenno, L., Deisseroth, K. & Malliaras, G. G. Next-generation probes, particles, and proteins for neural interfacing. *Science Advances* vol. 3 e1601649 (2017).

136. Decataldo, F. *et al.* Stretchable Low Impedance Electrodes for Bioelectronic Recording from Small Peripheral Nerves. *Sci. Rep.* **9**, 1–9 (2019).

137. Rojas, H. C. *et al.* Polymer-based photocathodes with a solution-processable cuprous iodide anode layer and a polyethyleneimine protective coating. *Energy Environ. Sci.* **9**, 3710–3723 (2016).

138. Hursán, D., Kormányos, A., Rajeshwar, K. & Janáky, C. Polyaniline films photoelectrochemically reduce CO2 to alcohols. *Chem. Commun.* **52**, 8858–8861 (2016).

139. Yohannes, T., Solomon, T. & Inganäs, O. Polymer-electrolyte-based photoelectrochemical solar energy conversion with poly(3-methylthiophene) photoactive electrode. *Synth. Met.* **82**, 215–220 (1996).

140. Desilvestro, J. & Haas, O. Electrocatalytic behavior of polyaniline in the dark and under illumination. *Electrochim. Acta* **36**, 361–367 (1991).

141. Kilmartin, P. A. & Wright, G. A. Anion insertion and expulsion in polyaniline electrodes studied by photocurrent transients. *Electrochim. Acta* **43**, 3091–3103 (1998).

142. Giovannitti, A. *et al.* Energetic Control of Redox-Active Polymers toward Safe Organic Bioelectronic Materials. *Adv. Mater.* **32**, 1–9 (2020).

143. Kyndiah, A. *et al.* Charge Transfer and Percolation in C60/Pentacene Field-Effect Transistors. *Adv. Electron. Mater.* **1**, 1400036 (2015).

144. Tennyson, E. M. *et al.* Nanoimaging of Open-Circuit Voltage in Photovoltaic Devices. *Adv. Energy Mater.* **5**, 1–8 (2015).

145. Memming, R. *Semiconductor electrochemistry*. *Semiconductor Electrochemistry* (2015). doi:10.1007/978-3-319-29641-8_1.

146. Sugie, A., Han, W., Shioya, N., Hasegawa, T. & Yoshida, H. Structure-Dependent Electron Affinities of Perylene Diimide-Based Acceptors. *J. Phys. Chem. C* **124**, 9765–9773 (2020).

147. Krumova, K. & Cosa, G. Chapter 1. Overview of Reactive Oxygen Species. in *Singlet Oxygen - Applications in Biosciences and Nanosciences* 1–21 (The Royal Society of Chemistry, 2016). doi:10.1039/9781782622208-00001.

148. Krol, R. van de & Grätzel, M. PHOTOELECTROCHEMICAL HYDROGEN PRODUCTION. in *Solar-Hydrogen Energy Systems* 137–169 (1979). doi:10.1016/b978-0-08-022713-9.50013-6.

149. Fahlman, M. *et al.* Interfaces in organic electronics. *Nat. Rev. Mater.* **4**, 627–650 (2019).

150. Jonsson, A. *et al.* Bioelectronic neural pixel: Chemical stimulation and electrical sensing at the same site. *Proc. Natl. Acad. Sci. U. S. A.* **113**, 9440–9445 (2016).

151. Keene, S. T. *et al.* Exploiting mixed conducting polymers in organic and bioelectronic devices. *Phys. Chem. Chem. Phys.* **24**, 19144–19163 (2022).

152. Goetz, G. A. & Palanker, D. V. Electronic approaches to restoration of sight. *Reports Prog. Phys.* **79**, (2016).

153. Maya-Vetencourt, J. F. *et al.* A fully organic retinal prosthesis restores vision in a rat model of degenerative blindness. *Nat. Mater.* **16**, 681–689 (2017).

154. Botzanowski, B. *et al.* Noninvasive Stimulation of Peripheral Nerves using Temporally-Interfering Electrical Fields. *Adv. Healthc. Mater.* **11**, 1–10 (2022).

155. Silverå Ejneby, M. *et al.* Chronic electrical stimulation of peripheral nerves via deep-red light transduced by an implanted organic photocapacitor. *Nat. Biomed. Eng.* **6**, 741–753 (2022).

156. Ruprai, H. *et al.* Porous Chitosan Films Support Stem Cells and Facilitate Sutureless Tissue Repair. *ACS Appl. Mater. Interfaces* **11**, 32613–32622 (2019).

157. Mawad, D. *et al.* A single component conducting polymer hydrogel as a scaffold for tissue engineering. *Adv. Funct. Mater.* **22**, 2692–2699 (2012).

158. Wei, R., Gryszel, M., Migliaccio, L. & Głowacki, E. D. Tuning photoelectrochemical performance of poly(3-hexylthiophene) electrodes: Via surface structuring. *J. Mater. Chem. C* **8**, 10897–10906 (2020).

159. Martino, N. *et al.* Photothermal cellular stimulation in functional bio-polymer interfaces. *Sci. Rep.* **5**, 1–8 (2015).

160. Bellani, S. *et al.* Reversible P3HT/oxygen charge transfer complex identification in thin films exposed to direct contact with water. *J. Phys. Chem. C* **118**, 6291–6299 (2014).

161. Benfenati, F. & Lanzani, G. Reply to: Questions about the role of P3HT nanoparticles in retinal stimulation. *Nat. Nanotechnol.* **16**, 1333–1336 (2021).

162. Maity, A. *et al.* Resonant Enhancement of Polymer–Cell Optostimulation by a Plasmonic Metasurface. *ACS Omega* (2022) doi:10.1021/acsomega.2c04812.

163. Mitraka, E. *et al.* Electrocatalytic Production of Hydrogen Peroxide with Poly(3,4-ethylenedioxythiophene) Electrodes. *Adv. Sustain. Syst.* **3**, 1–6 (2019).

164. Suppes, G. M., Fortin, P. J. & Holdcroft, S. Photoelectrochemical Hydrogen Evolution: Single-Layer, Conjugated Polymer Films Bearing Surface-Deposited Pt Nanoparticles. *J. Electrochem. Soc.* **162**, H551–H556 (2015).

165. Yang, K. *et al.* Photoactive poly(3-hexylthiophene) nanoweb for optoelectrical stimulation to enhance neurogenesis of human stem cells. *Theranostics* vol. 7 4591–4604 (2017).

166. Panieri, E. & Santoro, M. M. ROS signaling and redox biology in endothelial cells. *Cell. Mol. Life Sci.* **72**, 3281–3303 (2015).

167. Sies, H. & Jones, D. P. Reactive oxygen species (ROS) as pleiotropic physiological signalling agents. *Nat. Rev. Mol. Cell Biol.* **21**, 363–383 (2020).

168. Sies, H. Oxidative stress: Concept and some practical aspects. *Antioxidants* **9**, 1–6 (2020).

169. Jones, D. P. & Sies, H. The Redox Code. *Antioxidants Redox Signal.* **23**, 734–746 (2015).

170. Zhang, L. *et al.* Biochemical basis and metabolic interplay of redox regulation. *Redox Biol.* **26**,

101284 (2019).

171. Andrienko, D. *et al. P3HT Revisited – from Molecular Scale to Solar Cell Devices*. (Springer, 2014).
172. Xue, Y. *et al.* Toward Scalable PbS Quantum Dot Solar Cells Using a Tailored Polymeric Hole Conductor. *ACS Energy Lett.* 2850–2858 (2019) doi:10.1021/acsenergylett.9b02301.
173. Yi, Y., Lyon, J. E., Beerbom, M. M. & Schlaf, R. Characterization of indium tin oxide surfaces and interfaces using low intensity x-ray photoemission spectroscopy. *J. Appl. Phys.* **100**, (2006).
174. Aygül, U. *et al.* Electronic properties of interfaces between PCPDTBT and prototypical electrodes studied by photoemission spectroscopy. *ChemPhysChem* **12**, 2345–2351 (2011).
175. Wang, C. *et al.* Ternary Organic Solar Cells with Minimum Voltage Losses. *Adv. Energy Mater.* **7**, 1–10 (2017).
176. Bencheikh, F., Duché, D., Ruiz, C. M., Simon, J. J. & Escoubas, L. Study of Optical Properties and Molecular Aggregation of Conjugated Low Band Gap Copolymers: PTB7 and PTB7-Th. *J. Phys. Chem. C* **119**, 24643–24648 (2015).
177. Dayal, S., Kopidakis, N., Olson, D. C., Ginley, D. S. & Rumbles, G. Photovoltaic devices with a low band gap polymer and CdSe nanostructures exceeding 3% efficiency. *Nano Lett.* **10**, 239–242 (2010).
178. Umeyama, T. *et al.* Efficient light-harvesting, energy migration, and charge transfer by nanographene-based nonfullerene small-molecule acceptors exhibiting unusually long excited-state lifetime in the film state. *Chem. Sci.* **11**, 3250–3257 (2020).
179. Zotti, G., Schiavon, G. & Zecchin, S. Irreversible processes in the electrochemical reduction of polythiophenes. Chemical modifications of the polymer and charge-trapping phenomena. *Synth. Met.* **72**, 275–281 (1995).
180. Choi, W. T. & Bard, A. J. Doping of the Semiconducting Polymer Poly(3-hexylthiophene) (P3HT) in Organic Photoelectrochemical Cells. *J. Phys. Chem. C* **124**, 3439–3447 (2020).
181. Hintz, H. *et al.* Photodegradation of P3HT - A systematic study of environmental factors. *Chem. Mater.* **23**, 145–154 (2011).
182. Brinkmann, M. Structure and morphology control in thin films of regioregular poly(3-hexylthiophene). *J. Polym. Sci. Part B Polym. Phys.* **49**, 1218–1233 (2011).
183. Kleinschmidt, A. T., Root, S. E. & Lipomi, D. J. Poly(3-hexylthiophene) (P3HT): Fruit fly or outlier in organic solar cell research? *J. Mater. Chem. A* **5**, 11396–11400 (2017).
184. Brixi, S., Melville, O. A., Boileau, N. T. & Lessard, B. H. The influence of air and temperature on the performance of PBDB-T and P3HT in organic thin film transistors. *J. Mater. Chem. C* **6**, 11972–11979 (2018).
185. Zheng, Z. *et al.* PBDB-T and its derivatives: A family of polymer donors enables over 17% efficiency in organic photovoltaics. *Mater. Today* **35**, 115–130 (2020).
186. Lu, L. & Yu, L. Understanding low bandgap polymer PTB7 and optimizing polymer solar cells based on IT. *Adv. Mater.* **26**, 4413–4430 (2014).
187. Guo, J., Ohkita, H., Benten, H. & Ito, S. Near-IR femtosecond transient absorption spectroscopy of ultrafast polaron and triplet exciton formation in polythiophene films with different regioregularities. *J. Am. Chem. Soc.* **131**, 16869–16880 (2009).

188. Zhou, Q. & Shi, G. Conducting Polymer-Based Catalysts. *J. Am. Chem. Soc.* **138**, 2868–2876 (2016).

189. Josephy, P. D., Eling, T. & Mason, R. P. The horseradish peroxidase-catalyzed oxidation of 3,5,3',5'-tetramethylbenzidine. Free radical and charge-transfer complex intermediates. *J. Biol. Chem.* **257**, 3669–3675 (1982).

190. Volpe, G., Compagnone, D., Draisci, R. & Palleschi, G. 3,3′,5,5′-Tetramethylbenzidine as electrochemical substrate for horseradish peroxidase based enzyme immunoassays. A comparative study. *Analyst* **123**, 1303–1307 (1998).

191. Marquez, L. A. & Dunford, H. B. Mechanism of the oxidation of 3,5,3',5'-tetramethylbenzidine by myeloperoxidase determined by transient- and steady-state kinetics. *Biochemistry* **36**, 9349–9355 (1997).

192. Rhee, S. G., Chang, T. S., Jeong, W. & Kang, D. Methods for detection and measurement of hydrogen peroxide inside and outside of cells. *Mol. Cells* **29**, 539–549 (2010).

193. Mitraka, E. *et al.* Electrocatalytic Production of Hydrogen Peroxide with Poly(3,4-ethylenedioxythiophene) Electrodes. *Adv. Sustain. Syst.* **3**, 1800110 (2019).

194. Petigara, B. R., Blough, N. V. & Mignerey, A. C. Mechanisms of hydrogen peroxide decomposition in soils. *Environ. Sci. Technol.* **36**, 639–645 (2002).

195. Feng, Z. *et al.* Selectively Photoelectrocatalytic Reduction of Oxygen to Hydroxyl Radical and Singlet Oxygen: Mechanism and Validation in Coal Wastewater. *Appl. Catal. B Environ.* **286**, 119908 (2021).

196. Xu, X. *et al.* The construction of conjugated organic polymers containing phenanthrenequinone redox centers for visible-light-driven H2O2 production from H2O and O2 without any additives. *Chem. Eng. J.* **454**, 139929 (2023).

197. Enengl, C. *et al.* Doping-Induced Absorption Bands in P3HT: Polarons and Bipolarons. *ChemPhysChem* **17**, 3830 (2016).

198. Hu, Z. *et al.* An insight into non-emissive excited states in conjugated polymers. *Nat. Commun.* **6**, (2015).

199. Wu, D. & Yotnda, P. Production and detection of reactive oxygen species (ROS) in cancers. *J. Vis. Exp.* 2–5 (2011) doi:10.3791/3357.

200. Oka, K., Winther-Jensen, B. & Nishide, H. Organic π-Conjugated Polymers as Photocathode Materials for Visible-Light-Enhanced Hydrogen and Hydrogen Peroxide Production from Water. *Adv. Energy Mater.* **11**, (2021).

201. Migliaccio, L., Gryszel, M., Derek, V., Pezzella, A. & Głowacki, E. D. Aqueous photo(electro)catalysis with eumelanin thin films. *Mater. Horizons* **5**, 984–990 (2018).

202. Yan, H. *et al.* Regulation the reactive oxygen species on conjugated polymers for highly efficient photocatalysis. *Appl. Catal. B Environ.* **314**, 121488 (2022).

203. Otep, S., Michinobu, T. & Zhang, Q. Pure Organic Semiconductor-Based Photoelectrodes for Water Splitting. *Sol. RRL* **4**, (2020).

204. Yao, L., Rahmanudin, A., Guijarro, N. & Sivula, K. Organic Semiconductor Based Devices for Solar Water Splitting. *Adv. Energy Mater.* **8**, 1–18 (2018).

205. Thangamuthu, M. *et al.* Polymer Photoelectrodes for Solar Fuel Production: Progress and Challenges. *Chemical Reviews* vol. 122 11778–11829 (2022).

206. Miyasaka, T. & Murakami, T. N. The photocapacitor: An efficient self-charging capacitor for direct storage of solar energy. *Appl. Phys. Lett.* **85**, 3932–3934 (2004).

207. Di Maria, F., Lodola, F., Zucchetti, E., Benfenati, F. & Lanzani, G. The evolution of artificial light actuators in living systems: From planar to nanostructured interfaces. *Chem. Soc. Rev.* **47**, 4757–4780 (2018).

208. Zhang, X., Dong, H. & Hu, W. Organic Semiconductor Single Crystals for Electronics and Photonics. *Adv. Mater.* **30**, 1–34 (2018).

209. Otellin, V. A. & Korzhevskii, D. E. Formation and structural organization of a barrier on the brain outer surface. *Morfologiia* **122**, 14–18 (2002).

210. El-Rashiedy, O. A. & Holdcroft, S. Photoelectrochemical properties of poly(3-alkylthiophene) films in aqueous solution. *J. Phys. Chem.* **100**, 5481–5484 (1996).

211. Chenais, N. A. L., Leccardi, M. J. I. A. & Ghezzi, D. Capacitive-like photovoltaic epiretinal stimulation enhances and narrows the network-mediated activity of retinal ganglion cells by recruiting the lateral inhibitory network. *J. Neural Eng.* **16**, ab3913 (2019).

212. DiFrancesco, M. L. *et al.* A hybrid P3HT-Graphene interface for efficient photostimulation of neurons. *Carbon N. Y.* **162**, 308–317 (2020).

213. Noori, K. & Giustino, F. Ideal energy-level alignment at the ZnO/P3HT photovoltaic interface. *Adv. Funct. Mater.* **22**, 5089–5095 (2012).

214. Oliveira, E. F. & Lavarda, F. C. Effect of the length of alkyl side chains in the electronic structure of conjugated polymers. *Mater. Res.* **17**, 1369–1374 (2014).

215. Schneider, M. *et al.* Band bending at the P3HT/ITO interface studied by photoelectron spectroscopy. *Org. Electron.* **15**, 1552–1556 (2014).

216. Li, H., Winget, P. & Brédas, J. L. Transparent conducting oxides of relevance to organic electronics: Electronic structures of their interfaces with organic layers. *Chem. Mater.* **26**, 631–646 (2014).

217. Suppes, G., Ballard, E. & Holdcroft, S. Aqueous photocathode activity of regioregular poly(3-hexylthiophene). *Polym. Chem.* **4**, 5345–5350 (2013).

218. Fumagalli, F. *et al.* Hybrid organic-inorganic H2-evolving photocathodes: Understanding the route towards high performance organic photoelectrochemical water splitting. *J. Mater. Chem. A* **4**, 2178–2187 (2016).

219. Saba, M. I. & Mattoni, A. Effect of thermodynamics and curvature on the crystallinity of P3HT thin films on ZnO: Insights from atomistic simulations. *J. Phys. Chem. C* **118**, 4687–4694 (2014).

220. Bellani, S. *et al.* Hybrid Organic/Inorganic Nanostructures for Highly Sensitive Photoelectrochemical Detection of Dissolved Oxygen in Aqueous Media. *Adv. Funct. Mater.* **25**, 4531–4538 (2015).

221. Porrazzo, R. *et al.* Field-effect and capacitive properties of water-gated transistors based on polythiophene derivatives. *APL Mater.* **3**, 2014–2015 (2015).

222. Yimer, Y. Y. & Dhinojwala, A. Interfacial properties of free-standing poly (3-hexylthiophene) films. *Jpurnal Chem. Phys.* **044703**, 1–2 (2012).

223. Bellani, S. *et al.* The study of polythiophene/water interfaces by sum-frequency generation spectroscopy and molecular dynamics simulations. *J. Mater. Chem. B* **3**, 6429–6438 (2015).

224. Hains, A. W., Liu, J., Martinson, A. B. F., Irwin, M. D. & Marks, T. J. Anode interfacial tuning via electron-blocking/hole-transport layers and indium tin oxide surface treatment in bulk-heterojunction organic photovoltaic cells. *Adv. Funct. Mater.* **20**, 595–606 (2010).

225. Chung, H. Y. *et al.* Influence of Intramolecular Charge-Transfer Characteristics of Excitons on Polaron Generation at the Donor/Acceptor Interface in Polymer Solar Cells. *J. Phys. Chem. C* **125**, 18352–18361 (2021).

226. Zhuo, J. M. *et al.* Direct spectroscopic evidence for a photodoping mechanism in polythiophene and poly(bithiophene-alt-thienothiophene) organic semiconductor thin films involving oxygen and sorbed moisture. *Adv. Mater.* **21**, 4747–4752 (2009).

227. Yao, L. *et al.* Establishing Stability in Organic Semiconductor Photocathodes for Solar Hydrogen Production. *J. Am. Chem. Soc.* **142**, 7795–7802 (2020).

228. Sakata, T., Kawai, T. & Tanimura, K. PHOTOVOLTAIC EFFECT AT THE INTERFACE BETWEEN SEMICONDUCTOR AND ELECTROLYTE. *Ber Bunsenges Phys Chem* **83**, 486–490 (1979).

229. Bisquert, J., Zaban, A. & Salvador, P. Analysis of the mechanisms of electron recombination in nanoporous TiO2 dye-sensitized solar cells. Nonequilibrium steady-state statistics and interfacial electron transfer via surface states. *J. Phys. Chem. B* **106**, 8774–8782 (2002).

230. Zucchetti, E. *et al.* Poly(3-hexylthiophene) nanoparticles for biophotonics: study of the mutual interaction with living cells. *J. Mater. Chem. B* **5**, 565–574 (2017).

231. Moccia, F., Antognazza, M. R. & Lodola, F. Towards Novel Geneless Approaches for Therapeutic Angiogenesis. *Front. Physiol.* **11**, (2021).

232. Fu, H., Wang, Z. & Sun, Y. Polymer Donors for High-Performance Non-Fullerene Organic Solar Cells. *Angew. Chemie - Int. Ed.* **58**, 4442–4453 (2019).

233. Couvreur, P. *Polyalkylcyanoacrylates as colloidal drug carriers*. *Critical reviews in therapeutic drug carrier systems* vol. 5 (1988).

234. Dekker, M. *Colloidal drug delivery systems*. *Journal of Controlled Release* (1994).

235. Rao, J. P. & Geckeler, K. E. Polymer nanoparticles: Preparation techniques and size-control parameters. *Prog. Polym. Sci.* **36**, 887–913 (2011).

236. Anton, N., Benoit, J. P. & Saulnier, P. Design and production of nanoparticles formulated from nano-emulsion templates-A review. *J. Control. Release* **128**, 185–199 (2008).

237. Mishra, B., Patel, B. B. & Tiwari, S. Colloidal nanocarriers: a review on formulation technology, types and applications toward targeted drug delivery. *Nanomedicine Nanotechnology, Biol. Med.* **6**, 9–24 (2010).

238. Fessi, H., Puisieux, F., Devissaguet, J. P., Ammoury, N. & Benita, S. Nanocapsule formation by interfacial polymer deposition following solvent displacement. *Int. J. Pharm.* **55**, R1–R4 (1989).

239. Li, N., Nikoubashman, A. & Panagiotopoulos, A. Z. Self-Assembly of Polymer Blends and Nanoparticles through Rapid Solvent Exchange. *Langmuir* **35**, 3780–3789 (2019).

240. Saad, W. S. & Prud'Homme, R. K. Principles of nanoparticle formation by flash nanoprecipitation. *Nano Today* **11**, 212–227 (2016).

241. Pagels, R. F., Edelstein, J., Tang, C. & Prud'homme, R. K. Controlling and Predicting Nanoparticle Formation by Block Copolymer Directed Rapid Precipitations. *Nano Lett.* **18**,

1139–1144 (2018).

242. Medina Leyte, D. J., Domínguez Pérez, M., Mercado, I., Villarrreal Molina, M. T. & Jacobo Albavera, L. applied sciences Use of Human Umbilical Vein Endothelial Cells ( HUVEC ) as a Model to Study Cardiovascular Disease : *Appl. Sci.* (2020).

243. Murthy, S. K. Nanoparticles in modern medicine: state of the art and future challenges. *Int. J. Nanomedicine* **2**, 129–41 (2007).